RATIONAL DESIGN OF CHEMICAL TOOLS FOR IN VIVO APPLICATIONS VIA PHOTOACOUSTIC IMAGING

BY

MELISSA LUCERO

DISSERTATION

Submitted in partial fulfillment of the requirements
for the degree of Doctor of Philosophy in Chemistry
in the Graduate College of the
University of Illinois Urbana-Champaign, 2022

Urbana, Illinois

Doctoral Committee:

Associate Professor Jefferson K. Chan, Chair
Professor Steven Zimmerman
Assistant Professor Hee-Sun Han
Assistant Professor Yun-Sheng Chen

ABSTRACT

The combination of activity-based sensing and photoacoustic imaging has allowed for the development of probes that can be used to image enzyme activity (e.g., NTR, FAAH, and MGL), reactive species (e.g., peroxynitrite, nitric oxide, and glutathione) and metal ions (e.g., iron, copper, and calcium). Activity-based sensing leverages the chemical reactivity of biological targets to elicit a readout that can be used to assess the activity of the target. Work in this area has proven to be essential for understanding biological processes and diseases in their native environment. This is made possible by photoacoustic imaging which uses safe, non-ionizing light to generate ultrasound in tissue of live animals. Chapter 1 will introduce how activity-based sensing has been used in the development of various photoacoustic probes. Specifically, this chapter will discuss the design and development of initial work in this area. Chapter 2 will describe work in developing photoacoustic tools for copper sensing in various human disease states. Chapter 3 presents the first application of photoacoustic imaging in the development of companion diagnostics. Importantly, this work introduces a physical organic approach towards probe development. Chapter 4 further establishes the physical organic approach with work that introduces first small-molecule NIR-II photoacoustic probe for in vivo sensing of nitric oxide in murine models of cancer. Lastly, chapter 5 discusses work on understanding the effects of lifestyle habits on inflammation by measuring the activity of fatty acid metabolism using enzyme specific probes. The work herein describes vast applications of photoacoustic imaging and promise in the clinical setting.

ACKNOWLEDGMENTS

I would like to first thank my advisor Prof. Jeff Chan for all the support and mentorship he has provided to me during my time at UIUC. I am appreciative and grateful for the opportunity to be a part of the Chan Lab. I thank you for challenging me and facilitating my development as a scientist. Through your mentorship, I have learned various new skills that will be valuable for the rest of my career as a scientist. It was important to me that you were not only passionate about research but also teaching and mentoring. This created an environment where I would not be reluctant to ask questions when necessary. Over the years, you have essentially become a role model for me in science. I would also like to thank the rest of my thesis committee for their support throughout all my degree milestones.

Next, I would like to acknowledge and thank my previous research mentors from my undergraduate career (Prof, Marcin Ptaszek, Dr. Joshua Akhigbe, Prof. Susan McConnell, and Dr. Whitney Heavner). They provided my first research experiences which kept me motivated and supported to move on to graduate school.

Finally, I would like to thank the Chan Lab for providing a collaborative and friendly environment to conduct research. The diverse environment was also important for providing new viewpoints and perspectives. In addition, I want to acknowledge all of the undergraduate students I had the pleasure of working with: David Moreno, Xin Huang, Chloe Zhang, Valeria Garcia, Yuqi Tang, Shengzhang Su, and Nathan Moretta. Importantly, I would like to thank my family for the consistent motivation, encouragement, and support throughout my time in graduate school since I would not have been able to do any of this without them.

To my family

TABLE OF CONTENTS

CHAPTER 1: ACTIVITY-BASED SENSING WITH PHOTOACOUSTIC IMAGING

1.1 Background and significance

Activity-based sensing (ABS) was first coined by Christopher Chang in 2007.[1] This type of approach mainly involved the application of fluorescence as the molecular imaging modality. ABS originates from supramolecular chemistry where lock and key recognition was pioneered. This work in molecular recognition was awarded the Nobel Prize in Chemistry in 1987.[2] It was Tsien and coworkers who expanded on the lock and key method from selective chelators to fluorescent sensors. Since then, a variety of reactions have been explored to sense the activity of enzymes and small molecule reactive species. Some examples include oxidative organic reactions for analysis of hydrogen peroxide, peroxynitrite, hypochlorous acid, and nitric oxide; reductive organic reactions for glutathione, hydrogen sulfide, and cysteine; and redox reactions with metal ions.

It is important to note that ABS probes have been implemented in a range of different imaging modalities aside from fluorescence. For instance, probes have been developed for magnetic resonance imaging (MRI), positron emission tomography (PET), luminescence imaging, and photoacoustic (PA) imaging. Each modality has their own set of unique advantages and limitations.

1.1.1 Magnetic resonance imaging

Although MRI is a common and clinically approved imaging technology, there are no MRI ABS agents approved for clinical use or diagnosis. There are a few reasons that make using MRI challenging for ABS applications. For instance, MRI is an expensive procedure that is uncomfortable for some patients. In addition, due to the strong magnetic field used it can potentially damage devices such as pacemakers that are implanted in the body. Currently, MRI

contrast agents almost exclusively use hydrophilic gadolinium chelates which have some safety concerns.[3]

1.1.2 Positron emission tomography

It is important to mention that all of these imaging modalities offer excellent contrast in certain tissue types. MRI provides good contrast in organs and bones, while PET allows for functional imaging of organs in real-time. Unlike MRI and some other imaging modalities, PET uses potentially harmful radiation, as well as radioisotopes for imaging. This raises some safety concerns for long term use in humans. In addition, there are very few ABS PET probes, all of which do not follow the exact definition of ABS. One example includes work by Chang and Wilson in which they developed a boronate-caged [^{18}F]FLT probe for hydrogen peroxide.[4] This was one of the first times where PET was shown it could potentially be used as an ABS probe. However, the probe relied on an "always-on" and accumulation type of approach. This is limiting in a few ways. Specifically, in this proof-of-principle work, a clinically approved PET agent called [^{18}F]FLT is caged with a boronic acid that can undergo a self-immolative reaction with hydrogen peroxide outside the cell and subsequently become trapped inside the cell after being phosphorylated by thymidine kinase. This means that the effectiveness of the PET probe relied on how fast it could both accumulate in target cells and clear from the body. This results in a relatively complex design strategy for *in vivo* applications. To that end, the hydrogen peroxide responsive PET probe was only demonstrated in cells. Although it is unclear if attempts were made to employ the probe in live animal models, possible limitations may include a low signal-to-noise ratio (due to the "always-on" approach) and short ^{18}F lifetime compared to the time necessary for uncaging and linker cleavage.

1.1.3 Luminescence imaging

Luminescence imaging is performed via two main methods: bioluminescence and chemiluminescence. Bioluminescence imaging is achieved by the emission of light from an enzymatic reaction. The reaction was first discovered over a century ago, but it was not until about 80 years ago where the enzyme was isolated and could be further pursued for molecular imaging.[5–7] The enzyme used in the reaction is found in fireflies and known as luciferase. Many research groups utilize bioluminescence however they also note the limitations which include limited depth, which results in limited *in vivo* applications. Unfortunately, many of the bioluminescent ABS probes to date lack resolution and are limited to cellular studies. However, there are a few notable examples that push this technology into deeper tissue by shifting the emission into the NIR region. Importantly, there are various groups who are engineering luciferase-based enzymes and substrates to move into the whole animal imaging setting.[8] One recent example of a bioluminescent ABS probe comes from our group where we used a substrate that emitted at 660 nm after the probe reacted with nitric oxide.[9] We were able to show the sensitivity of the probe which was made possible by carefully manipulating the reactivity towards nitric oxide. With this, we were able to show how nitric oxide, a biomarker for inflammation, is modulated by diets and how it can affect the severity and prognosis of cancer. Not only was this able to track nitric oxide in a subcutaneous model of cancer, but it could also be used to detect nitric oxide in a heterotopic liver metastasis model with very high signal intensity. It is apparent however that bioluminescence imaging requires a highly engineered system for this type of imaging to be effective. That is, while bioluminescence imaging can be used *in vivo*, the target analyte is in an environment that is inherently not found in nature. The cells or animal models must be genetically modified to express luciferase which is necessary for luciferin to generate light. This means that bioluminescence imaging is limited to biological or pathological discovery studies rather than biomedical

applications in the preclinical or clinical settings. In light of this issue, there is recent exciting and novel work that aims to circumvent highly engineered systems used in bioluminescence imaging. This was first reported in 2021 by Guon and coworkers where they show quantification of systemic enzymatic activity in non-transgenic cells, mice, and dogs.[10] This was accomplished using a three-component design that includes: 1) a bioluminescent ABS probe 2) a luciferase plug 3) and a portable light detector. The idea behind this approach relies on systemic administration of the probe and allowing the uncaged luciferin to reach the luciferase plug which is administered under the skin. Once the luciferin reaches the luciferase plug, the light that is emitted from oxidation by luciferase can be detected and quantified. As one can imagine, this new method can be applied to detect and quantify a variety of targets since the ABS probe is the only part that may need to be modified. This is an interesting approach that may be valuable for other imaging modalities that are limited to semiquantitative imaging, such as photoacoustic and fluorescence imaging. Although Guon demonstrated that the portable bioluminescence imaging allowed for quantification of biological processes, it is not the most significant impact of this work. The emphasis is on the ability to perform bioluminescence imaging on any biological system. However, with this approach they lose all spatial information about the target.

Chemiluminescence is defined as the release of light through a chemical reaction. This typically occurs from the decomposition of a 1,2-dioxetane. Like bioluminescence, chemiluminescence does not require the excitation of a chromophore or endogenous absorber to generate light. This results in essentially no background signal when performing chemiluminescence imaging. Chemiluminescence however does not have some of the same limitations as bioluminescence. For instance, a highly engineered luciferase-expressing system is not required. Shabat and others have utilized chemiluminescence extensively throughout their

work for a wide range of applications including imaging drug delivery, cancer, and inflammation. One notable example is collaborative work between Chang and Shabat where a chemiluminescent ABS probe for formaldehyde was developed. This tool relied on an aza-Cope rearrangement to uncage the phenoxy-dioxetane.[11] With this, they demonstrated that formaldehyde was produced during folate metabolism after administering tetrahydrofolate to live mice. While chemiluminescence holds some advantages over bioluminescence imaging, it still provides the same type of readout which means there is poor resolution and poor depth penetration. Although there are some examples of near-infrared and near-infrared II chemiluminescent probes,[12,13] the resolution of these images makes it difficult to distinguish the tissue or organs being visualized. In addition, chemiluminescence does not offer good quantum yields.

There is a great deal of work that has been accomplished in transitioning ABS approaches to every major imaging modality available to date. Clearly, MRI, PET, ultrasound, and PA imaging are still in their early stages. In fact, there are currently no examples of ultrasound ABS probes. PA imaging is the closest of the imaging modalities that incorporates ultrasound. That is, PA imaging is the most promising in terms of using ABS probes with an ultrasound readout in the clinic.

1.2 Photoacoustic imaging

PA imaging is an emerging imaging modality that has proven to be useful in a variety of settings.[14–17] The PA effect was first described by Alexander Graham Bell in 1880. It is most easily described as a "light in, sound out" technique. During PA imaging, a chromophore is excited by pulsed lasers and the energy is released through the non-radiative pathway as heat. The heat that is generated causes thermoelastic expansions within tissue which then propagate to produce sound waves that can be detected by ultrasound transducers. This leads to several advantages over the

imaging modalities mentioned above. For instance, since PA imaging is a hybrid of optical and acoustic imaging it lacks some of the disadvantages of both. With PA imaging, the main advantages are the depth penetration (up to 12 centimeters) and high spatial resolution (ten of microns). In contrast, purely optical based methods (light in, light out) are limited due to scattering of light within tissue. PA imaging does not face the same limitation since sound scatters 1000 times less in tissue. In ultrasound imaging (sound in, sound out), there is the issue of coherent addition of sound waves that leads to significant noise or speckles in the images. Apart from these advantages, PA imaging does not need a contrast agent for high quality images since deoxyhemoglobin (Hb), oxyhemoglobin (HbO_2), and melanin are endogenous chromophores that can act as contrast agents. Indeed, HbO_2 and HB have been used to study oxygenation in the blood and vasculature in cancer.[18–20] Melanin has also been exploited for imaging and tracking skin cancer. Although exogenous chromophores are necessary for detecting other biomarkers associated with diseases, PA imaging requires significantly less amounts of imaging agents compared to ultrasound (pg - μg compared to μg – mg).

It is important to clarify that each of the modalities described above have unique qualities which are summarized in the table below.[21] Out of the following imaging modalities, PA imaging offers the best temporal and spatial resolution where the depth of penetration due to light is the major limitation.

Imaging Modality	Temporal Resolution	Spatial Resolution	Depth of Penetration	Sensitivity	Ionizing Radiation	Used Clinically
MRI	Minutes-hours	~1 mm	Limitless	10^{-3} to 10^{-5} M	No	Yes
PET	Seconds-minutes	5–7 mm	Limitless	10^{-11} to 10^{-12} M	Yes	Yes
Ultrasound	Seconds-minutes	0.01–2 mm	mm-cm	~10-12 M	No	Yes
Fluorescence	Seconds-minutes	2–3 mm	<1 cm	~10^{-9} to 10^{-12} M	No	Emerging
Luminescence	Seconds-minutes	3–5 mm	1–2 cm	~10^{-15} to 10^{-17} M	No	Low potential
Photoacoustic	Seconds-minutes	~10 μm to 1 mm	<12 cm	Not determined	No	Emerging

Table 1. Comparison of temporal resolution, spatial resolution, depth of penetration, sensitivity, ionizing radiation, and clinical use of MRI, PET, ultrasound, fluorescence, luminescence, and PA imaging.

1.3 Pioneering photoacoustic activity-based sensing probes

ABS is defined as having the ability to leverage the chemical reactivity of a target to attain the necessary selectivity and sensitivity for an observable and quantifiable readout from a probe.[22,23] It was not until recently that PA imaging has been used in ABS approaches. Even now, PA imaging has been very successful in imaging various diseases without the use of ABS probes. However, with the development of new tools, specific processes such as drug response, inflammation, and metabolism can be observed in real-time. The first PA ABS probe was developed by Gambhir and coworkers in 2010.[24] This work inspired the molecular imaging field and began the area of PA ABS probes. The authors closely examined the effects of photophysical properties such as the fluorescence quantum yield (Φ_{Fl}), the molar absorptivity extinction coefficient (ε), photostability, excited state absorption, and relaxation kinetics on PA properties. In addition, they established important guidelines for developing PA ABS probes. For instance, the probes must have a strong enough PA signal and the reaction of interest must lead to a permanent change in the chromophore. This initial work was not applied to live animals until later but was demonstrated in cells and tissue-mimicking phantoms. In their design, they attach two chromophores to a peptide that can be cleaved by matrix metalloprotease-2 (MMP-2). The strategy enables the detection of two different wavelengths which can circumvent some issues that are present in single wavelength intensity-based designs. However, the way that the two wavelengths were used is not truly ratiometric as the two signals were simply subtracted. In 2013, Gambhir modified their design to enable the imaging of MMP-2 and MMP-9 for the detection of follicular thyroid carcinoma.[25]

In 2015, our group reported the first small molecule PA ABS probe for copper (Cu).[26] The Acoustogenic Probe for Cu, or APC, and was based on an aza-BODIPY dye platform. Two

versions of APC were synthesized (APC-1 and APC-2) since APC-1 was poorly soluble and required the use of surfactants. APC-2 included a water-solubilizing moiety that facilitated accurate characterization *in vitro*. APC-2 used a 2-picolinic ester to selectively bind to Cu(II) and undergo a hydrolytic cleavage. This design also involved using a truly ratiometric approach that compared the PA signals at 697 and 767 nm, where 697 nm corresponds to the unreacted APC-2 and 767 nm corresponds to the reacted probe. Since then, our group and others have rapidly contributed to the number of PA ABS probes in the literature.[27–32]

One notable example of a PA ABS probe is PhotoNOD which showcased the utility of PA imaging for applications beyond sensing.[33] PA imaging had not been extensively explored for delivery or monitoring of analytes. This work demonstrated the first small molecule near infrared activated nitric oxide donor. Similar to APC-2, PhotoNOD was based on an aza-BODIPY dye platform that could elicit a ratiometric readout. Essentially, PhotoNOD could be irradiated with near infrared light to generate nitric oxide and the red-shifted product rPhotoNOD. This resulted in a change in the PA signal ratio (PhotoNOD/rPhotoNOD). PhotoNOD was then employed in a breast cancer murine model to modulate the tumor progression.

Our work further helped to establish criteria for ABS probe design.[34,35] They are as follows: 1) the maximum absorbance wavelength must be greater than 680 nm to minimize tissue interference and increase depth penetration; 2) the Φ_{Fl} should be low since it is inversely correlated with the PA brightness factor; 3) the ε should be greater than 10^4 M^{-1} cm^{-1} to enhance the signal to background ratio; 4) the probe must not adversely interfere with the native environment; 5) the probe must be photostable; 6) the probe must be biocompatible and nontoxic. It is made clearer by the plot shown in Figure 1 why some of these criteria are necessary. The longer the wavelength

the less overlap there is with endogenous absorbers. In addition, these endogenous absorbances have ε that peak around 10^4 M^{-1} cm^{-1}.

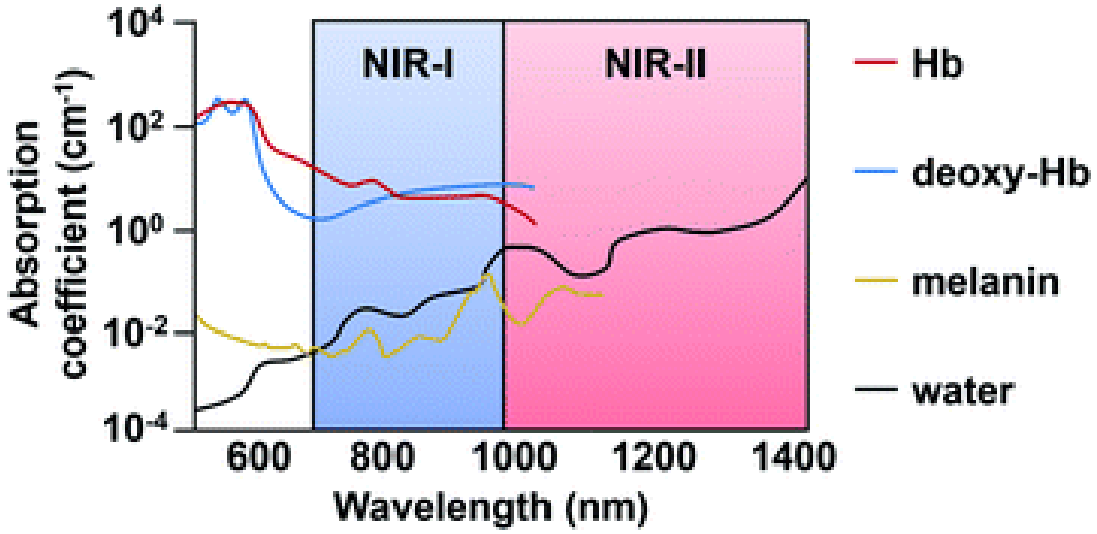

Figure 1. Molar absorptivity coefficient spectra of biological absorbers.[1]

1.4 Imaging-based biomedical applications

Currently, there are several avenues that molecular imaging has taken for biomedical applications. For instance, there are approved clinical procedures such as fluorescence-guided surgery, ultrasound-based diagnosis of cancers, and MRI-based diagnosis of diseases. The most well-known and established dye in the clinic that is Food and Drug Administration (FDA) approved is indocyanine green (ICG). ICG is a cyanine-based dye that has effectively been used in both near-infrared imaging and near-infrared II imaging.[36–39] Although its maximum is below 800 nm, ICG is known to have an emission tail above 950 nm. It is evident that ICG has been and will continue to be exploited in a variety of biomedical applications due to not bearing issues with FDA approval.

[1] This figure was reprinted with permission from the following publication: A. K. East, M. Y. Lucero and J. Chan, New directions of activity-based sensing for in vivo NIR imaging. *Chemical Science* **12**, 3 3393-3405 (2021).

Other dyes such as chlorin e6, which is a porphyrin-based dye, have also been used for clinical procedures such as photodynamic therapy.[40,41] Recently, Phillip Low from Purdue University has received FDA approval for Cytalux. Cytalux is a cyanine-based fluorescence imaging diagnostic for ovarian cancer. It uses a binding-based mechanism that takes advantage of the overexpression of the folate receptor on ovarian cancer cells.[42] It is administered before surgery to help surgeons locate and excise tumors.

While PA imaging is relatively new compared to fluorescence it has rapidly entered some clinical parts.[43–46] Firstly, it has shown promise in clinical trials for breast cancer detection. In addition, Jokerst and others have realized the use of PA imaging in monitoring chronic wound healing.[47,48] Lastly, companies have begun using PA imaging for dentistry, specifically imaging gum recession, tooth decay and infection.[49–51]

1.5 Summary and outlook

Briefly, ABS has been described in a variety of imaging modalities. There are several examples that demonstrate PA imaging as being superior to purely optical-based and acoustic-based techniques alone. With that, we have established guidelines for developing PA ABS probes that has led to their use in monitoring the tumor microenvironment, drug delivery, inflammation, and metabolism. It is important to note that all of the examples in this chapter involved using near-infrared light. That is, light extending from 650 nm to 950 nm. This spectral window is termed NIR-I which has some overlap with endogenous absorbers in the body. To circumvent interference with these biomolecules, the development of ABS probes is beginning to trend towards using NIR-II (> 950 nm) compatible dyes. There are only a handful of reported NIR-II PA probes, while most of the NIR-II field has relied on fluorescent probes or simply contrast agents in PA imaging.[52,53]

NIR-II light is nontoxic and provides many advantages for PA imaging.[54,55] For example, NIR-II agents typically have very high ε. Both ε and the long wavelength enhance the signal to noise ratio, which can potentially enhance the sensitivity of PA probes. This inherently improves the dynamic range of PA ABS probes which can improve quantification and utility in different applications. In chapter 4, we introduce the first small molecule NIR-II PA ABS probe for nitric oxide.

The following chapters entail the development PA ABS probes for applications beyond examples described above, including biopsy-free assessment, companion diagnosis, and prodrug therapy.

1.6 Software

Tables and figures were created using Microsoft PowerPoint.

CHAPTER 2: A RATIOMETRIC PHOTOACOUSTIC PROBE FOR BIOPSY-FREE ASSESSMENT OF COPPER[2]

2.1 Background and significance

The development of PA probes that can monitor disease biomarkers in deep tissue has the potential to replace invasive medical procedures such as biopsies.[56,57] Recently, there has been increasing progress in the development of activatable PA probes that has enabled great molecular specificity. Our laboratory has pioneered the development of PA probes for imaging properties of the tumor microenvironment (e.g., markers such as hypoxia and nitric oxide).[27,28,30,31,58] However, such probes must be highly optimized for *in vivo* performance and exhibit an exceptional safety profile. In this study, we have developed PACu-1, the first PA probe designed for biopsy-free assessment (BFA) of hepatic Cu via PA imaging.

At the onset of this work, we were interested in imaging intracellular Cu because this is the pool of Cu that is believed to cause cellular damage when Cu is dysregulated. Intracellular Cu is found in its +1-oxidation state due to the highly reductive environment of the cell. Importantly, the pool we are targeting is labile Cu which is weakly bound by glutathione (GSH). Since this form of Cu is freely available it can undergo reactions such as Fenton-like chemistry to produce reactive oxygen species that can damage DNA and proteins. Therefore, Cu must be tightly regulated in the body, especially in the liver and brain where the highest Cu concentrations are found. Dysregulation of Cu is known to be associated with several diseases such as Alzheimer's, Parkinson's, Wilson's disease, and cancer.

[2] Portions of this chapter are reprinted or adapted with permission from the following publication: Lucero, M. Y. *et al*. Activity-based photoacoustic probe for biopsy-free assessment of copper in murine models of Wilson's disease and liver metastasis. *Proceedings of the National Academy of Sciences of the United States of America* **118**, e2106943118 (2021).

In this work, we chose Wilson's disease (WD) as our primary model for imaging Cu. WD is a genetic disorder characterized by the accumulation of Cu in the liver. This is caused by a genetic defect in the Cu exporter ATP7B, which is only found in the liver. Eventually Cu overload in the liver leads to accumulation of Cu in other parts of the body such as the brain and, if untreated, leads to liver failure. The primary methods for diagnosis include biopsies for immunohistological or Cu staining, blood, and urine tests. All of these tests have different limitations, but all of them have the same common issue which is that they all detect total Cu levels rather than a specific oxidation state. In addition, biopsies are highly invasive and can often lead to false negative results since only a small part of the liver can be analyzed. Subsequent analysis with staining is also not reliable since the stains are typically indirect measurements of Cu that look at Cu-associated proteins. Finally, biopsies may lead to secondary infections after the procedure which is a highly undesirable event that we seek to circumvent by using molecular imaging.

In the context of cancer, Cu is elevated in many solid tumors including breast[59,60] and lung[61,62] cancers, which generally metastasize to the liver. Since Cu can promote angiogenesis and drive tumor progression, BFA of Cu in metastatic lesions is critical.

There are very few examples of small molecule imaging probes for intracellular Cu. The most notable ones are fluorescent probes that have been used to visualize labile Cu levels in cells and in mice.[63] However, these probes are typically reversible and must constantly compete with binding. In addition, fluorescence imaging is an optical-based technique that is limited by depth penetration and spatial resolution. Therefore, the development of a PA-based probe for Cu is essential for studying Cu in deep-tissue applications.

Although our group[26,64] and others[65] have developed Cu probes for PA imaging, these probes are designed to target Cu(II), whereas intracellular Cu exists predominantly in the +1 form

owing to the highly reducing environment of the cell. To overcome this challenge, we present the development of PACu-1, an acoustogenic probe for Cu(I), and its application in BFA of hepatic Cu in a WD model and a liver metastasis model. Moreover, we designed two unbiased BFA blind studies to identify WD mice from healthy wild-type (WT) controls using PACu-1.

2.2 Design and development of PACu-1

To selectively target the +1 oxidation state of Cu, a Cu(I)-responsive tris[(2-pyridyl)methyl]amine (TPA)[66] trigger was installed onto an optimized aza-BODIPY dye platform to yield PACu-1, which features ratiometric imaging capabilities. We hypothesized that capping of the phenol moiety on the aza-BODIPY will result in a blue shift of the wavelength of maximum absorbance (λ_{max}) relative to the uncapped probe. Once Cu(I) binds to TPA an oxidative cleavage event of the pendant ether linkage occurs to release the latent dye and the stable Cu(II)–TPA (Supplementary Figure 1). This design strategy allows us to selectively irradiate at two different wavelengths that correspond to the probe or turnover product. From this, we can determine a ratiometric fold turn-on. In addition, this has proven to be critical in situations where imaging the liver is involved since the liver is a large organ that holds much of the blood found in the body. Therefore, there will be significant background signal coming from the liver due to absorbers like HB and HbO_2. In the design, the aza-BODIPY dye platform was selected due to its large extinction coefficients (10^4 to 10^5 M^{-1} cm^{-1}) in the near infrared range and low fluorescence quantum yields, since both properties translate to a stronger PA signal. Importantly, we have observed that many of the aza-BODIPY–based probes we have developed intrinsically localize to the liver owing to its relatively high hydrophobic properties making it ideal for liver imaging.

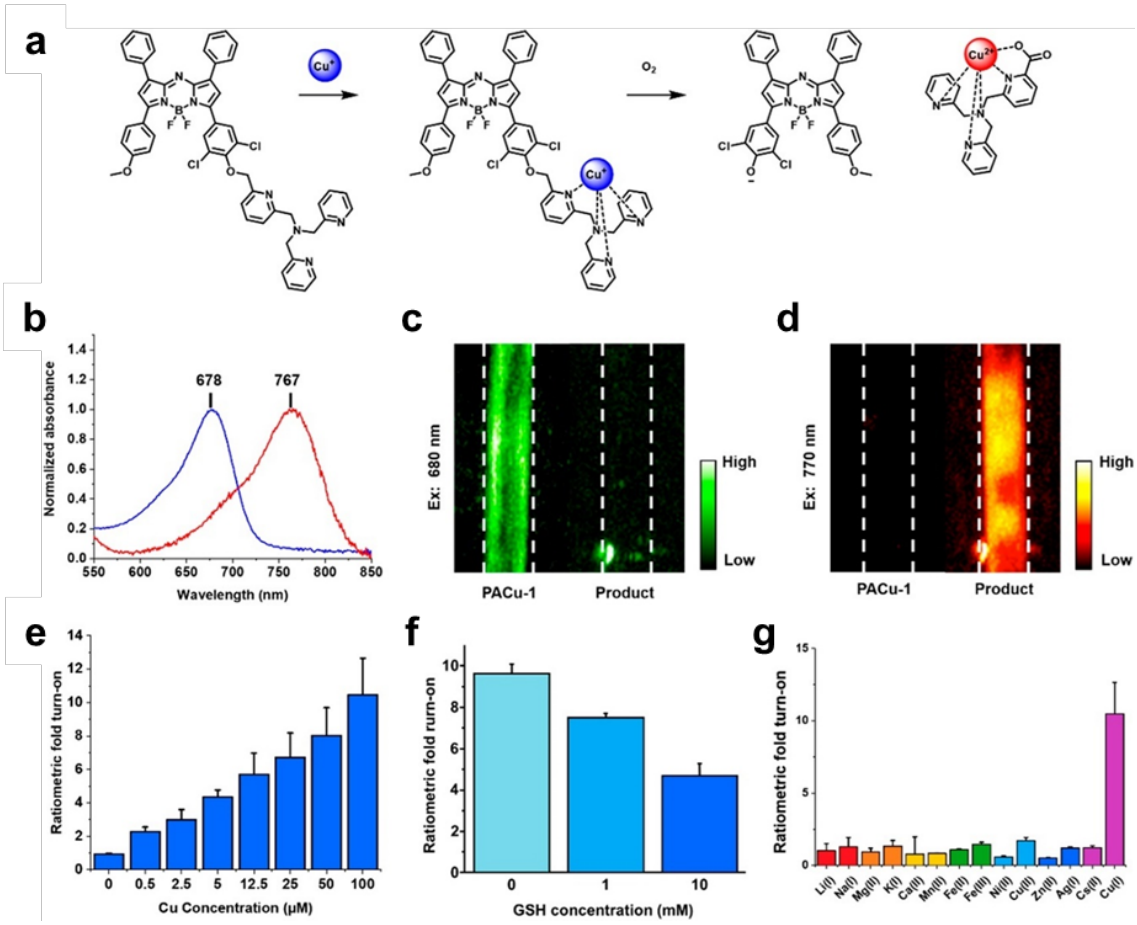

Figure 2. a. General reaction schematic of PACu-1 with Cu(I). b. Normalized absorbance spectra of PACu-1 (blue) and turnover product (red). PA image of c. PACu-1 and d. the product in a tissue-mimicking phantom excited at 680 and 770 nm. Images compiled from different phantoms. e. Ratiometric fold turn-on after incubating PACu-1 with 0, 0.5, 2.5, 5, 12.5, 25, 50, and 100 μM Cu(I). f. Ratiometric fold turn-on of PACu-1 after incubating with 100 μM Cu(I) and 0, 1, or 10 mM GSH. g. Ratiometric fold turn-on after incubating with 100 μM of various metal ions. The source of the Cu(I) used for all experiments was $[(CH_3CN)_4Cu]PF_6$. All assays were performed in 1:1 dimethylformamide:HEPES, pH 7.4 for 1 h. Values are reported as mean ± standard deviation (SD) (n = 3).

After synthesizing PACu-1 (Supplementary Scheme 1), we evaluated its *in vitro* performance. First, we examined its response to 20 equivalents of Cu(I) (introduced as $[Cu(CH_3CN)_4]PF_6$). After 1 h incubation at room temperature, we observed a large spectral shift of 91 nm from 678 nm (probe, $\varepsilon = 5.3 \times 10^4\ M^{-1} \cdot cm^{-1}$) to 767 nm (product, $\varepsilon = 3.7 \times 10^4\ M^{-1} \cdot cm^{-1}$). Next, we performed PA imaging in a tissue mimicking phantom. This demonstrated that irradiation at 680 nm will only generate signa from PACu-1, whereas irradiation at 770 nm will only generate a signal that corresponds to the turned-over product. Through a Cu gradient assay, PACu-1 exhibited a dose-dependent response to Cu (LOD = 0.2 μM). It was important to show that PACu-1 could react with Cu in the presence of GSH, a labile Cu binding competitor. GSH is known to be present at high levels in the liver and most solid tumors (up to 10 mM).[67,68] In addition, TPA has been shown to have excellent selectivity towards Cu(I). We performed a selectivity assay against a panel of monovalent and divalent metal ions as well as a competition assay to confirm using PACu-1 (Figure 2). As mentioned earlier, Cu induces an oxidative cleavage, which is an oxygen dependent reaction. To examine the dependency, we employed the nitrogen purge technique (for 40 min) and found that PACu-1 could still turn over, albeit at a slower rate, when oxygen levels were reduced to 0.2 to 0.4 ppm (Supplementary Figure 2).[69]

2.3 Evaluating the safety profile of PACu-1

It was critical to demonstrate that PACu-1 is not metabolized in the liver to give false positives and show that it is biocompatible with an excellent safety profile. To accomplish this, we treated PACu-1 with rat liver microsomes (RLM) rich in metabolic enzymes (e.g., Cytochrome P450s). After an incubation period of 1 h, we did not observe any change in the absorbance spectra indicating there would be minimal off-target activation of PACu-1 that can lead to false positive results (Supplementary Figure 4). These results were further confirmed with mass spectroscopy

analysis that showed that the aza-BODIPY was not being released in its uncapped form (Supplementary Figure 5). To show that PACu-1 will not be toxic to cells, we performed a cell viability assay. We treated Human embryonic kidney 293 cells with up to 25 μM of PACu-1 for 24 h. After adding the 3-(4,5-Dimethylthiazol-2-yl)-2,5-diphenyltetrazolium bromide (MTT) reagent and measuring the absorbance, we observed that there was no significant loss of viability. An identical experiment was performed using the authentic turnover product which also exhibited no toxicity in cells (Supplementary Figure 6).

To determine whether PACu-1 localizes to the liver, an *ex vivo* biodistribution experiment was performed via PA imaging. From this, we found that PACu-1 primarily accumulates in the liver over other vital organs (Supplementary Figure 7). After this desirable result, it was necessary to show that PACu-1 did not affect liver function. Therefore, we collected liver tissue for hematoxylin and eosin (H&E) staining. The nuclear staining patterns of liver tissue from mice treated with either vehicle or PACu-1 were essentially identical (Supplementary Figure 8). To confirm that PACu-1 was not toxic to the liver, we conducted a comprehensive liver function test to measure the levels of albumin, alkaline phosphatase, alanine aminotransferase, aspartate transaminase, bilirubin, blood urea nitrogen, cholesterol, and glucose in serum. Similarly, we did not observe any statistical difference between vehicle- and PACu-1–treated animals (Figure 3).

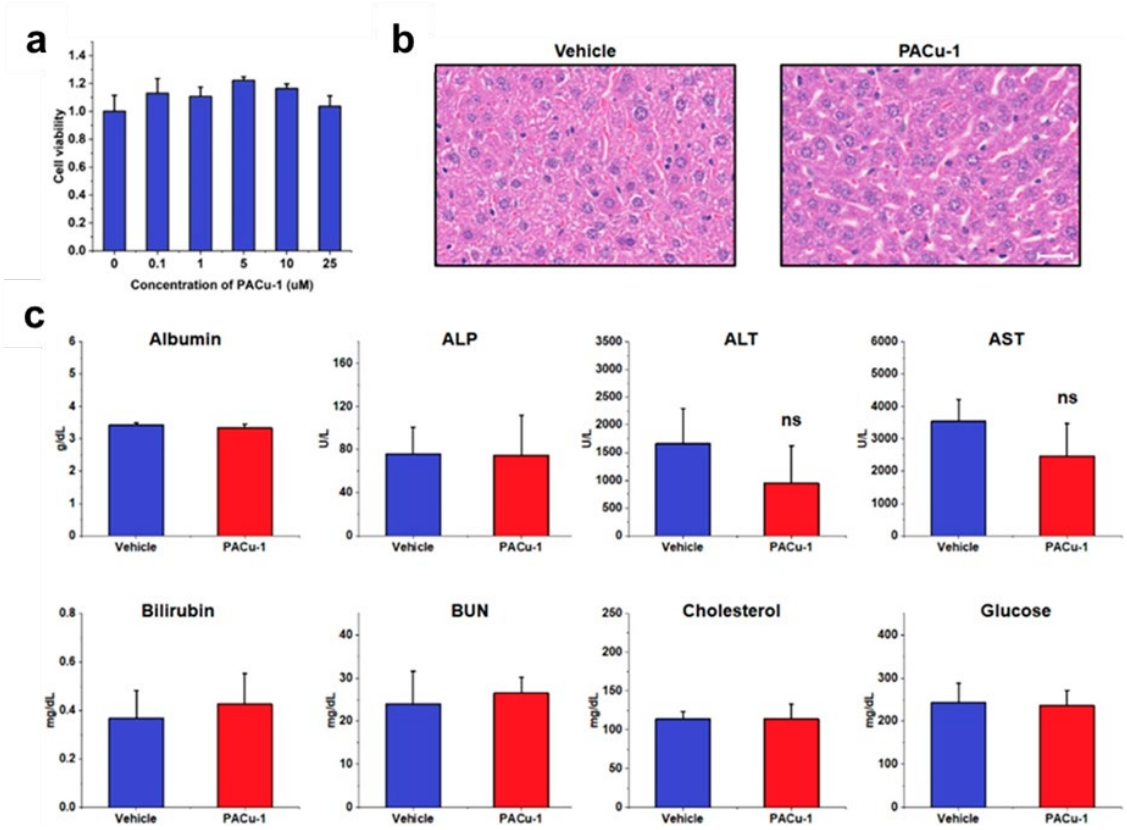

Figure 3. a. MTT assay measuring cell viability after incubating cells with 0, 0.1, 1, 5, 10, and 25 µM PACu-1 for 24 h. b. H&E stains of the liver after treating live mice with 0 or 50 µM PACu-1. (Scale bar, 25 µm.) c. Liver function assays on serum after treating live mice with 0 or 50 µM PACu-1. Values are reported as mean ± SD (n = 10). ALP, alkaline phosphatase; ALT, alanine aminotransferase; AST, aspartate aminotransferase; BUN, blood urea nitrogen.

2.4 Evaluating the *in vivo* performance of PACu-1

Next, we determined whether PACu-1 could be used to detect elevated hepatic Cu(I) in BALB/c mice. BALB/c mice were treated with $CuCl_2$ via intraperitoneal (IP) injection. Of note, the Cu(II) source is allowed to reduce to Cu(I) for 2 h via the highly reductive environment of cells. The supplementation was first confirmed via inductively coupled plasma mass spectrometry (ICP-MS) analysis, which revealed that the Cu concentration was doubled. With the same Cu supplementation procedure, we performed PA imaging with PACu-1 (Figure 4). In particular, the $PA_{770/680}$ ratio was 1.48 ± 0.23 for the Cu-treated animals, whereas the corresponding ratio for control animals not treated with Cu was 0.94 ± 0.13. After this standard imaging experiment, it was necessary to confirm that the enhanced PA signal was due to the detection of Cu(I). Therefore, ammonium tetrathiomolybdate (TM), a high-affinity FDA-approved Cu chelator drug (K_d = $\sim 10^{-20}$) (50), was co-administered with $CuCl_2$. This resulted in no significant activation (0.94 ± 0.13) and reveals that TM has a higher affinity for Cu(I). Furthermore, we developed a control probe named Ctrl-PACu-1 (Supplementary Scheme 2) to further confirm the enhanced PA signal. Interestingly, the $PA_{770/680}$ ratio (0.82 ± 0.12) was lower than when PACu-1 was used to image animals not receiving Cu supplementation and the TM-treated group. This suggests that PACu-1 may be capable of detecting basal levels of Cu that are present in the liver.

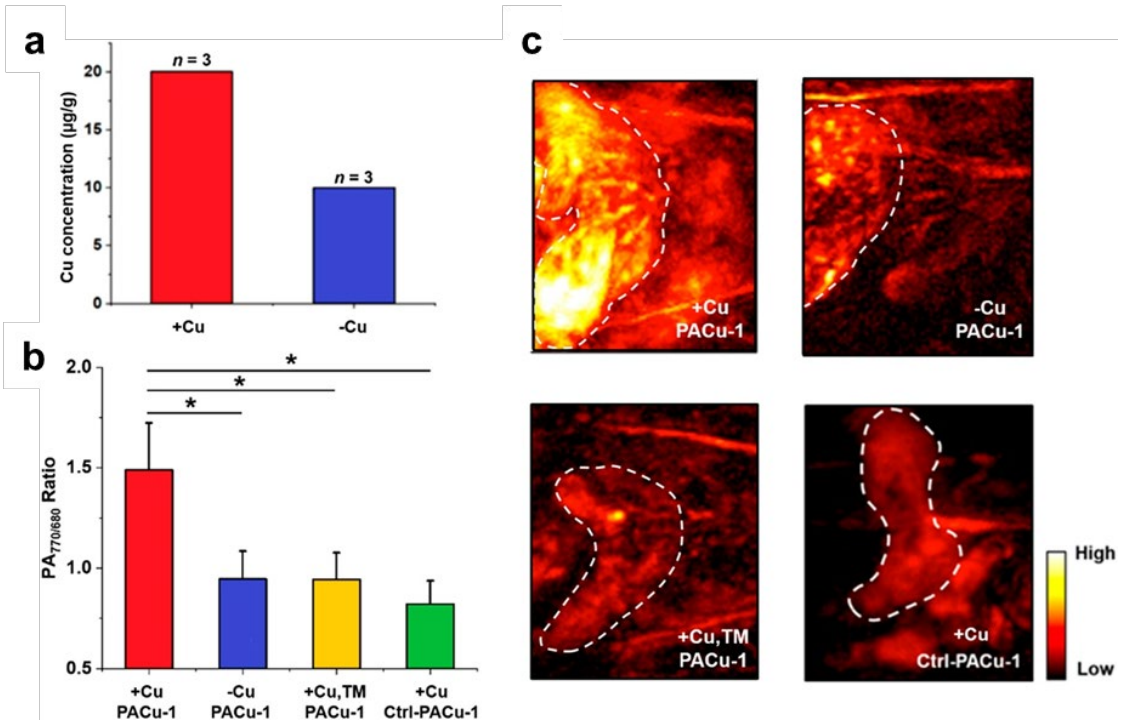

Figure 4. a. Cu concentration in the liver after pretreatment with 0 mg/kg $CuCl_2$ or 5 mg/kg $CuCl_2$ obtained via ICP-MS. b. PA ratio obtained using PACu-1 (50 μM). Red bar represents pretreatment with 5 mg/kg $CuCl_2$ ($n = 4$). Blue bar represents pretreatment with 0 mg/kg $CuCl_2$ ($n = 5$). Yellow bar represents pretreatment with 5 mg/kg $CuCl_2$ and TM ($n = 5$). Green bar represents pretreatment with 5 mg/kg $CuCl_2$ and imaging using Ctrl-PACu-1 (50 μM) ($n = 4$). c. Representative PA images of the liver (dashed white line) for each condition. Liver ROIs are for visualization purposes and were not used for quantification. Values are reported as mean ± SD. Statistical analyses were performed using the Kruskal–Wallis test; $*P < 0.05$.

2.5 Photoacoustic imaging of hepatic Cu(I) in Wilson's Disease

As stated, WD is caused by a genetic defect in a Cu exporter in the liver. As a result, liver biopsies have been critical for the diagnosis and monitoring of the disease. Using an established ATP7B genetic knockout model of WD developed by Lutsenko and coworkers (JAX stock No. 032624), we measured the levels of hepatic Cu in WT mice and WD mice using ICP-MS analysis after obtaining biopsied tissue. On average, we found that the Cu levels in WD mice were 17.5-fold greater than WT mice. Likewise, when we employed PACu-1 and PA imaging for BFA of Cu, we found that the $PA_{770/680}$ ratio was significantly higher in WD mice (1.24 ± 0.16) relative to WT mice (0.80 ± 0.11) (Figure 5). It is critical to note that while ICP-MS analysis reports on total Cu levels, PACu-1 can only access the labile pool, which is defined as Cu weakly associated with intracellular chelators such as GSH. Importantly, we confirmed these *in vivo* imaging results by performing PA imaging of the excised organs. The heart, kidneys, liver, and spleen were harvested from WD and WT mice which demonstrate that the PA signal intensity is higher in the liver of WD mice owing to activation of PACu-1 (Supplementary Figure 9).

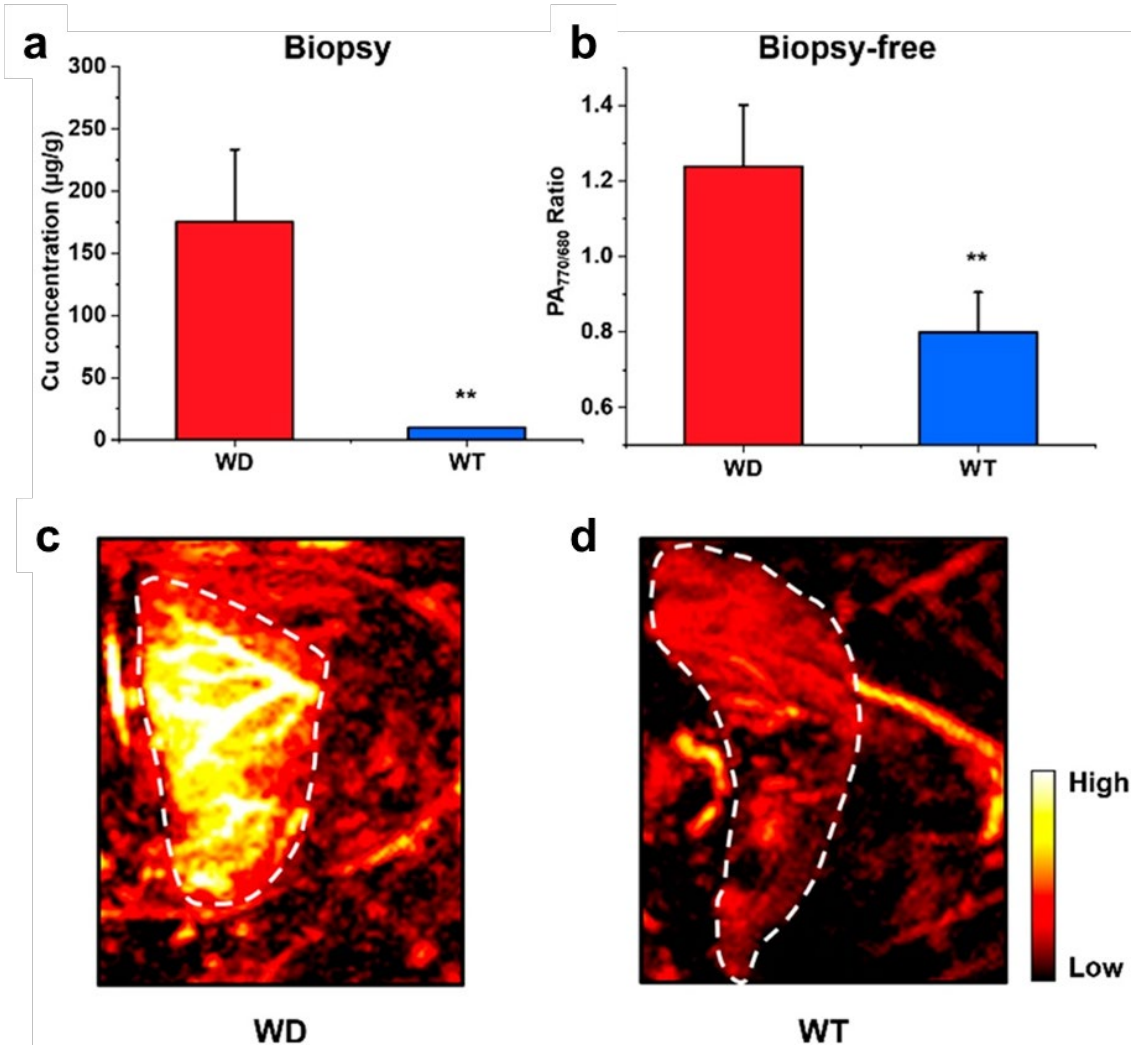

Figure 5. a. Cu concentration in the liver of WD and WT mice (n = 4) obtained via ICP-MS. b. PA ratiometric fold turn-on after treatment with PACu-1 (50 µM, 10% dimethylsulfoxide (DMSO) in saline) in live WD (n = 7) and WT (n = 3) mice. Representative PA image of the liver after treatment with PACu-1 (50 µM, 10% DMSO in saline) in live c. WD or d. WT mice. Liver ROIs are for visualization purposes and were not used for quantification. Values are reported as mean ± SD. Statistical analyses were performed using the Student's t test; $^{**}P < 0.01$.

2.6 Biopsy-free assessment of hepatic Cu(I) in Wilson's Disease using blind studies

To showcase the utility and reliability of PACu-1, we designed a blind study using a group of WT and WD mice. It is important to note that both the WT and WD mice belong to the same strain (B6). Specifically, the WT mice were the genetic controls of the WD mice, and it is impossible to distinguish between each mouse by physical appearance. First, one investigator tagged the group of mice (eight total). The identity of each mouse was concealed from the second researcher until the completion of the study. The second investigator then administered PACu-1 and performed PA imaging to identify the WD mice. Prior to BFA, a reliable diagnostic threshold was determined in WT mice, which is defined as the $PA_{770/680}$ ratio (0.82 ± 0.10). With this in mind, we identified seven animals with a $PA_{770/680}$ ratio (0.63, 0.72, 0.82, 0.86, 0.87, 0.93, and 0.94) within the diagnostic threshold (0.82 ±2 SD), which were assigned to Group 1 (WT mice) (Figure 6). In contrast, only one of the animals had a $PA_{770/680}$ ratio (1.16) greater than three SDs of the diagnostic threshold and was correspondingly assigned to Group 2 (WD mouse). When the identities of the eight animals were revealed at the end of the study, we were able to correctly identify the WD mouse and the WT controls (8/8) with greater than 99.7% confidence.

Since there was only one animal in the WD group, we decided to design a second blind experiment, which entailed utilizing PACu-1 to stratify a group of 12 mice consisting of six WD and six WT animals. Based on the performance of PACu-1 and the results from the first blind study, we hypothesized that the six animals with the highest liver PA signals would be WD mice. As before, each of the animals were tagged, randomized, and their identities were concealed. For this experiment, we elected to use the MSOT inVision 128 imaging system (iThera Medical), which is capable of whole-body cross-sectional imaging as well as spectral unmixing to distinguish the signals from PACu-1, its turnover product, and blood. The six animals with the lowest PA fold

turn-on (defined as $PA_{Final}/PA_{Initial}$) (1.00, 1.00, 1.12, 1.19, 1.20, and 1.31) were assigned to Group 1, which we predicted to be WT animals. The second group, which we projected to be WD mice, exhibited a significantly higher PA fold turn-on (1.71, 1.73, 1.92, 1.98, 2.00, and 2.17). Similar to the results obtained from the first blind experiment, we were again able to correctly identify each mouse using PACu-1 (12/12) (Supplementary Figure 10).

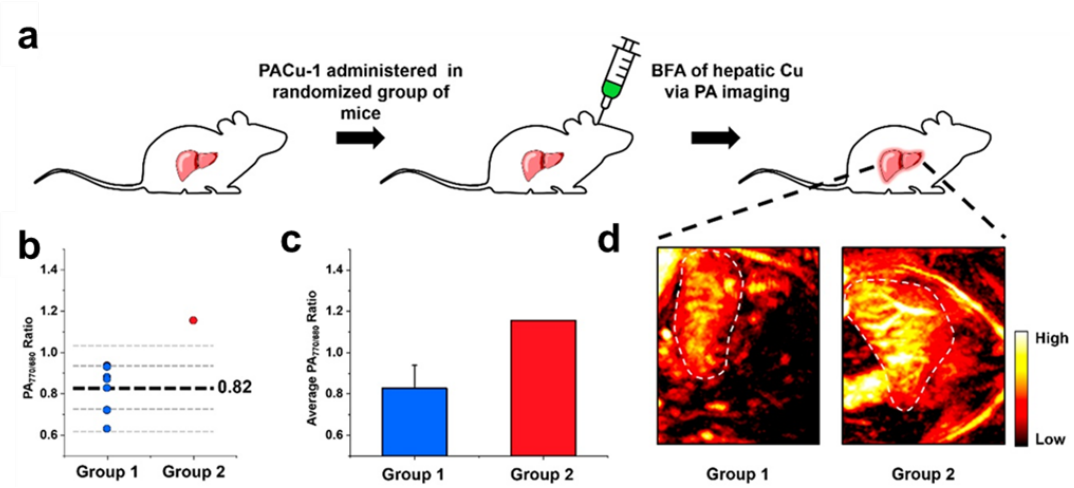

Figure 6. a. General schematic depicting experimental setup of the blind imaging study. b. PA ratiometric fold turn-on using PACu-1 stratified into Groups 1 and 2 based on diagnostic threshold. Total mice in the blind study were 8 (WT = 7, WD = 1). c. Average PA ratiometric fold turn-on shown in b. d. Representative PA images of livers (white dashed line) in Groups 1 and 2. Liver ROIs are for visualization purposes and were not used for quantification. Values are reported as mean ± SD.

2.7 Biopsy-free assessment of Cu(I) in a liver metastasis model

Finally, we utilized PACu-1 for the detection of elevated Cu in cancer. Cu has been associated with aggressive phenotypes and poorer prognosis in different types of cancer, including bone, breast, gastrointestinal tract, and lung cancer.[70] Currently, Cu chelation therapy is being pursued as a treatment to reduce the copper status in primary and metastatic tumors.[71,72] Since the liver is one of the most common sites of metastasis in the body, BFA of Cu(I) levels would facilitate real-time monitoring during tumor progression and treatment with a chelator. To establish a proxy for liver metastasis, Nu/J mice were either implanted with A549 cells in the liver. After 4 wk, PACu-1 was administered for PA imaging using the MSOT system. Compared to the animals that received sham surgeries (1.06 ± 0.28), the PA fold turn-on (after spectral unmixing) for the tumor-bearing mice was 2.31 ± 0.78 (Figure 7). With this, we have shown that PACu-1 can be used in different liver-associated disease models. Importantly, this also opens opportunities for modulating PACu-1 to target other organs or tumors in future studies.

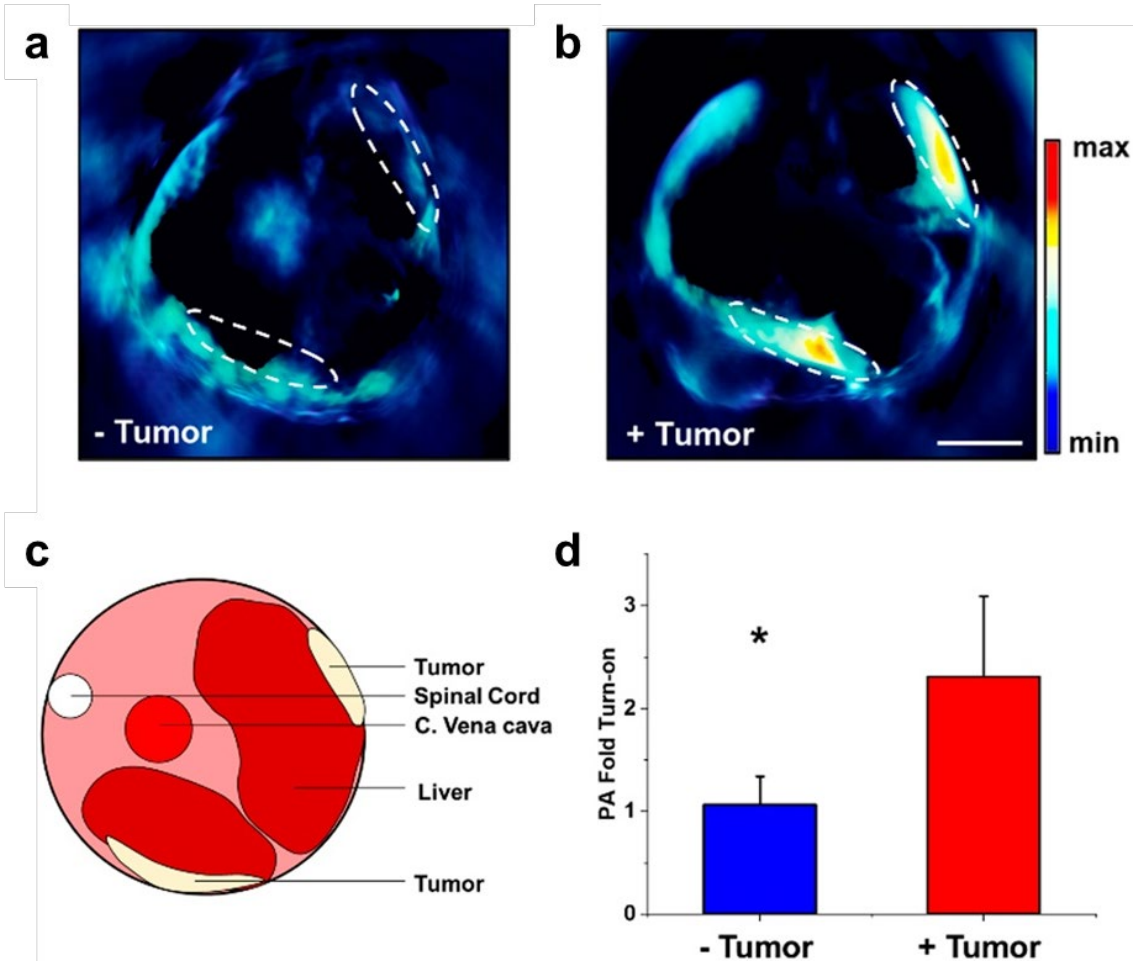

Figure 7. a. Cross section schematic of a mouse to reference the positioning of the liver and tumor. Representative spectrally unmixed MSOT images of the liver 1 h post-injection in b. non-tumor-bearing mice and c. tumor-bearing mice (Scale bar, 5 mm.) d. Average PA signal from MSOT imaging represented in b (n = 3) and c (n = 5). Statistical analysis was performed using the Student's t test; *; $P < 0.05$.

2.8 Progress on developing ABS probes to elucidate the mechanism of Cu in aging

Since the beginning of the development of PACu-1, we had always envisioned tuning the binding affinity towards Cu for a number of reasons. As mentioned, Cu is known to be dysregulated in a variety of diseases including cancer. For this reason, Cu chelation therapy has been employed for the treatment of breast cancer. Dysregulation of Cu can induce oxidative stress and have an adverse effect during different types of therapies. We envisioned that we could develop a PA probe that could not only detect Cu in cancer but also chelate Cu for removal from the cell. However, this had initially proved challenging due to the synthetic effort necessary for asymmetric aza-BODIPYs. In addition, a major challenge was simply being able to measure the binding affinities after synthesizing the probes. Since using this design strategy involves an oxidative cleavage to obtain a Cu(II) complex, we cannot easily measure the binding affinity for Cu(I). To address the first issue, we have attempted to accelerate the synthesis of different ligands by changing the aza-BODIPY to smaller or commercial dyes such as fluorescein, Tokyo green, and coumarins. However, this also raises other challenges that are intrinsic to the different dyes used. At the beginning of this strategy, we observed that the reactivity and binding was dye dependent. This would clearly make future characterization of binding more complex and difficult for comparison. To address the second issue, we have attempted to use an external probe with a known binding affinity to back calculate the binding affinity of our probes. However, this has not be successful to date due to spectral overlap and possible FRET interference, One other approach we have taken is to perform the reaction under hypoxic conditions to prevent oxidation of Cu. This reaction is highly sensitive to oxygen as was shown earlier where even at very low concentrations of oxygen PACu-1 can undergo oxidative cleavage. As of now, our design strategies have relied on hard soft acid base theory, completing the synthesis, and then collecting data for limit of

detection calculations. We have synthesized a panel of different ligands with similar geometry and binding to TPA.

The purpose of these new ligands is to detect small dynamic changes in Cu levels as a function of age. It has been reported that Cu levels increase with age. It is also interesting to note that Cu is elevated in age-related diseases such as Alzheimer's. Our goal is to image the changes of Cu during aging and determine what other factors cause these changes,

From our panel, we determined that the NPy_4 ligand exhibited enhanced binding compared to TPA. It could also turn-on at a higher rate. In addition, due to the additional pyridine ring the probe was more hydrophobic which further facilitates localization to the liver. With NPy4 in hand, we employed it in PA imaging in different age groups. We found that there was a steady increase in PA signal with age. We hypothesized with the increase in oxidative stress, GSH levels would be inversely proportional. Therefore, using one of our PA probes for GSH we performed PA imaging in the same sets of mice (Figure 8). These results demonstrate that while Cu is elevated reduced GSH concentrations are found in the liver. It is important to note that with this data we cannot report on the GSH/GSSG ratio which is a biomarker for redox homeostasis. However, it is reasonable to hypothesize that the ratio is significantly lower due to lower reduced GSH and likely higher oxidized GSH.

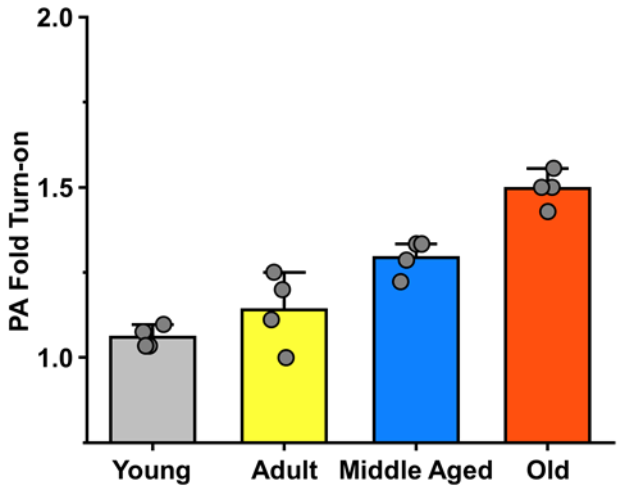

Figure 8. PA fold turn-on assessing Cu levels in young, adult, middle aged, and old mice using PACu-3 (NPy4 version of probe).

Furthermore, we have performed immunohistochemical analysis of liver tissue for important biomarkers of oxidative stress, including 4-hydroxynonenal, 8-hydroxyguonosine, aldehyde hydrogenase 1A1, and nitrotyrosine. Although the results of these analysis have been inconclusive due to technical issues with staining, we have ongoing experiments for proteomic analysis of aged livers. However, we expect that these oxidative stress markers will be elevated in the eldest mice. Of note, some of these biomarkers are related to stemness, such as ALDH1A1. Therefore, we hypothesized that during aging cells lose the ability to regenerate stem cells.

We have also designed a chelation experiment to determine whether oxidative stress can be reduced and stemness can be rescued. We envision that with the success of this work, the mechanism of Cu in aging can be further understood with the potential improve prognosis of certain age-related diseases and cancer.

2.9 Summary and outlook

One of the major goals of molecular imaging research is to develop high-performance chemical tools that can noninvasively detect and monitor disease biomarkers in a deep-tissue context. Despite the emergence of various acoustogenic probes (also known as ABS PA probes) for analyte sensing, none have been explored to date for BFA of disease biomarkers of the liver. This is particularly true for the liver due to high volume of blood that can cause background interference. Thus, our goal is to develop PA probes that can potentially replace or complement invasive biopsies currently in use to enable real-time monitoring.

In this study, we chose to target hepatic Cu to complement liver biopsies. Our group has previously developed several PA probes for Cu(II), however, we found that they were not stable when incubated with RLM. We suspect that the instability is due to the ester linkage. Likewise, after synthesizing RPS1, a PA probe designed to image Cu(II) in a murine Alzheimer's disease

model, we discovered that after supplementing mice with $CuCl_2$ it could not detect exogenous copper in the liver (Supplementary Figure 11). These results are not surprising, since we would expect a larger increase in Cu(I) concentration rather than Cu(II).

Noteworthy, we did not intentionally include only one WD animal in our first blind BFA experiment. However, we were satisfied with the outcome because WD occurs in approximately one in 30,000 to 40,000 people worldwide. Therefore, a study with fewer subjects with WD is more representative compared to a scenario in which the numbers are closer to parity. Despite this, we designed and successfully executed a second BFA experiment in which the goal was to use PACu-1 to stratify six WD and six WT mice based on their liver PA signals. In addition to detecting Cu in WD, we also demonstrate that PACu-1 can be used to assess elevated Cu in a liver metastasis model.

With the ability to perform BFA of hepatic Cu, we hope to use this approach to study the effects of Cu on aging. So far, the results look promising and trending towards a mechanism that implies Cu plays a major role in oxidative stress and cell regeneration. We envision that this work can be used to assist in the development of new Cu chelators or to monitor hepatic Cu changes in real time in tandem with treatments. In addition, we have demonstrated that these designs are compatible with different imaging systems, and potentially compatible with handheld sensors, wearable devices, and endoscopy setups.

2.10 Experimental methods

Materials. Materials were purchased from commercial vendors and used without further purification. All deuterated solvents were purchased from Cambridge Isotope Laboratories. Acetone, ammonium chloride, dichloromethane, DMSO, glacial acetic acid, phosphate buffered saline (PBS) (Corning), copper(II) chloride, sodium bicarbonate, sodium carbonate, sodium

chloride, and sodium hydroxide were purchased from Thermo Fisher Scientific. Thionyl chloride was purchased from TCI Chemicals. Anhydrous methanol and conc. hydrochloric acid were purchased from Macron Fine Chemicals. Acetic anhydride, anhydrous dichloromethane, anhydrous dimethylformamide, sodium hydride, β-Nicotinamide adenine dinucleotide 2′-phosphate reduced tetrasodium salt hydrate (NADPH), formaldehyde (37 % w/w in water), glutathione (reduced), TM, tetrakis(acetonitrile)copper(I) hexafluorophosphate, silver carbonate, hexanes, and RLM (pooled, male) were purchased from Millipore-Sigma Aldrich. Potassium iodide, 2,6-pyridinedimethanol, 4-pyridinecarbaldehyde, 4-aminomethylpyridine, cesium carbonate, dibenzylamine, and sodium sulfate (anhydrous) were purchased from Oakwood Chemicals. B6129SF2/J and B6;129S1-Atp7btm1Tcg/LtsnkJ mice were purchased from The Jackson Laboratory.

Instruments and Software. ^{1}H and ^{13}C NMR spectra were acquired on the Carver B500 spectrometer. The following abbreviations were used to describe coupling constants: singlet (s), doublet (d), triplet (t), or multiplet (m). Spectra were visualized and analyzed using MestReNova (version 14.0) and referenced to trace non-deuterated solvent. High-resolution mass spectra were acquired on a Waters Q-TOF Ultima ESI mass spectrometer or a Waters Synapt G2-Si ESI/LC-MS spectrometer. Ultraviolet-visible spectroscopy was performed on a Cary 60. Ultraviolet-visible spectroscopy and fluorimetry was performed with a micro fluorescence quartz cuvette (Science Outlet). SpectraMax M2 plate reader was used for cell viability assays. Data were analyzed using Microsoft Excel. PA imaging was performed using an Endra Nexus 128+ photoacoustic tomography system and MSOT inVision 128 (iThera Medical). PA images were analyzed using Horos or MSOT inVision software. Reported values correspond to mean PA signals in regions of interest (ROIs) of equal area.

Synthetic Procedures. Thin-layer chromatography (TLC) was performed on glass-backed TLC plates precoated with silica gel containing an UV254 fluorescent indicator (Macherey-Nagel). TLCs were visualized with a 254/365 nm UV hand-held lamp (UVP). Flash silica gel chromatography was performed using 0.04–0.063 mm 60 M silica (Macherey-Nagel). All glassware used under anhydrous reaction conditions were flame-dried under vacuum and cooled immediately before use.

Synthesis of RPS1.[65] **RPS1** was synthesized as previously reported, with minor modifications to the procedure. Specifically, the product of the Suzuki coupling reaction in step one was purified via column chromatography on neutral alumina with 1:9 v/v EtOAc:hexanes and triethylamine (1 drop per 100 mL). In addition, the product from the reduction was isolated as a green powder (rather than pink) and used in the subsequent Michael addition reaction without purification. The Michael addition was run under more dilute conditions (32 mM) compared to the original publication. Finally, **RPS1** was isolated using a preparative TLC with 80% ethyl acetate, 15% toluene and 5% methanol as the eluent.

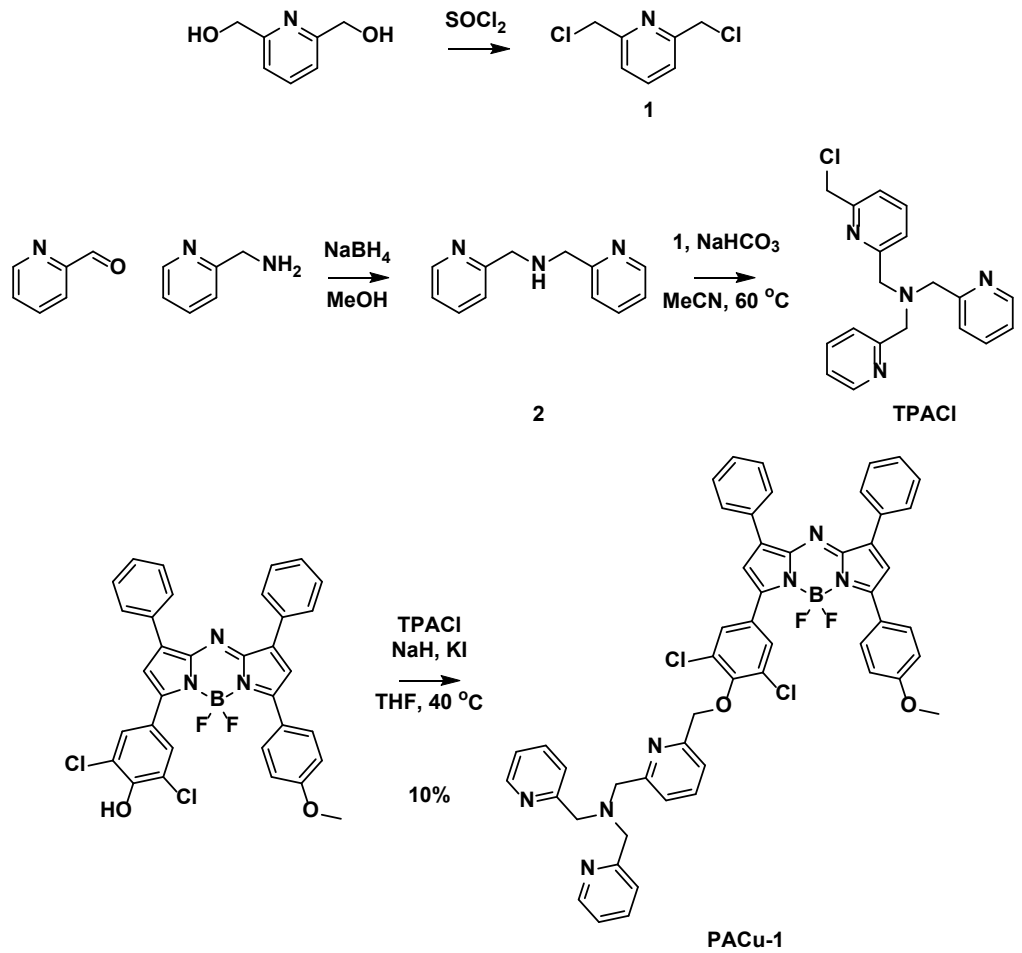

Supplementary Scheme 1. Synthesis of PACu-1

2,6-Bis(chloromethyl)pyridine (1). To 2,6-pyridinedimethanol (10 g, 71.9 mmol, 1.0 equiv.) was added neat $SOCl_2$ (100mL, 1.4 mol, 19.5 equiv.) at 0 °C. After 6 h of stirring at room temperature, **1** was precipitated using aq. NH_4OH. The white solid was vacuum filtered and used without further purification (quant. yield, 12.6g, 71.9 mmol). ^{1}H NMR (500 MHz, $CDCl_3$) δ 7.77 (td, J = 7.8, 1.5 Hz, 1H), 7.44 (dd, J = 7.8, 1.5 Hz, 2H), 4.67 (d, J = 1.5 Hz, 4H). ^{13}C NMR (125 MHz, $CDCl_3$) δ 156.41, 138.16, 122.12, 46.45.

Bis(pyridin-2-ylmethyl)amine (2). Dissolved 4-pyridinecarbaldehyde (0.40 g, 4.0 mmol, 1.0 equiv.) and 4-aminomethylpyridine (0.40 g, 4.0 mmol, 1.0 equiv.) in MeOH (40 mL). Stirred for

1 h at room temperature. Added $NaBH_4$ (0.45 g, 12.0 mmol, 3.0 equiv.) slowly. Continued to stir at room temperature overnight. The reaction was concentrated under reduced pressure and purified via flash chromatography (5% MeOH/CH_2Cl_2) to afford the title compound as a yellow oil (263 mg, 33% yield). ^{1}H NMR (500 MHz, $CDCl_3$) δ 8.00 (d, *J* = 4.3 Hz, 2H), 7.04 (td, *J* = 7.7, 1.9 Hz, 2H), 6.81 (d, *J* = 7.8 Hz, 2H), 6.56 (dd, *J* = 7.6, 4.9 Hz, 2H), 3.44 (s, 4H). ^{13}C NMR (125 MHz, $CDCl_3$) δ 159.40, 148.69, 135.83, 121.64, 121.35, 54.24.

TPA-Cl. To a solution of **2** (263 mg, 1.3 mmol, 1.0 equiv.) in MeCN (25 mL) was added **1** (699 mg, 3.9 mmol, 3.0 equiv.) and $NaHCO_3$ (111 mg, 1.3 mmol, 1.0 equiv.) at 60 °C. After 16 h, the reaction was filtered, and the filtrate was concentrated under reduced pressure. The crude residue was purified via flash chromatography (5% MeOH/CH_2Cl_2) to afford the title compound as a beige solid (163 mg, 36%). ^{1}H NMR (400 MHz, $CDCl_3$) δ 8.50 – 8.44 (m, 2H), 7.66 – 7.56 (m, 4H), 7.51 (dd, *J* = 15.8, 7.8 Hz, 3H), 7.26 (d, *J* = 7.7 Hz, 1H), 7.08 (ddd, *J* = 7.0, 5.0, 1.4 Hz, 2H), 4.58 (s, 2H), 3.84 (d, *J* = 2.7 Hz, 6H). ^{13}C NMR (125 MHz, $CDCl_3$) δ 153.53, 149.30, 142.66, 137.73, 136.81, 130.45, 123.36, 122.51, 122.37, 121.34, 60.35, 60.14, 47.03.

PACu-1. To a solution of the aza-BODIPY (100.0 mg, 0.16 mmol, 1.0 equiv.) in anhydrous THF (5 mL) was added NaH as a 60% oil dispersion (7.8 mg, 0.16 mmol, 1.0 equiv.) at 0 °C under N_2. Once the solution became purple-red from green, TPA-Cl (55.0 mg, 0.16 mmol, 1.0 equiv.) and cat. KI were added at 0 °C and flushed with N_2. The reaction was warmed to room temperature and stirred at 40 °C overnight. The reaction mixture was washed with brine and extracted with EtOAc three times. The combined organic fractions were dried (Na_2SO_4), filtered and concentrated under reduced pressure to afford the crude residue and purified via flash chromatography on an alumina column (CH_2Cl_2 → 5% MeOH/CH_2Cl_2) to afford the title compound as a dark green film (10% yield, 15.0 mg, 0.016 mmol). ^{1}H NMR (500 MHz, $CDCl_3$) δ 8.54 (dt, *J* = 5.0, 1.3 Hz, 2H),

8.22 – 8.13 (m, 2H), 8.04 (dddd, J = 14.7, 7.8, 6.3, 1.9 Hz, 4H), 7.98 (s, 2H), 7.76 (t, J = 7.6 Hz, 1H), 7.72 – 7.64 (m, 4H), 7.61 (d, J = 7.6 Hz, 2H), 7.57 – 7.52 (m, 2H), 7.46 (tt, J = 7.8, 4.5 Hz, 6H), 7.42 – 7.39 (m, 1H), 7.18 – 7.11 (m, 3H), 7.06 – 7.01 (m, 2H), 6.90 (s, 1H), 5.25 (s, 2H), 3.91 (d, J = 6.7 Hz, 9H). ^{13}C NMR (125 MHz, $CDCl_3$) δ 163.09, 162.06, 159.43, 158.82, 155.95, 152.23, 149.10, 147.05, 145.67, 144.07, 141.71, 137.20, 136.45, 132.58, 132.47, 132.43, 132.39, 132.16, 132.08, 131.96, 131.93, 131.80, 129.96, 129.89, 129.84, 129.81, 129.77, 129.57, 129.50, 129.20, 129.15, 128.69, 128.63, 128.56, 128.47, 123.02, 122.01, 120.21, 120.09, 117.57, 114.61, 75.58, 60.23, 60.02, 55.59, 29.72.

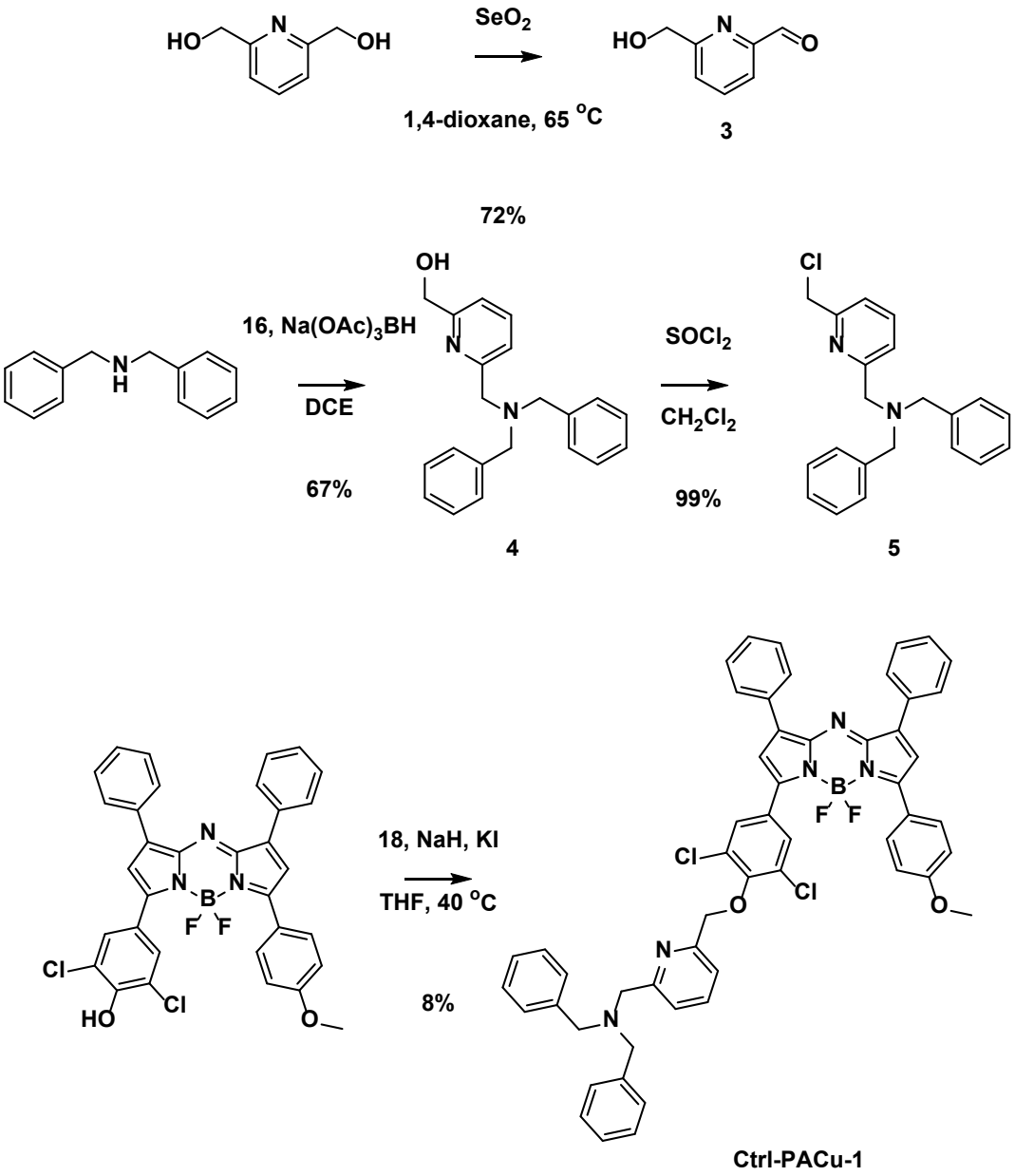

Supplementary Scheme 2. Synthesis of Ctrl-PACu-1

6-(Hydroxymethyl)picolinaldehyde (3). To a solution of 2,6-pyridinedimethanol (3.0 g, 21.5 mmol, 1.0 equiv.) in 1,4-dioxane (60 mL) was added SeO_2 (1.2 g, 10.8 mmol, 2.0 equiv.). The reaction was stirred at 65 ℃ for 30 h. The reaction was filtered through celite and washed with

CH_2Cl_2. The filtrate was concentrated. The crude residue was purified via flash column chromatography (CH_2Cl_2 to 5% MeOH/CH_2Cl_2) to obtain the product as a white solid (2.12 g, 72% yield). ^{1}H NMR (500 MHz, $CDCl_3$) δ 9.97 (d, *J* = 2.2 Hz, 1H), 7.85 – 7.75 (m, 2H), 7.52 (d, *J* = 7.6 Hz, 1H), 4.81 (d, *J* = 2.0 Hz, 2H). ^{13}C NMR (125 MHz, $CDCl_3$) δ 193.06, 160.59, 151.55, 137.82, 124.99, 120.63, 64.22.

(6-((Dibenzylamino)methyl)pyridin-2-yl)methanol (4). A solution of dibenzylamine (139 mg, 0.7 mmol, 1.0 equiv.) and **3** (95 mg, 0.7 mmol, 1.0 equiv.) in DCE was stirred for 1 h at room temperature. After, $Na(OAc)_3BH$ (193 mg, 0.9 mmol, 1.3 equiv.) was added and stirred overnight at room temperature. The reaction was quenched with 2 M HCl, then neutralized with 2 M NaOH. The mixture was extracted with CH_2Cl_2 (3×). The combined organic layers were dried over Na_2SO_4 and concentrated under reduced pressure. The crude residue was purified via flash column chromatography (15% EtOAc/Hexanes to EtOAc) to give the product as a light-yellow oil (150 mg, 67% yield). ^{1}H NMR (500 MHz, $CDCl_3$) δ 7.71 – 7.63 (m, 1H), 7.56 (dd, *J* = 8.1, 3.9 Hz, 1H), 7.47 (q, *J* = 5.9, 4.4 Hz, 4H), 7.38 (dd, *J* = 9.7, 5.8 Hz, 4H), 7.33 – 7.25 (m, 3H), 7.15 (dd, *J* = 8.0, 3.9 Hz, 1H), 4.82 – 4.75 (m, 2H), 4.54 (s, 1H), 3.85 – 3.77 (m, 2H), 3.72 – 3.61 (m, 4H). ^{13}C NMR (125 MHz, $CDCl_3$) δ 159.21, 158.30, 139.31, 137.26, 128.81, 128.38, 127.10, 121.22, 118.78, 64.07, 59.41, 58.36.

***N*,*N*-dibenzyl-1-(6-(chloromethyl)pyridin-2-yl)methanamine (5).** To a solution of **4** (240 mg, 0.7 mmol, 1 equiv.) in CH_2Cl_2 (5 mL) was added $SOCl_2$ (0.5 mL, 6.8 mmol, 9 equiv.) at 0 ℃. The reaction was stirred in a melting ice bath for 1 h. The reaction was cooled to 0 ℃ and quenched with sat. $NaHCO_3$. The mixture was extracted with CH_2Cl_2 two times. The combined organic layers were dried over Na_2SO_4 and concentrated under reduced pressure to afford the product as a yellow oil (250 mg, 99% yield). ^{1}H NMR (500 MHz, $CDCl_3$) δ 7.58 (t, *J* = 7.7 Hz, 1H), 7.50 (d, *J*

= 7.8 Hz, 1H), 7.35 (d, *J* = 7.8 Hz, 4H), 7.23 (dt, *J* = 14.7, 7.6 Hz, 5H), 7.16 (t, *J* = 7.4 Hz, 2H), 4.55 (s, 2H), 3.69 (s, 2H), 3.56 (s, 4H). ^{13}C NMR (125 MHz, $CDCl_3$) δ 160.33, 155.65, 139.29, 137.50, 128.89, 128.40, 127.12, 121.98, 120.98, 59.63, 58.38, 46.91.

Synthesis of Ctrl-PACu-1. To a solution of aza-BODIPY (50 mg, 0.08 mmol, 1.0 equiv.) in dry THF (3 mL) was added NaH (2 mg, 0.08 mmol, 1.0 equiv.) at 0 ℃ and stirred until the solution turned red. Then **5** (27 mg, 0.08 mmol, 1.0 equiv.) and cat. KI were added. The reaction was stirred at 40 ℃ overnight. The reaction was quenched with H_2O and extracted with CH_2Cl_2. The organic layer was collected, dried over Na_2SO_4, and concentrated under reduced pressure. The crude residue was purified via flash column chromatography (5% MeOH/CH_2Cl_2) to give the product as a green film (6.0 mg, 8% yield). ^{1}H NMR (500 MHz, CD_2Cl_2) δ 8.17 – 8.12 (m, 2H), 8.07 – 8.04 (m, 2H), 8.03 – 8.00 (m, 2H), 7.97 (s, 2H), 7.76 (t, *J* = 7.8 Hz, 1H), 7.61 (d, *J* = 7.6 Hz, 1H), 7.56 (d, *J* = 7.8 Hz, 1H), 7.48 – 7.38 (m, 10H), 7.29 (t, *J* = 7.6 Hz, 4H), 7.20 (d, *J* = 5.9 Hz, 4H), 7.07 – 7.01 (m, 2H), 5.19 (s, 2H), 3.88 (s, 3H), 3.69 (s, 2H), 3.59 (s, 4H). ^{13}C NMR (125 MHz, CD_2Cl_2) δ 165.18, 164.17, 161.65, 157.27, 154.14, 153.71, 149.06, 147.58, 145.99, 143.50, 141.44, 139.00, 134.45, 134.34, 133.65, 131.92, 131.79, 131.70, 131.42, 131.37, 131.09, 131.05, 130.74, 130.61, 130.55, 130.51, 130.11, 128.81, 124.95, 123.82, 122.47, 122.14, 119.61, 116.43, 77.84, 66.08, 61.29, 60.02, 57.56, 33.85, 31.61, 27.07, 24.62, 15.80, 2.68.

***In Vitro* Selectivity Assay.** The initial absorbance (400 to 800 nm) of PACu-1 (5 μM, 1:1 vol/vol dimethylformamide:HEPES, pH 7.4) was measured before the addition of a panel of metal ions (100 μM). These initial measurements were used to determine the initial $ratio_{770/680}$ via UV-vis (ultraviolet-visible) spectroscopy. After addition, the cuvette was sealed and incubated for 1 h. Final measurements were recorded, and the ratiometric fold turn-on was calculated by dividing the

final ratio by the initial ratio. All metal solutions were prepared in water from their chloride salt except for Ag_2CO_3, Cs_2CO_3, and tetrakis(acetonitrile)copper(I) hexafluorophosphate.

Live-Subject Statement. All animal experiments were performed with the approval of the Institutional Animal Care and Use Committee (IACUC) of the University of Illinois at Urbana–Champaign, following the principles outlined by the American Physiological Society on research animal use.

Biopsy Assessment of Hepatic Cu via ICP-MS. BALB/c mice were anesthetized using isoflurane (1.5 to 2.0%). The mice were then IP injected with a solution of $CuCl_2$ (5 mg/kg) or vehicle (sterilized saline). After 2 h, the mice were killed, and then the liver was excised and weighed for ICP-MS analysis. The 2-h incubation time was used to reduce Cu *in vivo*. To determine the Cu concentration in WT (B6129SF2/J) and WD (B6;129S1-*Atp7b*^{tm1Tcg}/LtsnkJ) mice, the livers were similarly prepared as the BALB/c mice for ICP-MS analysis, except no IP injections were performed.

Ex Vivo **Biodistribution of PACu-1 via PA Imaging.** BALB/c mice were anesthetized using isoflurane (1.5 to 2.0%) and retro-orbitally injected with either a solution of PACu-1 (50 μM) or vehicle (10% DMSO in sterilized saline, 50 μL). After 1 h, the mice were killed, and the liver, spleen, heart, and kidneys were excised. Photoacoustic imaging of the organs was performed at 680 and 770 nm using continuous mode with a 6-s rotation time (Nexus 128+, Endra Life Sciences). The ratio of the PA signals in PACu-1–treated mice obtained upon excitation at 680 nm and 770 nm was normalized to the ratio of the PA signals in vehicle-treated mice.

Determination of the Diagnostic Threshold. A group of 10 WT mice (B6129SF2/J), which are direct controls of the WD mice (B6;129S1-*Atp7b*^{tm1Tcg}/LtsnkJ), were used to determine the diagnostic threshold for hepatic Cu in WD via PA imaging. After the mice were anesthetized using

isoflurane (1.5 to 2.0%), their abdomens were shaved, and they were positioned in the PA tomographer to facilitate direct imaging of the abdomen. After an image was acquired, an ROI (region of interest) was drawn around the liver to determine the signal intensity. The ratio of the PA signals obtained upon excitation at 680 nm and 770 nm in the ROI provided the initial $PA_{770/680}$ ratio. The mice were then treated with a 50-μM solution of PACu-1 in saline containing 10% DMSO (50 μL) via retro-orbital injection. The mice were returned to their cages for 60 minutes while PACu-1 was allowed to react with the hepatic Cu. The mice were anesthetized, and their livers were imaged as described previously to obtain the final $PA_{770/680}$ ratio. The diagnostic threshold value (mean ± 2 × SD) was determined by dividing the final $PA_{770/680}$ ratio with the initial $PA_{770/680}$ ratio.

Identification of WD via PA Imaging in Blind Study No. 1. A group of eight mice consisting of one WD animal (B6;129S1-*Atp7b*^{tm1Tcg}/LtsnkJ) and seven WT animals (B6129SF2/J mice) was tagged and randomized by the first researcher. Their identity and the total number of WD mice present were concealed until the end of the study. Importantly, these mice had no distinguishing physical features that would allow us to identify them based on appearance. PA imaging of hepatic Cu using PACu-1 was then performed by a second researcher to determine the PA ratiometric fold turn-on for each animal. Mice with a $PA_{770/680}$ ratio value greater than 1.02 were assigned to Group 1 (WD), and mice with a $PA_{770/680}$ ratio value between 0.62 and 1.02 were assigned to Group 2 (WT). After PA imaging was performed on all animals, the assignment and identity were revealed to and validated by the corresponding author.

Stratification of WD and WT Mice via PA Imaging in Blind Study No. 2. A group of 12 mice consisting of six WD animals (B6;129S1-*Atp7b*^{tm1Tcg}/LtsnkJ) and six WT animals (B6129SF2/J mice) was tagged and randomized by the first researcher. Their identity was concealed until the

end of the study. A second researcher used a MSOT PA imaging system to identify the six WD animals based on the highest liver PA signals. Likewise, the six animals with the lowest liver PA signals were assigned to the WT group. The results were revealed by the corresponding author with both researchers present.

Statistical Analysis. Statistical analyses were performed in Microsoft Excel. Sample sizes in all experiments were sufficiently powered to detect at least a P value < 0.05, which was significant. All data are expressed as mean ± SD. Multiple group analysis was performed using the Kruskal–Wallis Test. All other *in vivo* imaging data were analyzed by performing the Student's t test (α = 0.05). *P > 0.05; **P > 0.01.

***In vitro* Buffer Preparation.** 1:1 HEPES/DMF buffer solutions were prepared by mixing freshly made 50 mM HEPES buffer (25 mL) with DMF (25 mL). Adjustments to the desired pH value was done via addition of 1 M HCl or 1 M NaOH. pH values were determined using a Mettler-Toledo SevenCompact pH meter calibrated using pH 4.0, 7.0 and 10.0 standard buffers at 25 °C.

Microsome Assay. The initial absorbance of 10 μM PACu-1 with 10 μL RLM in 0.1 M potassium phosphate buffer (pH 7.4) was measured. After addition of 50 μM NADPH, the reaction was incubated at 37 °C for 1 h. The final absorbance was measured after quenching with acetonitrile.

Cytotoxicity Assay. HEK293 cells were plated (5×10^4 cells/well) in a 24-well plate in EMEM (10% FBS) media for 24 h. HEK293 cells were then incubated with 0.0, 0.1, 5.0, 10.0, and 25 μM PACu-1 or the latent aza-BODIPY at 37 °C in serum-free DMEM media. After 24 h, media was replaced with 5 mg/mL MTT reagent (1:20 in PBS) and incubated for 1 h at 37 °C. Cells were then lysed using 500 μL DMSO, and absorbances were measured using a plate reader at 555 nm. Viability was measured relative to absorbance of control wells.

Tissue Phantom Preparation. Tissue phantoms were prepared by suspending agarose LE in a solution of 2% milk (1 mL) and deionized water (39 mL). The suspension was heated in a microwave until a viscous, translucent gel was produced. The hot gel was poured into a custom Teflon mold containing two copper tubes and cooled at 4 °C for at least 2 h. After cooling, the copper tubes were removed and the gel was removed from the mold, yielding a tissue phantom with two parallel channels for the placement of FEP tubes containing sample solutions.

***In Vivo* Imaging.** BALB/c mice were anesthetized using isoflurane (1.5 – 2.0%) prior to the treatment conditions below. PA images of the liver were acquired prior to and immediately following injection of probe and recorded up to 60 minutes post-injection. Images were acquired at 680 and 770 nm using continuous mode with a 6 second rotation time.

Condition 1: A vehicle control (no $CuCl_2$) was injected via IP, then incubated for 2 h. After, a 50 μM solution of PACu-1 in saline containing 10% DMSO (50 μL) was administered via retro-orbital injection.

Condition 2: A solution of $CuCl_2$ (5 mg/kg) was injected via IP, then incubated for 2 h. After, a 50 μM solution of PACu-1 in saline containing 10% DMSO (50 μL) was administered via retro-orbital injection.

Condition 3: A solution of TM (5 mg/kg) and $CuCl_2$ (5 mg/kg) was injected via IP, then incubated for 2 h. After, a 50 μM solution of PACu-1 in saline containing 10% DMSO (50 μL) was administered via retro-orbital injection.

Condition 4: A 50 μM solution of PACu-1 in saline containing 10% DMSO (50 μL) was administered via retro-orbital injection.

Condition 5: A solution of $CuCl_2$ (5 mg/kg) was injected via IP, then incubated for 2 h. After, a 50 μM solution of Ctrl-PACu-1 in saline containing 10% DMSO (50 μL) was administered via retro-orbital injection.

***Ex Vivo* Imaging.** BALB/c or WD mice were anesthetized using isoflurane (1.5 – 2.0%) and treated with either a 50 μM solution of PACu-1 or vehicle (10% DMSO in sterilized saline). A total volume of 50 μL for each condition was administered via retro-orbital injection. 60 minutes post-injection, the mice were euthanized, and the liver, spleen, heart, and kidneys were excised. Photoacoustic imaging of the organs was performed at 680 and 770 nm using continuous mode with a 6 second rotation time.

Liver Function Test. BALB/c mice were anesthetized using isoflurane (1.5 – 2.0%) and treated with either a 50 μM solution of PACu-1 or vehicle (10% DMSO in sterilized saline). A total volume of 50 μL for each condition was administered via retro-orbital injection. 60 minutes post-injection, the mice were sacrificed, and blood was collected after cardiac puncture. The blood samples were kept on ice and submitted to the Diagnostics Laboratory at the College of Veterinary Medicine (UIUC) where a liver chemistry panel test was performed.

***In Vivo* MSOT Imaging.** A549-Luc2 tumor bearing mice were administered PACu-1 (50 μM, 150 μL in saline containing 10% DMSO) via retro-orbital injection. The mice were continuously anesthetized using isoflurane and placed in the prone position in the animal holder for imaging immediately before injection and 1 h post injection. The temperature of the imaging chamber was set to 36 °C and the animal was allowed to equilibrate to the temperature for 10 minutes before imaging. Cross-sectional images were acquired either at the abdomen of the mouse for liver imaging with a step size of 0.3 mm. The imaging position was guided by the built-in anatomy atlas in the MSOT InVision 128 and was kept consistent for all scans. The excitation wavelengths used

were selected based on the absorbance of PACu-1 and endogenous absorbers. 10 frames were recorded at every imaging wavelength. Subsequently, spectral unmixing was used to separate signals coming from HB and HbO_2.

Field of View Selection. The field of view for all experiments performed on the Nexus 128+ imaging system (Endra Life Sciences) was selected by identifying a slice at the middle of the liver for a representative animal. We then kept the imaging depth consistent across all other subjects when analyzing the data. The field of view for all experiments performed on the MSOT inVision 128 imaging system (iTheraMedical) was selected by using the built-in, cross-sectional anatomy guide to correctly position the animals to image the liver and tumor.

Image Processing of Background Signal. An initial scan prior to the administration of PACu-1 or vehicle was performed for all PA imaging experiments. This is used to account for any background signal that originates from endogenous pigments such as hemoglobin found in blood. After the final scan is taken, a ratio ($PA_{Final}/PA_{Initial}$) is calculated to determine the change in PA intensity. Furthermore, for experiments conducted on the MSOT inVision 128 imaging system, we used the built-in spectral unmixing feature to distinguish between signal coming from PACu-1, the turned over product, and blood based on the absorbance spectra of HbO_2 and Hb.

2.11 Supplemental figures, tables, and spectra

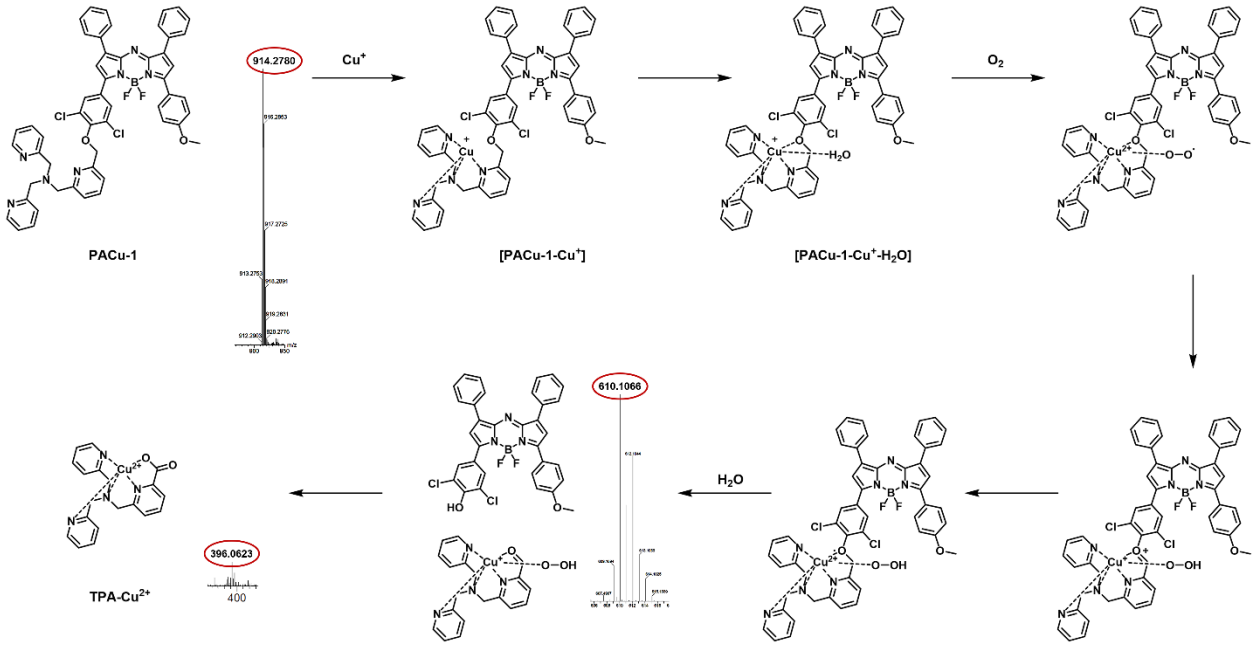

Supplementary Figure 1. Proposed mechanism detailing the reaction between PACu-1 and Cu(I) to yield TPA-Cu^{2+}. Mass spec data included in the insets for PACu-1, turned over aza-BODIPY product, and TPA-Cu^{2+} complex.

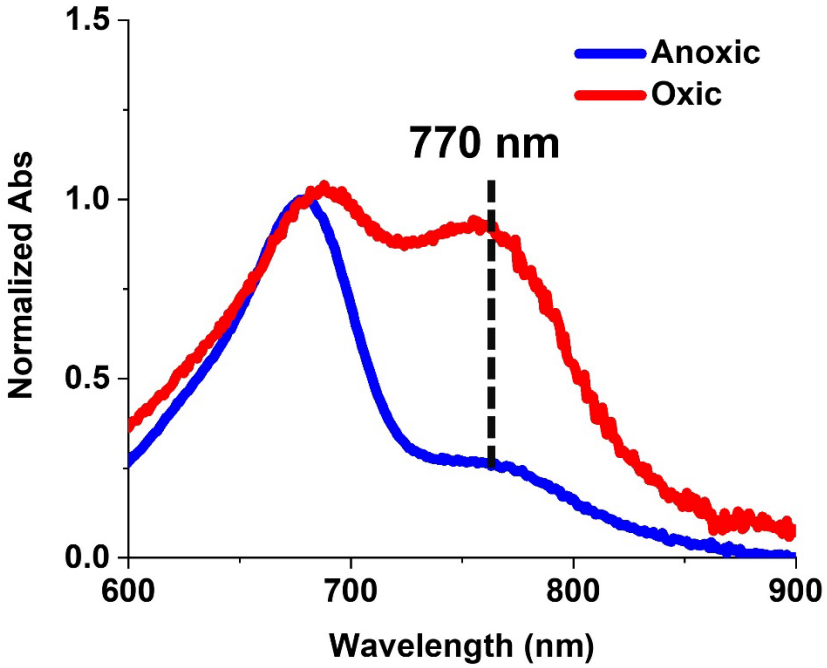

Supplementary Figure 2. Normalized absorbance spectra of PACu-1 treated with 20 equiv. Cu(I) under anoxic (blue) and oxic (red) conditions in 1:1 v/v DMF:HEPES (pH 7.4) after 15 minutes.

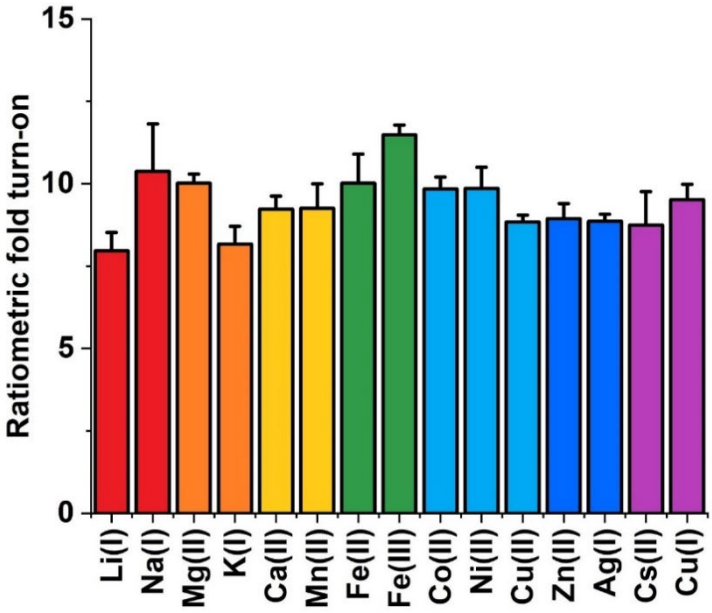

Supplementary Figure 3. Ratiometric fold turn-on after incubating PACu-1 (5 μM) with 100 μM Cu(I) in the presence of various metal ions at equimolar concentration. All assays were performed in 1:1 v/v DMF:HEPES, pH 7.4 for 1 h. Values are reported as mean ± SD (*n = 3)*.

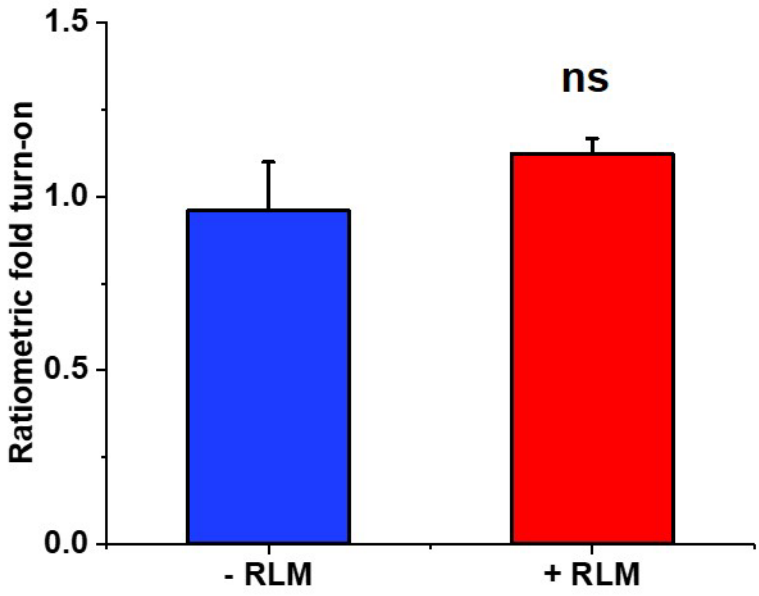

Supplementary Figure 4. Ratiometric fold turn-on after incubating PACu-1 with and without RLM. Data is reported as mean ± SD (n = 3).

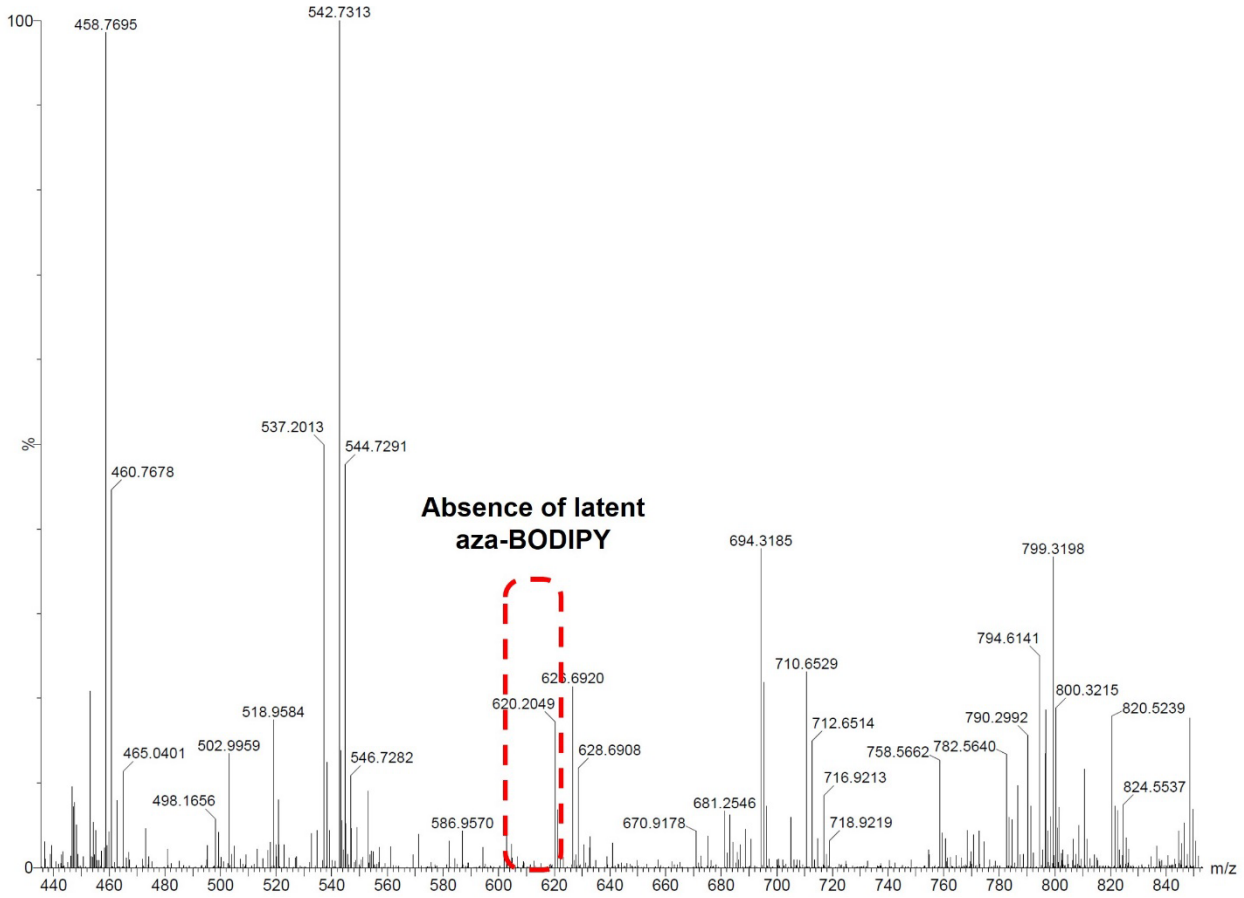

Supplementary Figure 5. High-resolution ESI experiment of PACu-1 treated with RLM demonstrates the absence of the latent aza-BODIPY product.

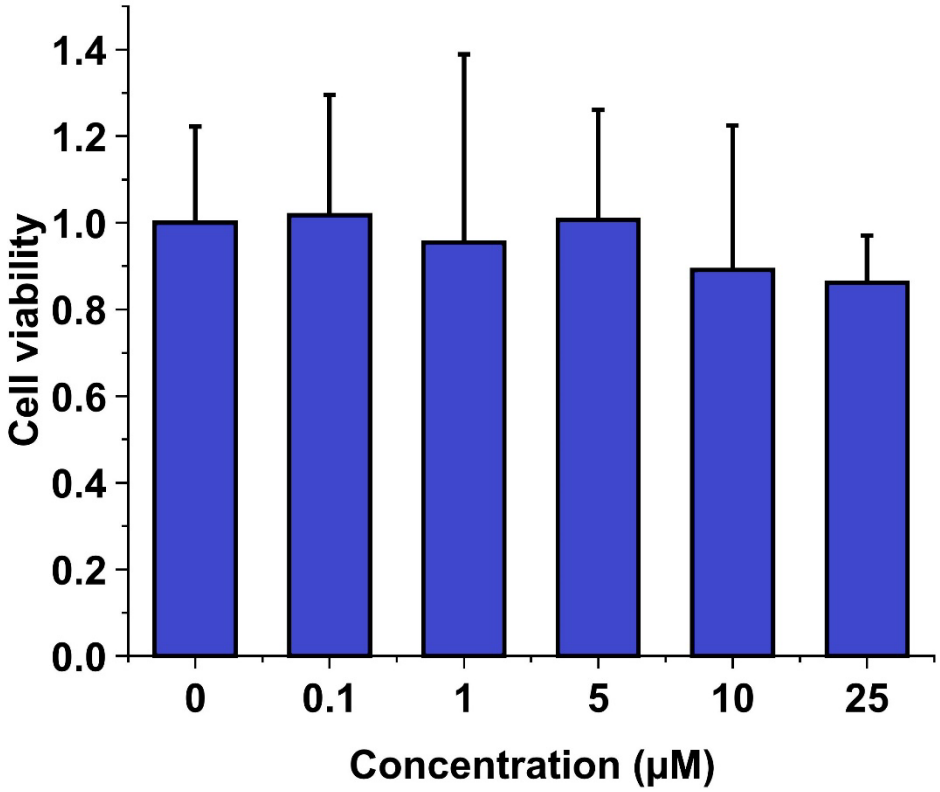

Supplementary Figure 6. MTT assay measuring cell viability after incubating cells with 0, 0.1, 1, 5, 10, and 25 μM of the latent aza-BODIPY product for 24 h.

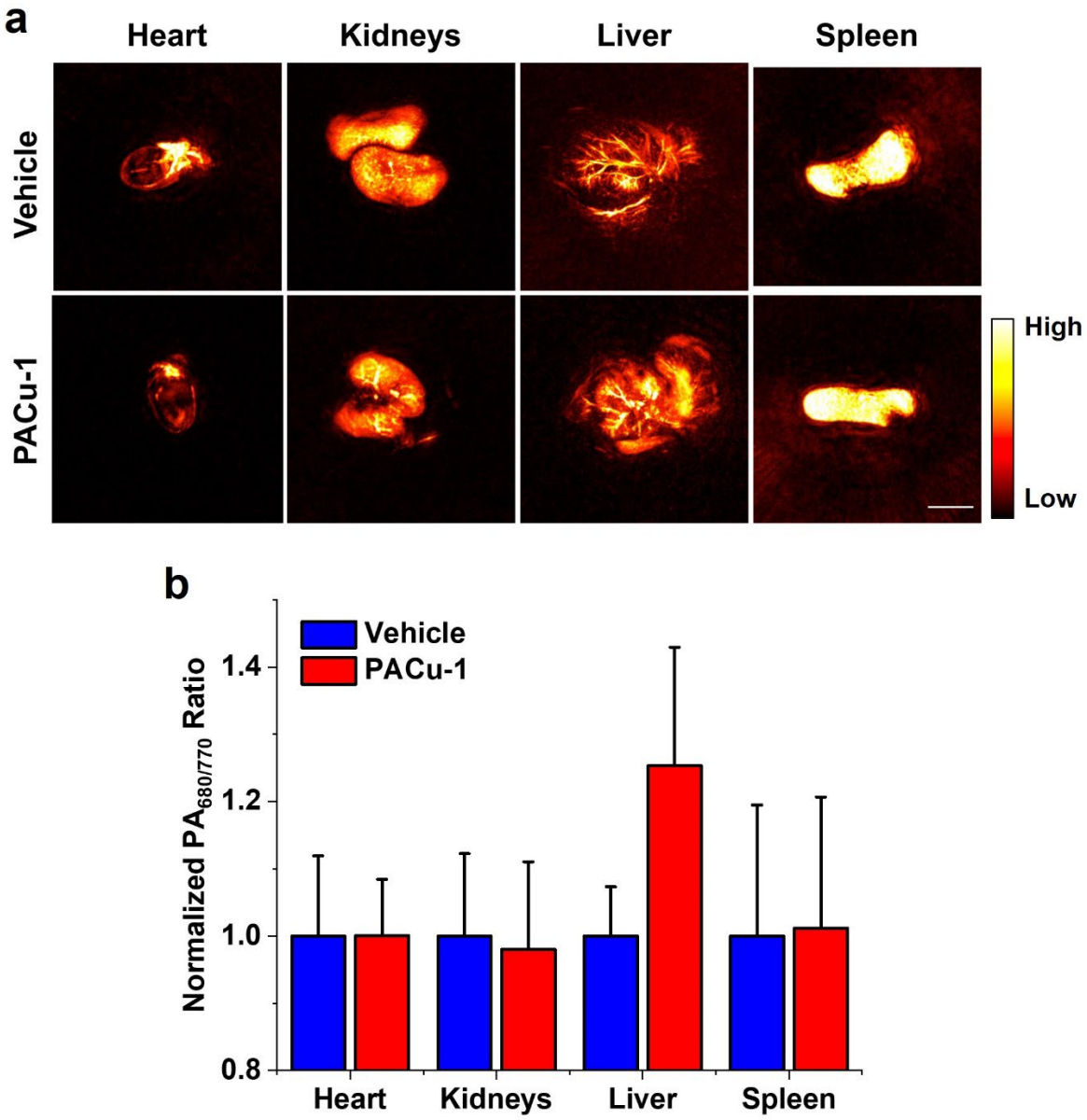

Supplementary Figure 7. a. *Ex vivo* PA images of the heart, kidneys, liver, and spleen after treating live mice with 0 or 50 μM of PACu-1. Scale bar represents 5 mm. b. Normalized $PA_{680/770}$ ratio for matching conditions in Supplementary Figure 7a (n = 3).

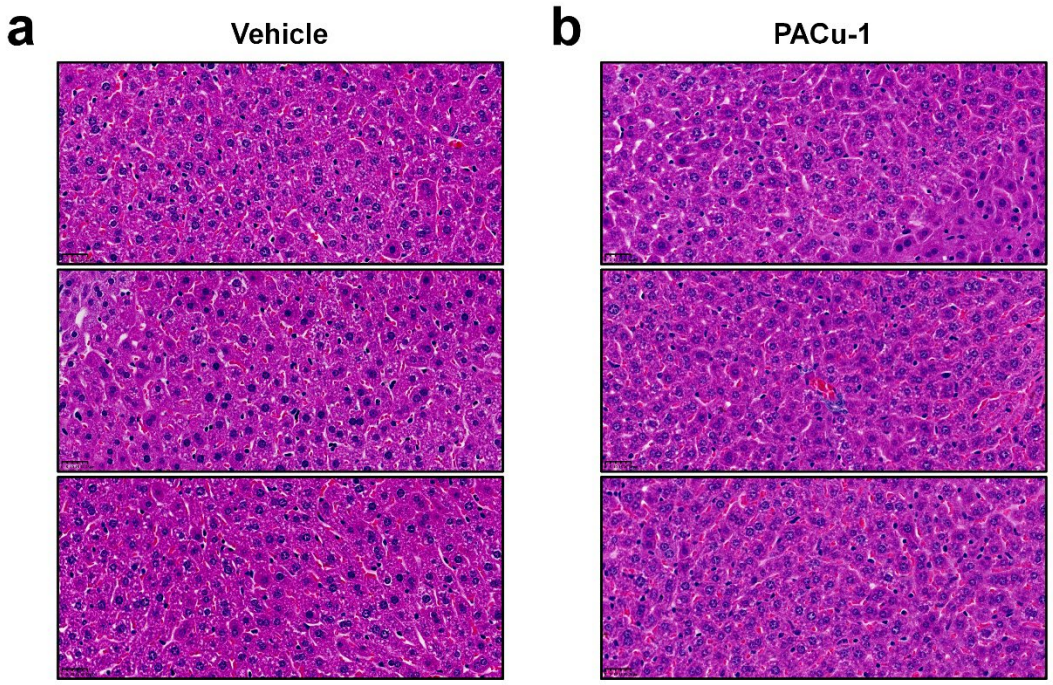

Supplementary Figure 8. Additional H&E stains of the liver after treating live mice with a. 0 or b. 50 μM of PACu-1. Scale bar represents 25 μm.

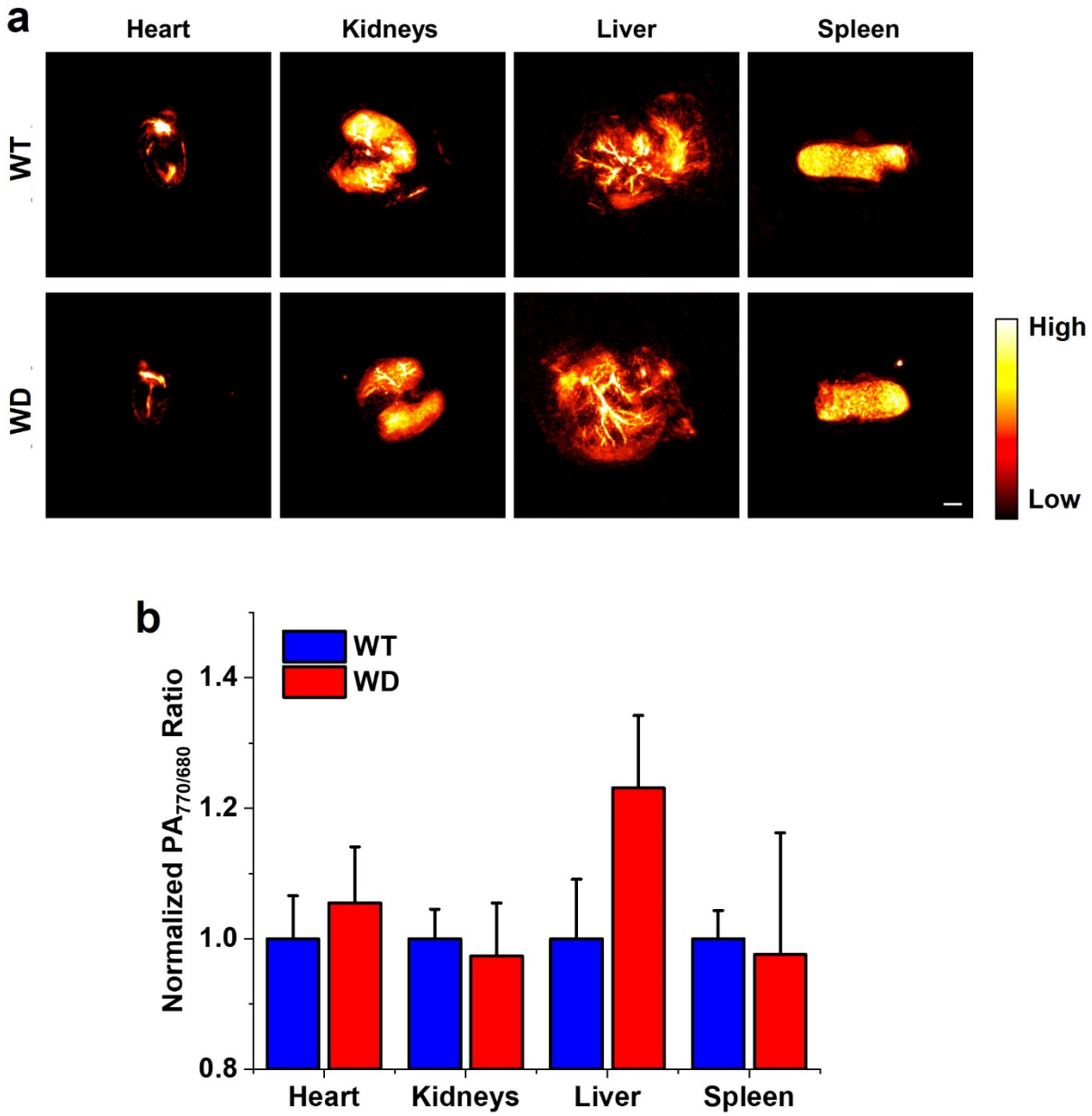

Supplementary Figure 9. a. *Ex vivo* PA images of the heart, kidneys, liver, and spleen after treating wildtype or WD mice 50 μM of PACu-1. Scale bar represents 2 mm. b. Normalized $PA_{770/680}$ ratio for matching conditions in Supplementary Figure 9a (n = 3).

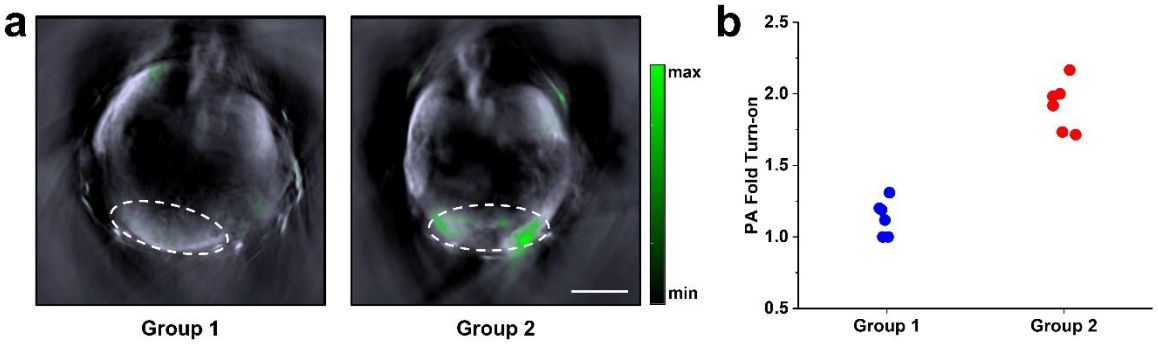

Supplementary Figure 10. a. Representative spectrally unmixed MSOT images of the liver of mice from Group 1 (wildtype) and Group 2 (WD) 1 h post-injection of PACu-1 (50 μM). White dotted ROIs were used to quantify the PA signal. Scale bar represents 5 mm. b. Individual PA fold turn-ons for Group 1 (n = 6) and Group 2 (n = 6) mice.

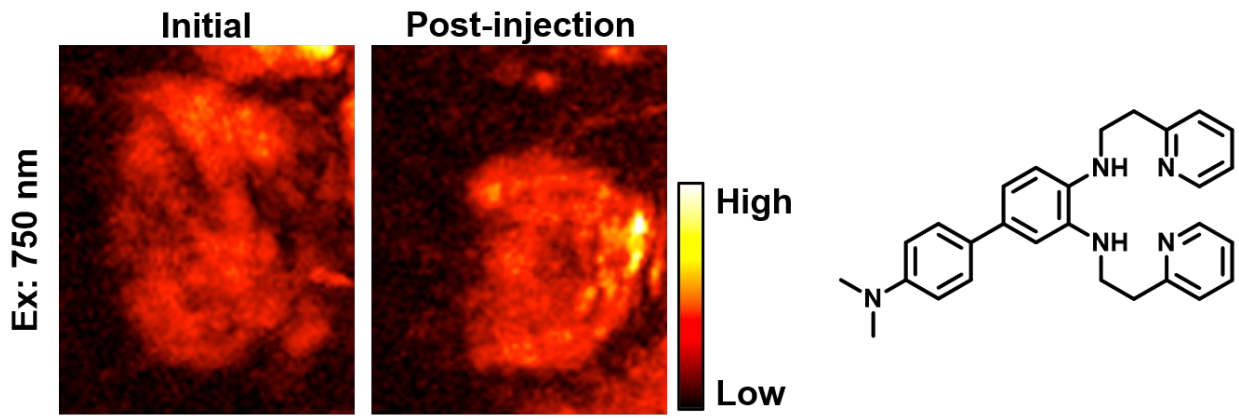

Supplementary Figure 11. Representative PA images of the liver of mice pre-treated with Cu before and after administration of RPS1. RPS1 structure is shown on the right.

Compound 1: ^{1}H NMR (500 MHz, $CDCl_3$)

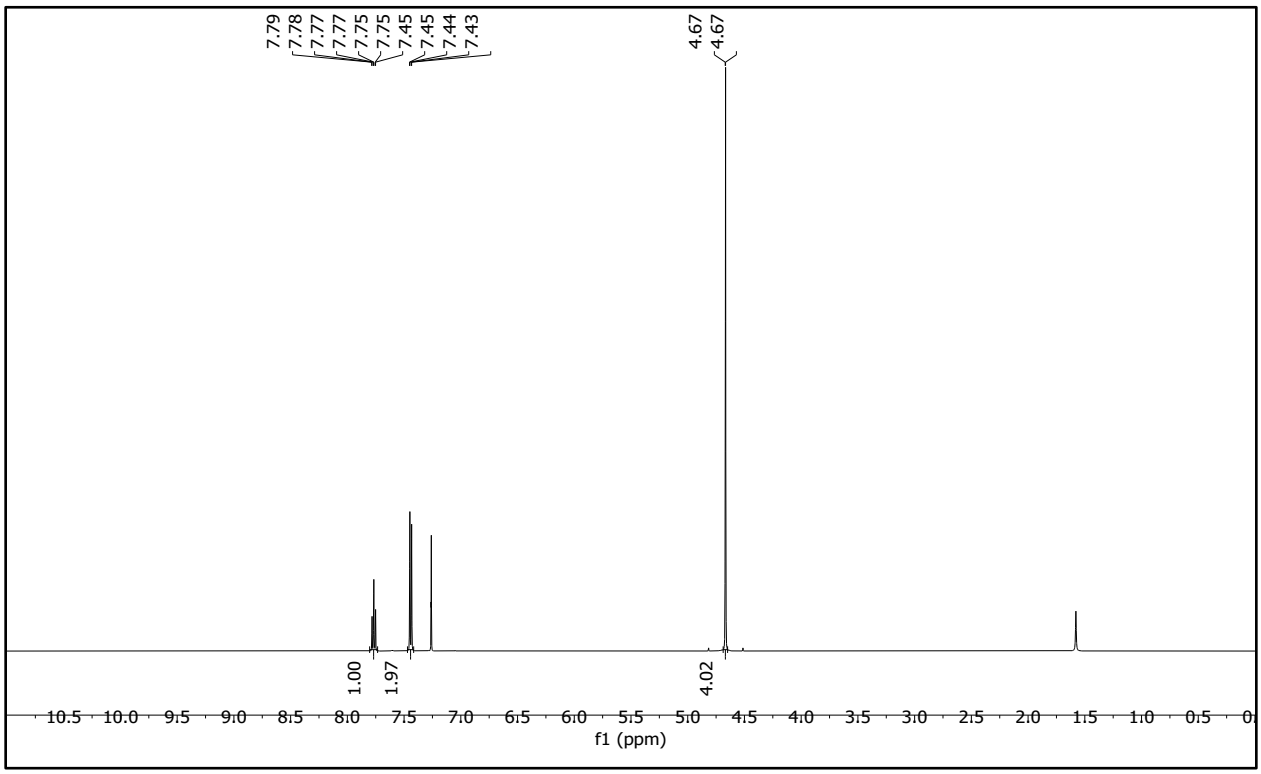

Compound 1: ^{13}C NMR (125 MHz, $CDCl_3$)

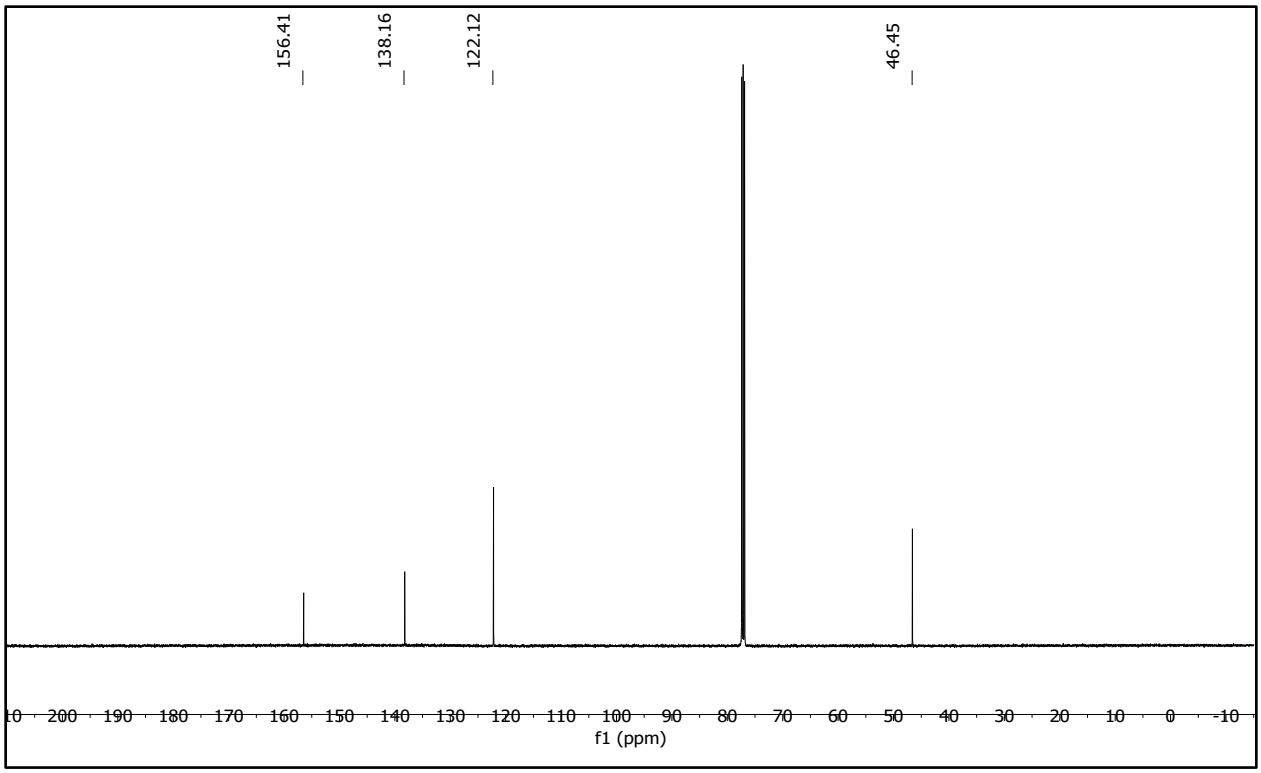

Compound 2: ^{1}H NMR (500 MHz, $CDCl_3$)

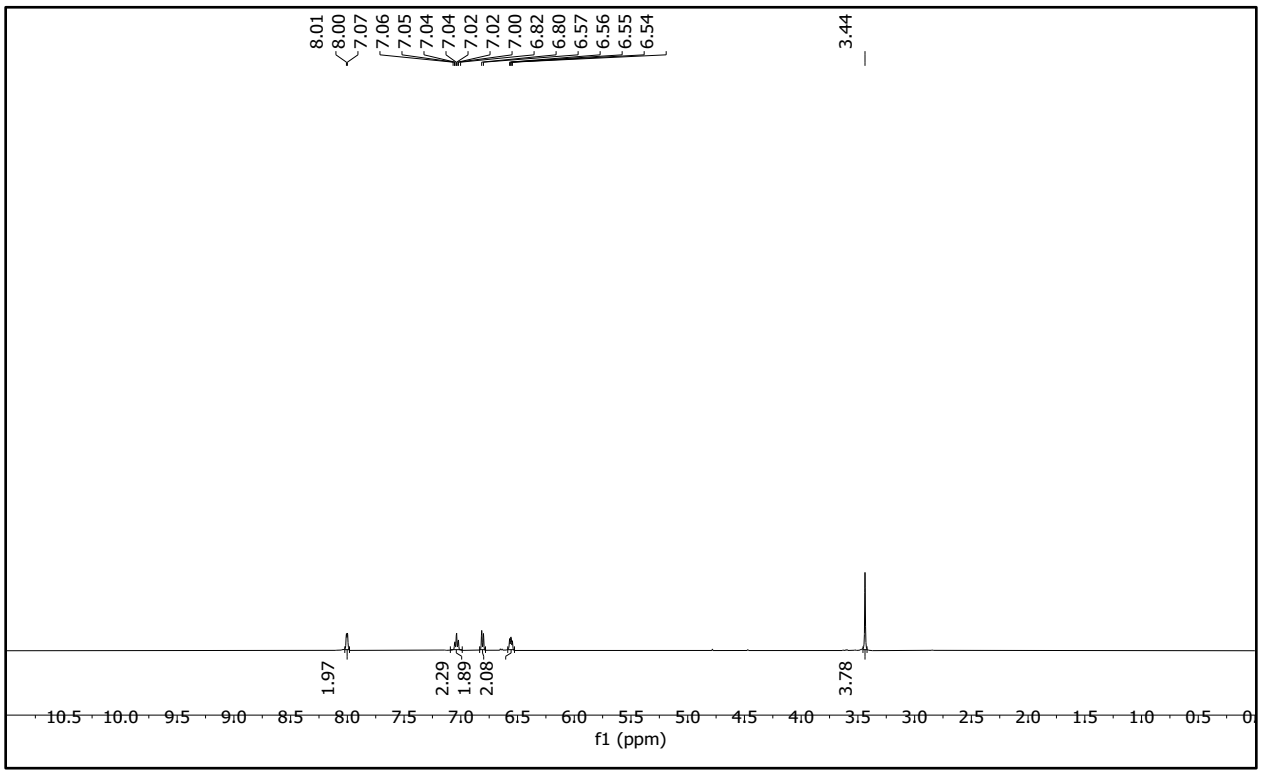

Compound 2: ^{13}C NMR (125 MHz, $CDCl_3$)

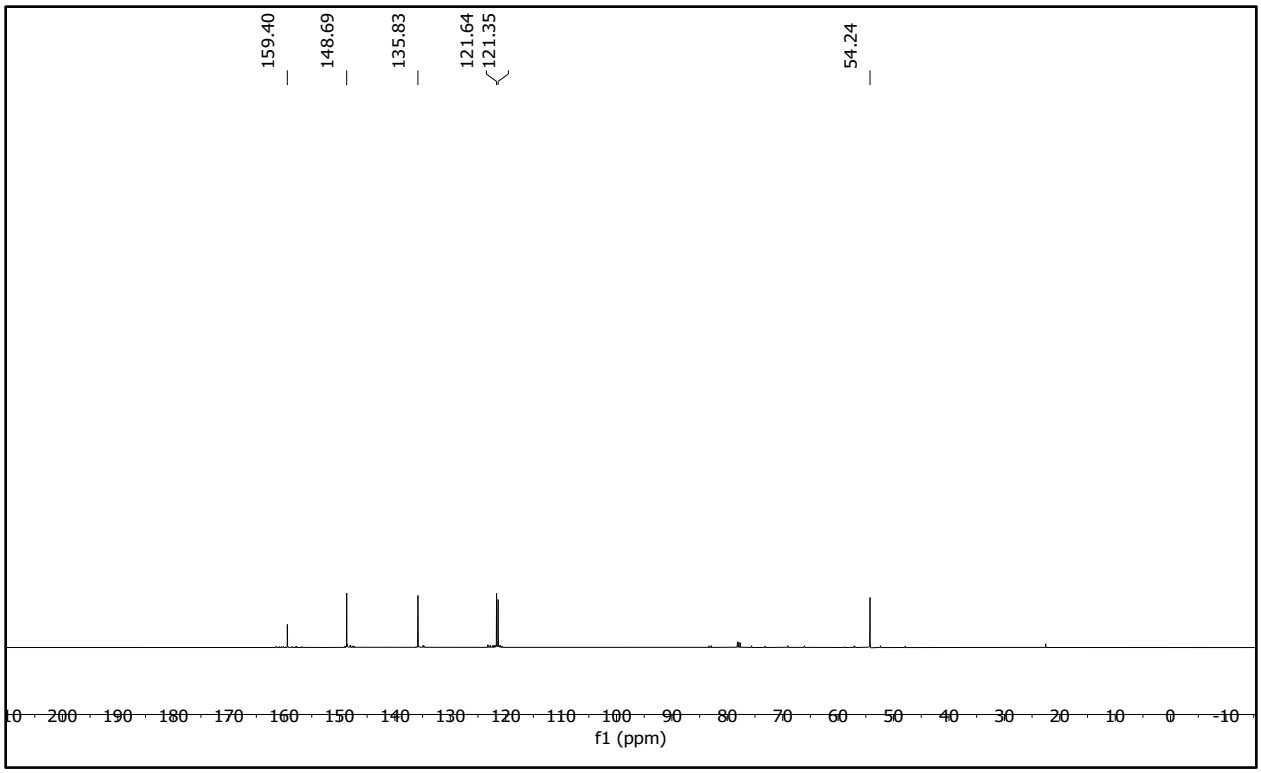

Compound TPA-Cl: ^{1}H NMR (400 MHz, $CDCl_3$)

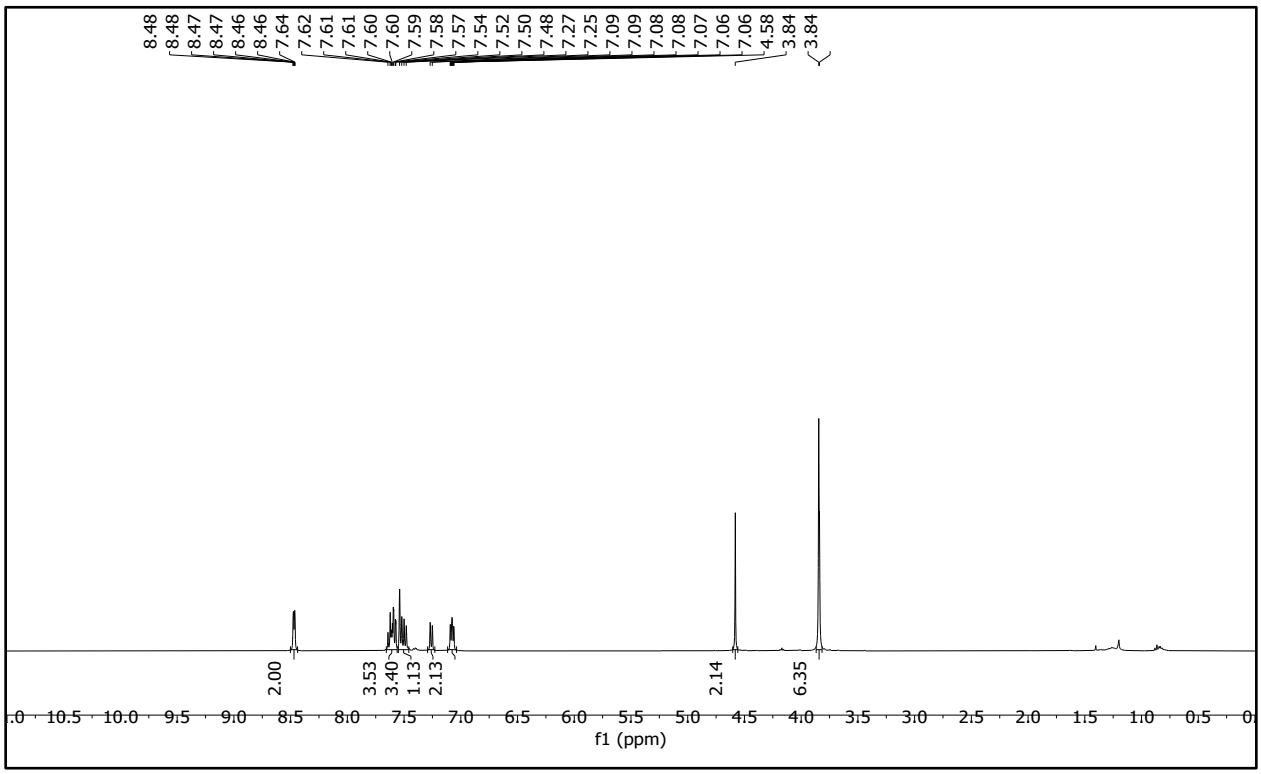

Compound TPA-Cl: ^{13}C NMR (125 MHz, $CDCl_3$)

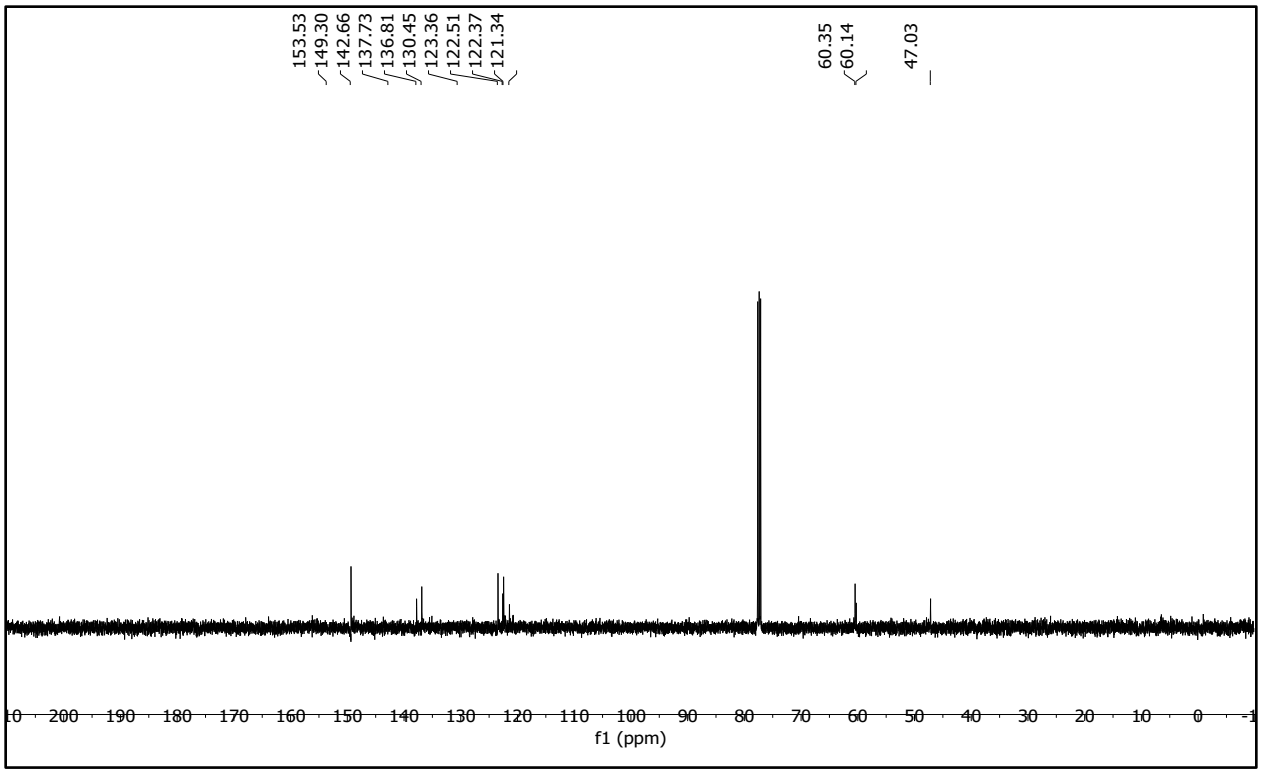

Compound PACu-1: ^{1}H NMR (500 MHz, $CDCl_3$)

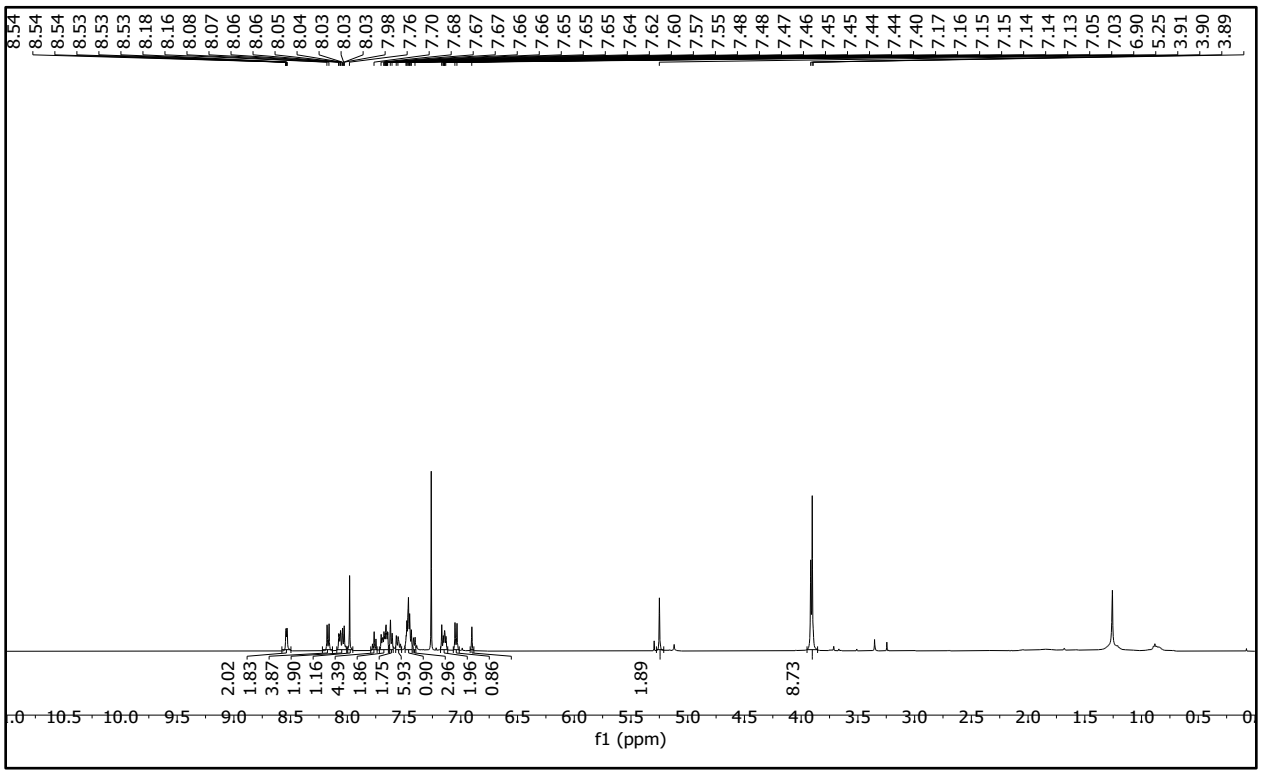

Compound PACu-1: ^{13}C NMR (125 MHz, $CDCl_3$)

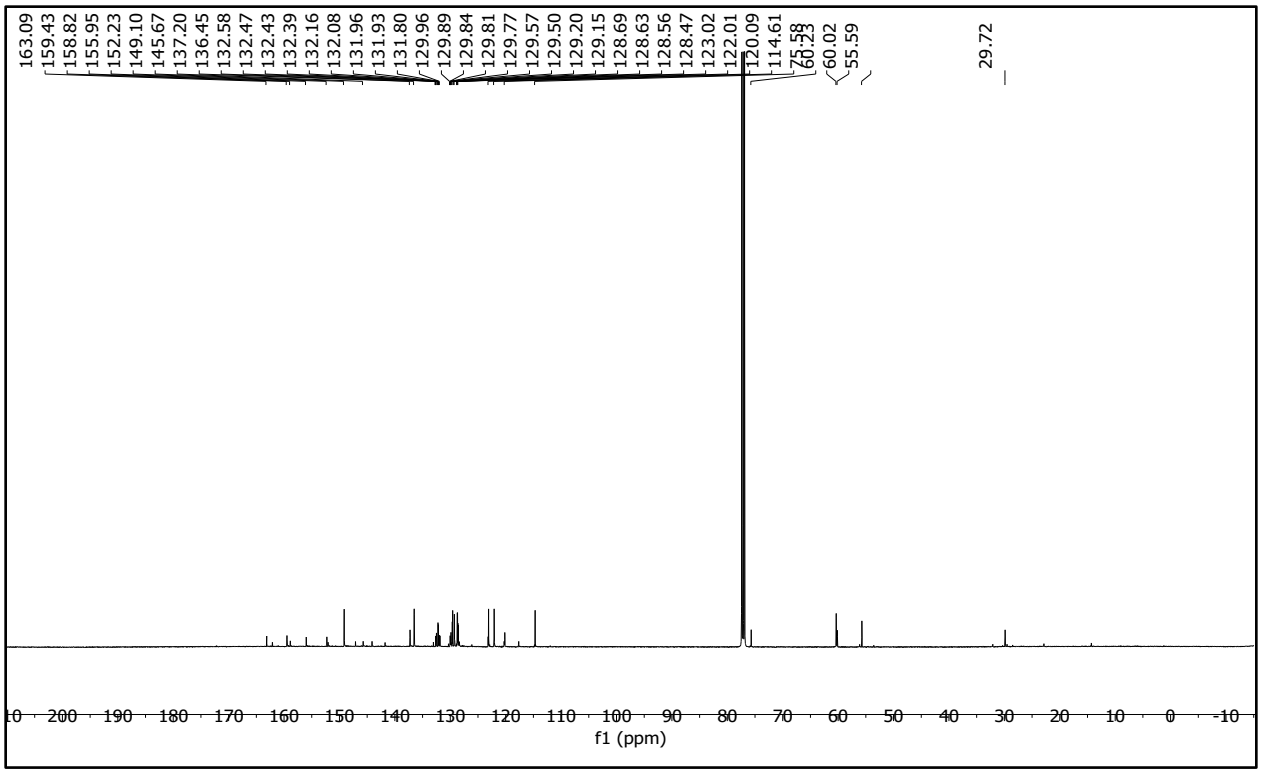

Compound 3: ^{1}H NMR (500 MHz, $CDCl_3$)

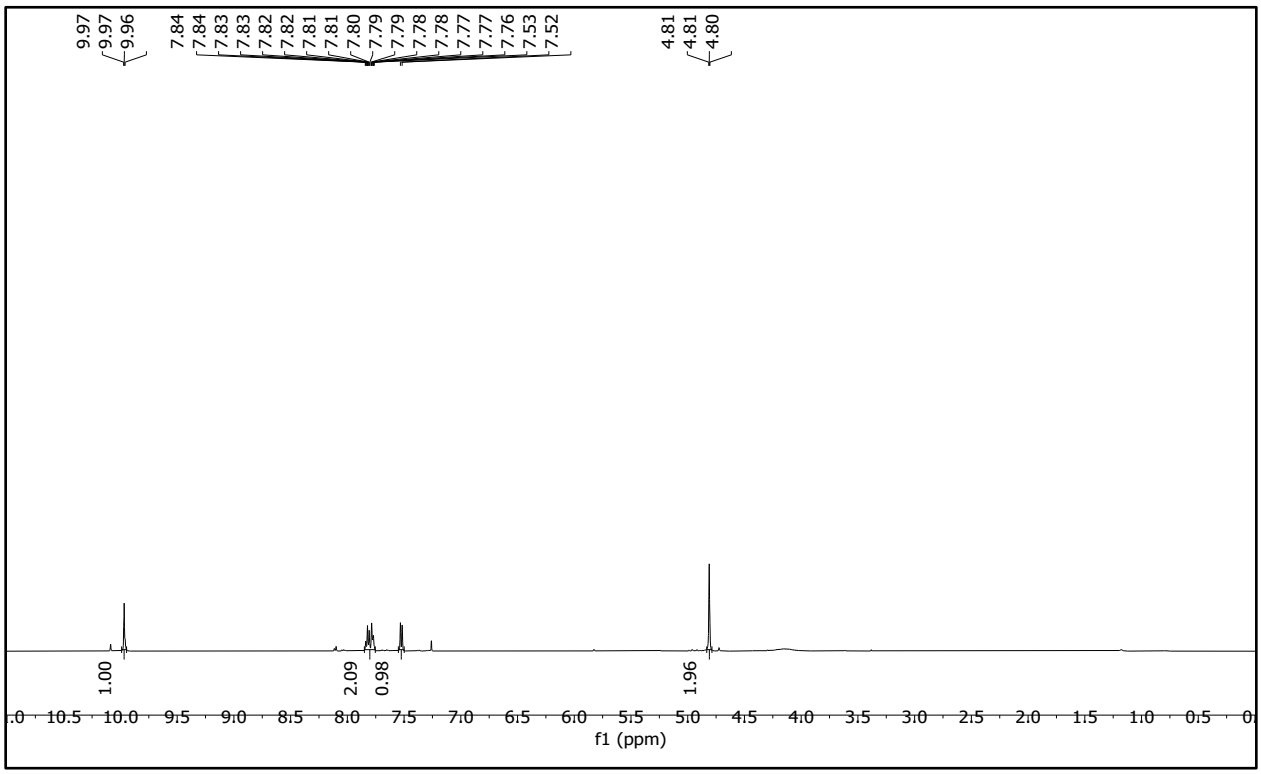

Compound 3: ^{13}C NMR (125 MHz, $CDCl_3$)

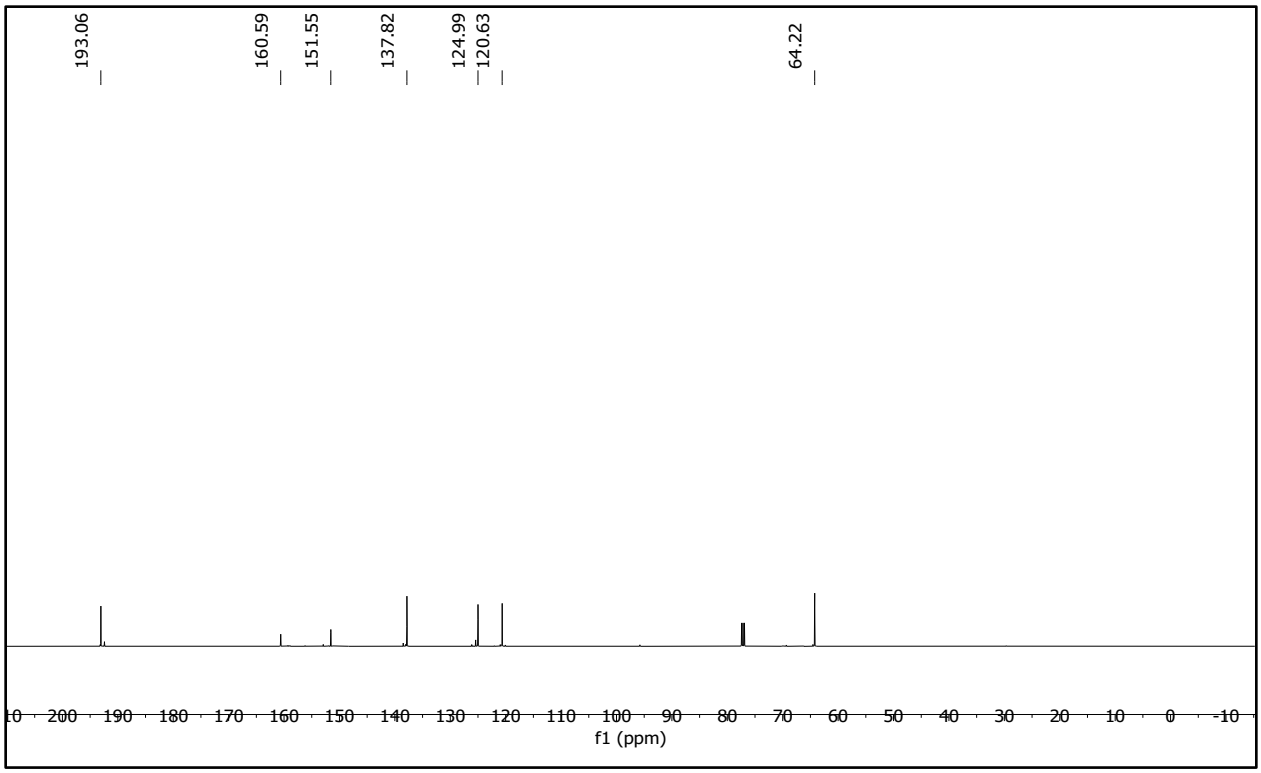

Compound 4: ^{1}H NMR (500 MHz, $CDCl_3$)

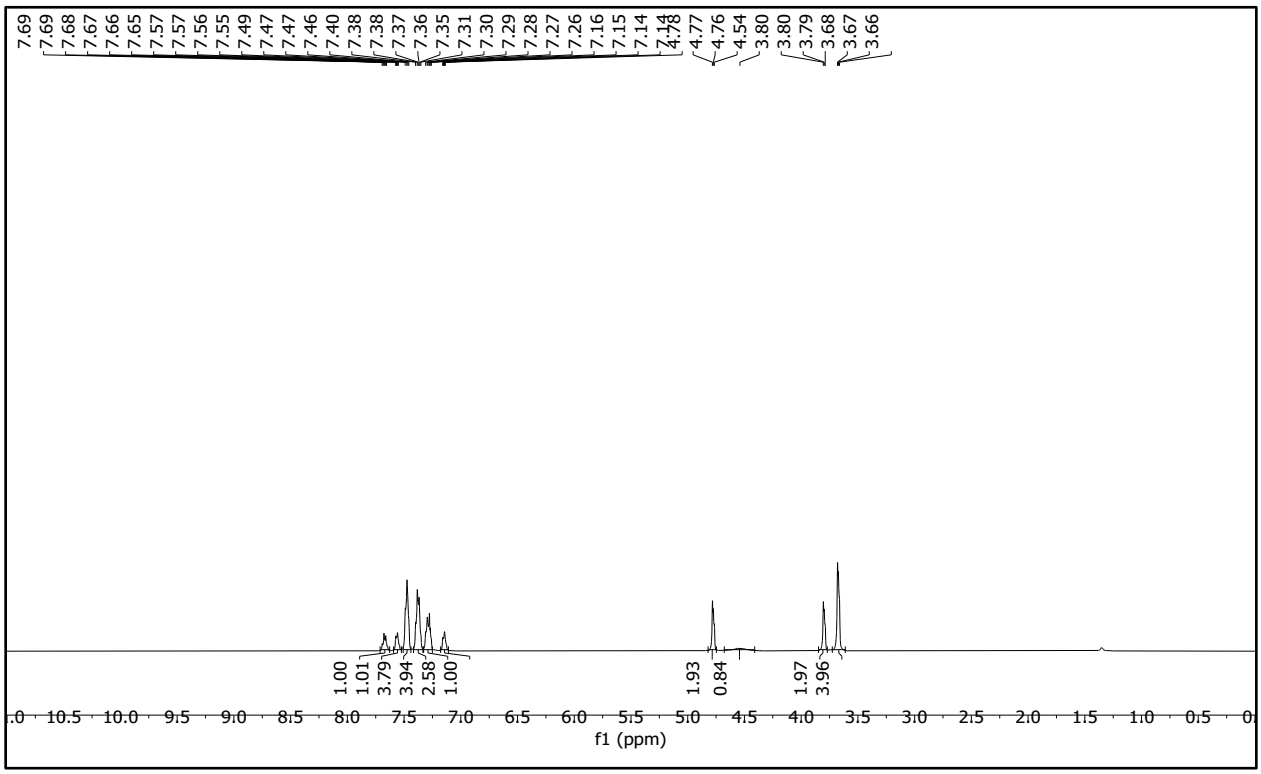

Compound 4: ^{13}C NMR (125 MHz, $CDCl_3$)

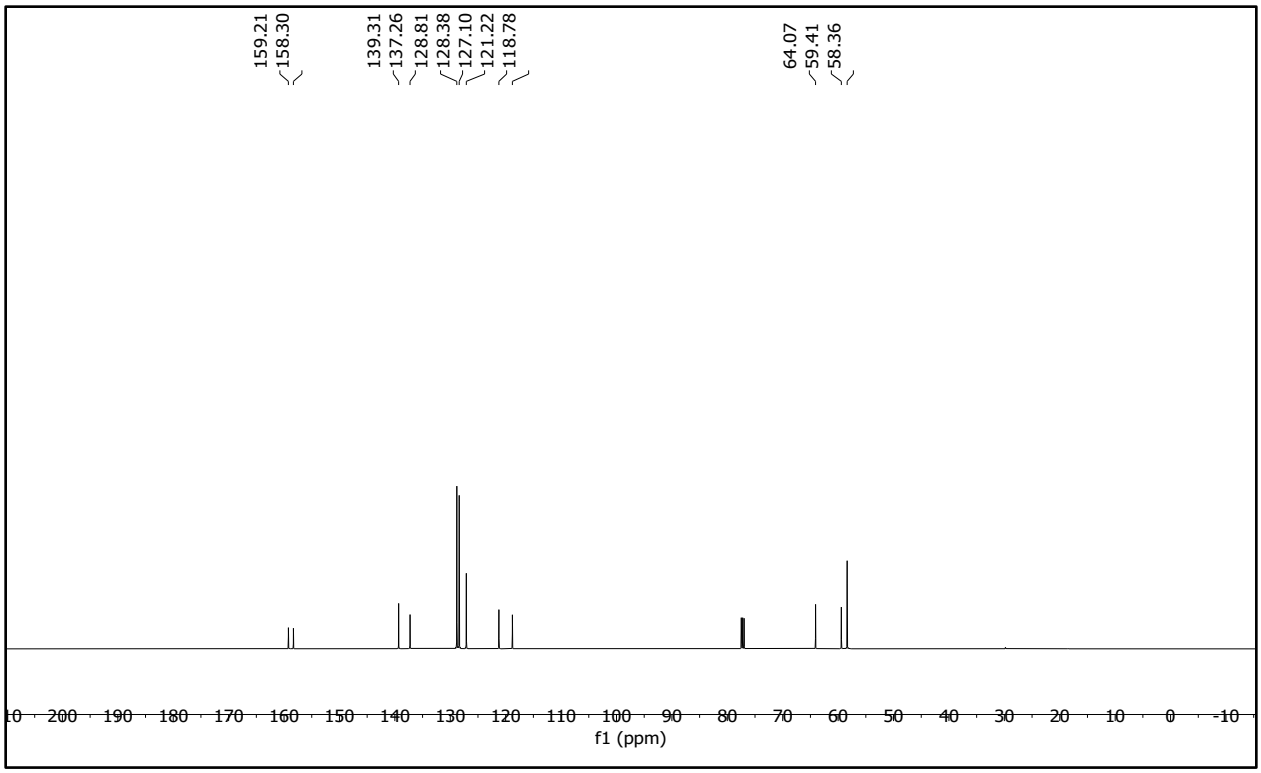

Compound 5: ^{1}H NMR (500 MHz, $CDCl_3$)

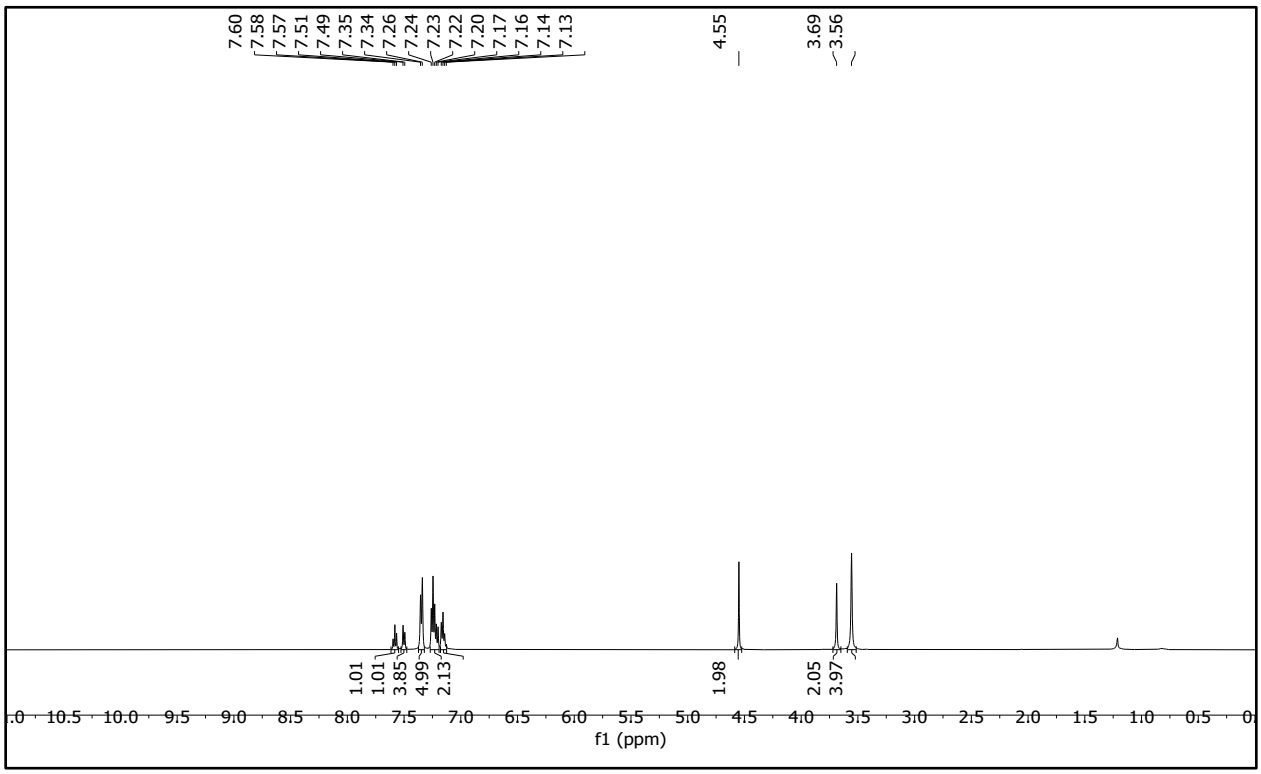

Compound 5: ^{13}C NMR (125 MHz, $CDCl_3$)

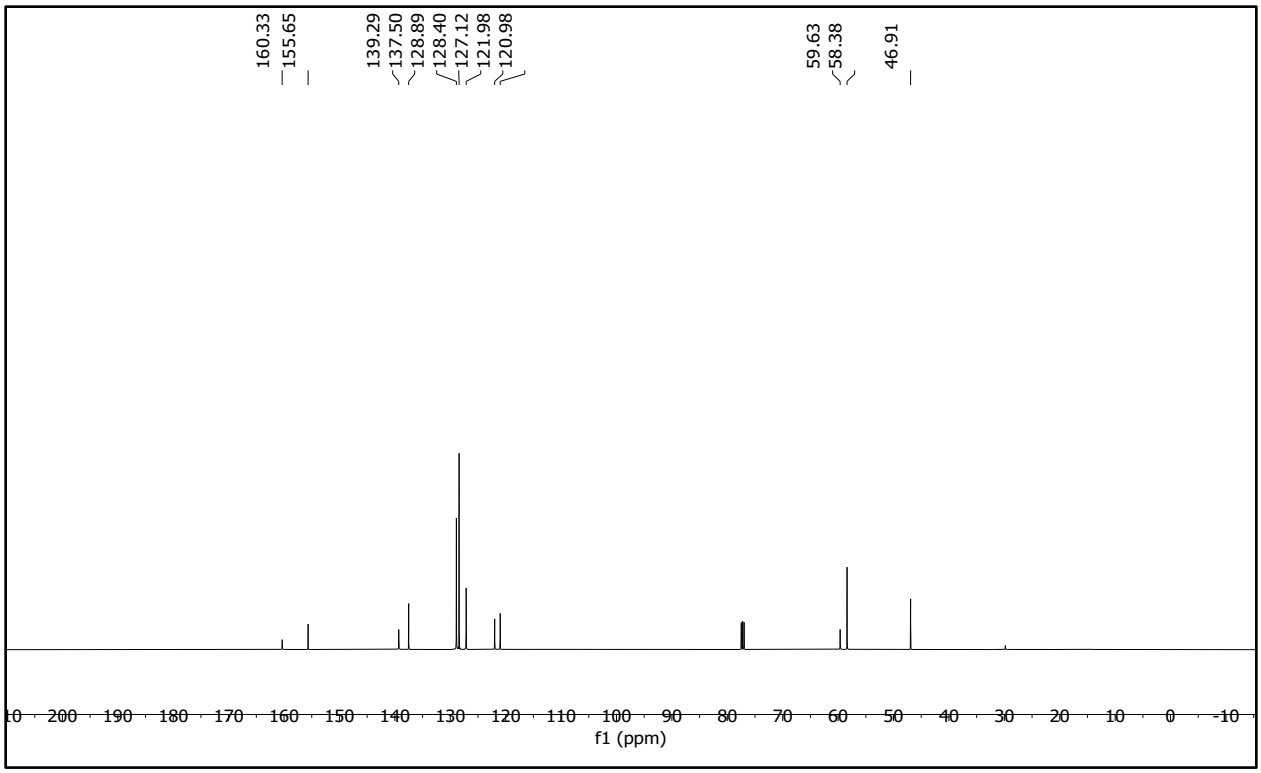

Compound Ctrl-PACu-1: ^{1}H NMR (500 MHz, CD_2Cl_2)

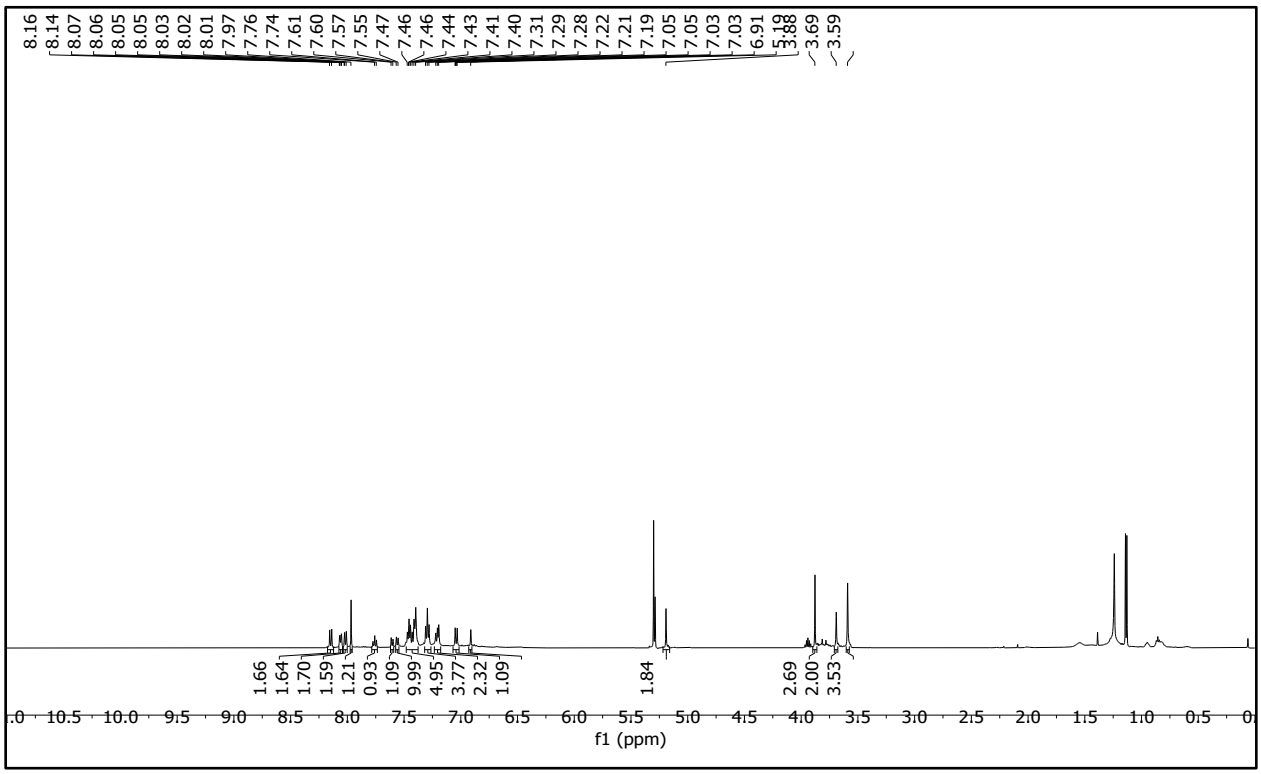

Compound Ctrl-PACu-1: ^{13}C NMR (125 MHz, CD_2Cl_2)

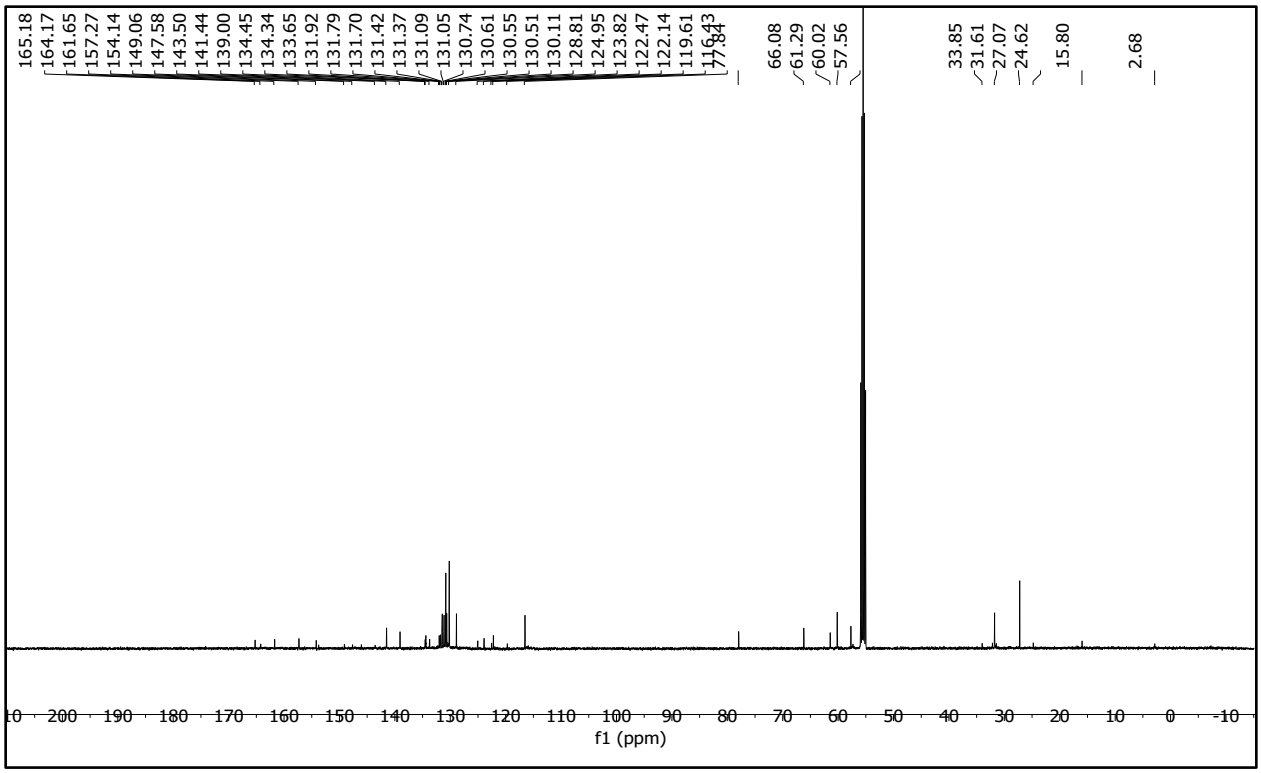

2.12 Acknowledgement of contributions

M.Y.L. synthesized PACu-1. Y.T., C.J.Z., V.G., X.H., and D.M. helped to synthesize PACu-1 analogs. J.A.F. synthesized RPS1. M.Y.L. performed all *in vitro* characterization experiments. M.Y.L. performed all animal imaging with help from S.S. and C.J.Z. M.Y.L. and S.S. conducted the blind BFA study.

CHAPTER 3: APPLICATION OF PHOTOACOUSTIC IMAGING IN COMPANION DIAGNOSIS[3]

3.1 Background and significance

Personalized medicine is a medical model that aims to improve patient outcomes by predicting treatment response through diagnostic and detection-based assays. Currently, more than 30 commercially available companion diagnostics (CDx) have been developed in an effort to match therapies to patients.[73] CDx are defined as tests that provide essential information for determining which patients may benefit from a particular treatment by detecting biomarkers that are critical for drug activation.[74] However, the only successful CDx thus far are limited to *in vitro* studies. With this in mind, *in vivo* imaging tools are critical for providing accurate, real-time information to aid physicians in diagnosis and treatment selection. Prodrugs, which are designed to reduce systemic toxicity and activated by environmental ques (e.g., pH, enzymatic activity, oxidative stress, biothiols) in tumors, have great potential as personalized therapeutics. Unfortunately, this kind of approach is difficult to implement without prior knowledge as to whether a specific tumor exhibits characteristics for prodrug activation. In this study, we develop a PA companion diagnostic (PACDx) specifically for imaging increased concentrations of glutathione (GSH) in cancer, along with a photoacoustic-trackable prodrug (PARx).

Since GSH is the most abundant thiol found in the body it plays important roles in cell function and redox homeostasis.[75] However, GSH is a double-edged sword such that high GSH concentrations have been associated with a variety of cancer types including breast, ovarian, and

[3] Portions of this chapter are reprinted or adapted with permission from the following publication: Lucero, M. Y. & Chan, J. Photoacoustic imaging of elevated glutathione in models of lung cancer for companion diagnostic applications. *Nature Chemistry* **13**, 1248–1256 (2021).

lung cancer.[76] For instance, GSH was reported to be 4-fold higher in non-small cell lung carcinoma (NSCLC) patient-derived tissue samples[77] and 7-fold higher in NSCLC human cell lines[78,79] compared to healthy lung tissue and cells. Although a number of drug delivery systems utilize GSH to trigger the release of a drug, the reactivity is typically not tuned to distinguish between healthy and cancerous tissue (generally reported to have up to 10 mM GSH).

Most clinically approved imaging agents for cancer target cell surface biomarkers through binding events. In addition, binding-based strategies suffer from poor signal-to-noise and precludes the detection of small-molecule targets, such as GSH. ABS is a powerful alternative that that can overcome some of these challenges since it relies on the selective detection of chemical reactivity. In the ABS strategy, we leverage classic principles in physical organic chemistry to guide the development of PACDx. Application of PACDx and PARx in an unprecedented blind study allowed us to successfully identify and treat mice with lung cancer, respectively. Additionally, our new CDx was employed in orthotopic lung cancer and liver metastasis models to demonstrate its broad utility. This work overcomes an outstanding challenge in the field of PA imaging and presents the first successful application of PA imaging of the lung region.

3.2 Design and development of PACDx

The design of PACDx features two key elements, a PA dye capable of generating a strong PA signal upon irradiation and a trigger for detecting GSH in its reduced form. The well-established hemicyanine dye (HD) platform was selected due to the large extinction coefficient ($\varepsilon = >10^4\,M^{-1}\,cm^{-1}$) in the near-infrared region and lipophilic cationic character, which can enhance uptake by tumor cells. These desirable properties also resulted in a probe that was a poor substrate for glutathione S-transferase (GST), an abundant cytosolic enzyme that catalyzes the

conjugation of GSH to electrophilic centers.[80,81] This was a considerably important aspect in the design since GST expression varies in cancer and may cause cross-reactivity that can confound the imaging results. After selecting the dye platform, we employed a physical organic approach to develop a precision-tuned, GSH-responsive trigger that can distinguish cancer-related levels of GSH. Current GSH probes rely on Michael addition, disulfide exchange[82] and S_NAr[83] chemistries which are too reactive. For example, when we installed the commonly used 2,4-dinitrobenzenesulfonate trigger onto the HD, the probe was unable to distinguish GSH levels across several mammalian cell lines (Supplementary Figure 12), as it was fully activated by only 100 μM GSH within minutes (Figure 9). To begin the redesign, we established a structure–reactivity relationship by first synthesizing a panel of nine probes featuring a range of electron-withdrawing and -donating groups at the *para* position. With this panel, a Hammett plot was constructed that revealed a linear correlation between $\log(k_X/k_H)$ and the corresponding σ^- constants (k_X and k_H are rate constants for when the *para*-substituent is X or H, respectively; σ is the substituent constant).[84] A ρ value of +1.10 was calculated which indicated that electron-deficient substituents at the *para* position were more efficient at stabilizing the Meisenheimer complex, resulting in enhanced reactivity (ρ is the reaction constant). Although the most reactive probe in this series (*p*-nitro) was only partially activated (5.6-fold turn-on), we were encouraged by these results as there was a clear dose- and time-dependent response. To optimize the reactivity, we synthesized an additional four probes with both *ortho*- and *para*-electron-withdrawing groups (Supplementary Figure 13). We found that installation of a fluoro substituent at the *ortho* position and retaining a nitro substituent at the *para* position resulted in a highly optimized trigger. Specifically, we noted complete attenuation in turn-on of PACDx under physiological conditions. In addition, PACDx exhibited a dose-dependent signal increase of up to 31.6-fold when incubated

with 10 mM GSH for 1 h. To further understand the reaction, rate constants for PACDx, the *p*-nitro analog and the 2,4-dinitro congener were measured at various temperatures to construct the corresponding Eyring plots. The derived activation parameters for PACDx are $\Delta H^{\ddagger} = 70.5$ kJ mol^{-1} and $\Delta S^{\ddagger} = -117.1$ J mol^{-1} K^{-1}. Overall, this suggests that the S_NAr reaction involves a highly ordered transition state, which is probably due to effective stabilization of the Meisenheimer complex. The Gibbs free energy of activation ($\Delta G^{\ddagger}$) for PACDx was calculated to be 106.8 kJ mol^{-1}, which indicates that the S_NAr reaction was energetically more favorable than the *p*-nitro analog, but less favorable compared to the 2,4-dinitro congener. Finally, we constructed two Brønsted relationship graphs where the pK_a values of the corresponding phenols were plotted against $\Delta G^{\ddagger}$ and log(k). The R^2 values of 1.00 for both Brønsted plots implies that this information can guide probe design involving S_NAr chemistry. All other pertinent results are summarized in Supplementary Table 1.

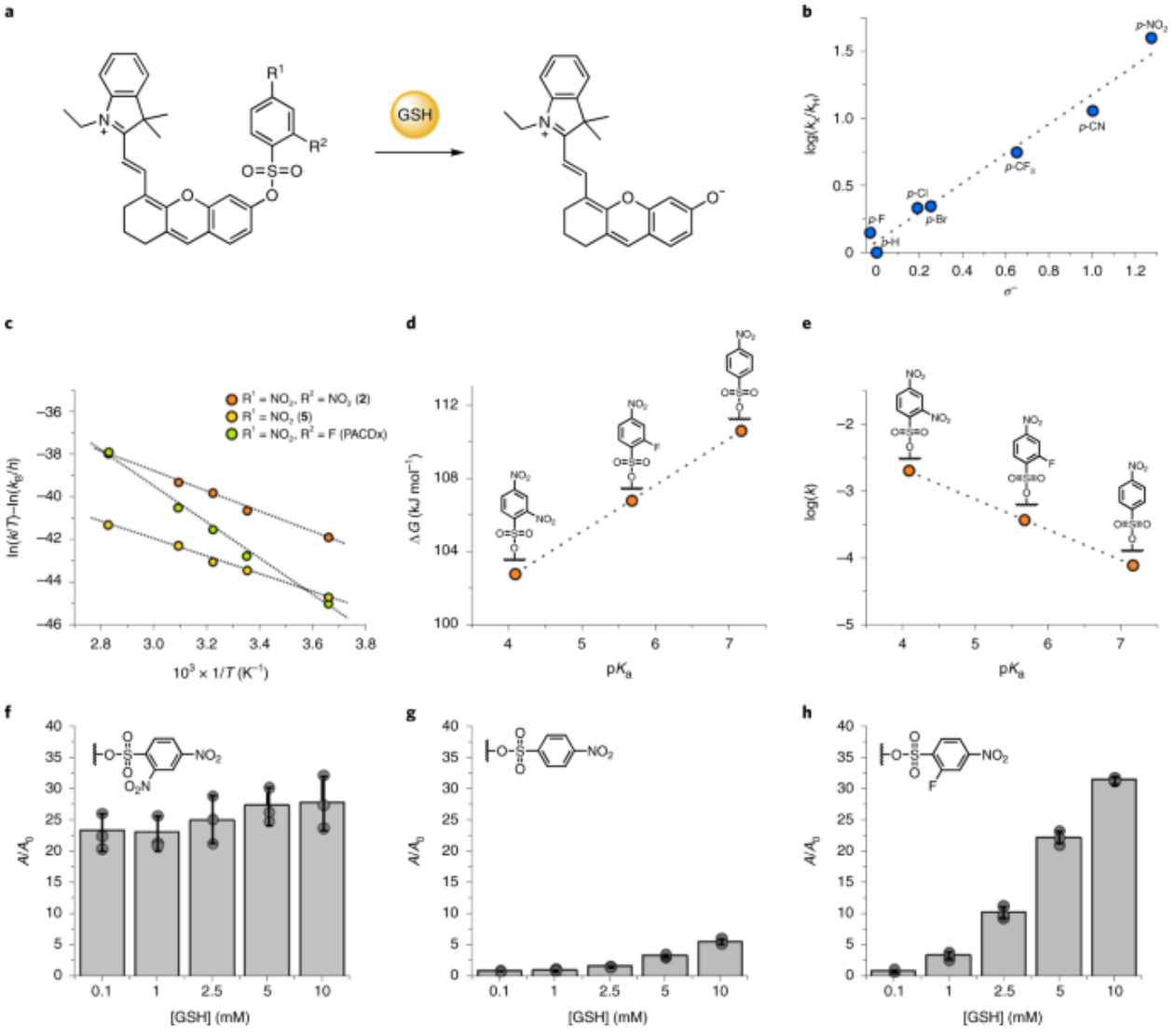

Figure 9. a. General schematic for GSH-responsive photoacoustic companion diagnostics. b. Hammett plot for the S_NAr reaction between *para*-substituted benzenesulfonyls and 10 mM GSH at 120 °C. The dotted line is the best linear fit of the rate constant data. k_X and k_H are rate constants for when the *para*-substituent is X or H, respectively. c. Eyring plots for **2**, **5** and PACDx reacting with GSH (structures of **2**, **5** and PACDx are shown as insets in f–h). The dotted lines represent the best linear fits. *k,* rate constant; *T*, temperature; k_B, Boltzmann constant; *h*, Planck's constant. Brønsted plots indicating the linear relationship between ΔG and d. log(*k*) and e. pK_a (R^2 = 1.0 and 0.99, respectively) for **2**, **5** and PACDx reacting with GSH at 37 °C. Dose-dependent activation of f. **2,** g. **5** and PACDx, with h. [GSH] of 0.1–10 mM. *A* and A_0 are defined as the final and initial absorbance values, respectively. All assays were performed at pH 7.4, 70% PBS/MeCN. Data are presented as mean values ± SD (n = 3 independent experiments).

3.3 Evaluating PACDx *in vitro* and in live cells

Before treatment with GSH, PACDx does not absorb strongly within the PA window (680–950 nm) which essentially affords an intensity-based PA probe. Incubating PACDx with GSH results in a bathochromic shift in absorbance. PA imaging in tissue-mimicking phantoms gives similar results where irradiation at λ_{max} (690 nm) yields the strongest PA response *in vitro*. PACDx exhibited a dose-dependent signal enhancement with a limit of detection of 0.39 mM. Importantly, PACDx had no noticeable turn-on in the presence of biothiols such as cysteine (200 μM) or homocysteine (100 μM) (Supplementary Figure 16). After obtaining optimal results *in vitro*, we evaluated the performance of PACDx in A549 lung cancer cells, U87 glioblastoma cells and HEK 293 cells (a non-cancerous cell line) using confocal microscopy. PACDx exhibited the highest fluorescent signal in A549 cells, with a cytosolic and mitochondrial staining pattern, compared to the other mammalian cell lines. To confirm that these results were from elevated GSH levels, cells were pretreated with *N*-ethylmaleimide (NEM), a reagent used to reduce the levels of intracellular thiols. This led to a decrease in fluorescent signal of ~50%. To verify that the decrease in intensity was due to GSH depletion, a third set of cells was treated with a non-responsive control probe (Ctrl-PACDx, Supplementary Figure 17). The same experiment was performed in U87 cells with similar results (Supplementary Figure 18). As mentioned earlier, it is important for PACDx to be GST-independent. To demonstrate this, A549 and U87 cells were pretreated with ethacrynic acid (EA), a potent reversible inhibitor of human GST, which had no effect on probe activation was observed (Supplementary Figure 19).[85]

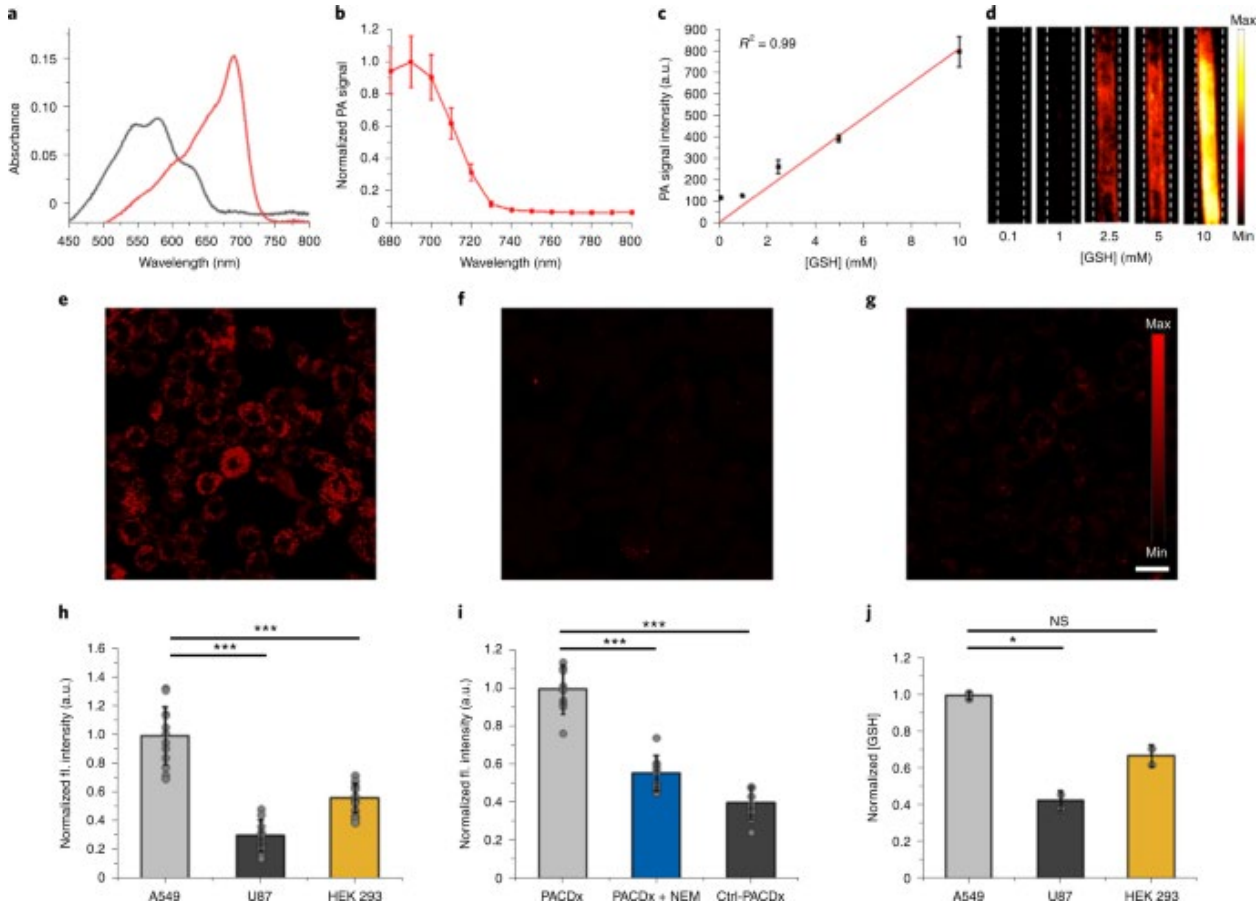

Figure 10. a. Absorbance profile of 5 µM PACDx before (black line) and after (red line) treatment with 10 mM GSH. **b**, PA spectra of 50 µM turned-over HD. c. PA signal ($n = 3$ independent experiments) and d. PA images of PACDx in response to GSH. Samples were irradiated at 690 nm. All *in vitro* assays were performed at 37 °C, pH 7.4, with 70% PBS/MeCN, and data were collected after 1 h. Confocal microscopy image representing A549 cells treated with e. 5 µM PACDx for 1 h at 37 °C A549 cells pretreated with 1 mM NEM then incubated with f. 5 µM PACDx for 1 h at 37 °C and A549 cells treated with g. 5 µM Ctrl-PACDx for 1 h at 37 °C. Scale bar, 20 µm. h. Normalized fluorescence intensity obtained from cell imaging under the conditions in e–g. Data are presented as mean values ± SD ($n = 12$ biologically independent samples). i. Normalized fluorescence intensity obtained from cell imaging A549, U87 and HEK 293 cells with 5 µM PACDx for 1 h at 37 °C. Data are presented as mean values ± SD ($n = 12$ biologically independent samples). j. Normalized [GSH] obtained from Ellman's assay. Data are presented as mean values ± SD ($n = 2$ biologically independent samples). Statistical analysis was performed using a two-tailed Student's *t*-test ($\alpha = 0.05$), ***$P < 0.001$, **$P < 0.01$, *$P < 0.05$. NS, not significant.

It is essential for PACDx to accurately differentiate the relative GSH levels in lung cancer cells compared to healthy cells. That is, although the intensity of PACDx in A549 cells was indeed the highest relative to U87 and HEK 293 cells, it was important to account for possible variations in probe uptake and retention. Therefore, we incubated PACDx with cell lysates and obtained data that was consistent with cell imaging (Supplementary Figure 20). The data further supports the literature and the potential effectiveness of PACDx. The cell lysate experiment was performed using the well-established Ellman's assay, which allows for accurate quantification of GSH levels (Figure 10).[86]

3.4 Design and development of PARx

Next, we ported PACDx into a prodrug design. We reasoned that it would be possible to add a chemotherapeutic cargo linked by a carbonate to the PACDx core by strategically installing a hydroxymethyl handle *ortho* to the phenolic alcohol. Upon reacting with GSH, the formed phenolate intermediate can fragment via a 1,4-elimination pathway to release the drug and the corresponding dye (HD-CH_2OH) for PA imaging. We decided to attach gemcitabine, an FDA-approved drug, since it is commonly used to treat non-small cell lung cancer through the inhibition of DNA synthesis.[87,88] Like many chemotherapeutics, gemcitabine indiscriminately targets any rapidly dividing cell in the body, which results in adverse effects such as severe liver toxicity.[89] In our design, we mask the primary alcohol of gemcitabine as it has been reported to attenuate cytotoxicity until activation with a variety of different masking groups.[90] Although one other strategy we had in mind involved directly modifying gemcitabine with our new 2-fluoro-4-nitrobenzenesulfonyl trigger, we wanted to leverage the PA imaging capabilities and lipophilic

cationic character of the resulting prodrug (herein named PARx) to monitor drug release in real time.

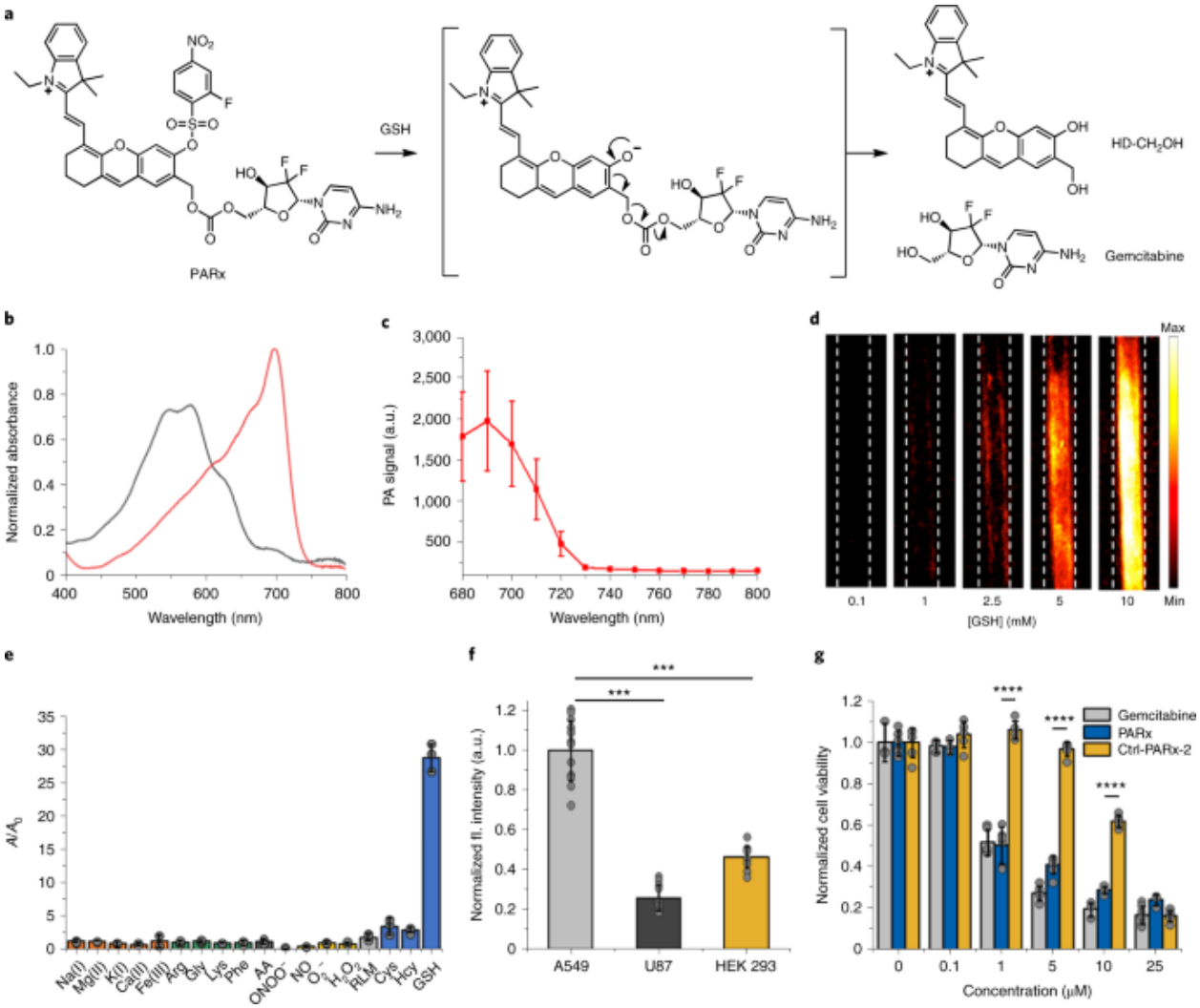

Figure 11. a. Reaction scheme of PARx with GSH to release HD-CH_2OH and gemcitabine. b. Normalized absorbance profile of 5 μM PARx before (black line) and after (red line) treatment with 10 mM GSH at 37 °C for 1 h (pH 7.4, 70% PBS/MeCN). c. PA spectra of 50 μM turned-over HD-CH_2OH dye in 70% PBS/MeCN. d. PA images of PARx in response to GSH. Samples were irradiated at 690 nm. e. Reactivity of PARx with biologically relevant metals, amino acids, RLM, ascorbic acid (AA), reactive nitrogen species, reactive oxygen species and thiols after incubation for 1 h at 37 °C. f. Normalized fluorescence intensity obtained from cell imaging A549, U87 and HEK 293 cells with 5 μM PARx for 1 h at 37 °C. Data are presented as mean values ± SD ($n = 12$ biologically independent samples). Statistical analysis was performed using a two-tailed Student's *t*-test ($\alpha = 0.05$), ***$P < 0.001$, **$P < 0.01$, *$P < 0.05$. g. Cell viability assay using various concentrations of gemcitabine, PARx and Ctrl-PARx-2 after a 48-h incubation with A549 cells. Data are presented as mean values ± SD ($n = 6$ biologically independent samples). Statistical analysis was performed using a two-way analysis of variance with a Dunnett's multiple comparisons test ($\alpha = 0.05$); ****adjusted $P > 0.0001$.

The synthesis of PARx began with the sequential reduction of 2,4-dihydroxybenzaldehyde and *tert*-butyl(dimethyl)silyl protection to afford **21** in 61% yield (Supplementary Information). *In situ* deprotection of the phenolic alcohols with sodium hydride enabled a nucleophilic substitution and retro-Knoevenagel sequence with Cy7-Cl to obtain **22**. The GSH-responsive trigger was installed, and the primary alcohol was deprotected under acidic conditions to yield **23** (Ctrl-PARx-2) in 46% over two steps. Finally, phosgene was used to generate the chloroformate intermediate then reacted with gemcitabine to obtain PARx (Supplementary Information).

3.5 Evaluating PARx *in vitro* and in live cells

After synthesizing PARx, the *in vitro* performance was re-evaluated to confirm that gemcitabine had no effect on the reactivity (Supplementary Figure 21). Interestingly, we observed that PARx consistently yielded a more intense PA signal compared to PACDx, presumably due to the larger PA brightness value ($\varepsilon \times (1 - \Phi_{Fl})$). In addition, we demonstrated that PARx displayed exceptional selectivity against a panel of metal ions, amino acids, reductants, reactive nitrogen and oxygen species, metabolic liver enzymes and competing thiols. To demonstrate the GSH-mediated release of gemcitabine, we employed MS and NMR analyses (Supplementary Figures 22 and 23). In addition, we prepared a control compound (Ctrl-PARx-1) that is unresponsive to GSH to undergo the same MS experiment (Supplementary Figure 24). MS analysis revealed that both the trigger and carbonate linkage of Ctrl-PARx-1 were stable in the presence of 10 mM GSH for at least 1 h (Supplementary Figure 25). Like PACDx, PARx could distinguish GSH levels in live A549, U87 and HEK 293 cells, independent of GST activity (Supplementary Figures 27 and 28). Finally, we performed MTT assays using PARx in A549 cells and observed dose-dependent toxicity that is comparable to free gemcitabine. By contrast, treatment with either Ctrl-PARx-1 or

Ctrl-PARx-2 led to significant attenuation of cytotoxicity (Figure 11). MTT assays in U87 cells established that PARx requires the elevated levels of GSH found in A549 cells to effectively mediate gemcitabine release (Supplementary Figure 29).

3.6 Assessing the performance of PACDx and PARx *in vivo*

PACDx and PARx were evaluated in an A549 xenograft model of lung cancer *in vivo*. Once the tumors had grown to ~100 mm^3, we administered PACDx via intratumoral injection and irradiated at 680 nm (the optimal *in vivo* wavelength) 1 h post-injection. This resulted in a ~1.5-fold PA turn-on response relative to the control flank. Next, we introduced PARx via systemic injection to determine its biodistribution profile, as well as potential off-target cytotoxic effects. After performing *ex vivo* PA imaging, we found that the average PA signals from the heart, kidneys, liver, and spleen were comparable between the treatment and control groups. Finding that the average PA intensity was 1.2-fold higher in the tumor for the PARx-treated animals suggested selective activation, drug release, and no apparent off-target toxicity. To further confirm these results, histological staining was performed which revealed no toxicity in all vital organs. However, PARx was highly toxic in tumor tissue, as indicated by the decrease in the number of stained nuclei. Importantly, terminal deoxynucleotidyl transferase dUTP nick end labelling (TUNEL) staining revealed that PARx-treated tumors experienced significantly greater cell death via apoptosis (54.3 ± 7.4%) compared to control tumors (1.9 ± 1.9%) (Figure 12).

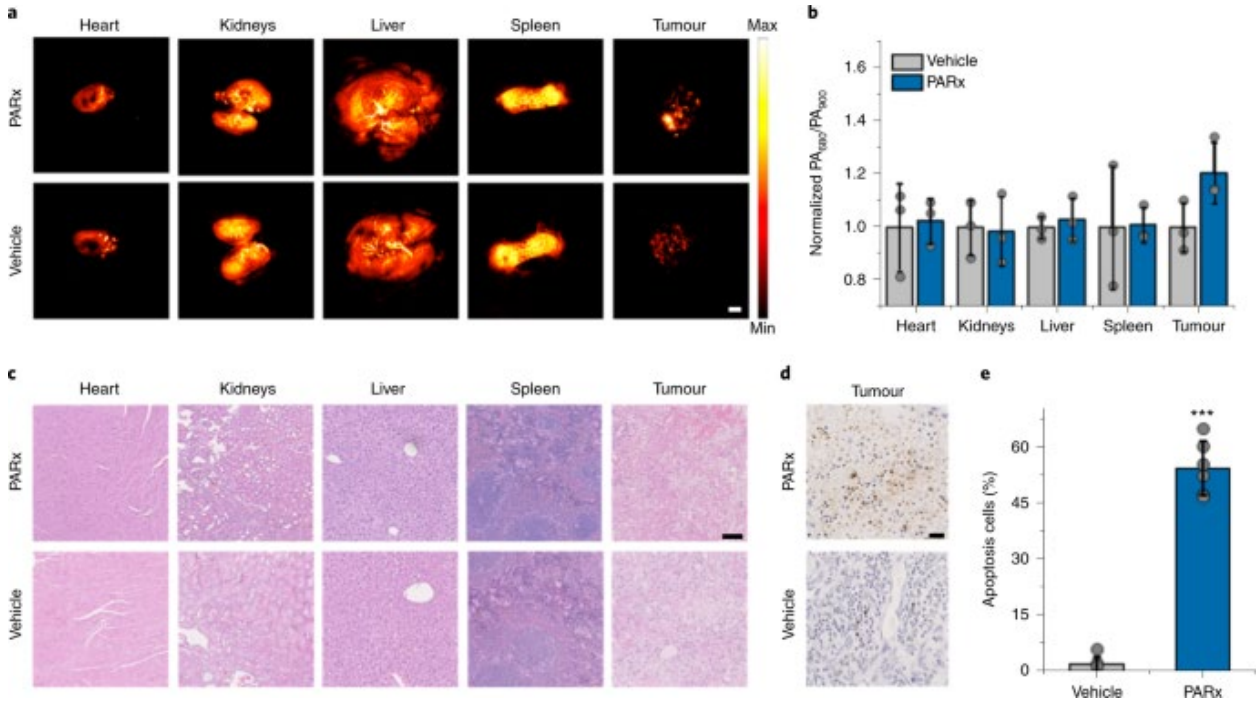

Figure 12. a. Representative *ex vivo* PA images of heart, kidneys, liver, spleen and tumor after systemic injection of PARx (400 µM, 10% DMSO/PBS, retro-orbital injection) or vehicle. Samples were irradiated at 680 nm. Scale bar, 2 mm. b. Normalized PA signal relative to the PA signal at 900 nm (PARx does not absorb at this wavelength) after systemic injection of PARx or vehicle. Data are presented as mean values ± SD ($n = 3$ independent animals). c. H&E staining of heart, kidney, liver, spleen and tumor tissue from PARx-treated and untreated A549 xenografts. Scale bar, 100 µm. d. TUNEL staining of tumor tissue from PARx-treated and untreated A549 xenografts. Brown staining indicates apoptotic cell death. Scale bar, 25 µm. e. Quantification of TUNEL staining. Data are presented as mean values ± SD ($n = 6$ biologically independent samples). Statistical analysis was performed using two-tailed Student's *t*-test ($\alpha = 0.05$), $***P < 0.001$.

To assess the therapeutic capability of PARx, we first opted for local administration because we wanted to bypass systemic and metabolic processes. Mice were treated with a weekly dose of PARx for a period of 21 days. PA imaging was performed 1 h after treatment to monitor gemcitabine release (Supplementary Figure 30). The higher PA signal in PARx-tumors indicates PARx activation and led to complete attenuation of tumor growth. By contrast, tumors that were treated with the vehicle control grew up to ~600 mm^3 in size. Next, we turned our attention to evaluating the systemic compatibility of PARx. Using the same treatment plan, PARx was administered via retro-orbital injection weekly for 21 days. We observed similar results as the previous experiment. In addition, the body weight of each animal was monitored as a measure of general toxicity. Of note, no loss of weight (Figure 13) or change in behavior was observed.[91] To showcase the selectivity of PARx, we increased the dosing frequency to once every three days for 21 days (Supplementary Figure 20). Given the success of the two last experiments, we suspected that we would not see any adverse effects, especially in the liver, where severe damage is common with free gemcitabine. To our delight, we did not observe a change in the body weight (Supplementary Figure 32) or liver damage.

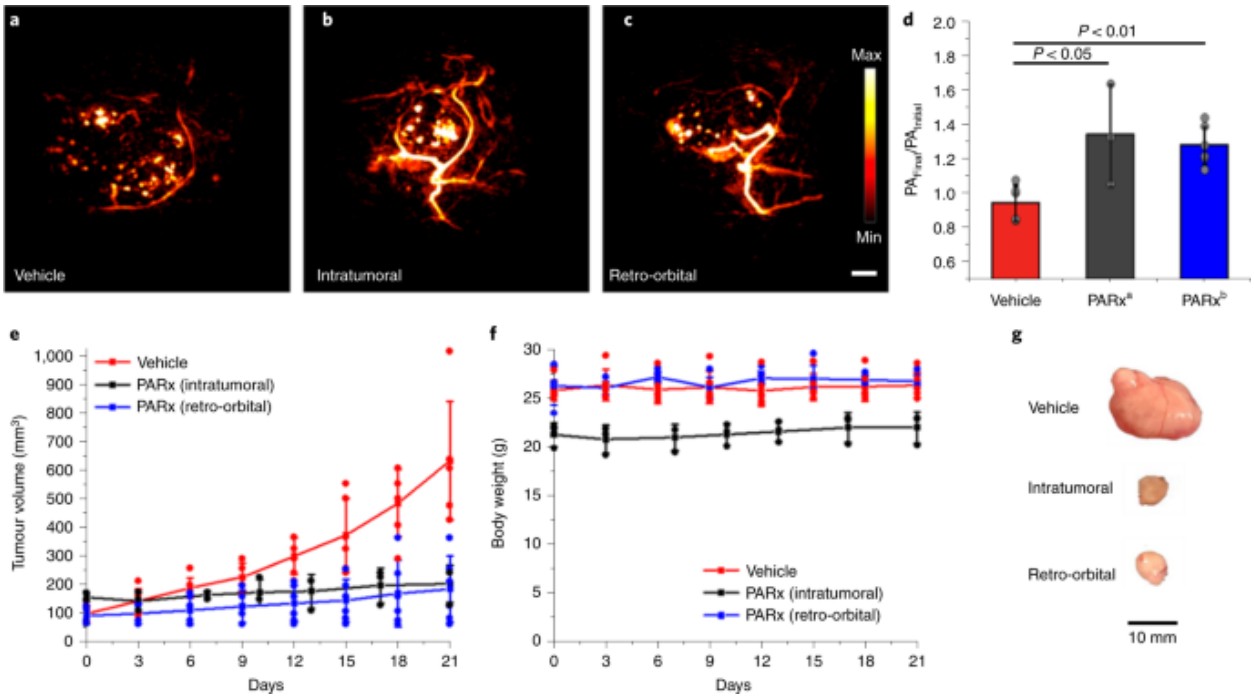

Figure 13. PA images of tumors after treatment with a. vehicle (10% DMSO/PBS) b. intratumoral injection of PARx (100 µM, 10% DMSO/PBS) or c. retro-orbital injection of PARx (400 µM, 10% DMSO/PBS). Samples were irradiated at 680 nm. Scale bar, 2 mm. d. PA signal after treatment with vehicle ($n = 6$ independent animals) or PARx ([a]intratumoral injection, $n = 3$ independent animals; [b]retro-orbital injection, $n = 6$ independent animals). Data are presented as mean values ± SD (imaging performed when the tumor volume was <200 mm^3). e. Average tumor volume after treatment with vehicle ($n = 6$ independent animals) or intratumoral ($n = 3$ independent animals) or retro-orbital injection ($n = 6$ independent animals) of PARx over 21 days. f. Average body weight after treatment with vehicle or intratumoral or retro-orbital injection of PARx over 21 days. g. Representative tumors that were treated with vehicle ($n = 6$ independent animals), intratumoral injection of PARx ($n = 3$ independent animals) or retro-orbital injection of PARx ($n = 6$ independent animals). Statistical analysis was performed using the Kruskall–Wallis test (Bonferroni correction: $\alpha = \alpha/n = 0.05/3 = 0.01667$).

3.7 First application of a photoacoustic imaging-based companion diagnostic in a blind study

To mimic a real-world situation, we designed a blind study to identify animals with lung cancer based on GSH levels. First, a group of nude mice were implanted with either A549 or U87 cells. Then, the animals were randomized and tagged by a second researcher. The identity of each mouse was kept hidden from the researcher conducting the imaging and image processing until completion of the study. It is important to note that a second tumor model (U87) was employed to ensure that there would be no biasing of the results based on appearance. Next, we established a diagnostic threshold by measuring the PA intensity change after administration of a vehicle control to healthy tissue (1.06 ± 0.17, $n = 9$). That is, if a tumor exhibited a PA signal greater than 1.23, then it was placed in 'group 1'. If not, the mouse was placed in 'group 2'. Tumors were imaged only after they had reached a volume of ~100 mm^3. We identified one animal that was one SD above the mean (1.30) and two animals two SD above the mean (1.47 and 1.61). These three subjects (out of seven, total) were categorized to 'group 1', which we assigned to be mice bearing A549 tumors. The remaining four animals (0.84, 1.05, 1.06 and 1.07) were grouped into 'group 2'. Although the aim of the study would allow us to use PACDx to identify which mice would benefit from PARx, we decided to treat both groups with PARx. The reason for this was because it would further demonstrate the selectivity of PARx. We suspected that the administration of PARx to the second group would afford no PA signal enhancement due to lower intratumoral GSH levels and thus no attenuation in tumor growth. All animals received PARx via retro-orbital injection once every three days for 21 days. Indeed, no notable increase in tumor size was observed in group 1, whereas the tumor volume of group 2 had increased to over 1,000 mm^3 and the mice had lost substantial body weight. When the identity of each animal was revealed, we found that we were accurate in each instance, with six of seven mice correctly assigned with greater than 95%

confidence. Although the blind study was successful, it is important to consider the possibility that gemcitabine is intrinsically less effective for U87 tumors or that PARx has decreased uptake in U87 tumors. However, it is reasonable to conclude that PARx is not being activated in the U87 tumors owing to a lack of PA signal enhancement *in vivo*, which is supported by the *in vitro* and cell-based assays we have previously performed.

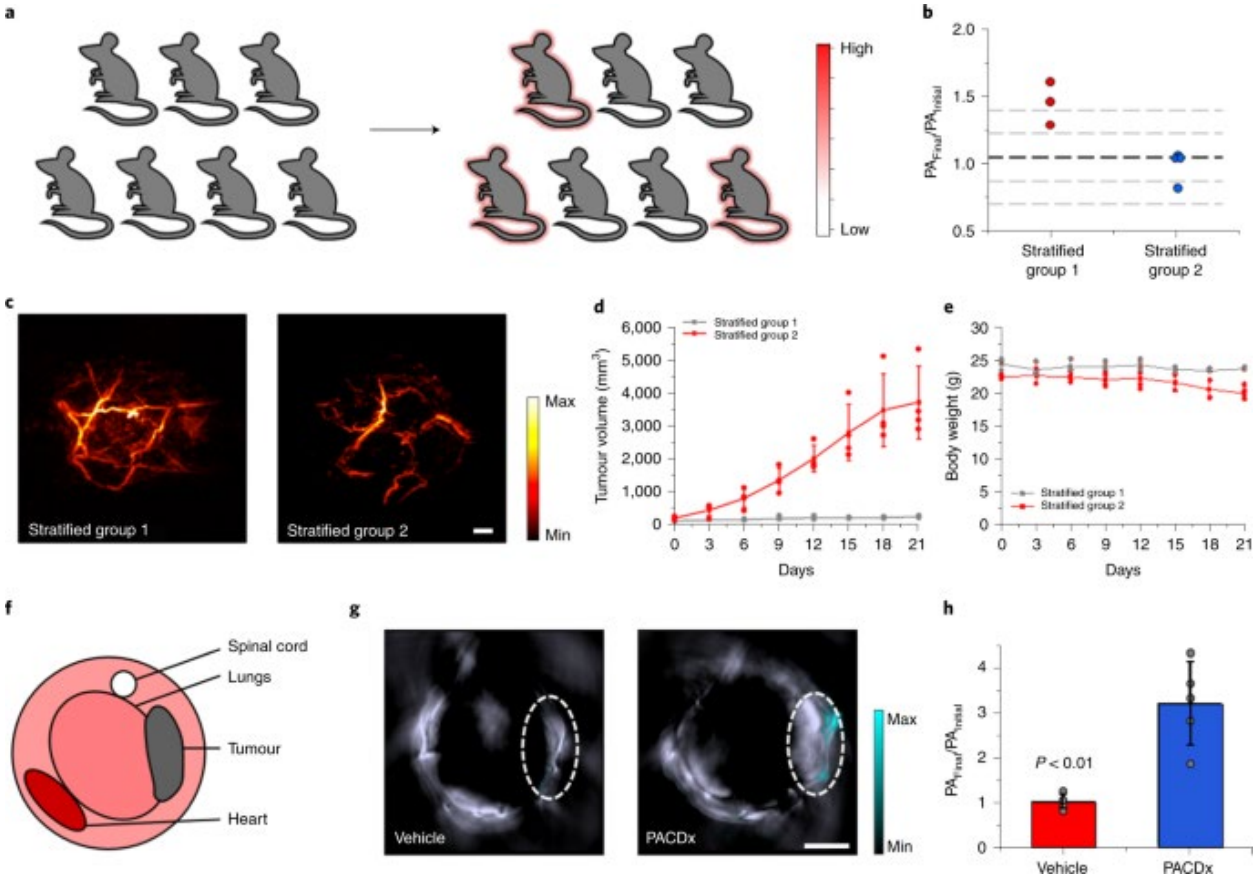

Figure 14. a. Schematic illustrating the stratification of a patient group based on PA signal intensity in a blind study. b. Stratification based on PA fold turn-on after retro-orbital injection of PACDx (400 µM, 150 µl, 10% DMSO in saline). The diagnostic threshold was defined as the mean PA fold turn-on after retro-orbital injection of vehicle (150 µl, 10% DMSO in saline, $n = 9$ independent animals) in healthy mice +2 SD to obtain 95% confidence. The black dashed line indicates the diagnostic threshold, and the grey dashed lines indicate SD Normalized PA turn-on of stratified groups 1 ($n = 3$ independent animals) and 2 ($n = 4$ independent animals) are shown. Data are presented as mean values ± SD c. Representative PA images of stratified groups 1 ($n = 3$ independent animals) and 2 ($n = 4$ independent animals) after administration of PACDx. Samples were irradiated at 680 nm. Scale bar, 2 mm. d. Average tumor volume and e. body weight of stratified groups 1 ($n = 3$ independent animals) and 2 ($n = 4$ independent animals) during a 21-day treatment period with PARx. Data are presented as mean values ± SD f. Cross-section schematic of a mouse to reference the positioning of the lungs and tumor. g. Representative spectrally unmixed multi-spectral optoacoustic tomography (MSOT) images of the lungs 1 h post-injection of vehicle (150 µl, 10% DMSO in saline) or PACDx (400 µM, 150 µl, 10% DMSO in saline). Scale bar, 5 mm. h, Average PA signal from MSOT imaging ($n = 5$ independent animals). Statistical analysis was performed using a two-tailed Mann–Whitney U test ($\alpha = 0.05$, $P = 0.007$).

3.8 Evaluating PACDx in orthotopic and heterotopic models of lung cancer

It has been an outstanding challenge in PA imaging field to image the lung due to a limited acoustic window through the rib cage and attenuation of the acoustic signal by gas present in air sacs. However, here we have shown the first successful attempt of lung imaging using a PA ABS probe. So far, all of our tumor models for *in vivo* imaging involved implanting lung cancer cells subcutaneously. That is, the model is not highly relevant to clinical applications that CDx are intended for. To establish a more clinically relevant model, we implanted A549 luciferase cells to generate orthotopic lung tumors for PA imaging. One advantage of using luciferase-expressing cells is that bioluminescence can be used to visualize whether the inoculation was successful and to subsequently track tumor growth. To ensure that GSH levels were elevated in the genetically modified cell line, we performed confocal imaging again with PACDx and found that the signal was indistinguishable from normal A549 cells (Supplementary Figure 38). After 6 weeks, IVIS imaging was used to show a strong bioluminescent signal in the lung region, indicating successful inoculation (Supplementary Figure 39). Furthermore, we were able to locate the vascularized region of the tumor via cross-sectional PA imaging (Supplementary Figure 41). The identity of the tumors was confirmed *ex vivo* at the conclusion of the study (Supplementary Figure 42). After employing *in vivo* PA imaging with PACDx, we determined the ratio in the tumor region was 3.17 ± 0.91 after spectral unmixing, indicating that PACDx had successfully detected elevated GSH in an orthotopic lung cancer model (Figure 14).

Next, we wanted to go beyond imaging of the primary tumor since it has been reported that ~40% of lung tumors have metastasized by the time of diagnosis, with liver being the most common metastatic site.[92] However, when we attempted to achieve metastasis using the orthotopic

lung cancer model described above, it proved to be difficult due to inconsistent growth and distribution. Therefore, we generated a heterotopic liver cancer model using A549-Luc2 cells as a proxy for metastasis. After systemic administration of PACDx in this model, we observed a significantly enhanced spectrally unmixed PA signal compared to the vehicle control ($PA_{Final}/PA_{Initial} = 3.03 \pm 0.97$) (Supplementary Figure 43). This key experiment further demonstrates the broad utility of PACDx.

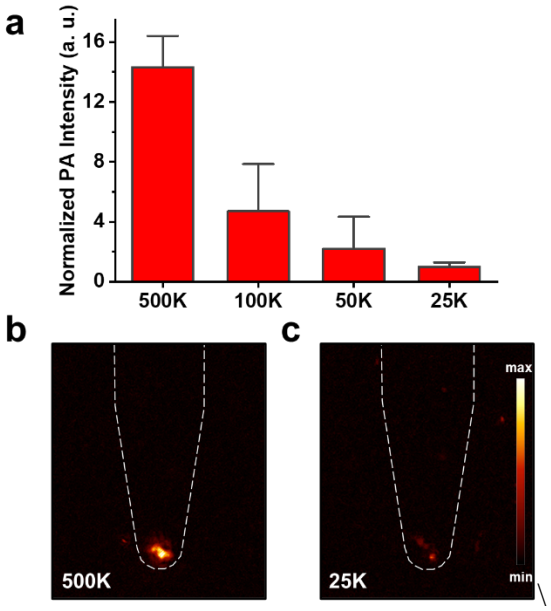

Figure 15. a. Normalized PA intensity of A549 cell pellets containing 500,000, 100,000, 50,000, or 25,00 cells after treatment with 10 μM of PA-HD-GSH. b. Representative PA image of a cell pellet containing 500,000 cells. c. Representative PA image of a cell pellet containing 25,000 cells.

3.9 Progress on developing an optimized PACDx for brain metastasis

During the development of PACDx and PARx, our group was simultaneously working on improving the PA imaging ability of HDs. As demonstrated previously, the most used HD uses oxygen as the heteroatom in the core of the dye. However, recently it has been shown that exchanging the oxygen atom with sulfur in a different dye platform can enhance the photophysical properties.[93] Thus, our group found that replacing the oxygen with a sulfur in the HD could cause a bathochromic shift, enhance the ε, and lower the pK_a.

Utilizing this improved dye platform provides many advantages for *in vivo* imaging. Therefore, we proposed that with the optimal sensitivity of our trigger and the optimized dye we can image micro metastases of lung cancer in regions such as the brain. It is important to note that the brain has one of the lowest basal concentrations of GSH. For this reason, we suspect that the significantly higher concentration in A549 cells will facilitate a higher signal to background ratio. To this end, we synthesized PA-HD-GSH following published procedures.[94] With PA-HD-GSH in hand, we fortunately found that the *in vitro* reactivity was highly similar to that of PACDx. To determine if PA-HD-GSH could detect small numbers of lung cancer cells, we designed an experiment where we imaged a range of a number of cells via PA imaging (Figure 15). This data shows that PA-HD-GSH is highly promising for imaging micrometastasis. We are currently pursuing different models for imaging micrometastasis, however we have successfully demonstrated that PA-HD-GSH can image small subcutaneous lung cancer tumors (Figure 16).

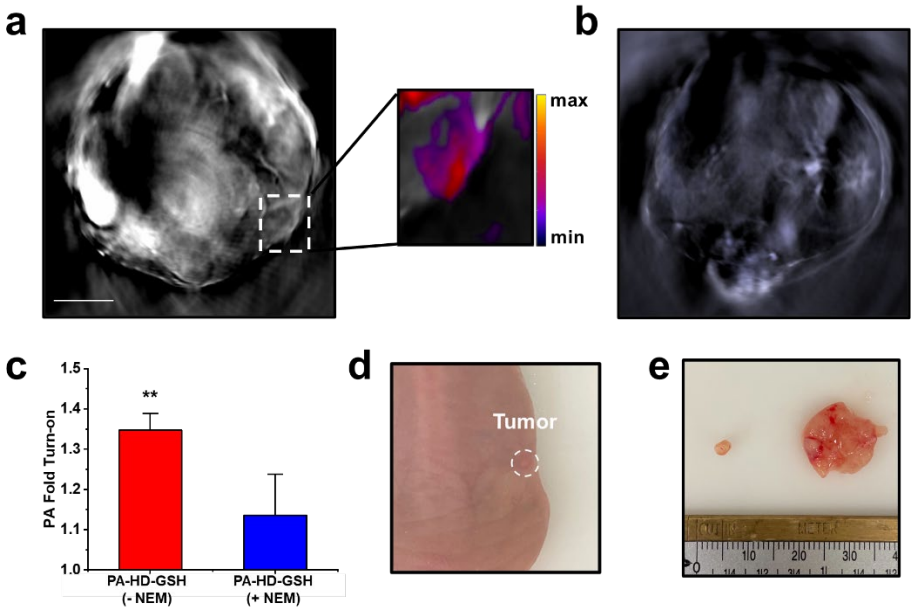

Figure 16. a. Representative cross-sectional PA image of the flank with a subcutaneous A549 tumor. Inset highlights the spectrally unmixed signal of PA-HD-GSH in a tumor less than 10 mm^3. b. Representative PA image cross-sectional PA image of the flank with a subcutaneous A549 tumor after treatment with PA-HD-GSH and NEM. c. PA fold turn-on of experiments represented in a and b. d. Representative photograph of tumor in a. e Representative photograph of excised tumors in a and b.

3.10 Summary and outlook

This study demonstrated a variety of applications using PA imaging. We used a physical organic approach to guide the development of a PA imaging-based CDx for the detection of GSH in murine models of lung cancer. This also demonstrated the potential to use a similar approach for the development of other probes, which can be seen in chapter 4. Although there are commercially available GSH probes, such as GSH Red, most do not absorb in the near infrared region which is the region that facilitates deep tissue imaging.[95] It is important to mention that GSH is typically not considered to be an ideal cancer biomarker because current sensing strategies are too reactive to distinguish between normal and pathological levels. In the case of GSH Red, 5 μM GSH was sufficient to fully activate the probe within 1 h. We rationalized that we could overcome this challenge by precisely tune the commonly used S_NAr design for GSH detection. This approach enabled us to reliably differentiate GSH in the 0.1–10 mM range within the same timeframe. While CDx are conventionally *in vitro* tests, employing an imaging-based approach can potentially allow us to visualize changes that occur during disease progression in real-time.

To go beyond CDx, we developed a highly effective prodrug that utilizes the same GSH-mediated activation mechanism to selectively release gemcitabine from a PA imaging dye. We envision further exploiting this design to append other cargo and selectively deliver them to tumors. With regards to our current prodrug-like design, we were able to demonstrate through different dosing regimens (every 7 days versus every 3 days for 21 days) that PARx did not display any off-target toxicity.

Although the initial aim of this study was to develop a PA imaging-based CDx that could identify subjects with lung cancer based on elevated GSH levels, we found that PACDx had the

potential to stratify cancer with sufficient GSH levels to respond to a GSH-responsive therapy. Therefore, an unprecedented blind study was used to evaluate the performance of PACDx in the context of these two aims. Through the application of PACDx, we were able to stratify seven mice bearing different tumor types into two groups. When the identity of each animal was revealed, we were pleased to find that we could accurately distinguish between different cancer types based on PA imaging of GSH. In addition, treating with PARx showed selectivity towards tumors with high GSH levels.

Furthermore, we have demonstrated the versatile nature of PACDx through successful fluorescent imaging of cells via confocal microscopy. We envision that the optimized chemical reactivity and NIR capabilities of PACDx will make it ideal for the detection of GSH in patient-derived tumor organoids and patient-derived xenografts via optical imaging. Because PACDx was optimized to discriminate high GSH levels from physiological concentrations, we were able to use it in our study to detect lung cancer. Moreover, beyond targeting lung tumors, we anticipate PACDx and PARx can be employed to detect other conditions and tumor types featuring elevated GSH levels. In addition, it is possible that PACDx can be used to aid drug development efforts by confirming and aiding quantification of delivery in real-time. Our work here is limited to preclinical applications due to being limited by instrumentation. However, with instrumentation that facilitates imaging beyond several cm this tool can be used to image at higher depths, such as using handheld or endoscopic PA set-ups.

Finally, with the current progress of optimizing PACDx we believe that this will further move PA ABS probes closer to a clinical setting. Although our aim is to image micrometastatic

lesions in the brain, PA-HD-GSH may be used to image micro metastatic lesions in other organs. Furthermore, we show that our finely tuned trigger is compatible with various dye platforms.

3.11 Experimental methods

Materials. Materials were purchased from commercial vendors and used without further purification. All deuterated solvents were purchased from Cambridge Isotope Laboratories. Acetone, ammonium chloride, dichloromethane, DMSO, glacial acetic acid, PBS (Corning), Matrigel (Corning), sodium bicarbonate, sodium carbonate, sodium chloride, sodium hydroxide were purchased from Thermo Fisher Scientific. Anhydrous methanol and conc. hydrochloric acid were purchased from Macron Fine Chemicals. Acetic anhydride, anhydrous dichloromethane, anhydrous dimethylformamide, sodium hydride, phosgene (15 wt. % in toluene), NADPH, formaldehyde (37 % w/w in water), glutathione (reduced), hexanes, l-ascorbic acid, L-cysteine, l-phenylalanine, l-arginine, glycine, l-lysine, RLM (pooled, male), and trypan blue powder were purchased from Millipore-Sigma Aldrich. Potassium iodide, 2,4-dihydroxybenzaldehyde and sodium sulfate (anhydrous) were purchased from Oakwood Chemicals. Gemcitabine HCl and D-Luciferin were purchased from AK Scientific. NEM was purchased from Pierce Chemical Company. A549, A549-Luc2, HEK 293, U87, and 4T1 cells were purchased from ATCC. Cells were generally incubated at 37 °C under 5% CO_2.

Instruments and Software. ^{1}H and ^{13}C NMR spectra were acquired on the Carver B500 spectrometer. The following abbreviations were used to describe coupling constants: singlet (s), doublet (d), triplet (t), or multiplet (m). Spectra were visualized and analyzed using MestReNova (version 10.0) and referenced to trace non-deuterated solvent. High-resolution mass spectra were acquired on a Waters Q-TOF Ultima ESI mass spectrometer or a Waters Synapt G2-Si ESI/LC-

MS spectrometer. Ultraviolet-visible spectroscopy was performed on a Cary 60. Fluorescence spectra were acquired on a QuantaMaster400 scanning spectrofluorometer. Ultraviolet-visible spectroscopy and fluorimetry was performed with a micro fluorescence quartz cuvette (Science Outlet). Cells were visualized on an EVOS FL epifluorescence microscope and cellular imaging was performed using a Zeiss LSM 700 confocal microscope. SpectraMax M2 plate reader was used for cell viability assays. Confocal images were analyzed using Fiji.[96] Data was analyzed using Microsoft Excel. PA imaging was performed using an Endra Nexus 128+ photoacoustic tomography system. PA images were analyzed using Horos software. *In vivo* bioluminescence imaging was performed using an IVIS Spectrum CT live-animal imaging system (Perkin-Elmer, USA). MSOT imaging was performed using the MSOT InVision 128 from iTheraMedical. Reported values correspond to mean PA signals in regions of interest (ROIs) of equal area.

Statistical Analysis and Reproducibility. Statistical analysis was performed using Microsoft Excel. For cellular studies with equal variance, two-tailed *t*-tests were performed relative to a control where a single variable was tested. For *in vivo* imaging, the non-parametric tests were performed. For all tests, significance was defined as $P < 0.05$ (*), $P < 0.01$ (**), and $P < 0.001$ (***).

Histology experiments were repeated three times independently with similar results. PA imaging of A549 tumors with PACDx was repeated once independently with the corresponding sample size. Stratification using PA imaging was repeated once independently with the corresponding sample size.

Synthetic Procedures. TLC was performed on glass-backed TLC plates precoated with silica gel containing an UV254 fluorescent indicator (Macherey-Nagel). TLC's were visualized with a 254/365 nm UV hand-held lamp (UVP). Flash silica gel chromatography was performed using

0.04 – 0.063 mm 60 M silica (Macherey-Nagel). All glassware used under anhydrous reaction conditions were flame-dried under vacuum and cooled immediately before use.

Synthesis of 6. Compound **6** was synthesized by following a published protocol.[97]

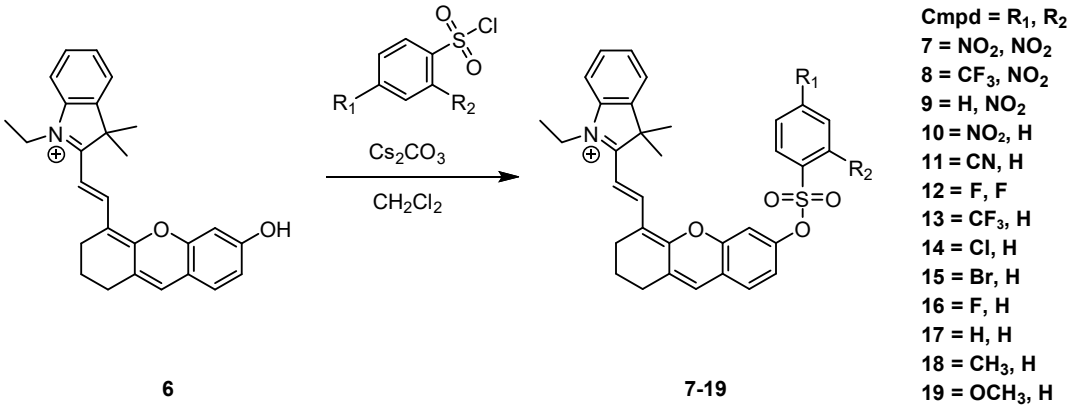

6 7-19

Cmpd = R_1, R_2
7 = NO_2, NO_2
8 = CF_3, NO_2
9 = H, NO_2
10 = NO_2, H
11 = CN, H
12 = F, F
13 = CF_3, H
14 = Cl, H
15 = Br, H
16 = F, H
17 = H, H
18 = CH_3, H
19 = OCH_3, H

General synthesis of 7-19. To a solution of **6** and the appropriate benzenesulfonyl chlorides (4.0 equiv.) in CH_2Cl_2 was added Cs_2CO_3 (0.5 equiv.). The reaction was monitored by TLC. After stirring at room temperature, the reaction was concentrated under reduced pressure to afford the crude residue which was purified via flash chromatography on a silica column (1:19 v/v MeOH:CH_2Cl_2) to afford compounds **7-19** as purple films.

Compound 7. 41% yield. ^{1}H NMR (500 MHz, $CDCl_3$) δ 8.68 (t, *J* = 1.7 Hz, 1H), 8.64 – 8.58 (m, 2H), 8.37 (ddd, *J* = 14.0, 8.6, 1.3 Hz, 2H), 8.28 (dt, *J* = 8.7, 1.7 Hz, 1H), 8.25 (t, *J* = 1.7 Hz, 1H), 7.54 (t, *J* = 7.7 Hz, 2H), 7.48 (t, *J* = 7.1 Hz, 2H), 7.33 (dd, *J* = 8.5, 1.2 Hz, 1H), 7.21 (d, *J* = 2.2 Hz, 1H), 7.03 (dt, *J* = 8.4, 1.7 Hz, 1H), 6.98 (s, 1H), 6.75 (d, *J* = 15.2 Hz, 1H), 4.60 (q, *J* = 7.2 Hz, 2H), 2.77 (t, *J* = 6.1 Hz, 2H), 2.71 (t, *J* = 6.1 Hz, 2H), 1.92 (p, *J* = 6.1 Hz, 2H), 1.81 (s, 6H), 1.56 (t, *J* = 7.2 Hz, 3H). ^{13}C NMR (125 MHz, $CDCl_3$) δ 178.71, 158.45, 152.99, 151.14, 149.37, 148.93, 148.25, 147.46, 146.56, 145.39, 142.51, 140.86, 134.24, 133.19, 131.90, 129.45, 129.02, 128.60,

128.37, 127.10, 125.28, 122.63, 121.72, 120.46, 118.48, 118.24, 116.02, 113.38, 110.11, 107.25, 51.34, 41.82, 29.71, 29.58, 27.78, 24.14, 20.08, 13.20.

Compound 8. 82% yield. ^{1}H NMR (500 MHz, $CDCl_3$) δ 8.60 (d, *J* = 14.4 Hz, 1H), 8.30 (d, *J* = 8.0 Hz, 2H), 8.10 (s, 2H), 7.69 (dd, *J* = 8.3, 1.8 Hz, 1H), 7.64 (s, 1H), 7.48 (ddt, *J* = 23.6, 14.6, 7.2 Hz, 4H), 7.36 (d, *J* = 8.3 Hz, 1H), 7.18 (s, 1H), 7.01 (d, *J* = 9.8 Hz, 2H), 6.73 (d, *J* = 14.8 Hz, 1H), 4.59 (s, 2H), 2.74 (s, 2H), 2.67 (d, *J* = 6.0 Hz, 2H), 1.86 (d, *J* = 11.6 Hz, 2H), 1.79 (s, 6H), 1.53 (d, *J* = 6.2 Hz, 3H). ^{13}C NMR (125 MHz, $CDCl_3$) δ 178.61, 158.62, 152.94, 149.51, 148.72, 148.29, 146.51, 143.11, 142.50, 140.85, 133.51, 131.62, 131.50, 131.26, 129.77, 129.45, 128.80, 128.31, 127.48, 127.45, 123.88, 122.62, 122.41, 122.38, 121.64, 119.93, 119.90, 119.87, 118.60, 115.91, 113.47, 110.09, 107.11, 51.28, 41.87, 29.71, 29.54, 27.83, 24.18, 20.09, 13.26.

Compound 9. 32% yield. ^{1}H NMR (500 MHz, $CDCl_3$) δ 8.57 (d, *J* = 15.2 Hz, 1H), 8.17 (dd, *J* = 7.9, 1.4 Hz, 1H), 8.04 (dd, *J* = 8.0, 1.3 Hz, 1H), 7.93 (td, *J* = 7.7, 1.4 Hz, 1H), 7.88 (dd, *J* = 7.9, 1.4 Hz, 1H), 7.79 (td, *J* = 7.7, 1.5 Hz, 1H), 7.54 – 7.48 (m, 3H), 7.45 (ddt, *J* = 9.0, 3.7, 2.6 Hz, 2H), 7.37 (dtd, *J* = 15.0, 7.9, 1.5 Hz, 2H), 7.30 (d, *J* = 8.5 Hz, 1H), 7.14 (d, *J* = 2.2 Hz, 1H), 6.99 (dd, *J* = 8.4, 2.3 Hz, 1H), 6.97 (s, 1H), 6.81 (d, *J* = 15.4 Hz, 1H), 4.64 (q, *J* = 7.3 Hz, 2H), 2.77 (t, *J* = 6.1 Hz, 2H), 2.66 (d, *J* = 5.8 Hz, 2H), 1.86 (t, *J* = 6.2 Hz, 2H), 1.78 (s, 6H), 1.53 (t, *J* = 7.3 Hz, 3H). ^{13}C NMR (125 MHz, $CDCl_3$) δ 178.58, 158.43, 152.89, 149.82, 148.59, 148.40, 146.42, 142.49, 140.92, 139.54, 136.31, 132.64, 132.15, 131.62, 130.89, 130.79, 130.17, 129.60, 129.42, 129.13, 128.41, 128.20, 127.78, 125.09, 122.53, 121.40, 118.70, 116.08, 113.51, 110.08, 107.43, 51.22, 41.87, 29.71, 29.56, 27.83, 24.11, 20.09, 13.28.

Compound 10. 57% yield. ^{1}H NMR (500 MHz, $CDCl_3$) δ 8.57 (d, *J* = 14.9 Hz, 1H), 8.44 (d, *J* = 8.5 Hz, 2H), 8.13 (dd, *J* = 12.0, 8.6 Hz, 4H), 8.05 (d, *J* = 8.8 Hz, 2H), 7.54 (t, *J* = 7.1 Hz, 2H), 7.49 (t, *J* = 7.7 Hz, 2H), 7.28 (s, 1H), 7.05 (d, *J* = 2.2 Hz, 1H), 6.97 (s, 1H), 6.83 (d, *J* = 15.0 Hz, 1H),

6.74 (dd, J = 8.4, 2.1 Hz, 1H), 4.67 (d, J = 7.1 Hz, 2H), 2.79 (s, 2H), 2.69 (d, J = 6.5 Hz, 2H), 1.87 (s, 2H), 1.79 (s, 6H), 1.57 (t, J = 6.6 Hz, 3H). ^{13}C NMR (125 MHz, $CDCl_3$) δ 178.64, 158.44, 153.40, 152.93, 151.27, 149.98, 147.85, 146.42, 142.45, 140.84, 140.63, 131.61, 130.05, 129.54, 129.12, 128.45, 128.38, 127.46, 124.65, 123.19, 122.62, 121.38, 118.59, 115.98, 113.46, 110.25, 107.44, 51.25, 41.94, 29.71, 29.58, 27.83, 24.19, 20.08, 13.34.

Compound 11. 74% yield. ^{1}H NMR (500 MHz, $CDCl_3$) δ 8.57 (d, J = 15.2 Hz, 1H), 8.08 – 8.03 (m, 2H), 8.01 (d, J = 8.2 Hz, 2H), 7.94 – 7.89 (m, 2H), 7.59 – 7.45 (m, 6H), 7.28 (d, J = 8.5 Hz, 1H), 7.04 – 6.98 (m, 2H), 6.81 (d, J = 15.3 Hz, 1H), 6.73 (dd, J = 8.4, 2.3 Hz, 1H), 4.66 (q, J = 7.3 Hz, 2H), 2.77 (t, J = 6.1 Hz, 2H), 2.68 (t, J = 6.2 Hz, 2H), 1.86 (p, J = 6.1 Hz, 2H), 1.80 (s, 6H), 1.56 (t, J = 7.2 Hz, 3H). ^{13}C NMR (125 MHz, $CDCl_3$) δ 178.60, 158.55, 152.92, 151.67, 150.03, 146.43, 142.44, 140.82, 139.13, 133.22, 132.46, 131.81, 129.53, 129.30, 129.26, 128.42, 127.08, 122.67, 121.34, 118.90, 118.69, 118.45, 116.80, 115.94, 113.43, 112.22, 110.24, 107.28, 51.26, 41.87, 29.71, 29.56, 27.86, 24.17, 20.07, 13.32.

Compound 12. 30% yield. ^{1}H NMR (500 MHz, $CDCl_3$) δ 8.57 (d, J = 14.9 Hz, 1H), 8.01 – 7.84 (m, 2H), 7.57 – 7.42 (m, 4H), 7.31 (d, J = 8.4 Hz, 1H), 7.13 – 7.04 (m, 3H), 7.00 (s, 1H), 6.92 (d, J = 15.2 Hz, 1H), 6.87 (dd, J = 8.5, 2.2 Hz, 1H), 6.72 (dtd, J = 16.0, 9.4, 8.8, 2.4 Hz, 2H), 4.74 (d, J = 7.5 Hz, 2H), 2.82 (t, J = 5.8 Hz, 2H), 2.68 (t, J = 6.0 Hz, 2H), 1.92 – 1.84 (m, 2H), 1.79 (s, 6H), 1.55 (t, J = 6.5 Hz, 3H).^{13}C NMR (125 MHz, $CDCl_3$) δ 178.52, 158.49, 152.89, 149.95, 146.40, 142.44, 140.92, 133.42, 133.34, 131.55, 131.16, 130.88, 129.50, 129.23, 128.43, 128.24, 122.46, 121.30, 119.76, 119.68, 118.46, 116.18, 113.59, 112.63 (dd, J = 22.3, 3.8 Hz), 110.00, 109.81 (d, J = 20.8 Hz), 107.66, 106.67 – 105.98 (t), 104.13 (t, J = 26.0 Hz). 51.14, 42.07, 29.71, 29.60, 27.89, 24.28, 20.12, 13.40.

Compound 13. 42% yield. ^{1}H NMR (500 MHz, $CDCl_3$) δ 8.56 (d, *J* = 15.1 Hz, 1H), 8.04 (dd, *J* = 19.9, 8.1 Hz, 4H), 7.87 (d, *J* = 8.1 Hz, 2H), 7.51 (dd, *J* = 7.7, 4.0 Hz, 4H), 7.49 – 7.43 (m, 2H), 7.28 (d, *J* = 8.5 Hz, 1H), 7.05 – 6.99 (m, 2H), 6.82 (d, *J* = 15.2 Hz, 1H), 6.73 (dd, *J* = 8.4, 2.2 Hz, 1H), 4.66 (q, *J* = 7.2 Hz, 2H), 2.76 (t, *J* = 6.0 Hz, 2H), 2.67 (t, *J* = 6.0 Hz, 2H), 1.85 (t, *J* = 6.0 Hz, 2H), 1.77 (s, 6H), 1.54 (t, *J* = 6.7 Hz, 3H).^{13}C NMR (125 MHz, $CDCl_3$) δ 178.52, 158.64, 152.90, 150.73, 150.15, 146.43, 142.42, 140.85, 138.65, 131.48, 129.52, 129.44, 129.15, 128.43, 128.33, 126.71, 126.69, 126.66, 126.63, 126.60, 124.87, 124.84, 124.81, 124.78, 122.52, 121.27, 118.75, 115.96, 113.49, 110.19, 107.25, 51.17, 41.88, 29.70, 29.54, 27.83, 24.16, 20.08, 13.33.

Compound 14. 23% yield. ^{1}H NMR (500 MHz, $CDCl_3$) δ 8.56 (d, *J* = 15.0 Hz, 1H), 7.88 – 7.81 (m, 3H), 7.57 (d, *J* = 8.4 Hz, 2H), 7.55 – 7.43 (m, 4H), 7.26 (d, *J* = 8.5 Hz, 3H), 7.24 – 7.20 (m, 1H), 6.99 (t, *J* = 2.4 Hz, 2H), 6.91 (d, *J* = 15.2 Hz, 1H), 6.71 (dd, *J* = 8.4, 2.1 Hz, 1H), 4.73 (q, *J* = 7.1 Hz, 2H), 2.80 (d, *J* = 6.0 Hz, 2H), 2.67 (t, *J* = 6.0 Hz, 2H), 1.87 (t, *J* = 6.1 Hz, 2H), 1.78 (s, 6H), 1.58 – 1.52 (m, 3H).^{13}C NMR (125 MHz, $CDCl_3$) δ 178.53, 158.52, 152.89, 150.31, 146.42, 146.07, 142.46, 141.61, 140.93, 134.43, 133.46, 131.51, 129.98, 129.85, 129.51, 129.24, 128.27, 128.25, 127.86, 127.77, 122.48, 121.17, 118.82, 116.16, 113.56, 110.24, 107.67, 51.14, 42.06, 29.71, 29.61, 27.91, 24.27, 20.14, 13.43.

Compound 15. 65% yield. ^{1}H NMR (500 MHz, $CDCl_3$) δ 8.55 (d, *J* = 15.2 Hz, 1H), 7.81 – 7.70 (m, 6H), 7.56 – 7.50 (m, 2H), 7.50 – 7.43 (m, 2H), 7.41 – 7.35 (m, 2H), 7.27 (s, 1H), 7.02 – 6.97 (m, 2H), 6.88 (d, *J* = 15.3 Hz, 1H), 6.72 (dd, *J* = 8.4, 2.2 Hz, 1H), 4.70 (q, *J* = 7.2 Hz, 2H), 2.79 (t, *J* = 6.0 Hz, 2H), 2.67 (t, *J* = 6.1 Hz, 2H), 1.86 (t, *J* = 6.1 Hz, 2H), 1.78 (s, 6H), 1.54 (t, *J* = 7.1 Hz, 3H). ^{13}C NMR (125 MHz, $CDCl_3$) δ 178.51, 158.54, 152.88, 150.31, 146.49, 146.40, 142.45, 140.92, 134.00, 132.84, 131.48, 130.74, 130.22, 129.97, 129.51, 129.29, 128.81, 128.29, 128.25,

128.14, 122.84, 122.48, 121.17, 118.82, 116.09, 113.55, 110.22, 107.53, 51.15, 41.95, 29.71, 29.58, 27.90, 24.19, 20.11, 13.37.

Compound 16. 36% yield. ^{1}H NMR (500 MHz, $CDCl_3$) δ 8.57 (d, *J* = 15.0 Hz, 1H), 7.91 (ddd, *J* = 11.5, 8.6, 5.3 Hz, 3H), 7.55 – 7.49 (m, 3H), 7.47 (dt, *J* = 7.6, 5.7 Hz, 1H), 7.31 – 7.25 (m, 5H), 7.02 (s, 1H), 6.98 (d, *J* = 2.2 Hz, 1H), 6.96 – 6.84 (m, 2H), 6.71 (dd, *J* = 8.4, 2.1 Hz, 1H), 4.72 (q, *J* = 7.0 Hz, 2H), 2.82 (t, *J* = 5.8 Hz, 2H), 2.68 (t, *J* = 5.8 Hz, 2H), 1.88 (p, *J* = 5.2 Hz, 2H), 1.78 (s, 6H), 1.55 (t, *J* = 6.6 Hz, 3H).^{13}C NMR (125 MHz, $CDCl_3$) δ 178.47, 167.30, 165.25, 158.71, 152.84, 150.36, 146.46, 142.40, 140.88, 131.57, 131.50, 131.40, 130.96, 130.93, 129.51, 128.45, 128.38, 128.32, 128.24, 122.52, 121.11, 118.91, 117.02, 116.84, 116.06, 114.47, 114.30, 113.50, 110.26, 107.37, 51.13, 42.00, 29.70, 29.58, 27.89, 24.26, 20.14, 13.39.

Compound 17. 26% yield. ^{1}H NMR (500 MHz, $CDCl_3$) δ 8.57 (d, *J* = 15.2 Hz, 1H), 7.91 – 7.86 (m, 2H), 7.77 – 7.69 (m, 1H), 7.59 (t, *J* = 7.9 Hz, 2H), 7.55 – 7.50 (m, 3H), 7.46 (ddd, *J* = 6.9, 5.5, 3.0 Hz, 1H), 7.06 – 6.99 (m, 2H), 6.95 (d, *J* = 15.2 Hz, 1H), 6.68 (dd, *J* = 8.4, 2.2 Hz, 1H), 4.80 (q, *J* = 7.3 Hz, 2H), 2.86 (t, *J* = 6.1 Hz, 2H), 2.69 (t, *J* = 5.6 Hz, 2H), 1.91 (t, *J* = 6.1 Hz, 2H), 1.78 (s, 6H), 1.55 (t, *J* = 7.2 Hz, 3H). ^{13}C NMR (125 MHz, $CDCl_3$) δ 178.43, 158.87, 152.85, 150.57, 146.50, 142.39, 140.91, 134.94, 134.85, 131.32, 129.70, 129.52, 129.49, 128.51, 128.25, 128.21, 122.52, 121.00, 118.95, 116.12, 113.50, 110.35, 107.38, 103.06, 51.10, 42.12, 29.70, 29.58, 27.97, 24.43, 20.16, 13.41.

Compound 18. 23% yield. ^{1}H NMR (500 MHz, $CDCl_3$) δ 8.60 (d, *J* = 15.2 Hz, 1H), 7.79 – 7.74 (m, 2H), 7.57 – 7.50 (m, 3H), 7.50 – 7.43 (m, 1H), 7.39 – 7.35 (m, 2H), 7.24 (d, *J* = 8.4 Hz, 1H), 7.11 – 7.06 (m, 1H), 7.00 (d, *J* = 14.7 Hz, 2H), 6.66 (dd, *J* = 8.4, 2.2 Hz, 1H), 4.81 (q, *J* = 7.3 Hz, 2H), 2.89 (t, *J* = 6.1 Hz, 2H), 2.71 (t, *J* = 5.4 Hz, 2H), 2.47 (s, 3H), 1.93 (dd, *J* = 8.6, 3.9 Hz, 2H), 1.80 (s, 6H), 1.56 (t, *J* = 7.2 Hz, 3H).^{13}C NMR (125 MHz, $CDCl_3$) δ 178.46, 158.82, 152.88,

150.67, 146.53, 146.08, 142.43, 140.95, 131.93, 131.35, 130.04, 129.53, 129.48, 128.53, 128.14, 128.08, 122.45, 120.90, 118.86, 116.26, 113.43, 110.44, 107.54, 51.08, 42.07, 29.71, 29.63, 27.96, 24.35, 21.83, 20.21, 13.40.

Compound 19. 47% yield. ^{1}H NMR (500 MHz, $CDCl_3$) δ 8.58 (d, *J* = 15.1 Hz, 1H), 7.82 – 7.75 (m, 2H), 7.52 (d, *J* = 3.7 Hz, 3H), 7.45 (dq, *J* = 10.9, 4.3 Hz, 1H), 7.30 (d, *J* = 8.4 Hz, 1H), 7.09 (s, 1H), 7.05 – 6.98 (m, 3H), 6.89 (d, *J* = 15.2 Hz, 1H), 6.68 (dd, *J* = 8.4, 2.2 Hz, 1H), 4.77 (q, *J* = 7.1 Hz, 2H), 3.88 (s, 3H), 2.84 (t, *J* = 6.0 Hz, 2H), 2.70 (t, *J* = 5.9 Hz, 2H), 1.90 (p, *J* = 5.9 Hz, 2H), 1.77 (s, 6H), 1.54 (t, *J* = 7.0 Hz, 3H).^{13}C NMR (125 MHz, $CDCl_3$) δ 178.32, 164.56, 159.16, 152.85, 150.81, 146.53, 142.35, 140.89, 131.11, 130.85, 130.16, 129.52, 128.35, 128.17, 125.99, 122.53, 120.88, 119.15, 115.98, 114.67, 113.45, 110.38, 107.01, 55.99, 51.07, 42.07, 29.69, 29.55, 27.96, 20.16, 13.38.

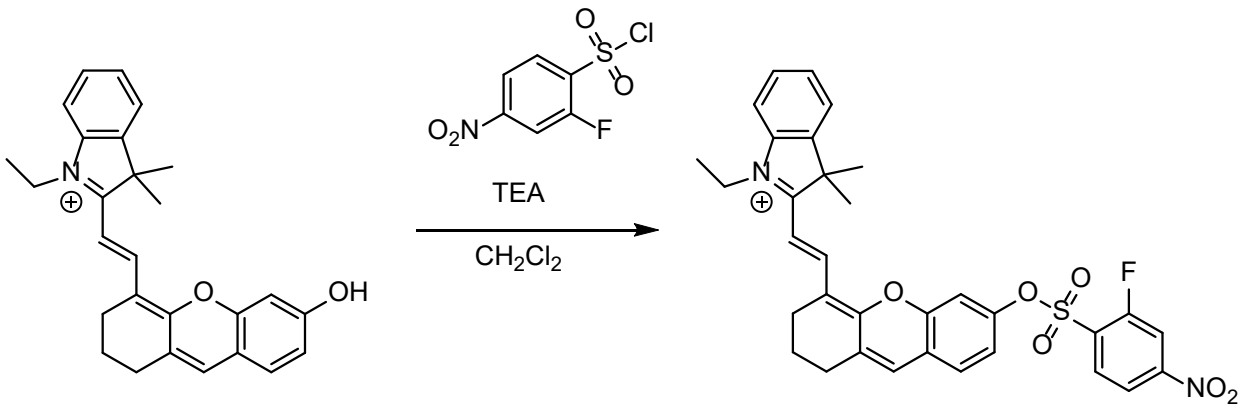

1 60% **20**

Synthesis of 20. To a solution of **6** (30.0 mg, 0.075 mmol, 1.0 equiv.) in CH_2Cl_2 (5 mL) was added 2-fluoro-4-nitrobenzenesulfonyl chloride (60.0 mg, 0.25 mmol, 3.3 equiv.) and triethylamine (10 µL, 0.075 mmol, 1.0 equiv.). The color of reaction rapidly changed from blue to purple and reaction was complete by TLC. The reaction was concentrated under reduced pressure to afford the crude residue which was purified via flash chromatography on a silica column (1:9 v/v

MeOH:CH_2Cl_2) to afford **20** (30.0 mg, 0.05 mmol, 60% yield) as a purple film. ^{1}H NMR (500 MHz, $CDCl_3$) δ 8.59 (d, *J* = 15.2 Hz, 1H), 8.23 (dd, *J* = 8.6, 2.2 Hz, 1H), 8.21 – 8.12 (m, 2H), 7.58 – 7.45 (m, 4H), 7.37 (d, *J* = 8.5 Hz, 1H), 7.13 (d, *J* = 2.3 Hz, 1H), 7.08 (s, 1H), 6.91 (dd, *J* = 8.4, 2.3 Hz, 1H), 6.83 (d, *J* = 15.2 Hz, 1H), 4.75 (q, *J* = 7.4 Hz, 2H), 2.88 (t, *J* = 6.1 Hz, 2H), 2.75 – 2.69 (m, 2H), 1.93 (p, *J* = 6.2 Hz, 2H), 1.81 (s, 6H), 1.57 (t, *J* = 7.3 Hz, 3H). ^{13}C NMR (125 MHz, $CDCl_3$) δ 178.47, 158.77, 152.97, 149.57, 146.42, 142.41, 140.83, 132.85, 131.73, 129.54, 129.37, 128.70, 128.40, 122.65, 121.60, 119.90, 119.87, 119.00, 118.29, 116.20, 113.62, 113.48, 113.42, 109.97, 107.60, 51.24, 42.87, 29.70, 29.56, 27.95, 25.11, 20.02, 13.48.

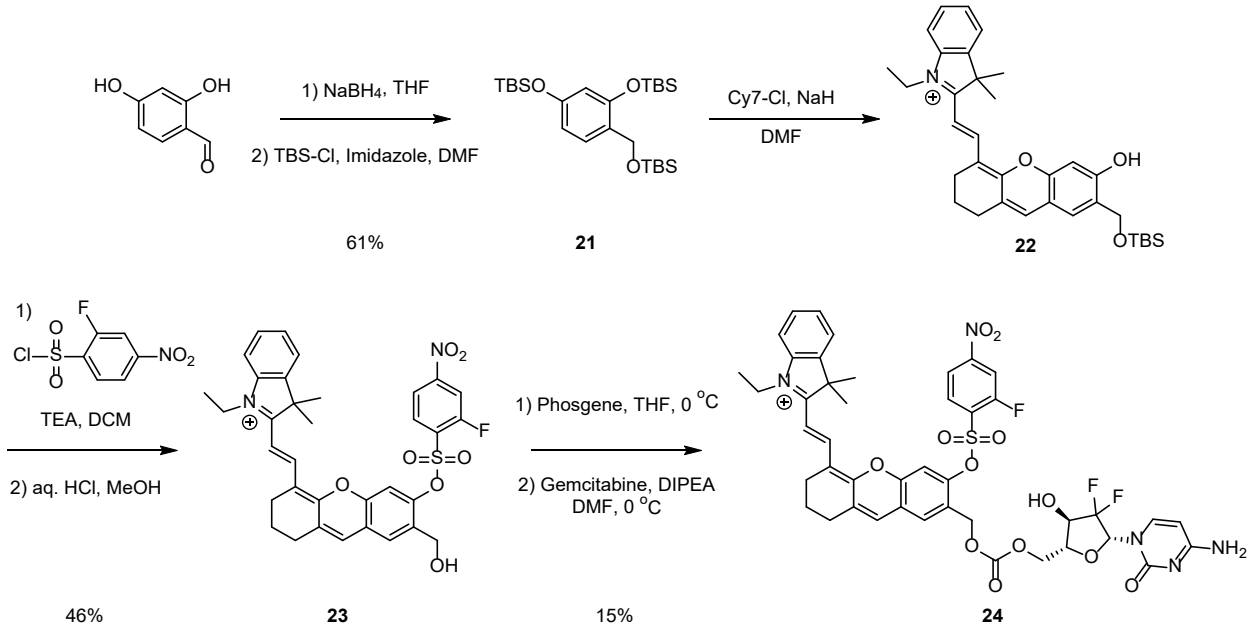

Synthesis of 21. To a solution of 2,4-dihydroxybenzaldehyde (5.0 g, 36.0 mmol, 1.0 equiv.) in anhydrous THF (25 mL) was added $NaBH_4$ (1.4 g, 36.0 mmol, 1.0 equiv.). The reaction was stirred at room temperature. The reaction was then treated with sat. NH_4Cl (1 mL), filtered to remove solids and the filtrate was concentrated under reduced pressure to obtain crude 4-(hydroxymethyl)benzene-1,3-diol as a white solid which was used in the subsequent step without purification. The crude intermediate was dissolved in anhydrous DMF (25 mL) and treated with

imidazole (9.7 g, 140.0 mmol, 3.89 equiv.) and TBS-Cl (22.0 g, 140.0 mmol, 3.89 equiv.). After stirring overnight at room temperature, the reaction was transferred to a separatory funnel, diluted with EtOAc (200 mL), and washed with brine (3×). The aqueous fractions were back-extracted with EtOAc (1×) and the combined organic fractions were dried (Na_2SO_4), filtered and concentrated under reduced pressure to afford the crude residue which was purified via flash chromatography on a silica column (1:9 v/v EtOAc:Hex) to afford **21** as a colorless liquid (10.5 g, 21.7 mmol, 61.0 % yield). ^{1}H NMR (500 MHz, $CDCl_3$) δ 7.37 (d, J = 8.3 Hz, 1H), 6.58 (dd, J = 8.3, 2.3 Hz, 1H), 6.40 (d, J = 2.3 Hz, 1H), 4.80 (s, 2H), 1.12 (s, 9H), 1.09 (s, 9H), 1.05 (s, 9H), 0.33 (s, 6H), 0.29 (s, 6H), 0.19 (s, 6H). ^{13}C NMR (125 MHz, CDCl3) δ 155.37, 152.98, 128.22, 125.46, 113.29, 110.69, 60.71, 26.37, 26.09, 26.07, 18.75, 18.54, -3.90, -4.06, -4.93.

Synthesis of 22. A solution of **21** (10.3 g, 21.3 mmol, 2.0 equiv.) in anhydrous DMF (30 mL) was cooled to 0 °C in an ice-bath. NaH (60% oil dispersion, 853.3 mg, 21.3 mmol, 2.0 equiv.) was added portion-wise and stirred until all solids were dissolved, typically yielding a deep orange solution. Cy7-Cl (5.46 g, 10.7 mmol, 1.0 equiv.) was added and stirred overnight at room temperature. The reaction was concentrated to near dryness by flowing air over the flask at room temperature. The crude residue was dissolved in CH_2Cl_2 (100 mL), treated with sat. NH_4Cl (50 mL), transferred to a separatory funnel, and washed with brine (3×). The organic fraction was dried (Na_2SO_4), filtered and concentrated under reduced pressure. The crude residue was triturated with Et_2O to afford a dark blue solid after vacuum filtration. Of note, the solid was a mixture of compound **22** and the deprotected benzyl alcohol dye (NMR reported as **22-1**) which was used without further purification (5.64 g). ^{1}H NMR (500 MHz, DMSO-d_6) δ 8.55 (d, J = 14.8 Hz, 1H), 7.79 – 7.73 (m, 1H), 7.71 – 7.60 (m, 2H), 7.55 – 7.50 (m, 2H), 7.46 – 7.37 (m, 1H), 6.93 (s, 1H), 6.47 (d, J = 14.9 Hz, 1H), 4.72 – 4.68 (m, 2H), 4.39 (q, J = 7.2 Hz, 2H), 2.77 – 2.65 (m, 4H), 1.83

(p, J = 6.2 Hz, 2H), 1.74 (s, 6H), 1.37 (t, J = 7.2 Hz, 3H), 0.94 (s, 9H), 0.11 (s, 6H). ^{13}C NMR (125 MHz, DMSO-d_6) δ 178.29, 163.88, 161.55, 155.87, 146.75, 144.39, 143.91, 137.90, 131.54, 130.33, 129.09, 128.55, 128.40, 125.48, 116.94, 116.47, 115.17, 105.32, 103.85, 62.06, 52.66, 30.14, 28.56, 28.50, 22.72, 20.81, 15.19, -2.63.

Synthesis of 23. To a solution of **22** (360.0 mg, 0.66 mmol, 1.0 equiv., values obtained by assuming the solid only contained **22**) in CH_2Cl_2 (10 mL) was added 2-fluoro-4-nitrobenzenesulfonyl chloride (180 mg, 0.71 mmol, 1.13 equiv.) and triethylamine (92 µL, 0.66 mmol, 1.0 equiv.). The color of the reaction changed from blue to purple and reaction was determined to be complete by TLC. The reaction was concentrated under reduced pressure. The crude residue was dissolved in 1:1 v/v MeOH:CH_2Cl_2 (300 mL) and treated with 2 M aq. HCl (30 mL). After the reaction was complete it was transferred to a separatory funnel, treated with brine (200 mL), and extracted with CH_2Cl_2 (3×). The combined organic fractions were dried (Na_2SO_4), filtered and concentrated under reduced pressure to afford the crude residue which was purified via flash chromatography on a silica column (1:9 v/v MeOH:CH_2Cl_2) to afford **23** as a deep purple film (190.0 mg, 0.30 mmol, 45.5% yield). ^{1}H NMR (500 MHz, $CDCl_3$) δ 8.57 (d, J = 15.0 Hz, 1H), 8.25 – 8.13 (m, 3H), 7.99 (dd, J = 8.5, 6.9 Hz, 1H), 7.82 (dd, J = 8.5, 2.1 Hz, 1H), 7.74 (dd, J = 9.0, 2.1 Hz, 1H), 7.68 (s, 1H), 7.52 (ddd, J = 20.7, 7.5, 1.3 Hz, 2H), 7.46 (td, J = 7.9, 2.6 Hz, 2H), 7.11 (s, 1H), 7.07 (s, 1H), 6.57 (d, J = 15.1 Hz, 1H), 4.54 – 4.45 (m, 4H), 2.68 (q, J = 6.3 Hz, 4H), 1.87 (p, J = 6.3 Hz, 2H), 1.79 (s, 6H), 1.54 (t, J = 7.2 Hz, 3H). ^{13}C NMR (125 MHz, $CDCl_3$) δ 178.08, 159.80, 152.50, 151.40, 148.59, 147.04, 146.48, 142.20, 140.76, 132.96, 132.53, 131.40, 130.72, 130.46, 129.47, 128.47, 128.21, 122.69, 121.01, 119.92, 118.31, 115.33, 113.81, 113.61, 113.00, 111.85, 111.63, 109.32, 105.47, 58.14, 51.12, 41.37, 29.38, 27.88, 24.15, 20.08, 13.05.

Synthesis of 24 (PARx). To a solution of **23** (28.0 mg, 0.044 mmol, 1.0 equiv.) in anhydrous THF (15 mL) at 0 °C under N_2 was added phosgene (15 wt. % in toluene, 39.8 µL, 0.58 mmol, 13.2 equiv.). Reaction was stirred at room temperature for 3 h, then N_2 was bubbled through reaction for 20 minutes to obtain the chloroformate intermedia. The chloroformate solution was added to a solution of gemcitabine (117 mg, 0.44 mmol, 10.0 equiv.) and DIPEA (77.2 µL, 0.44 mmol, 10.0 equiv.) in DMF (30 mL) at 0 °C. After 2 h, the reaction was treated with sat. NH_4Cl and extracted with CH_2Cl_2. The collected organic fraction was washed with brine, then dried over Na_2SO_4, filtered and concentrated under reduced pressure to afford the crude residue which was purified via flash chromatography on a silica column (1:9 v/v MeOH:CH_2Cl_2) to afford **24** (6.0 mg, 0.007 mmol, 15% yield) as a purple film. ^{1}H NMR (500 MHz, CD_3OD) δ 8.69 (d, *J* = 15.2 Hz, 1H), 8.43

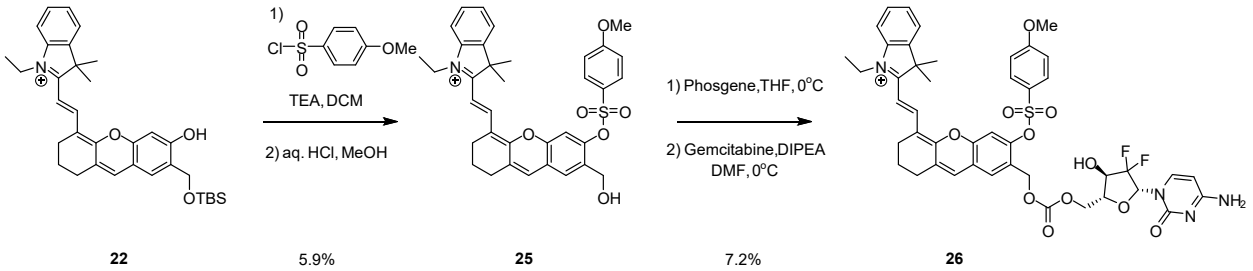

22 5.9% **25** 7.2% **26**

(dd, *J* = 9.5, 2.0 Hz, 1H), 8.36 – 8.24 (m, 3H), 7.75 – 7.65 (m, 4H), 7.65 – 7.59 (m, 1H), 7.59 – 7.52 (m, 1H), 7.22 (d, *J* = 15.4 Hz, 3H), 6.69 (d, *J* = 15.3 Hz, 1H), 6.27 – 6.21 (m, 1H), 5.20 (s, 2H), 4.50 (q, *J* = 7.2 Hz, 2H), 4.30 (td, *J* = 12.0, 8.4 Hz, 1H), 4.24 – 4.17 (m, 1H), 4.01 – 3.93 (m, 2H), 3.85 – 3.76 (m, 1H), 2.75 (dt, *J* = 24.6, 6.1 Hz, 4H), 1.93 (p, *J* = 6.2 Hz, 2H), 1.79 (s, 6H), 1.51 (t, *J* = 7.3 Hz, 3H). ^{13}C NMR (125 MHz, CD_3OD) δ 179.24, 167.94, 163.77, 158.54, 152.67, 147.98, 146.50, 142.83, 140.84, 132.49, 131.67, 131.01, 129.22, 129.11, 128.96, 128.46, 128.21, 125.84, 122.59, 121.46, 119.90, 115.07, 113.82, 113.61, 113.29, 109.55, 106.28, 67.71, 61.32, 58.86, 51.31, 40.86, 38.78, 30.23, 29.35, 29.00, 28.74, 26.28, 23.55, 22.63, 19.96, 13.00, 11.83, 10.00.

Synthesis of 25. To a solution of **22** (2.0 g, 3.68 mmol, 1.0 equiv.) in CH_2Cl_2 was added 4-methoxybenzenesulfonyl chloride (373 mg, 3.68 mmol, 1.0 equiv.) and triethylamine (514 µL, 3.68 mmol, 1.0 equiv.). Color of reaction rapidly changed from blue to purple and reaction was complete by TLC. The reaction was concentrated under reduced pressure to afford the crude residue which was purified via flash chromatography on a silica column (1:9 v/v MeOH:CH_2Cl_2) to obtain a mixture of **25** and the TBS protected form of **25**. The mixture was dissolved in CH_2Cl_2 (100 mL) and treated with 1 M HCl (50 mL, 1:1 v/v MeOH:H_2O) and stirred for 2 h at room temperature. The reaction was washed 3 times with brine. The combined organic fractions were dried (Na_2SO_4), filtered and concentrated under reduced pressure to afford the crude residue which was purified via flash chromatography on a silica column (1:9 v/v MeOH:CH_2Cl_2) to afford **25** (130 mg, 0.2 mmol, 5.9% yield) as a purple film. ^{1}H NMR (500 MHz, $CDCl_3$) δ 8.54 (d, *J* = 14.6 Hz, 1H), 7.86 – 7.70 (m, 3H), 7.48 (dt, *J* = 33.2, 7.5 Hz, 4H), 7.13 – 6.99 (m, 4H), 6.71 (d, *J* = 14.9 Hz, 1H), 4.64 (s, 2H), 4.40 (s, 2H), 3.89 (s, 3H), 2.79 – 2.57 (m, 4H), 1.86 (s, 2H), 1.78 (s, 6H), 1.53 (d, *J* = 6.6 Hz, 3H). ^{13}C NMR (125 MHz, $CDCl_3$) δ 177.78, 164.69, 160.07, 151.40, 147.86, 146.30, 142.19, 140.93, 134.00, 131.88, 130.62, 130.23, 129.41, 128.16, 127.89, 126.16, 122.57, 120.46, 115.51, 114.94, 112.96, 109.35, 105.75, 57.75, 56.05, 50.92, 29.71, 29.43, 28.04, 20.17, 13.17.

Synthesis of 26 (Ctrl-PARx-1). To a solution of **25** (31.0 mg, 0.052 mmol, 1.0 equiv.) in anhydrous THF (15 mL) at 0 °C under N_2 was added phosgene (15 wt. % in toluene, 46.5 µL, 0.67 mmol, 13.0 equiv.). Reaction was stirred at room temperature for 3 h, then N_2 was bubbled through the reaction for 20 minutes to obtain the chloroformate. The chloroformate solution was added to a solution of gemcitabine (136 mg, 0.52 mmol, 10.0 equiv.) and DIPEA (90.2 µL, 0.52 mmol, 10.0 equiv.) in DMF (25 mL) at 0 °C. After 2 h, the reaction was treated with sat. NH_4Cl and extracted

with CH_2Cl_2. The collected organic fraction was washed with brine, then dried over Na_2SO_4, filtered and concentrated under reduced pressure to afford the crude residue which was purified via flash chromatography on a silica column (1:9 v/v MeOH: CH_2Cl_2) to afford **26** (3.3 mg, 0.003 mmol, 7.2% yield) as a purple film. ^{1}H NMR (500 MHz, CD_3OD) δ 8.71 (d, *J* = 15.2 Hz, 1H), 8.32 (d, *J* = 7.6 Hz, 1H), 7.88 (dd, *J* = 9.6, 2.7 Hz, 2H), 7.75 – 7.49 (m, 6H), 7.27 (d, *J* = 7.5 Hz, 1H), 7.20 (s, 1H), 7.17 – 7.11 (m, 3H), 6.67 (d, *J* = 15.2 Hz, 1H), 6.28 – 6.20 (m, 1H), 5.47 (s, 1H), 5.03 (s, 2H), 4.48 (q, *J* = 7.3 Hz, 2H), 4.29 (d, *J* = 8.7 Hz, 1H), 4.19 (dd, *J* = 5.7, 2.2 Hz, 1H), 4.00 – 3.92 (m, 2H), 3.85 (s, 3H), 3.83 – 3.76 (m, 1H), 2.78 – 2.69 (m, 4H), 1.92 (s, 2H), 1.81 (s, 6H), 1.50 (t, *J* = 7.2 Hz, 3H). ^{13}C NMR (125 MHz, CD_3OD) δ 179.10, 167.93, 165.07, 163.86, 158.92, 152.56, 148.80, 146.51, 142.78, 140.88, 131.20, 131.00, 130.71, 129.49, 129.08, 128.82, 128.46, 128.09, 126.23, 125.99, 122.59, 120.85, 114.90, 114.71, 113.20, 109.79, 105.93, 95.61, 67.70, 61.32, 58.86, 55.21, 51.29, 40.80, 38.78, 30.23, 28.96, 28.74, 26.41, 23.56, 22.63, 20.01, 12.99, 11.81, 10.00.

***In Vitro* Buffer Preparation.** To 70% PBS/MeCN buffer solutions were added reduced GSH for final concentrations of 0, 0.1, 1, 2.5, 5, and 10 mM. Adjustments to pH were made via addition of 1 M HCl or 1 M NaOH. pH values were determined using a Mettler-Toledo SevenCompact pH meter calibrated using pH 4.0, 7.0 and 10.0 standard buffers at 25 °C.

Selectivity Studies. The initial absorbance (400–800 nm) was measured before the addition of amino acids (2.5 mM), reductants (2.5 mM), thiols (2.5 mM Cys and Hcy, 10 mM GSH), reactive metals (2.5 mM), oxygen (50 μM), and nitrogen species (50 μM). After addition, the reaction was sealed and incubated at 37 °C for 1 h. Final measurements were recorded, and relative turn-on was determined by change in absorption at λ_{max}. All metal solutions were prepared in water from their chloride salt. Superoxide anion was added as a solution of potassium superoxide in DMSO. NO

was generated *in situ* from a solution of MAHMA-NONOate in degassed 10 mM potassium hydroxide. Peroxynitrite was synthesized according to a literature report.[98] All other analytes were prepared by dilution from commercially available sources.

Microsome Assay. The initial absorbance of 10 μM PARx with 10 μL RLM in 0.1 M potassium phosphate buffer (pH 7.4) was measured. After addition of 50 μM NADPH, the reaction was incubated at 37 °C for 1h. The final absorbance was measured after quenching with acetonitrile.

Live Cell Imaging. A549 cells were plated in a poly-lysine coated microwell plate in Ham's F12-K (10% FBS) media for 24 h. A549 cells were then incubated with or without 1 mM NEM in 1% DMSO:PBS or culture medium, respectively, for 30 minutes at 37 °C. After removing NEM, NEM-treated and untreated cells were further incubated with PACDx (5 μM, 1% DMSO:DMEM) for 1 h at 37 °C. Another set of cells were incubated with ctrl-PACDx (5 μM, 1% DMSO:DMEM) for 1 h at 37 °C. Cells were also imaged after incubation with PARx (5 μM, 1% DMSO:DMEM) for 1 h at 37 °C.

U87 cells were plated in a poly-lysine coated microwell plate in EMEM (10% FBS) media for 24 h. U87 cells were then incubated with or without 1 mM NEM in 1% DMSO:PBS or culture medium, respectively, for 30 minutes at 37 °C. After removing NEM, NEM-treated and untreated cells were further incubated with PACDx (5 μM, 1% DMSO:DMEM) for 1 h at 37 °C. Another set of cells were incubated with ctrl-PACDx (5 μM, 1% DMSO:DMEM) for 1 h at 37 °C. Cells were also imaged after incubation with PARx (5 μM, 1% DMSO:DMEM) for 1 h at 37 °C.

HEK293 cells were plated in a poly-lysine coated microwell plate in EMEM (10% FBS) media for 24 h. HEK293 cells were then incubated with PACDx (5 μM, 1% DMSO:DMEM) for 1 h at 37 °C. Another set of cells were incubated with PARx (5 μM, 1% DMSO:DMEM) for 1 h at 37 °C.

A549-Luc2 cells were plated in a poly-lysine coated microwell plate in ATCC Ham's F12-K (10% FBS and 8 μg/mL Blasticidin) media for 24 h. A549-Luc2 cells were then incubated with or without 1 mM NEM in 1% DMSO:PBS or culture medium, respectively, for 30 minutes at 37 °C. After removing NEM, NEM-treated and untreated cells were further incubated with PACDx (5 μM, 1% DMSO:DMEM) for 1 h at 37 °C. Another set of cells were incubated with Ctrl-PACDx (5 μM, 1% DMSO:DMEM) for 1 h at 37 °C.

All cell imaging experiments were performed using Zeiss LSM700 confocal microscope with an excitation filter of 639 nm. Imaging results were quantified relative to fluorescent intensity for each relevant control experiment using Fiji.

Cytotoxicity Assay. A549 cells were plated ($5x10^4$ cells/well) in a 24-well plate in Ham's F12-K (10% FBS) media for 24 h. A549 cells were then incubated with 0.0, 0.1, 5.0, 10.0, and 25 μM PARx, Ctrl-PARx-2, or gemcitabine HCl at 37 °C in serum free DMEM. After 48 h, media was replaced with 5 mg/mL MTT reagent (1:20 in PBS) and incubated for 1 h at 37 °C. Cells were then lysed using 500 μL DMSO, transferred to a 96-well plate and absorbances were measured using a plate reader at 555 nm. Viability was measured relative to absorbance of control wells.

Tissue Phantom Preparation. For PA imaging on the Nexus 128+: Tissue phantoms were prepared by suspending agarose LE in a solution of 2% milk (1 mL) and deionized water (39 mL). The suspension was heated in a microwave until a viscous, translucent gel was produced. The hot gel was poured into a custom Teflon mold containing two copper tubes and cooled at 4 °C for at least 2 h. After cooling, the copper tubes were removed and the gel was removed from the mold, yielding a tissue phantom with two parallel channels for the placement of FEP tubes containing sample solutions.

For PA imaging on the MSOT InVision 128: Tissue phantoms were prepared by suspending agarose LE (750 mg) in deionized water (50 mL). The suspension was heated for 1 minute in a microwave until a viscous, translucent gel was produced. Immediately, 1 mL of 2% milk was added. The hot gel was poured into a cylindrical mold containing two plastic straws (3 mm diameter) and cooled at room temperature for at least 20 minutes. After cooling, the straws were removed and the gel was removed from the mold, yielding a tissue phantom with two parallel channels for the placement of FEP tubes containing sample solutions.

Tissue Phantom PA Imaging. For PA imaging on the Nexus 128+: Various GSH solutions were prepared (0, 0.1, 1, 2.5, 5, 10 mM in 70% PBS/MeCN, pH 7.4). After incubating either PACDx or PARx (50 μM) in the appropriate solution for 1 h, 400 μL of solution was injected into FEP tubes which were then inserted into the tissue phantom. After positioning over the center of the laser, images were acquired at 690 nm using continuous mode with a 6 second rotation time. To acquire a spectrum, the tissue phantom was excited at 680 nm, 690 nm, 700 nm, 710 nm, 720 nm, 730 nm, 740 nm, 750 nm, 760 nm, 770 nm, 780 nm, 790 nm, and 800 nm using continuous mode with a 6 second rotation time.

For PA imaging on the MSOT InVision 128: A solution of HD (50 μM, 70%PBS/MeCN, pH 7.4) was injected into a tube which was then inserted into the cylindrical tissue phantom for imaging. The phantom was placed into the holder and excited at 670 nm, 680 nm, 690 nm, 700 nm, 730 nm, 760 nm, 800 nm, 850 nm and 900 nm. The spectrum that was obtained was later used for spectral unmixing.

Limit of Detection. Using the following equations, we calculated the limit of detection to be 0.39 mM GSH: $LoD = LoB + 1.645(SD_{low\ concentration\ sample})$

$LoB = mean_{blank} + 1.645(SD_{blank})$

The LoB was calculated by using the mean PA intensity of 70% PBS/MeCN and the SD from 3 different samples after exciting at 690 nm. This value was used in the LoD equation where we used the SD from 3 different samples of PACDx (50 μM in 70% PBS/MeCN containing 0.1 mM GSH, pH 7.4).

Live-subject Statement. All animal experiments were performed with the approval of the IACUC of the University of Illinois at Urbana–Champaign, following the principles outlined by the American Physiological Society on research animal use.

A549 Xenograft Model. 4 to 5-week-old Nu/J mice were subcutaneously injected with $5x10^6$ cells (50 μL, 1:1 PBS:Matrigel) in the lower right flank. Tumors were measured using calipers and volumes were calculated using the equation: $V= (W^2*L)/2$. Tumors were grown to 100 mm^3 before being treated with PACDx, PARx or vehicle.

U87 Xenograft Model. 4 to 5-week-old Nu/J mice were subcutaneously injected with $5x10^6$ cells (50 μL, 1:1 PBS:Matrigel) in the lower right flank. Tumors were measured using calipers and volumes were calculated using the equation: $V= (W^2*L)/2.^{99}$ Tumors were grown to 100 mm^3 before being treated with PACDx, PARx or vehicle.

4T1 Allograft Model. 6 to 8-week-old female BALB/c mice were inoculated with 4T1 cells (100 μL of 1 × 106 cells/mL in 1:1 serum-free RPMI 1640 media and Matrigel) via subcutaneous injection into the flank. After 30 days, the tumors had grown to a final volume of 300-400 mm^3.

***In vivo* Imaging.** Intratumoral route: Tumor-bearing mice were anesthetized using isoflurane (1.5 - 2%). A 50 μL solution of PARx (100 μM) in saline containing 10% DMSO was administered via intratumoral injection. PA images of tumor-bearing flanks were acquired immediately before injection and 60 minutes post-injection. Images were acquired at 680 nm using continuous mode with a 6 second rotation time.

Retro-orbital route: Tumor-bearing mice were anesthetized using isoflurane (1.5 - 2%). A 150 μL solution of PARx or PACDx (400 μM) in saline containing 10% DMSO was administered via retro-orbital injection. PA images of tumor-bearing flanks were acquired immediately before injection and 60 minutes post-injection. Images were acquired at 680 nm using continuous mode with a 6 second rotation time. MSOT images were obtained using the same conditions.

Tumor Growth Inhibition. Intratumoral route: Tumor-bearing mice were anesthetized using isoflurane (1.5 - 2%). A 50 μL solution of PARx (100 μM) in saline containing 10% DMSO was administered via intratumoral injection. Injections were performed once a week for 3 weeks and tumors growth was monitored over 3 weeks.

Retro-orbital route: Tumor-bearing mice were anesthetized using isoflurane (1.5 - 2%). A 150 μL solution of PARx (400 μM) in saline containing 10% DMSO was administered via retro-orbital injection. Injections were performed once a week for 3 weeks and tumors were measured every 3 days. For the higher frequency treatment, injections were performed, and tumors were measured every 3 days for 3 weeks.

Tissue Histology. 10% neutral buffered formalin was made with the following: 10 mL 37-40% formaldehyde solution, 90 mL DI water, 400 mg sodium phosphate monobasic, 650 mg sodium phosphate dibasic. To prepare tissue for histology staining, mice were sacrificed, and the liver, kidneys, spleen, heart, and tumor were immediately dissected. Each tissue was placed immediately in cooled 10 mL freshly made 10% formalin. Tissues were measured to be approximately 5 mm in thickness or less. Kidneys were slightly punctured rather than sliced for better fixative penetration. Other larger tissues were sliced. Tissues were fixed for at least 48 h at 4 °C. Tissues were then transferred to 10 mL 70% EtOH. Tissue samples were submitted to the histology lab at the College of Veterinary Medicine at UIUC for H&E and TUNEL staining.

Orthotopic Bioluminescent Lung Cancer Animal Models. Intrapleural injection: intrapleural injections were performed using the trans-thoracic approach on 4 to 5-week-old Nu/J mice. The anesthetized mouse was laid in left lateral decubitus, and the right lateral chest was prepped. The sixth and seventh rib were identified under the elbow region by manual palpation. While an assistant extended the forelimbs and hindlimbs, cells were injected under the 6th or 7th rib. The needle was elevated gently to confirm by lifting the ribs up that it is well positioned in the intrapleural space, and $5x10^6$ cells (50 µL, 1:1 PBS:Matrigel) was injected into the intrapleural space with a 27G needle. This is described as previously published (Retrograde Neuroanatomical Tracing of Phrenic Motor Neurons in Mice, Vanderweerd, J Vis Exp 2018), and has been trialed successfully and recommended by DAR veterinarians. Tumor growth was monitored for up to 6 weeks via bioluminescence imaging. A trans-diaphragmatic approach was also used however the trans-thoracic approach was found to be more efficient and reliable. To perform the intrapleural injection using this second method, 4 to 5-week-old Nu/J mice were anesthetized and aseptic technique was followed throughout the procedure. The skin was tented, and a 5-10 mm incision was made with scissors. The subcutaneous tissue was dissected gently while providing countertraction with forceps to expose the chest wall. Adequate dissection exposed the liver, lungs, and diaphragm. The needle was slowly inserted caudad to the intercostal space between the diaphragm and lung at a shallow angle of 15°, needle bevel up, entering the pleural space through the diaphragm. After entering the pleural space, $5x10^6$ cells (50 µL, 1:1 PBS:Matrigel) was injected slowly. After injection, 5-0 Vicryl sutures was used to close the abdominal wall with 2 single interrupted sutures. Wound clips were used to close the skin, then removed after 10 days.

Intrahepatic injection: 4 to 5-week-old Nu/J mice were used to surgically inject cancer cells into the liver. The mice were anesthetized, and aseptic technique was followed throughout the

procedure. The skin was grabbed with forceps and a ~1-centimeter horizontal incision from the midline toward the left upper abdomen was made. The skin was freed from the peritoneum. The peritoneum was lifted straight upward, and a small incision was made. The incision was extended horizontally while ensuring not to injure underlying organs. A cotton-tipped applicator was inserted into the abdomen under the lobe of the liver. The cotton-tipped applicator was slowly moved and gently rotated towards the operator. The liver was stabilized with the left hand against the underlying cotton-tipped applicator. The needle was inserted into the liver and slowly injected $5x10^6$ cells (50 µL, 1:1 PBS:Matrigel). After injection, 5-0 Vicryl sutures was used to close the abdominal wall with 2 single interrupted sutures. Wound clips were used to close the skin, then removed after 10 days. Tumor growth was monitored for up to 6 weeks via bioluminescence imaging.

We acknowledge Drs. Herndon and Xu for performing these procedures.

***In Vivo* Bioluminescence Imaging.** A fresh solution of D-Luciferin in DPBS (15 mg/mL) was prepared before imaging. Each mouse was administered 150 mg D-Luciferin/kg of body weight via IP injection. After 15 minutes, each mouse was imaged using the IVIS Spectrum CT to monitor tumor burden in luciferase expressing A549 xenografts.

***In Vivo* MSOT Imaging.** A549-Luc2 tumor bearing mice were given a retro-orbital injection of PACDx (400 µM, 150 µL in saline containing 10% DMSO). The mice were continuously anesthetized using isoflurane and placed in the prone position in the animal holder for imaging immediately before injection and 1 h post injection. The temperature of the imaging chamber was set to 36 °C and the animal was allowed to equilibrate to the temperature for 10 minutes before imaging. Cross-sectional images were acquired either at the chest or abdomen of the mouse for either lung or liver imaging with a step size of 0.3 mm. The imaging position was guided by the

built-in anatomy atlas in the MSOT InVision 128 and was kept consistent for all scans. The major wavelengths used were selected based on the absorbance of PACDx and endogenous absorbers (670 nm, 680 nm, 690 nm, 700 nm, 730 nm, 760 nm, 800 nm, 850 nm and 900 nm). 10 frames were recorded at every imaging wavelength. Subsequently, spectral unmixing was used to separate signals coming from HB and HbO_2.

Field of View Selection. The field of view for all experiments performed on the Nexus 128+ imaging system (Endra Life Sciences) was selected by identifying a slice at the middle of the tumor for a representative animal. We then kept the imaging depth consistent across all other subjects when analyzing the data. The field of view for all experiments performed on the MSOT inVision 128 imaging system (iTheraMedical) was selected by using the built-in, cross-sectional anatomy guide to correctly position the animals to image the lungs or liver.

Image Processing of Background Signal. An initial scan prior to the administration of PACDx, PARx or vehicle was performed for all PA imaging experiments. This is used to account for any background signal that originates from endogenous pigments such as hemoglobin found in blood. After the final scan is taken, a ratio ($PA_{Final}/PA_{Initial}$) is calculated to determine the change in PA intensity. Furthermore, for experiments conducted on the MSOT inVision 128 imaging system, we used the built-in spectral unmixing feature to distinguish between signal coming from PACDx and blood based on the absorbance spectra of HbO_2 and Hb.

3.12 Supplemental figures, tables, and spectra

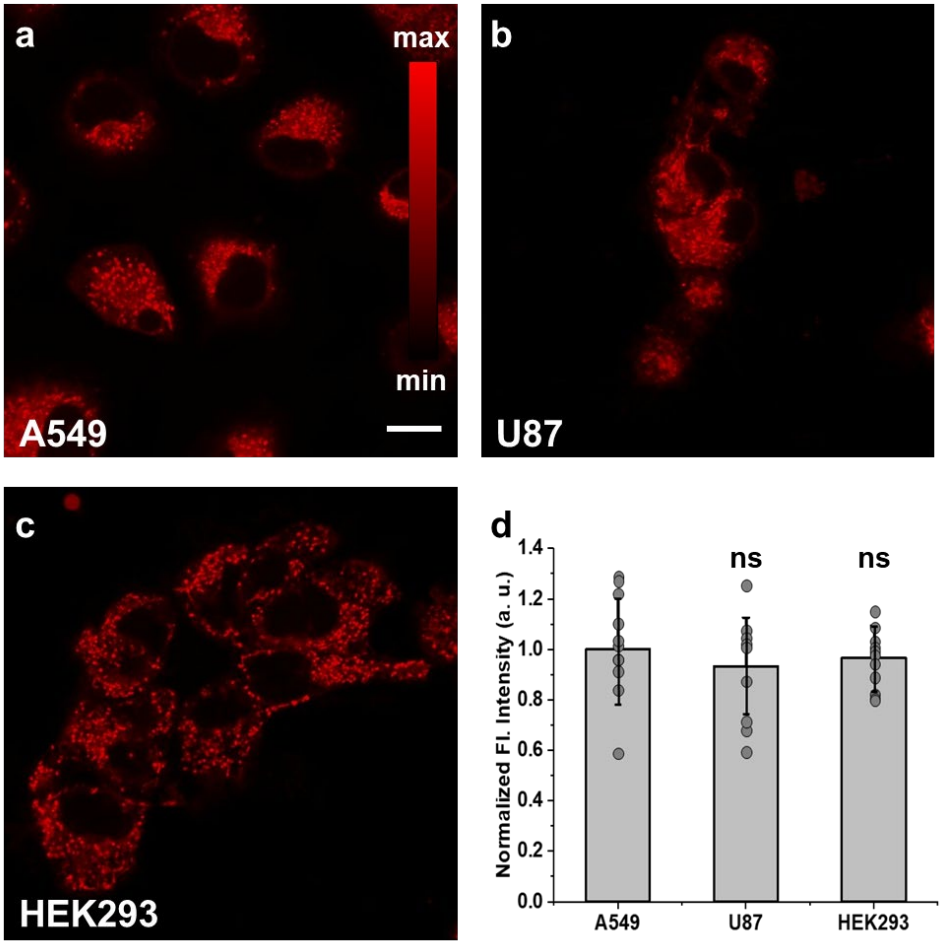

Supplementary Figure 12. Representative confocal images of a) A549, b) U87, and c) HEK293 cells treated with 5 μM **7** (dinitrobenzenesulfonyl trigger). Scale bar represents 20 μm. d) Normalized fluorescence intensity obtained from cell imaging represented in a-c. Data are presented as mean values ± SD (n = 12 biologically independent samples). Statistical analysis performed using a two-tailed Student's t-test.

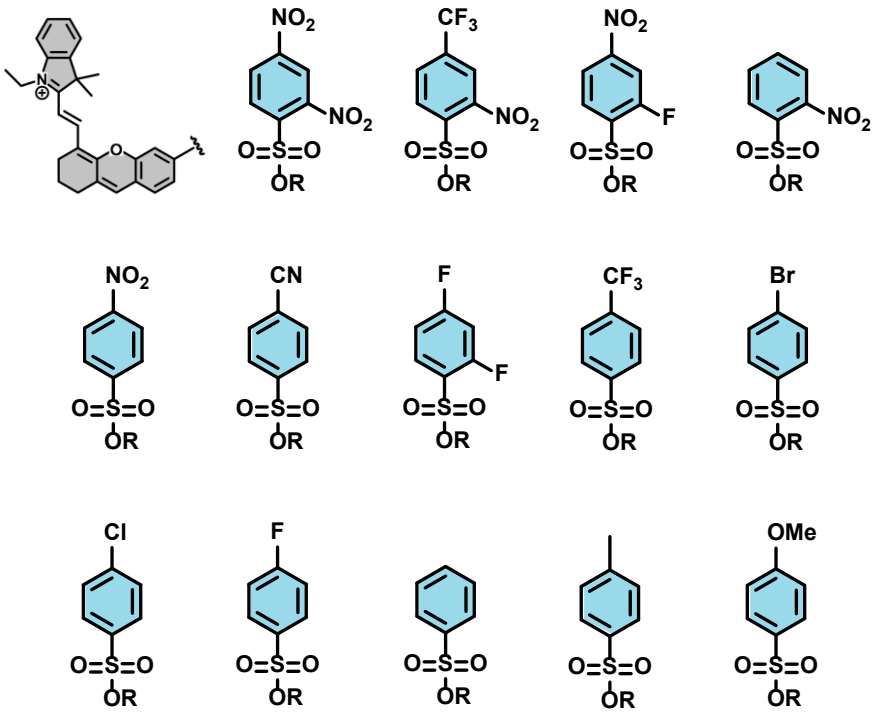

Supplementary Figure 13. Chemical structures of the panel of PA probes featuring different 2,4-disubstituted, 2-monosubstituted, and 4-monosubstituted, and unsubstituted benzenesulfonyl triggers for GSH detection.

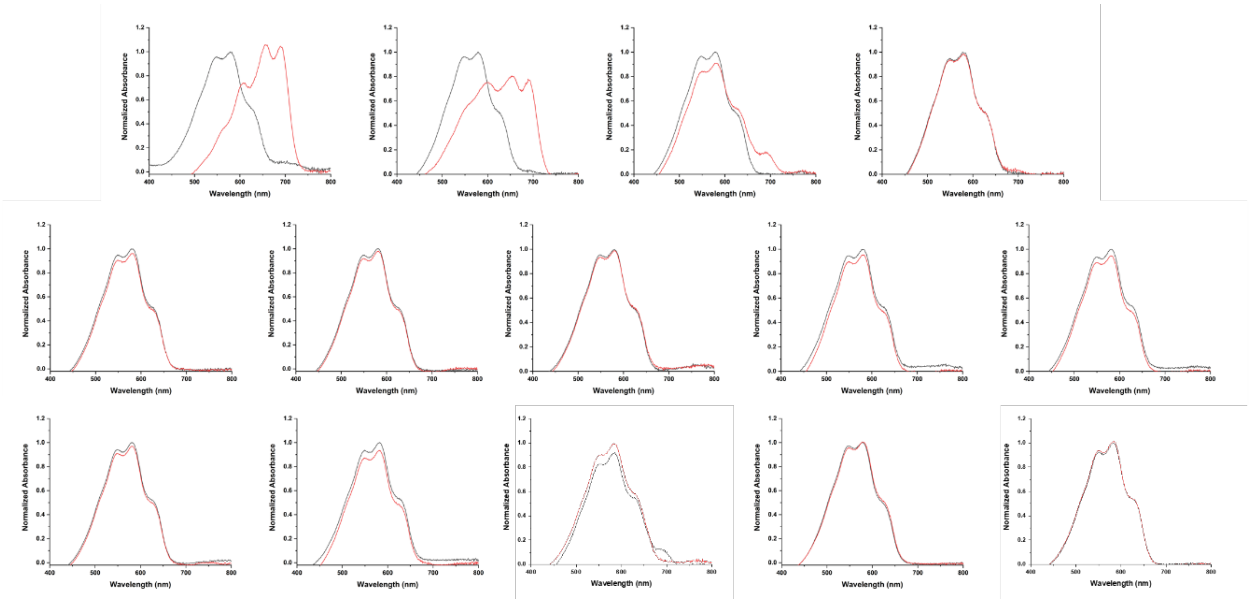

Supplementary Figure 14. Absorbance spectra of each probe in Supplementary Figure 1 after incubation with 1 mM GSH (70% PBS/MeCN, pH 7.4, 37 °C). Top row (from left to right): Compound 7, 8, PACDx, 9. Second row (from left to right): Compound 10, 11, 12, 13, 14. Third row (from left to right): Compound 15, 16, 17, 18, 19. Black line represents initial time point and red line represents the 1 h time point.

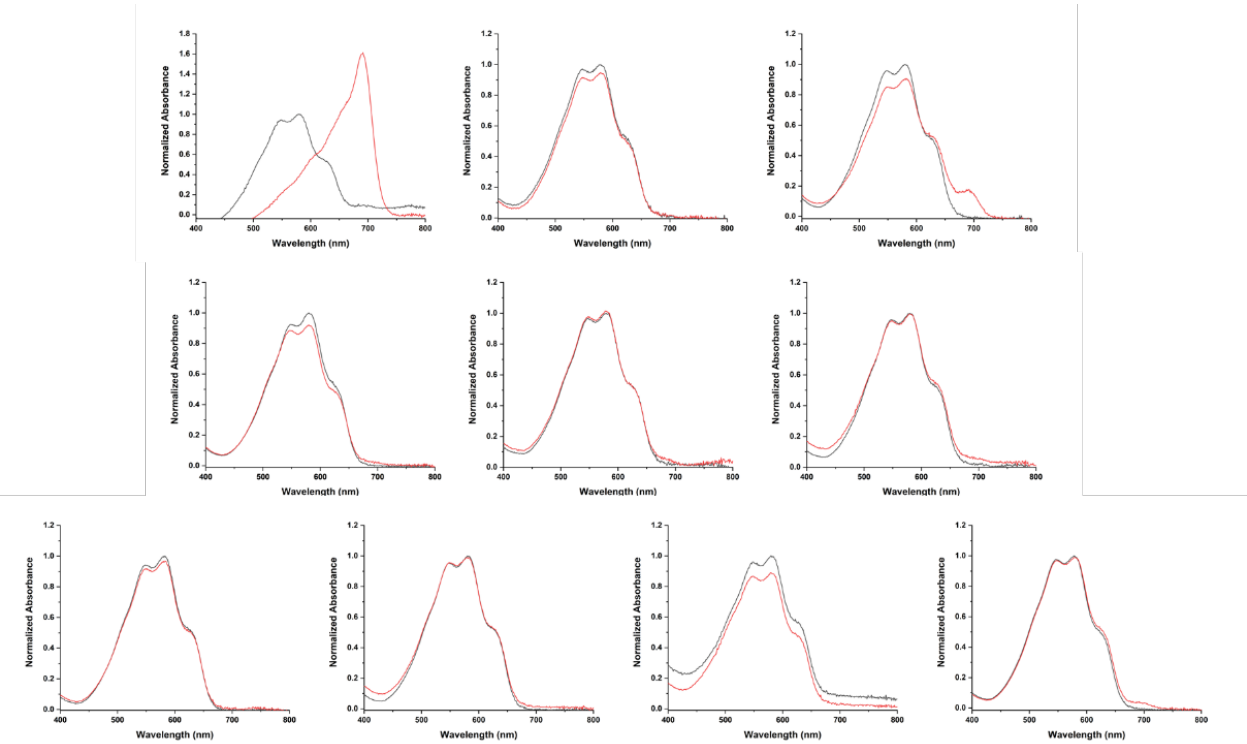

Supplementary Figure 15. Absorbance spectra of probes after incubation with 10 mM GSH (70% PBS/MeCN, pH 7.4, 37 °C). Top row (from left to right): Compound PACDx, 9, 10. Second row (from left to right): Compound 11, 12, 13. Third row (from left to right): Compound 14, 15, 16**,** and 17. Black line represents initial time point and red line represents the 1 h time point.

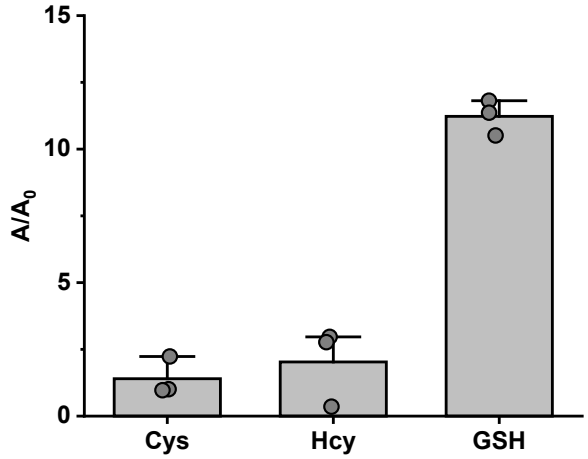

Supplementary Figure 16. Fold change in absorbance after 1 h incubation of PACDx with 200 μM Cys, 100 μM Hcy, and 2.5 mM GSH (70% PBS/MeCN, pH, 7.4, 37 °C). Data are presented as mean values ± SD (*n* = 3 independent experiments).

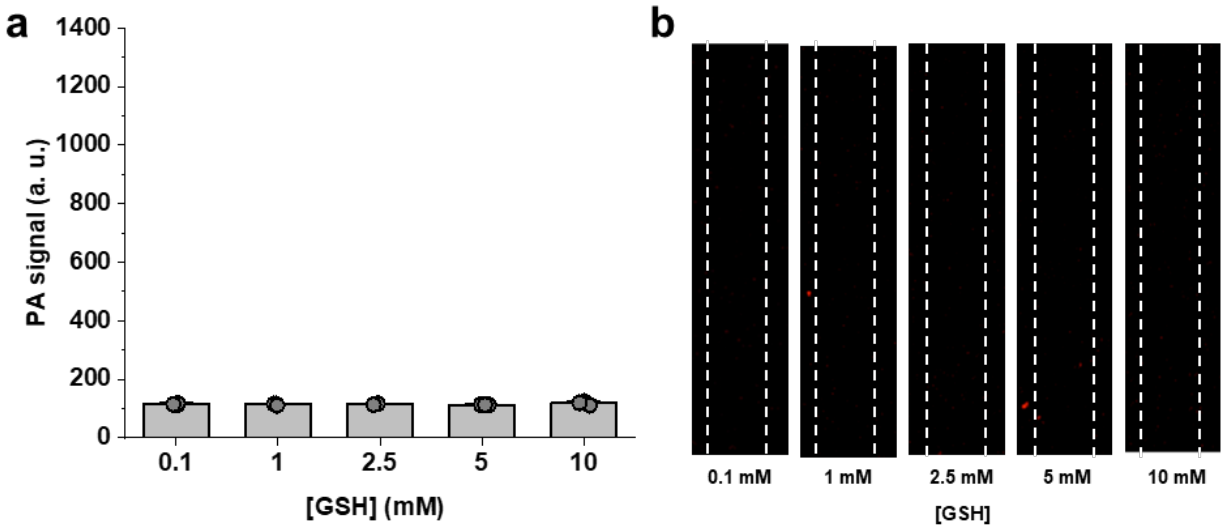

Supplementary Figure 17. a. PA signal and b. PA images of Ctrl-PACDx in response to GSH after 1 h (70% PBS/MeCN, pH 7.4, 37 °C). Data are presented as mean values ± SD (*n* = 3 independent experiments).

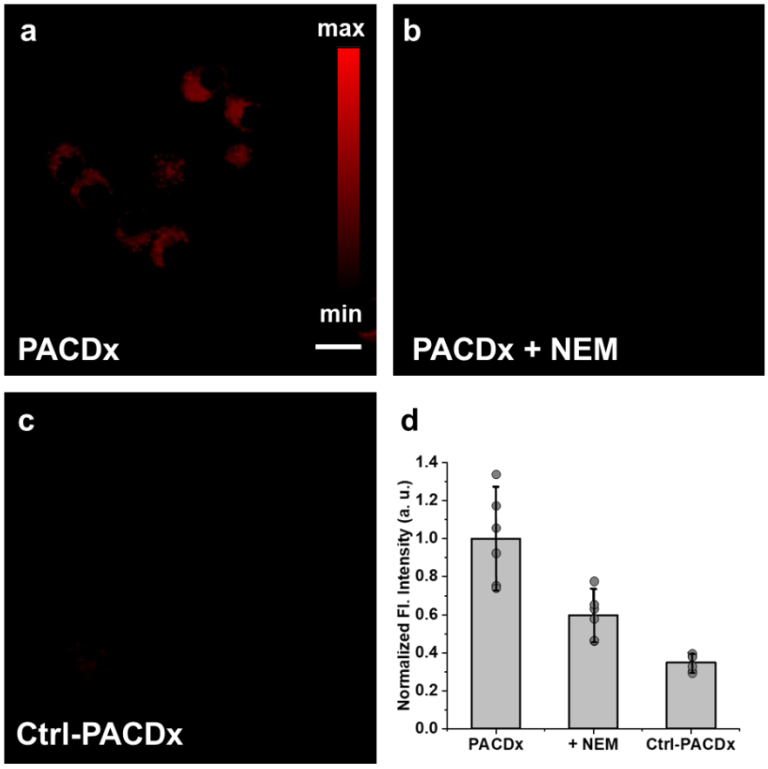

Supplementary Figure 18. a. Representative confocal image of U87 cells treated with 5 μM PACDx. b. Representative confocal image of U87 cells pre-treated with 1 mM NEM and incubated with 5 μM PACDx. c. Representative confocal image of U87 cells treated with 5 μM Ctrl-PACDx. Scale bar represents 20 μm. d. Normalized fluorescence intensity obtained from cell imaging under conditions represented in a-c. Data are presented as mean values ± SD (n = 9 biologically independent samples).

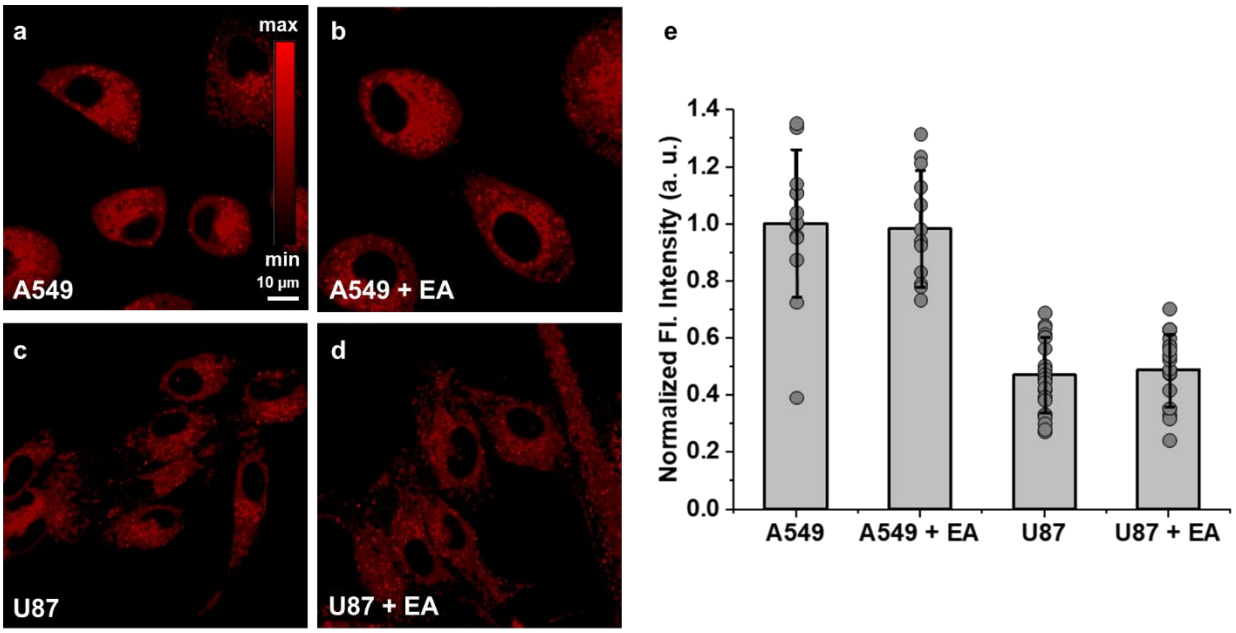

Supplementary Figure 19. a. Representative confocal image of A549 cells treated with 5 µM PACDx. b. Representative confocal image of A549 cells pre-treated with 100 µM EA and incubated with 5 µM PACDx. c. Representative confocal image of U87 cells treated with 5 µM PACDx. d. Representative confocal image of U87 cells pre-treated with 100 µM EA and incubated with 5 µM PACDx. e. Normalized fluorescence intensity obtained from imaging A549 (n = 12 biologically independent samples) and U87 (n = 24 biologically independent samples) cells with and without EA. Data are presented as mean values ± SD.

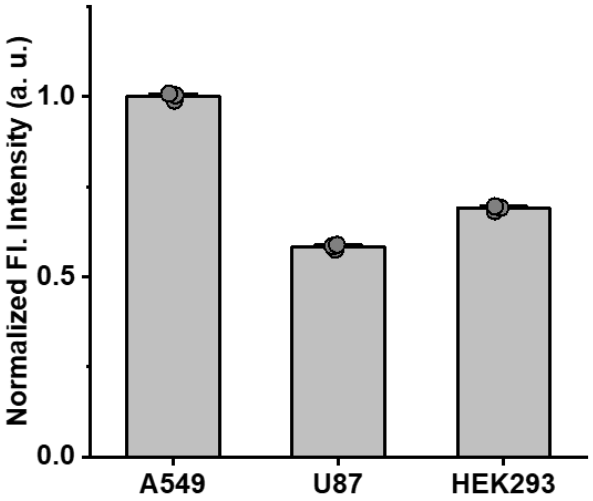

Supplementary Figure 20. Normalized fluorescence intensity obtained from treating A549, U87, and HEK293 cell lysates with 5 μM PARx. Excitation wavelength used was 690 nm. Data are presented as mean values ± SD (n = 3 biologically independent samples).

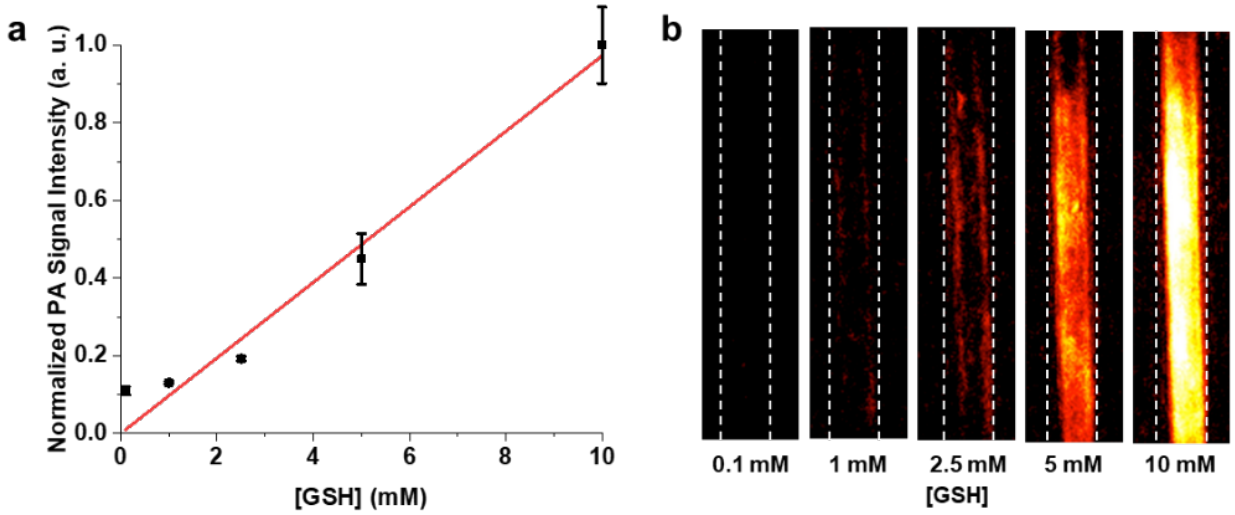

Supplementary Figure 21. a. Normalized PA signal and b. PA images of PARx in response to GSH after 1 h (70% PBS/MeCN, pH 7.4, 37 °C). Data are presented as mean values ± SD (*n* = 3 independent experiments).

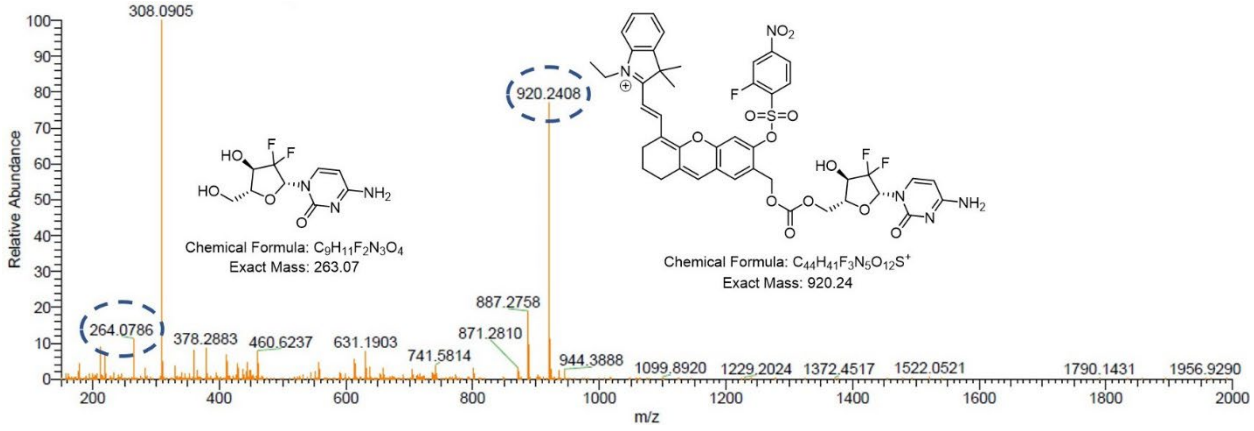

Supplementary Figure 22. ESI-MS spectra of PARx treated with 10 mM GSH.

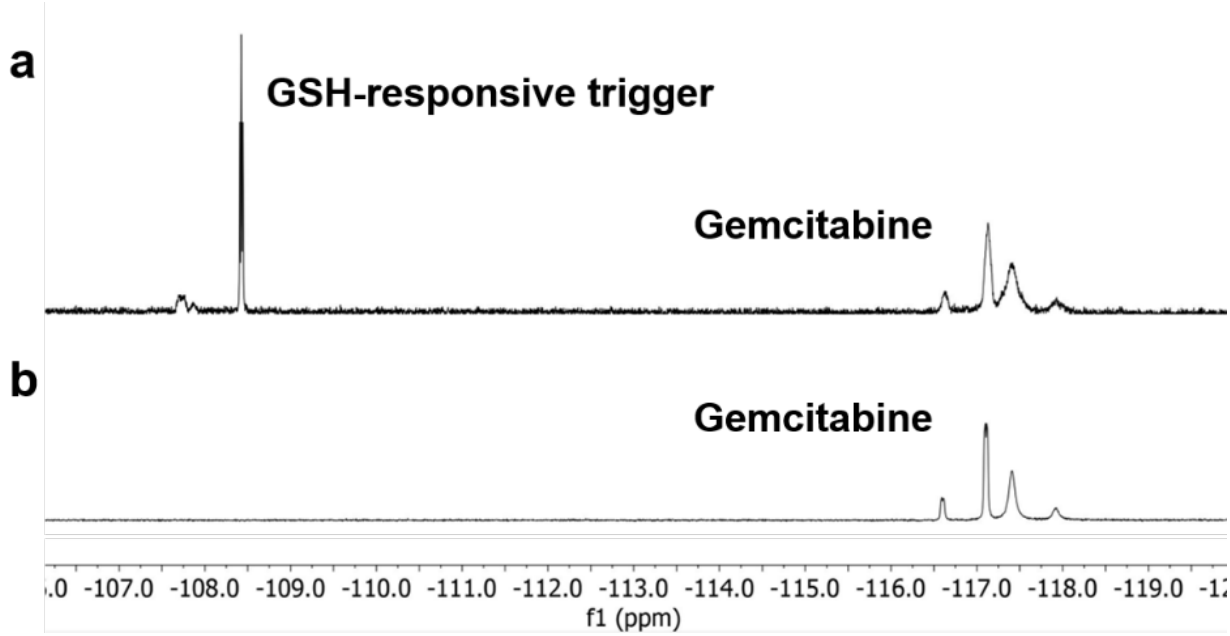

Supplementary Figure 23. ^{19}F NMR indicating the release of gemcitabine from a. PARx after incubation with 10 mM GSH. b. ^{19}F NMR of gemcitabine in D_2O/CD_3CN.

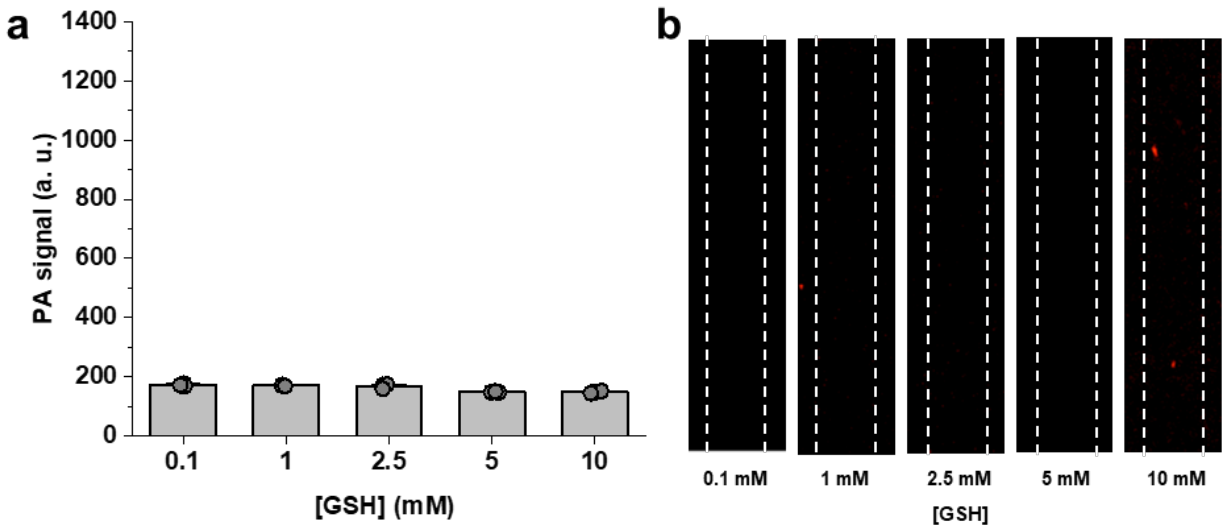

Supplementary Figure 24. a. PA signal and b. PA images of Ctrl-PARx in response to GSH after 1 h (70% PBS/MeCN, pH 7.4, 37 °C). Data are presented as mean values ± SD (*n* = 3 independent experiments).

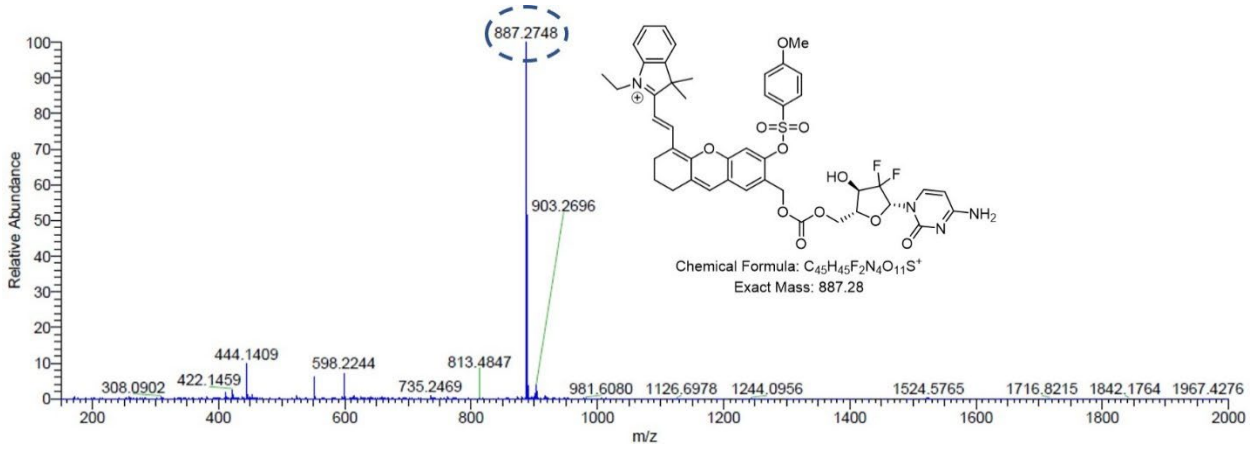

Supplementary Figure 25. ESI-MS spectra of Ctrl-PARx-1 treated with 10 mM GSH.

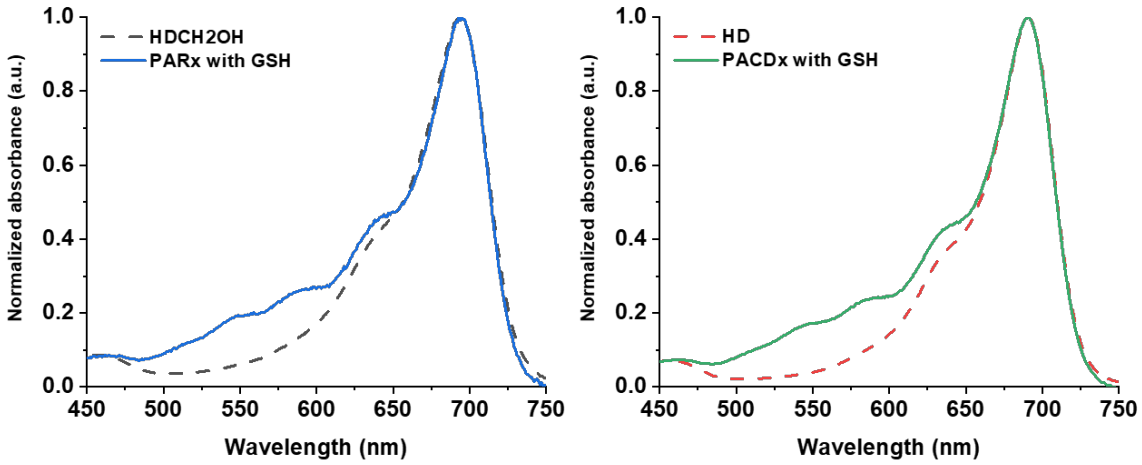

Supplementary Figure 26. Normalized absorbance spectra of PARx with 10 mM GSH (blue line) and corresponding turnover product $HDCH_2OH$ (black dashed line). Normalized absorbance spectra of PACDx with 10 mM GSH (green line) and corresponding turnover product HD (red dashed line). Spectra were taken in 70% PBS/MeCN pH 7.4.

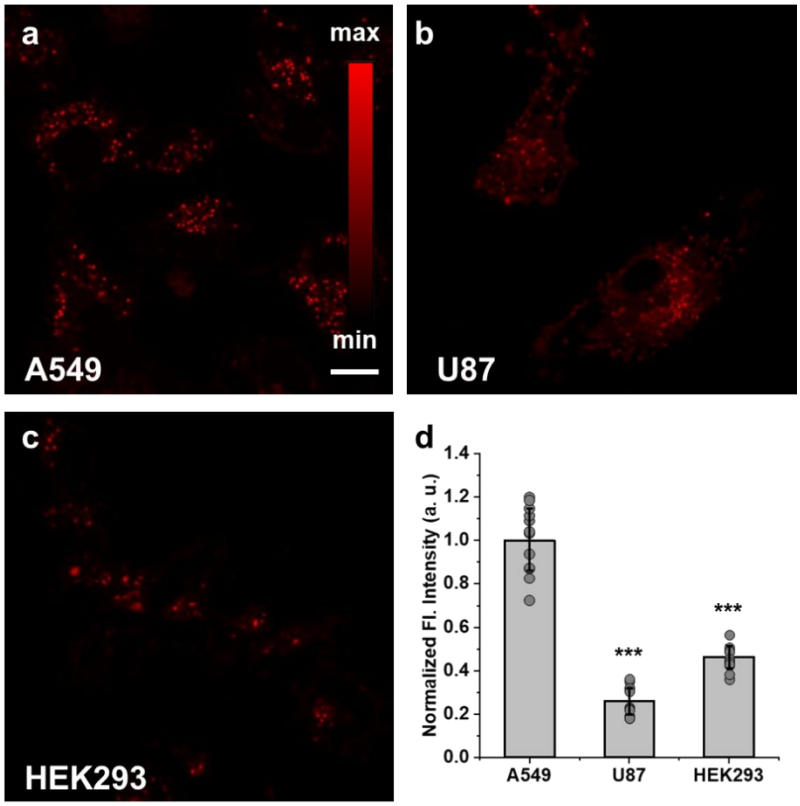

Supplementary Figure 27. Representative confocal images of a. A549, b. U87, and c. HEK293 cells treated with 5 μM PARx. Scale bar represents 10 μm. d. Normalized fluorescence intensity obtained from cell imaging represented in a-c. Data are presented as mean values ± SD (n = 12 biologically independent samples). Statistical analysis was performed using a two-tailed Student's t-test.

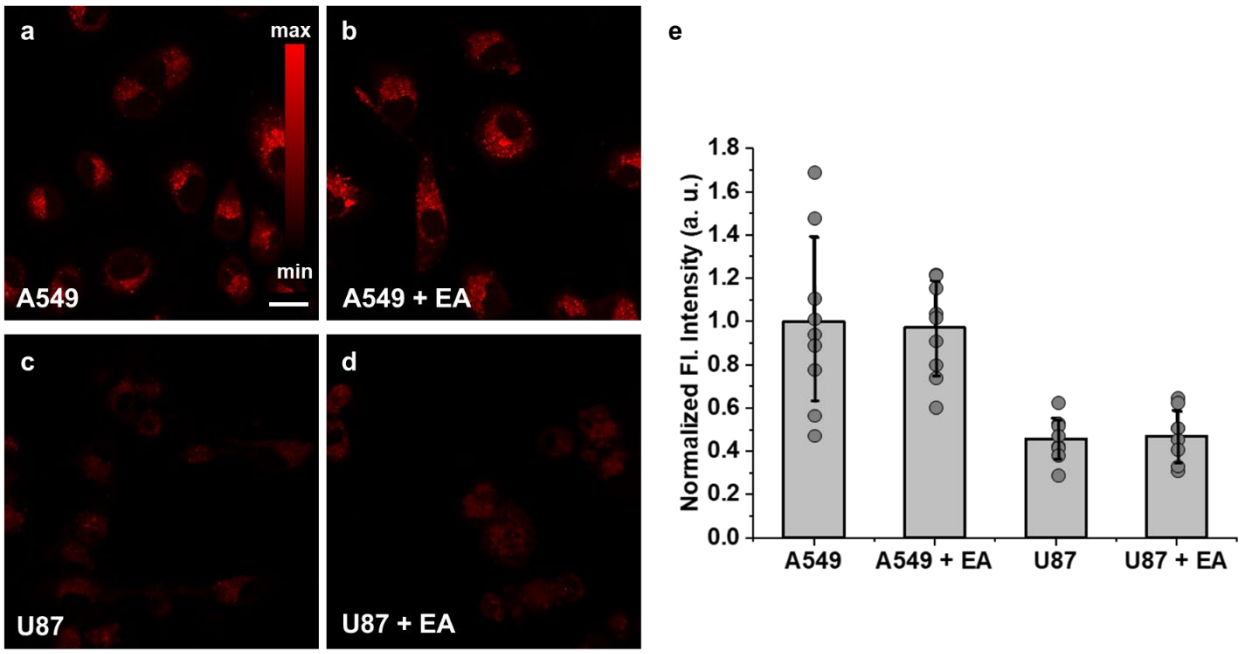

Supplementary Figure 28. a. Representative confocal image of A549 cells treated with 5 µM PARx. b. Representative confocal image of A549 cells pre-treated with 100 µM EA and incubated with 5 µM PARx. c. Representative confocal image of U87 cells treated with 5 µM PARx. d. Representative confocal image of U87 cells pre-treated with 100 µM EA and incubated with 5 µM PARx. Scale bar represents 20 µm. e. Normalized fluorescence intensity obtained from imaging A549 and U87 cells with and without EA. Data are presented as mean values ± SD (n = 9 biologically independent samples).

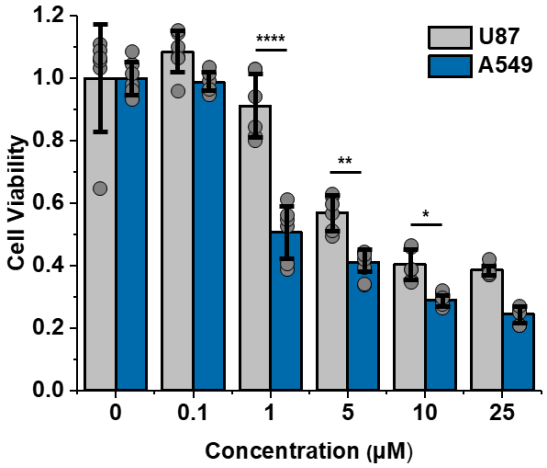

Supplementary Figure 29. Cell viability after 48 h incubation with PARx at 0, 0.1, 1, 5, 10, and 25 μM in U87 and A549 cells. Data are presented as mean values ± SD (n = 6 biologically independent samples). Statistical analysis was performed using Two-way ANOVA (α = 0.05) and Šidák's multiple comparisons test (****: adjusted P > 0.0001, **: adjusted P > 0.01, *: adjusted P > 0.05).

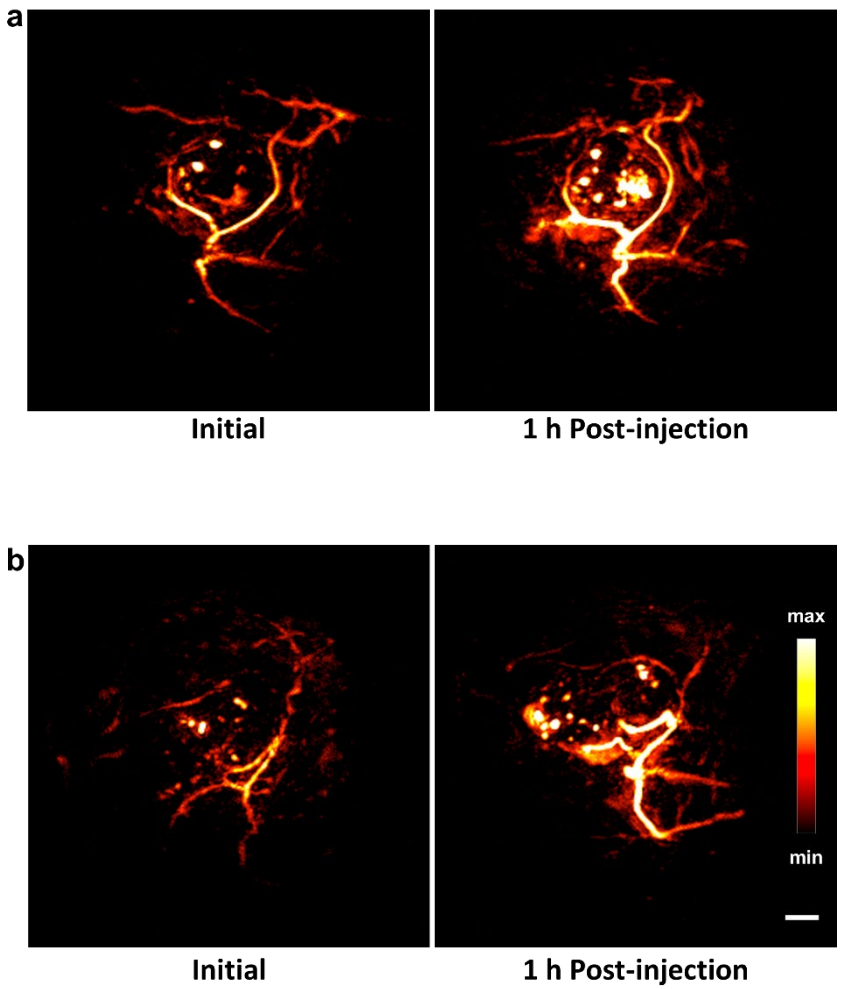

Supplementary Figure 30. Representative PA images of A549 tumors before and 1 h after a. intratumoral and b. retro-orbital injection. Scale bar represents 2 mm.

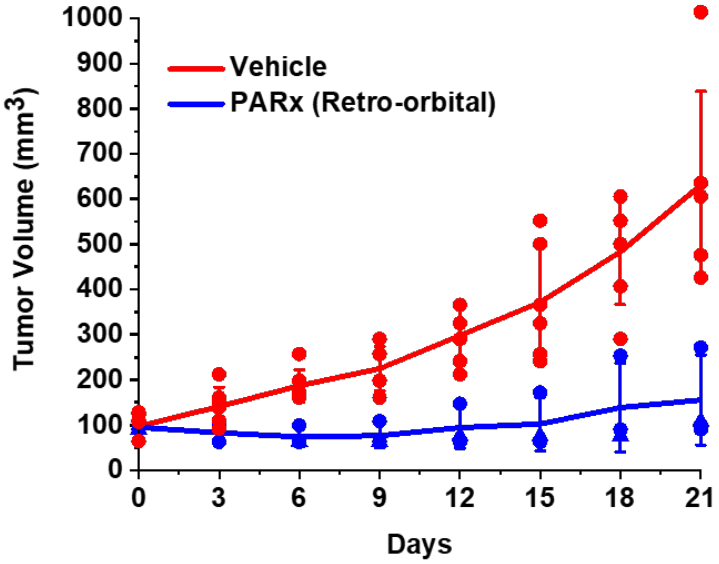

Supplementary Figure 31. Monitoring tumor volume growth after retro-orbital injection of PARx every 3 days for 21 days (n = 3 independent animals). Vehicle included for comparison. Data are presented as mean values ± SD.

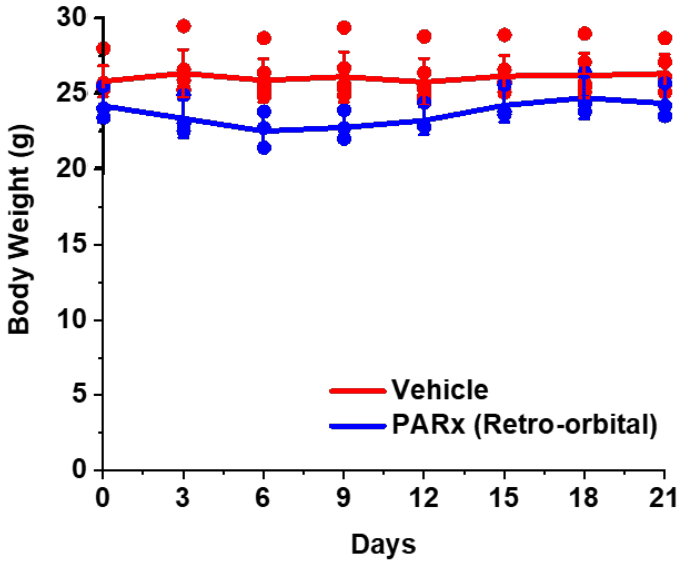

Supplementary Figure 32. Monitoring body weight after retro-orbital injection of PARx every 3 days for 21 days ($n = 3$ independent animals). Vehicle included for comparison. Data are presented as mean values ± SD.

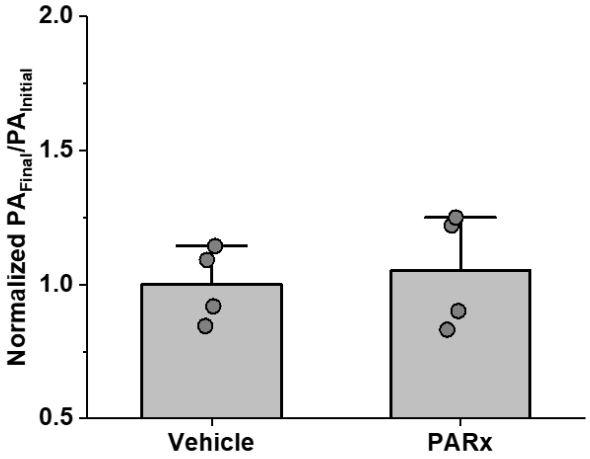

Supplementary Figure 33. Normalized PA turn-on after intratumoral injection of PARx (100 μM) or vehicle in U87 xenograft mice (n = 4 independent animals). Data are presented as mean values ± SD.

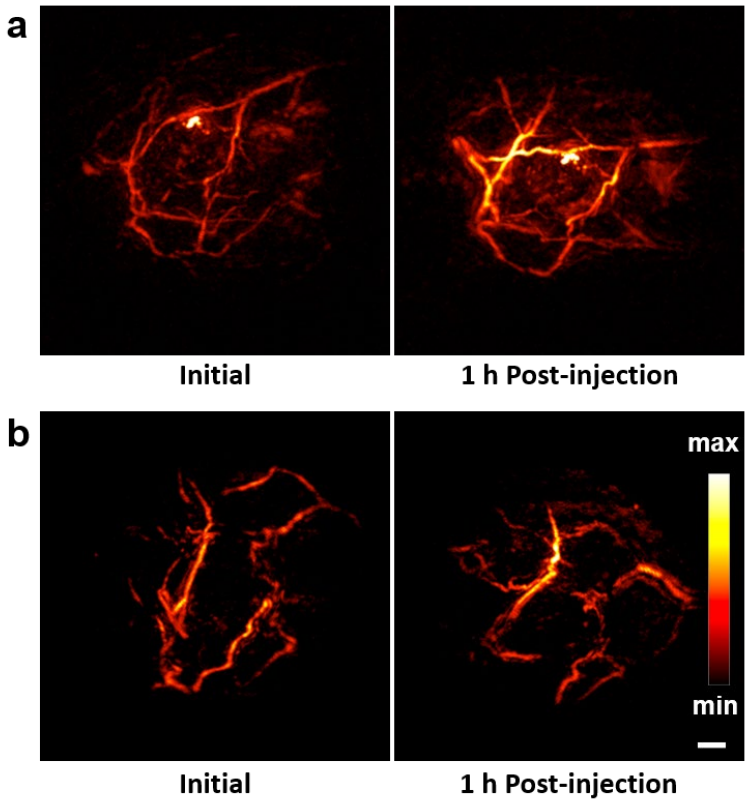

Supplementary Figure 34. Representative PA images of tumors in a. stratified group 1 and b. 2 before and 1 h after retro-orbital injection. Scale bar represents 2 mm.

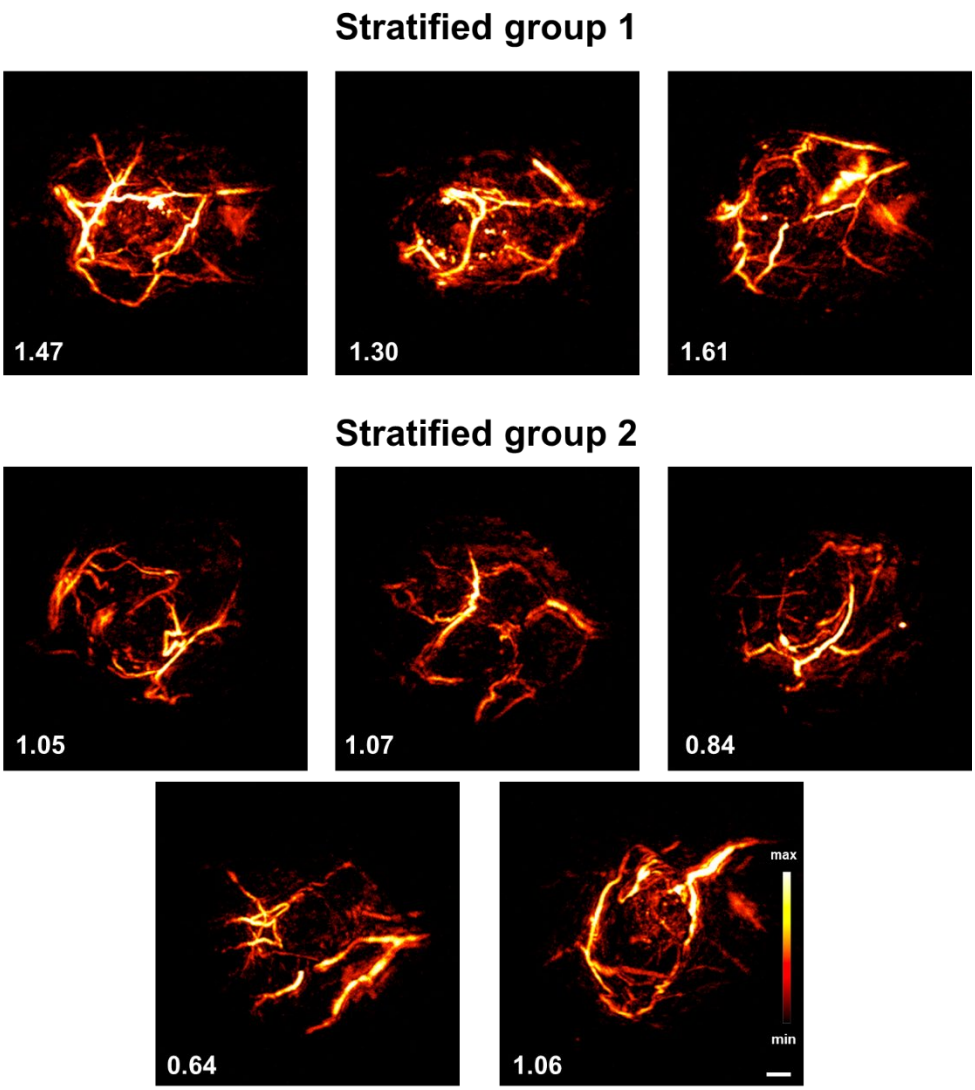

Supplementary Figure 35. PA images corresponding to Figure 12c. PA images were acquired by irradiating at 680 nm. PA turn-on values shown in white. Scale bar represents 2 mm.

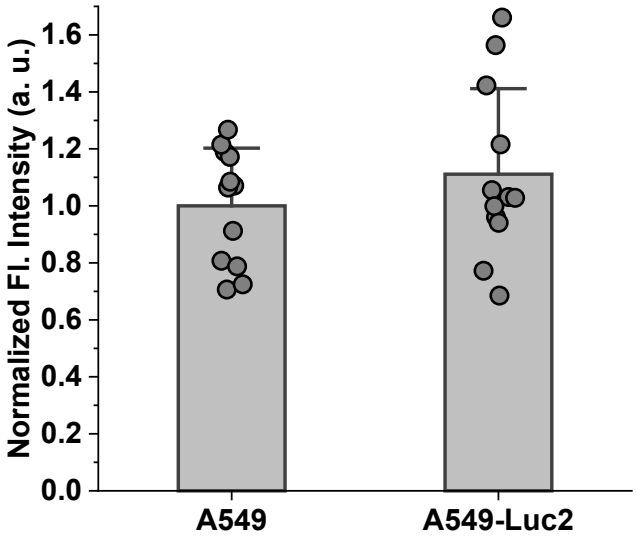

Supplementary Figure 36. Normalized fluorescence intensity from confocal imaging after treating A549 and A549-Luc2 cells with PACDx (5 μM, 1% DMSO:DMEM) for 1 h at 37 °C. Data are presented as mean values ± SD (n = 12 biologically independent samples).

.

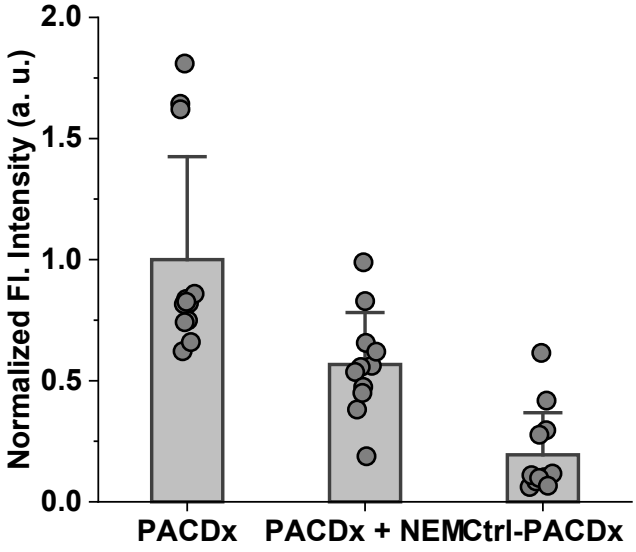

Supplementary Figure 37. Normalized fluorescence intensity from confocal imaging after treating A549-Luc2 cells with PACDx, Ctrl-PACDx, or with PACDx (5 μM, 1% DMSO:DMEM) after pre-treatment with NEM (1 mM). Data are presented as mean values ± SD (n = 12 biologically independent samples)

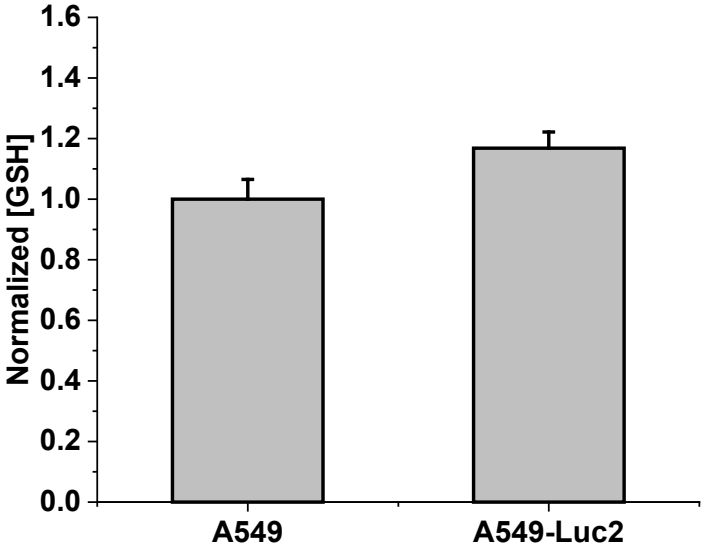

Supplementary Figure 38. Normalized [GSH] for A549 and A549-Luc2 cells measured using the Ellman's assay. Data are presented as mean values ± SD (n = 2 biologically independent samples).

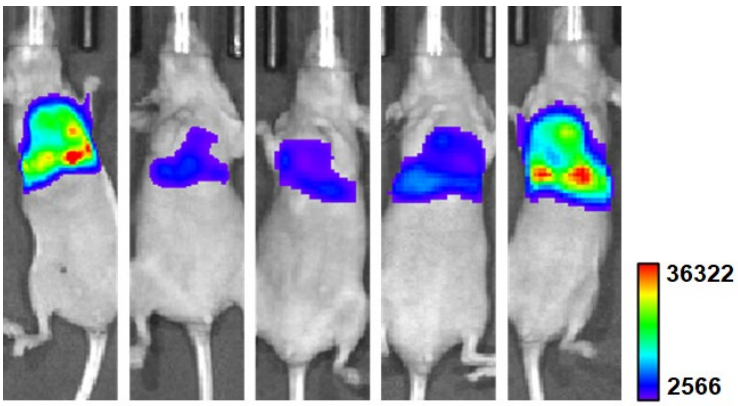

Supplementary Figure 39. Bioluminescence images of luciferase expressing A549 orthotopic xenografts 15 minutes post-IP injection of 150 mg/kg D-Luciferin. Xenografts generated by intrapleural injections.

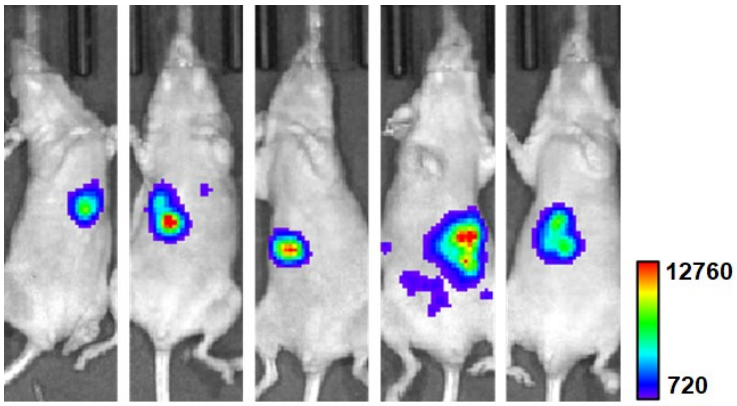

Supplementary Figure 40. Bioluminescence images of luciferase expressing A549 orthotopic xenografts 15 minutes post-IP injection of 150 mg/kg D-Luciferin. Xenografts generated by intrahepatic injections.

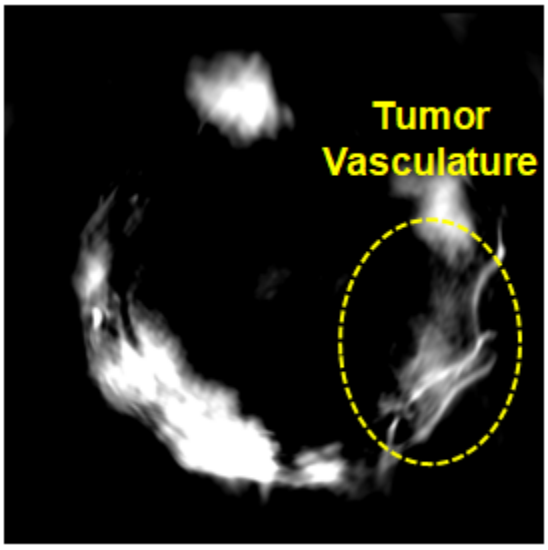

Supplementary Figure 41. Representative PA image of tumor vasculature in orthotopic lung cancer model generated via intrapleural injection.

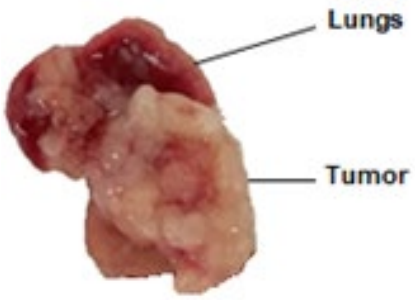

Supplementary Figure 42. Photograph of tumor after dissection from an orthotopic lung cancer model generated via intrapleural injection.

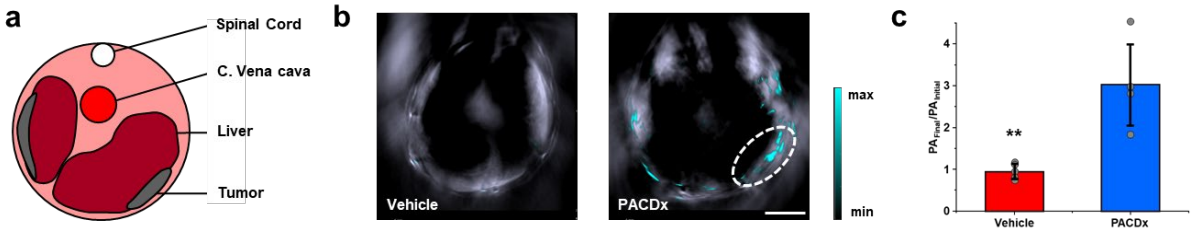

Supplementary Figure 43. a. Schematic of imaging field of view. b. Representative spectrally unmixed PA images of the liver after retro-orbital injection of vehicle or PACDx (400μM, 150 μL, 10% DMSO in saline) into a A549-Luc2 intrahepatic model. ROI is indicated by white dashed oval. Scale bar represents 5 mm. c. PA turn-on after retro-orbital injection of vehicle or PACDx (400 μM). Data are presented as mean values ± SD (n = 5 independent animals). Statisitical analysis was perfromed using a two-tailed Mann-Whitney U test, **: $P = 0.007$.

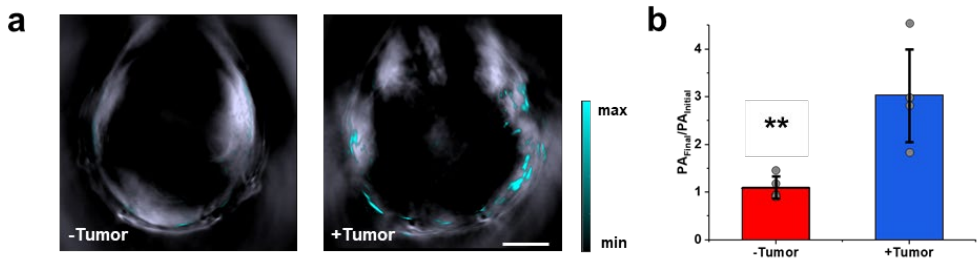

Supplementary Figure 44. a. Representative spectrally unmixed PA images of the liver after retro-orbital injection of PACDx (400μM, 150 μL, 10% DMSO in saline) into a healthy control mouse or A549-Luc2 intrahepatic model. Scale bar represents 5 mm. b. PA turn-on after retro-orbital injection of PACDx (400 μM). Data are presented as mean values ± SD (n = 5 independent animals). Statisitical analysis was perfromed using a two-tailed Mann-Whitney U test, **: P = 0.007.

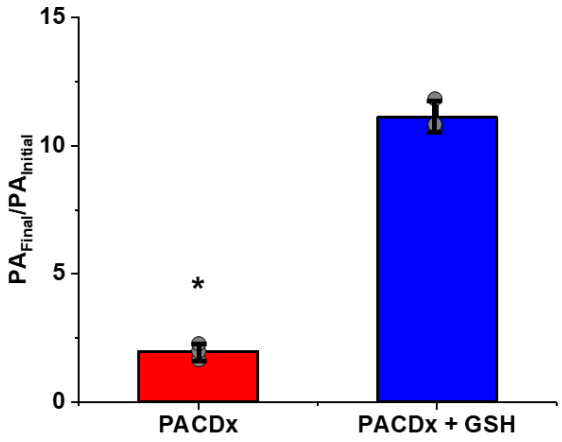

Supplementary Figure 45. PA turn-on after intratumoral injection of PACDx (100 μM) in 4T1 allografts treated with 0 mM GSH or 10 mM GSH. Data are presented as mean values ± SD (n = 3 independent animals). Statisitical analysis was perfromed using a two-tailed Kruskall Wallis test ($\alpha = 0.05$), *: $P < 0.05$.

	2,4-dinitro (2)	p-nitro (5)	4-trifluoromethyl-2-nitro (3)	2-fluoro-4-nitro (PACDx)
$\Delta H^{\ddagger}$ (kJ/mol)	39.20699	34.28949	48.78939	70.46077
$\Delta S^{\ddagger}$ (J/mol)	-204.957	-245.904	-180.926	-117.117
$\Delta G^{\ddagger}$ (kJ/mol)	102.7743	110.5567	104.9035	106.7846

Supplementary Table 1.

Compound	**Ɛ ($M^{-1}cm^{-1}$)**
PACDx (activated)	79,000
HbO_2	276
Hb	2,052

Supplementary Table 2.

Compound 7: ^{1}H NMR (500 MHz, $CDCl_3$)

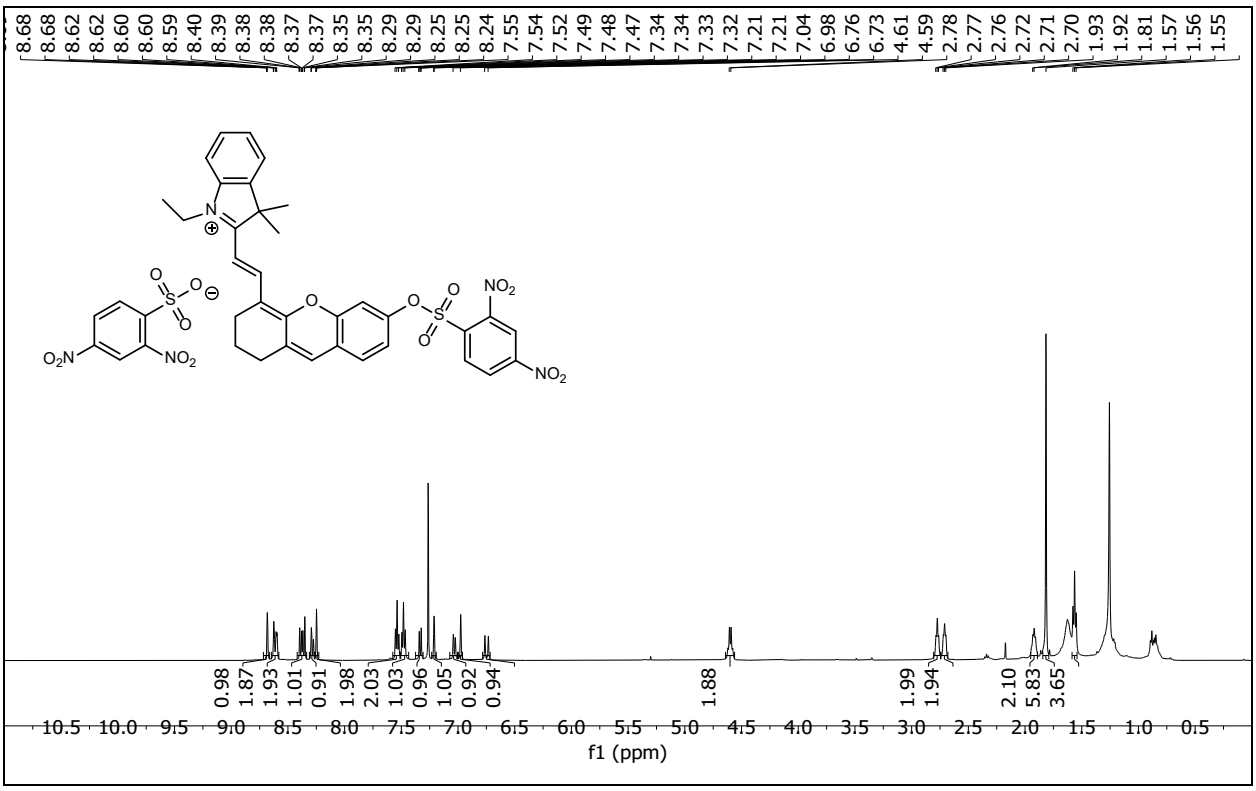

Compound 7: ^{13}C NMR (125 MHz, $CDCl_3$)

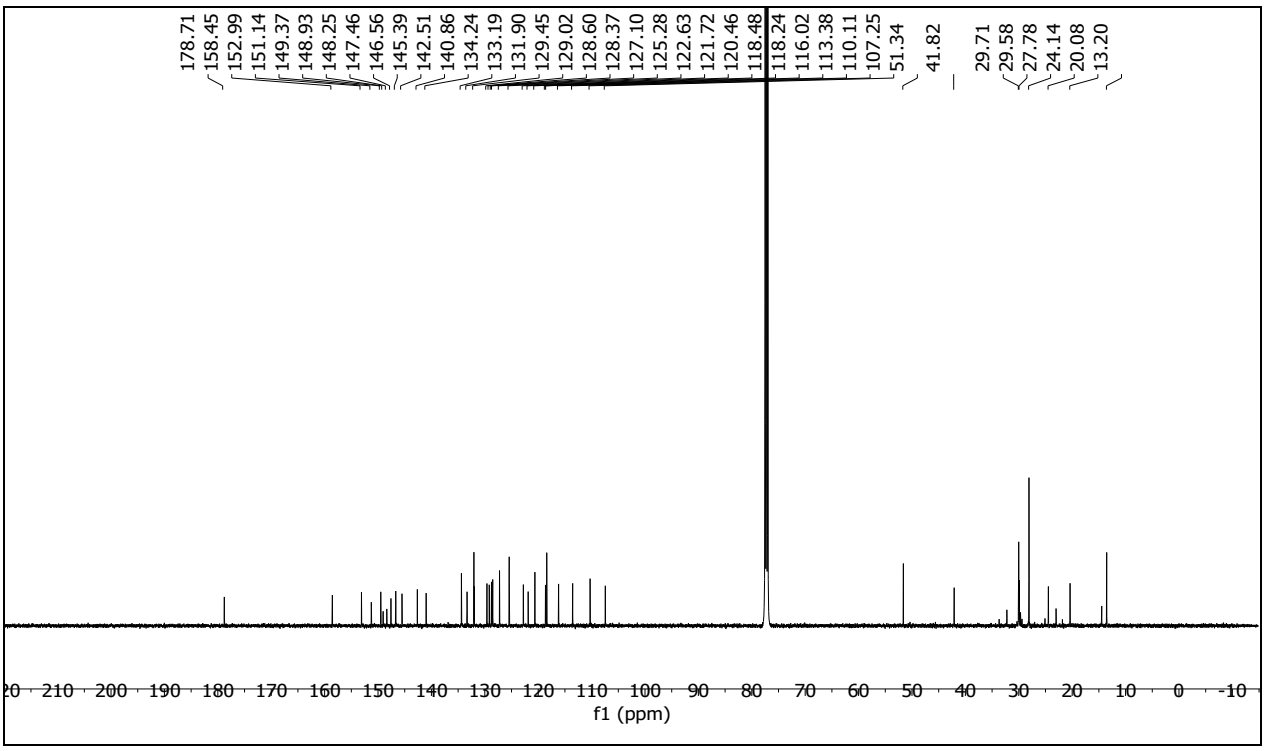

Compound 8: ^{1}H NMR (500 MHz, $CDCl_3$)

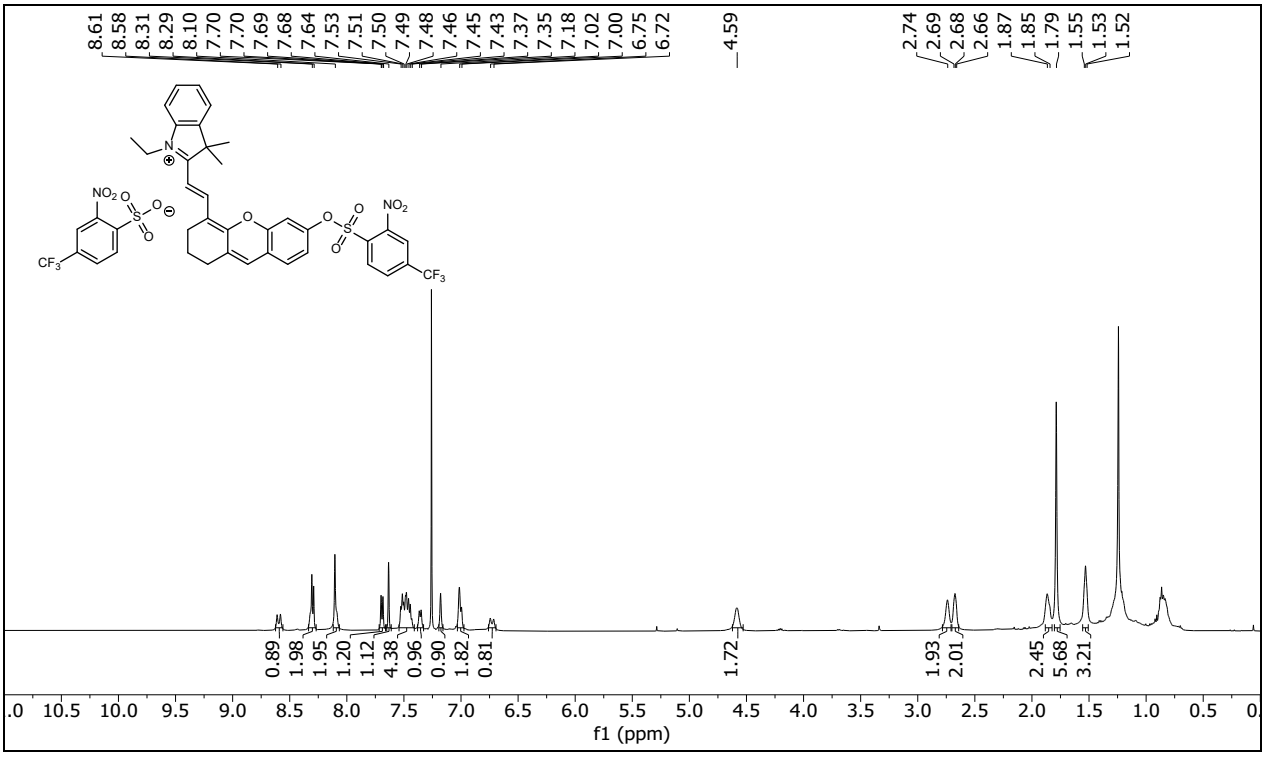

Compound 8: ^{13}C NMR (125 MHz, $CDCl_3$)

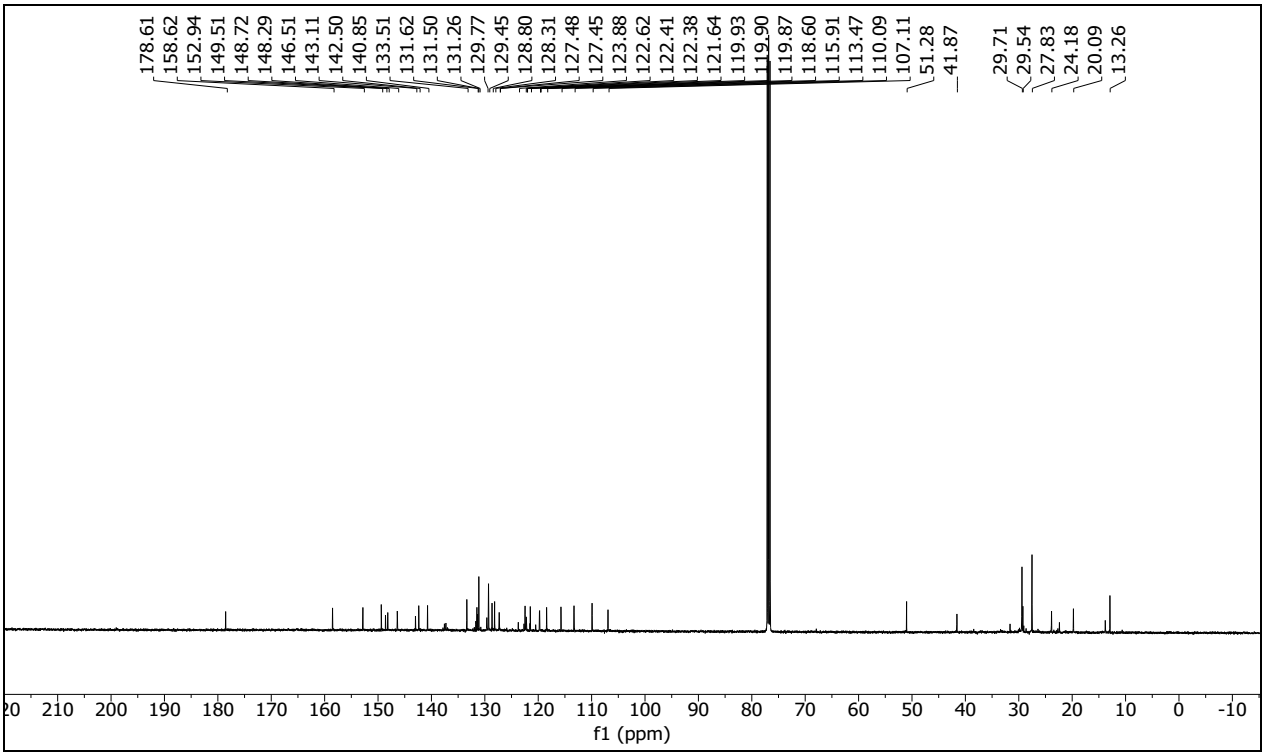

Compound 9: ^{1}H NMR (500 MHz, $CDCl_3$)

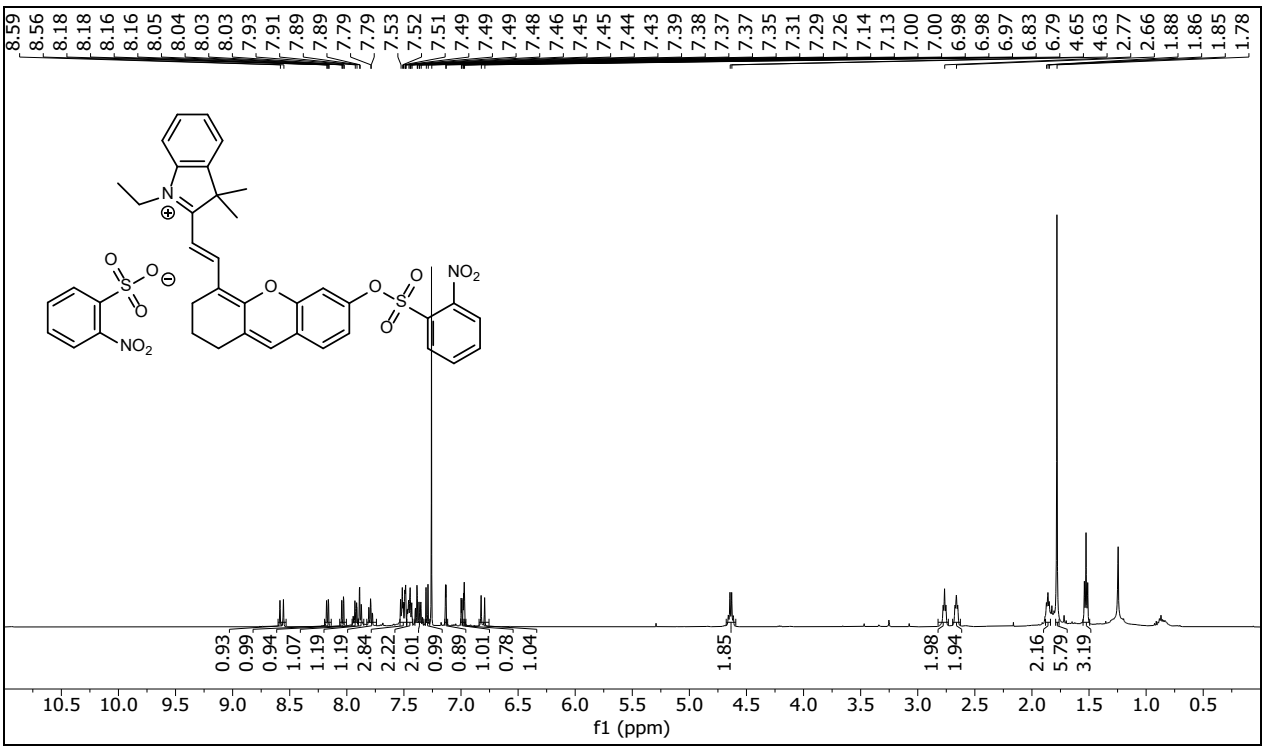

Compound 9: ^{13}C NMR (125 MHz, $CDCl_3$)

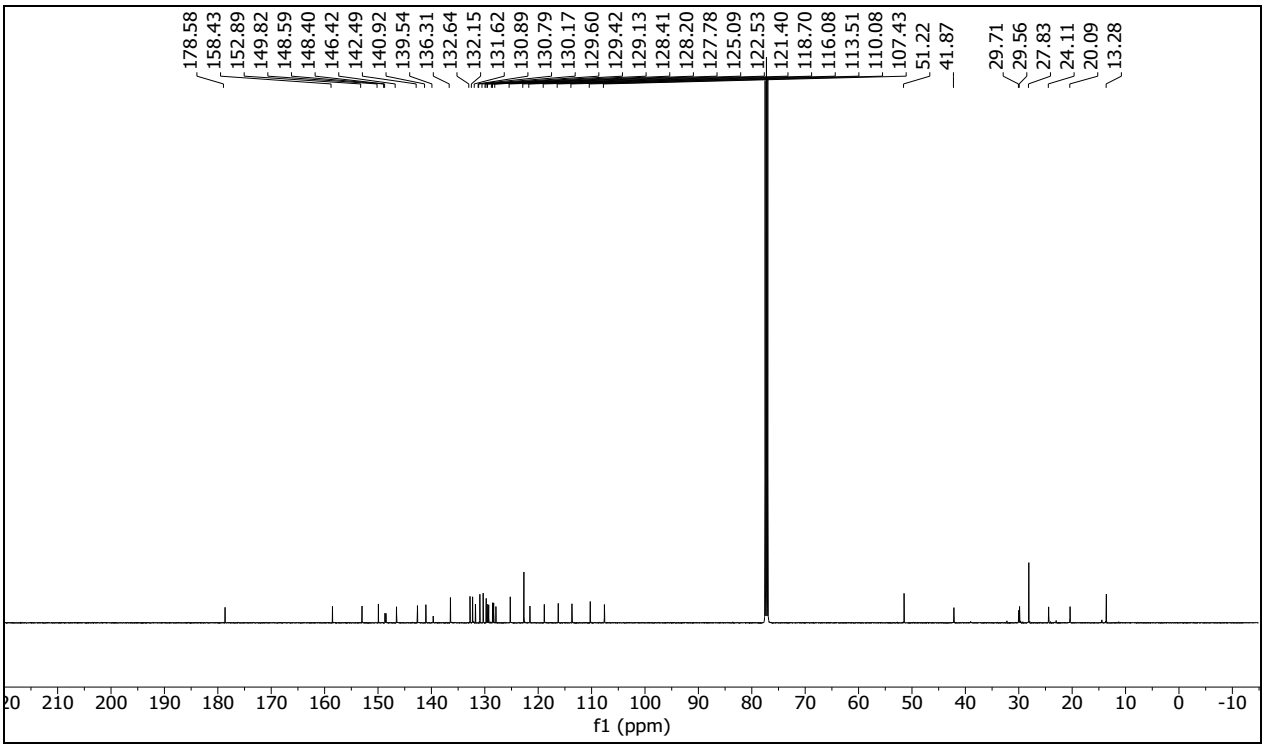

Compound 10: ^{1}H NMR (500 MHz, $CDCl_3$)

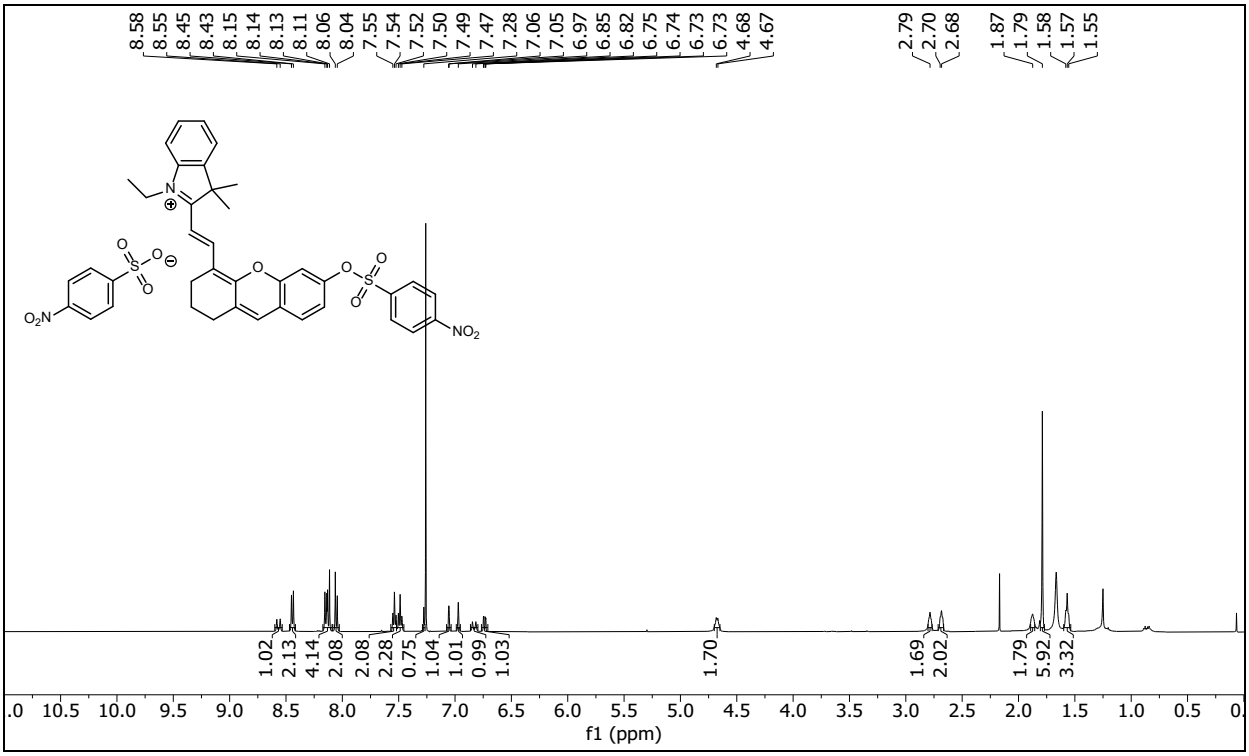

Compound 10: ^{13}C NMR (125 MHz, $CDCl_3$)

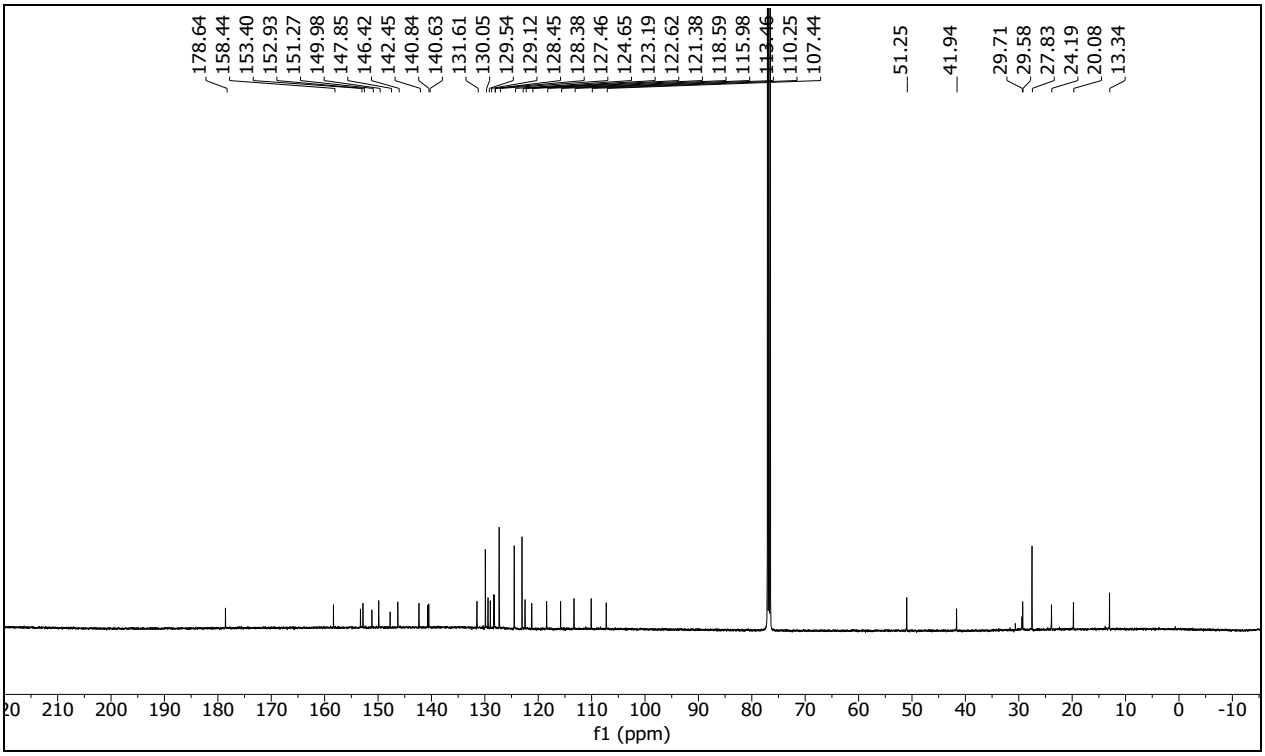

Compound 11: ^{1}H NMR (500 MHz, $CDCl_3$)

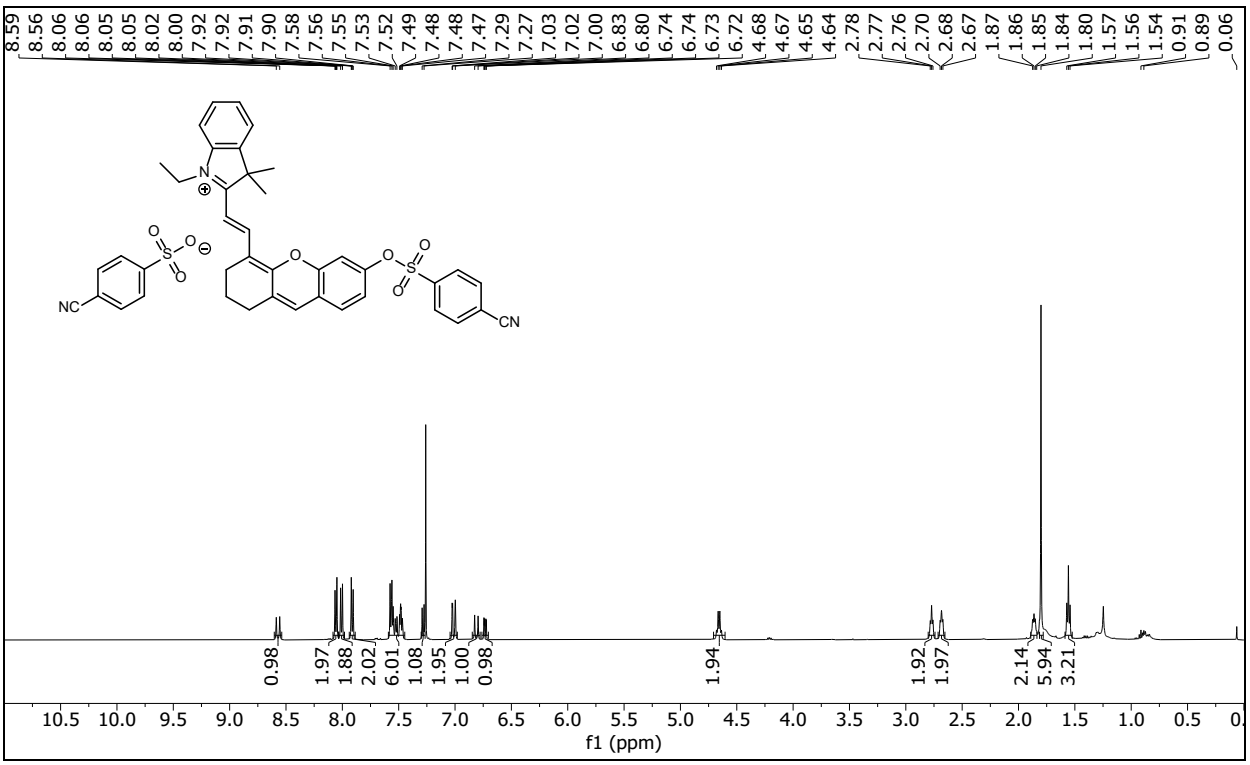

Compound 11: ^{13}C NMR (125 MHz, $CDCl_3$)

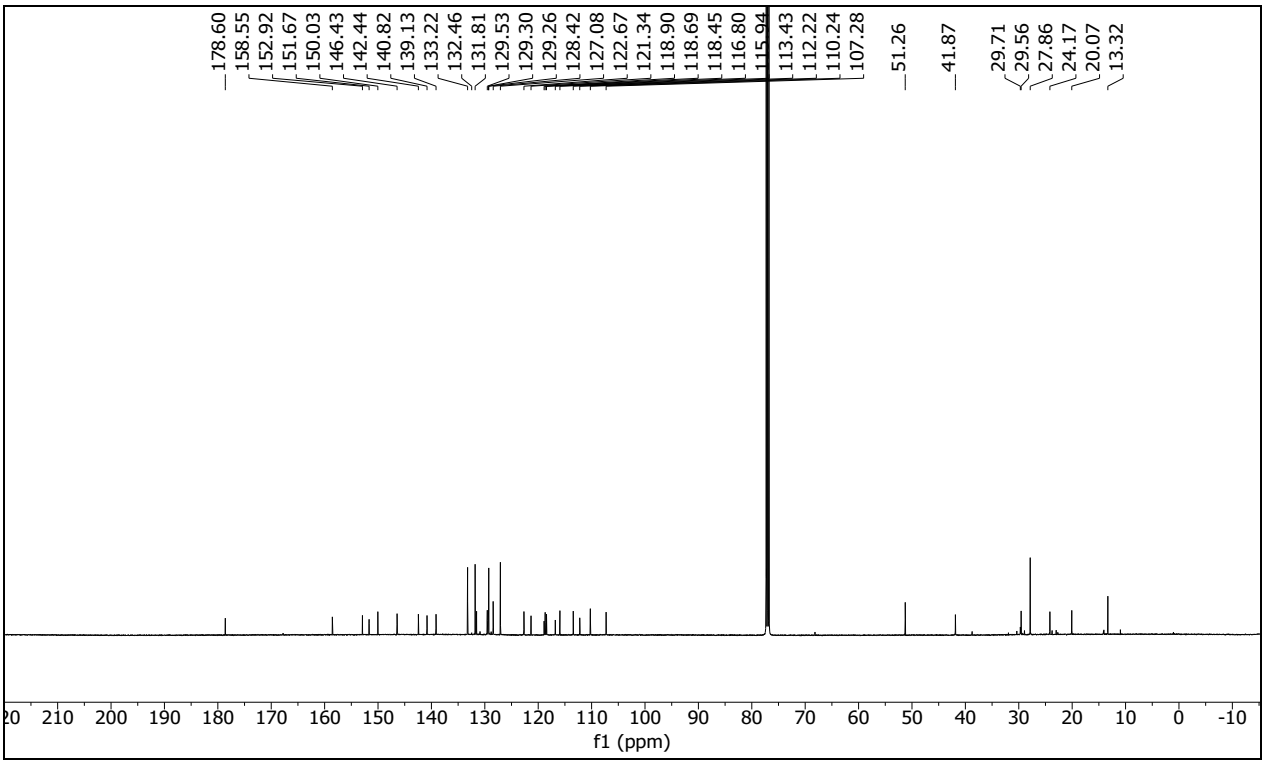

Compound 12: ^{1}H NMR (500 MHz, $CDCl_3$)

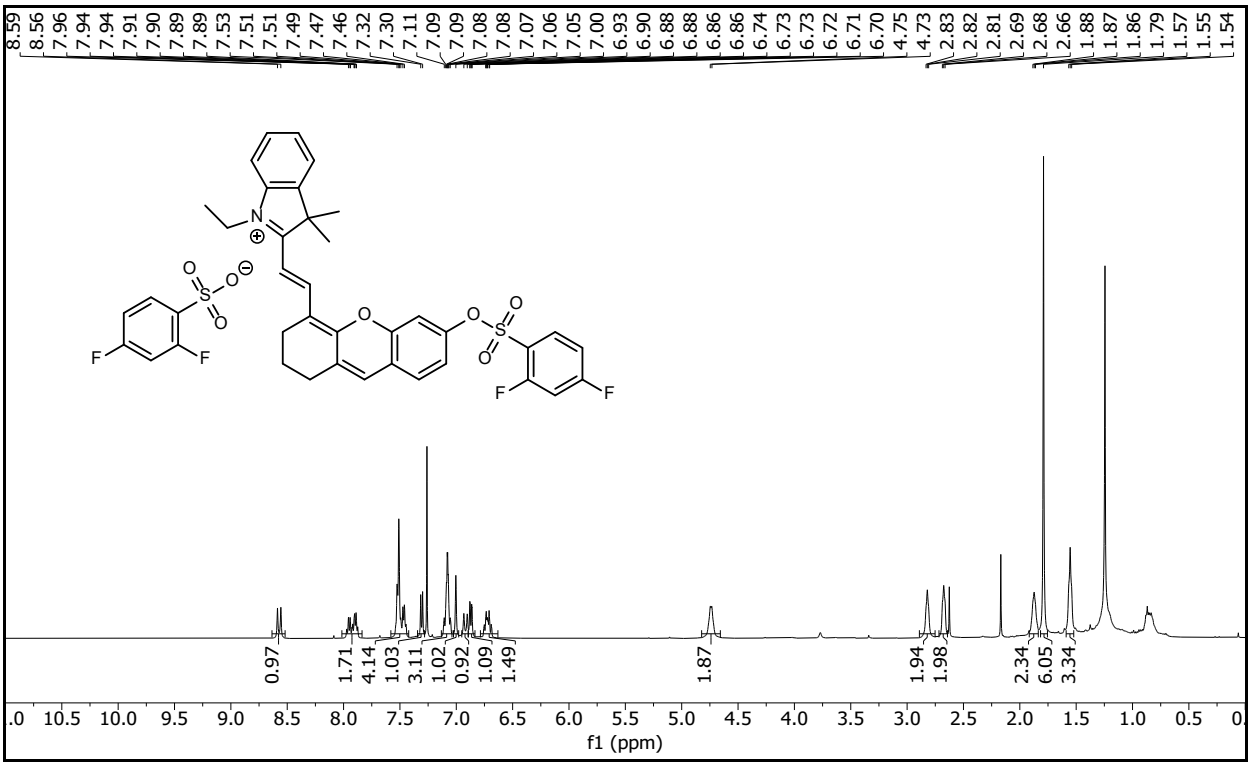

Compound 12: ^{13}C NMR (125 MHz, $CDCl_3$)

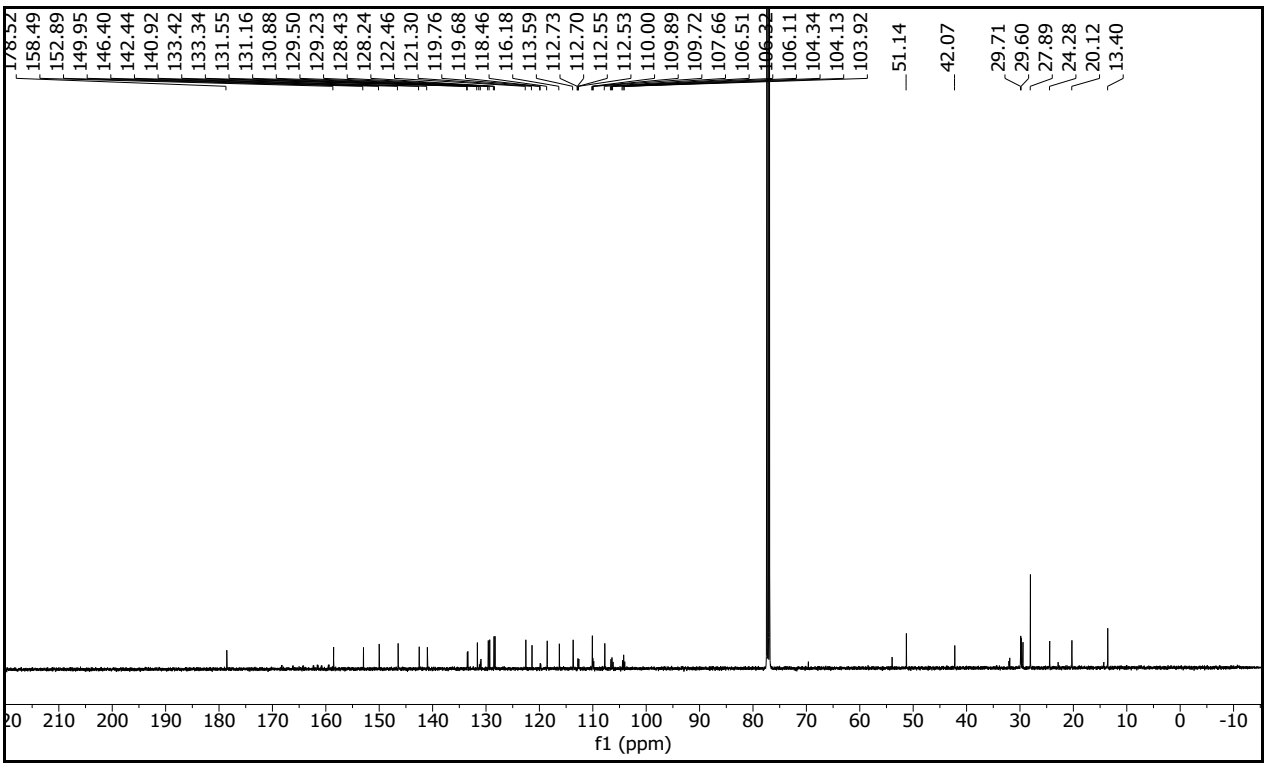

Compound 13: ^{1}H NMR (500 MHz, $CDCl_3$)

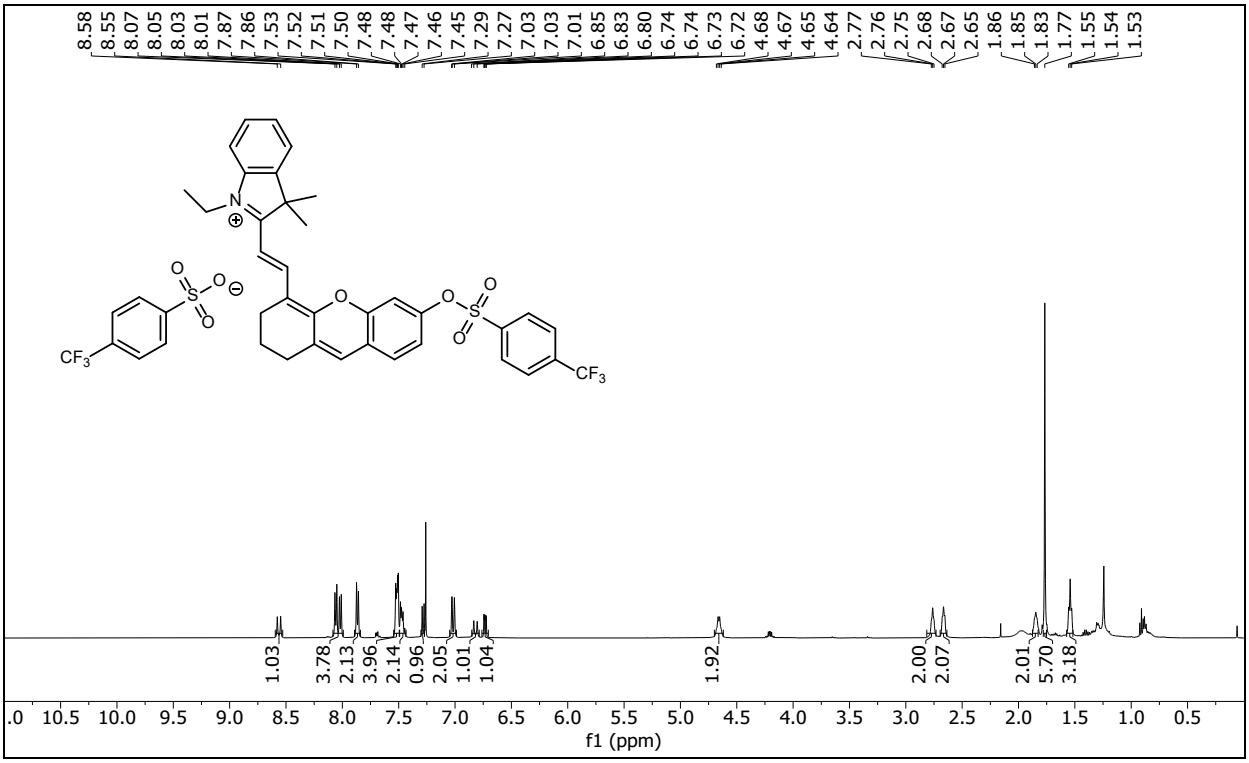

Compound 13: ^{13}C NMR (125 MHz, $CDCl_3$)

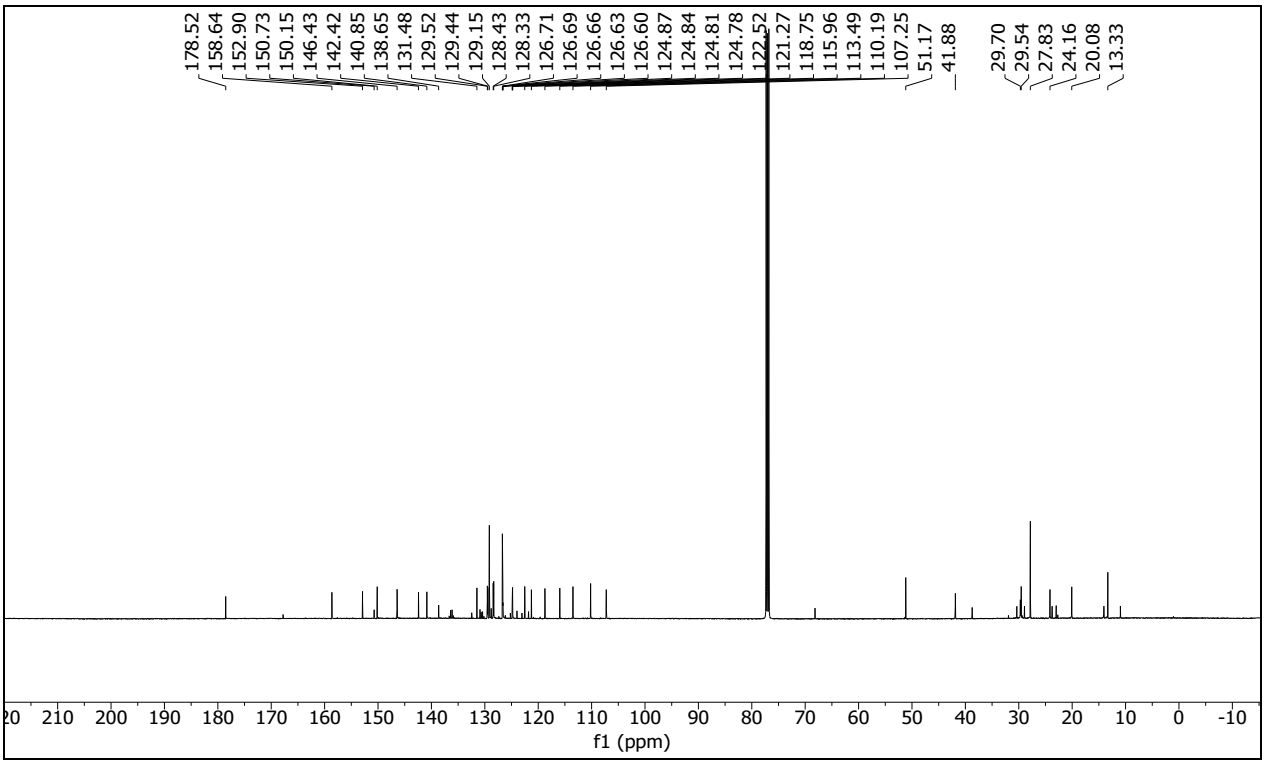

Compound 14: ^{1}H NMR (500 MHz, $CDCl_3$)

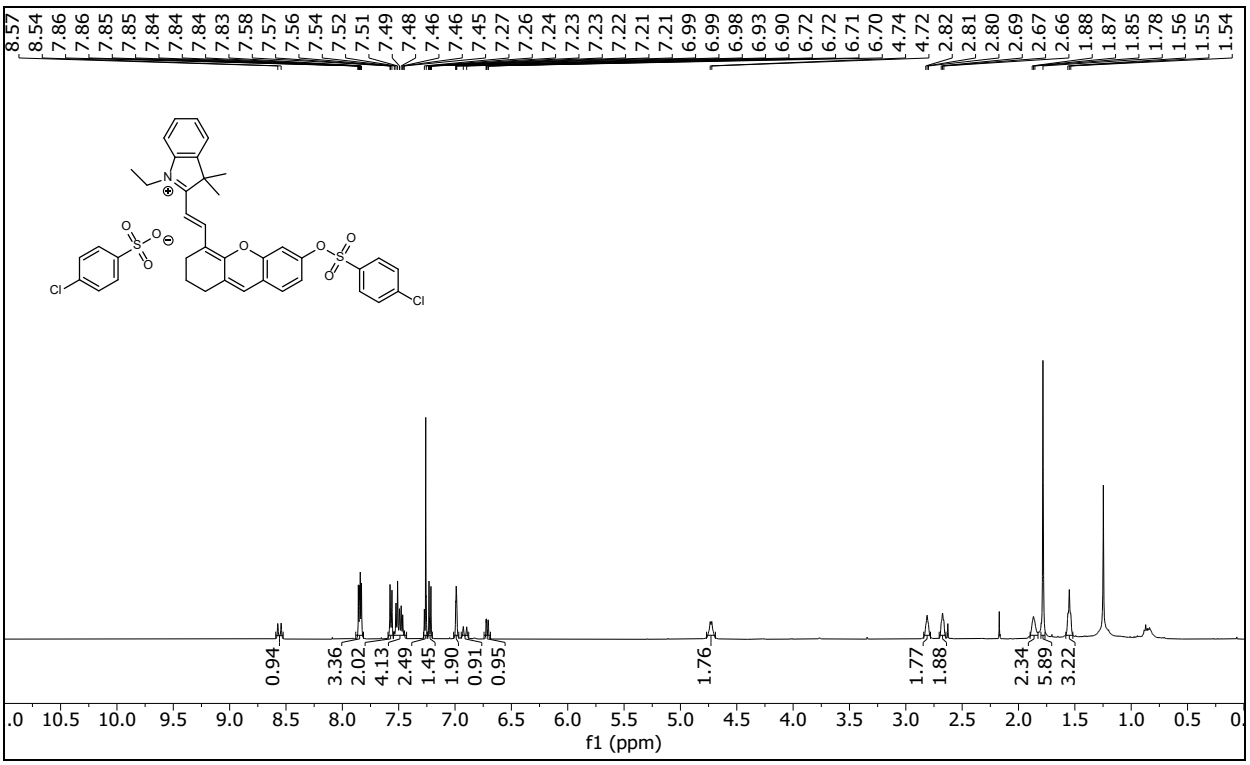

Compound 14: ^{13}C NMR (125 MHz, $CDCl_3$)

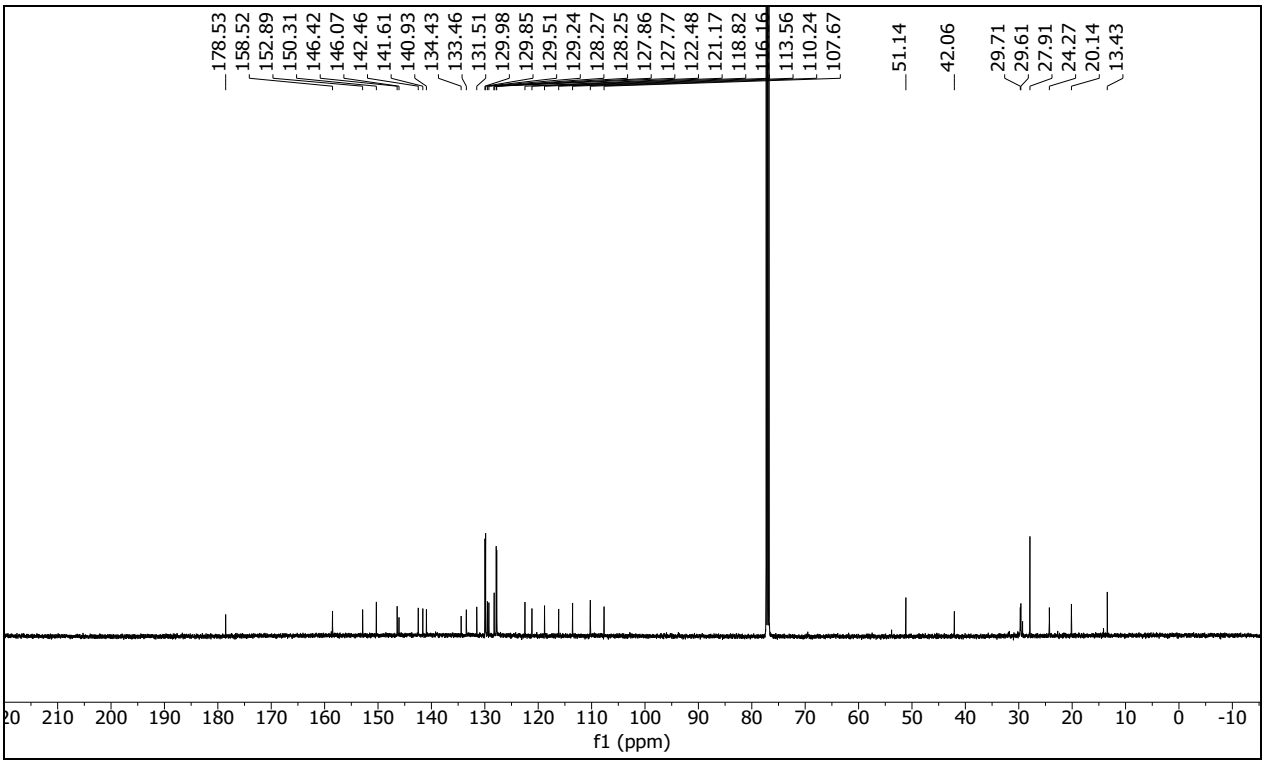

Compound 15: ^{1}H NMR (500 MHz, $CDCl_3$)

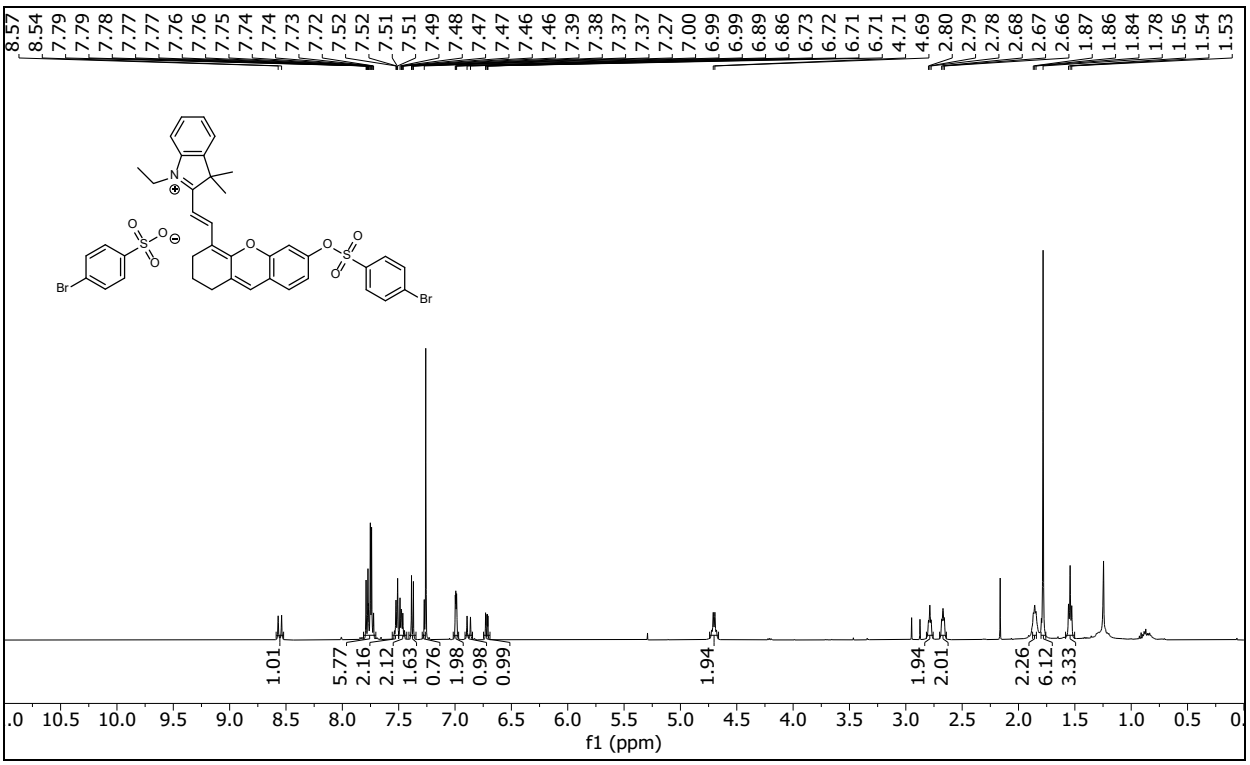

Compound 15: ^{13}C NMR (125 MHz, $CDCl_3$)

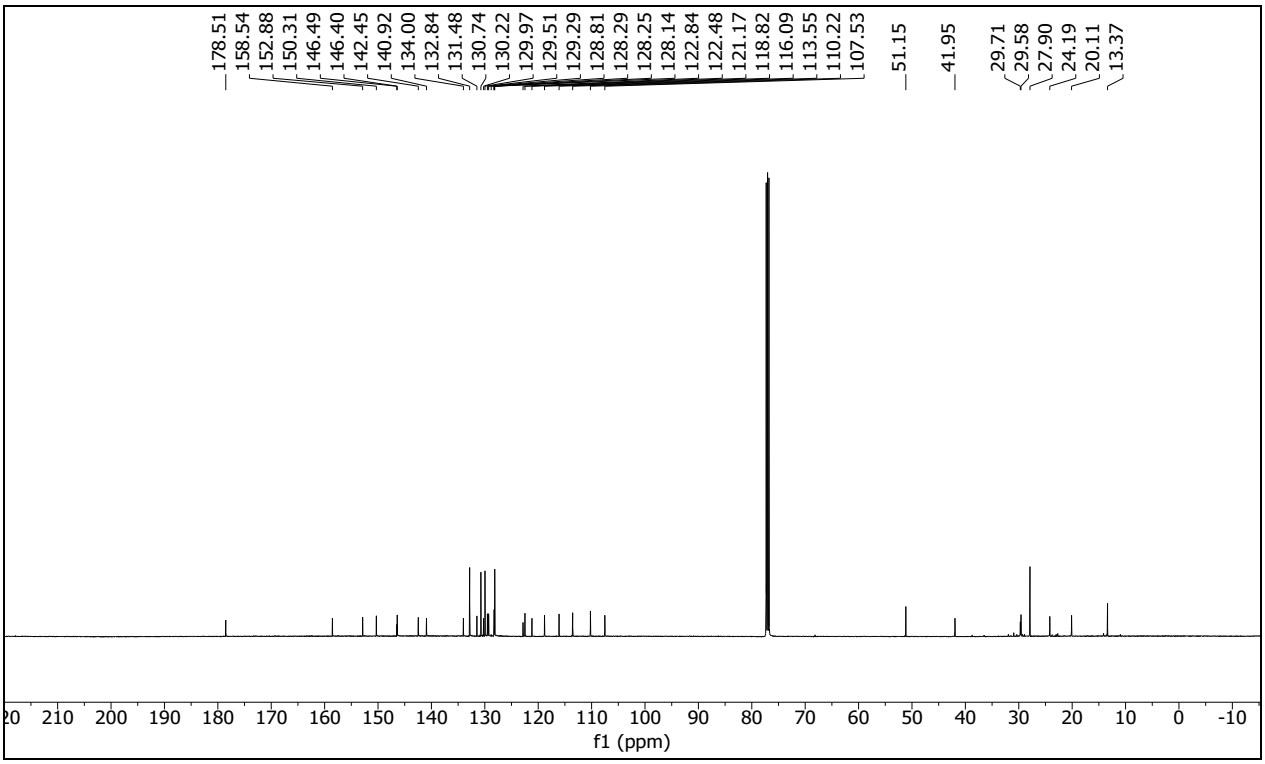

Compound 16: ^{1}H NMR (500 MHz, $CDCl_3$)

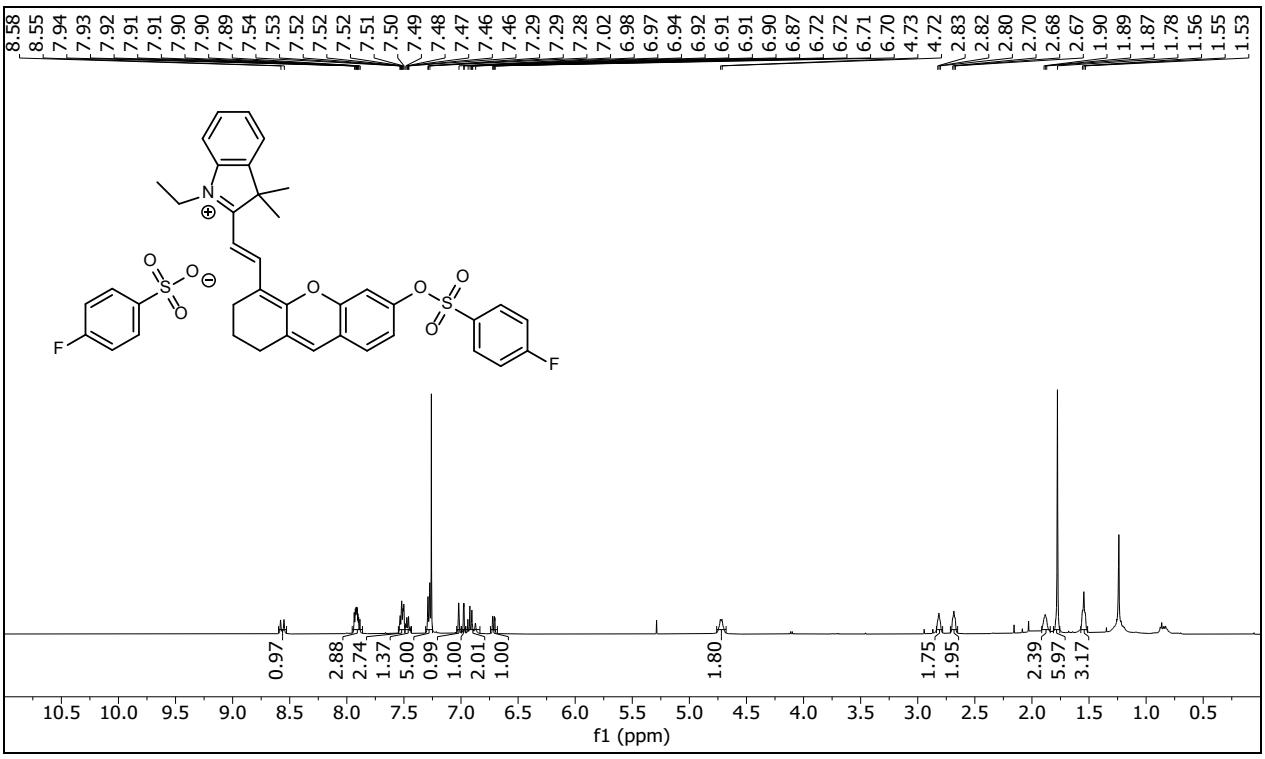

Compound 16: ^{13}C NMR (125 MHz, $CDCl_3$)

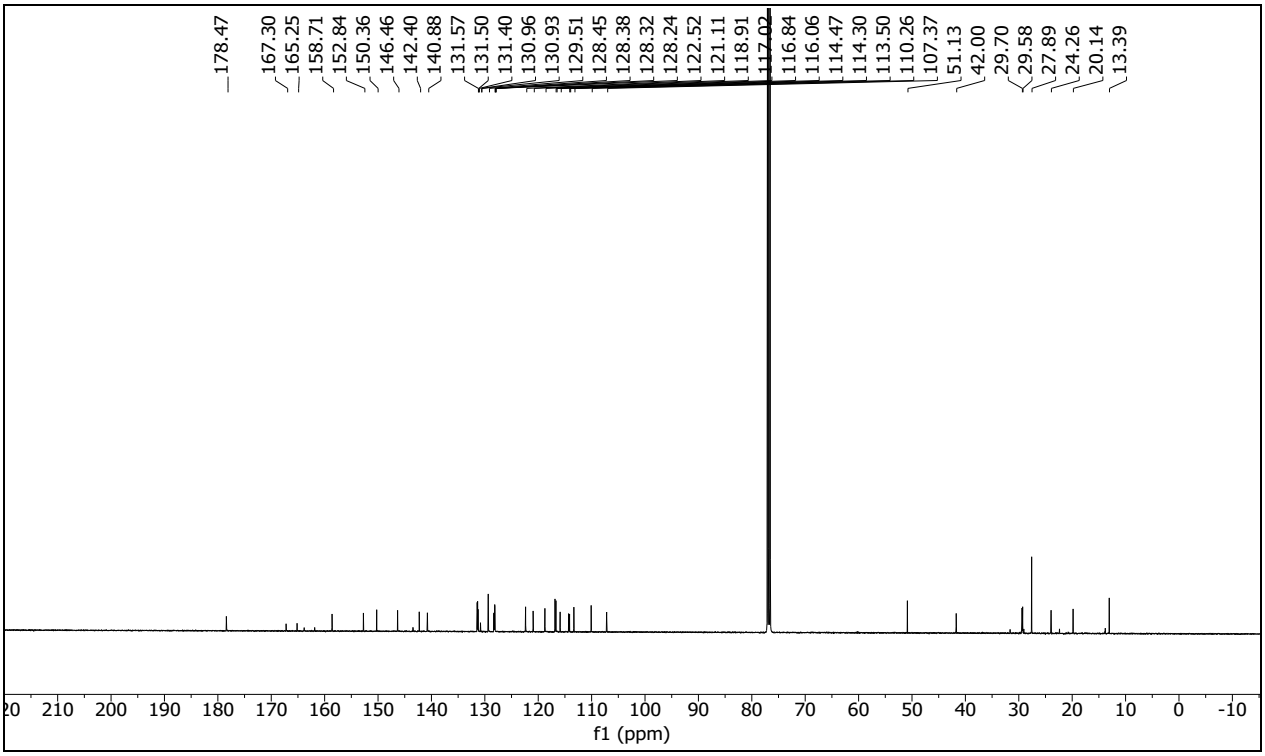

Compound 17: ^{1}H NMR (500 MHz, $CDCl_3$)

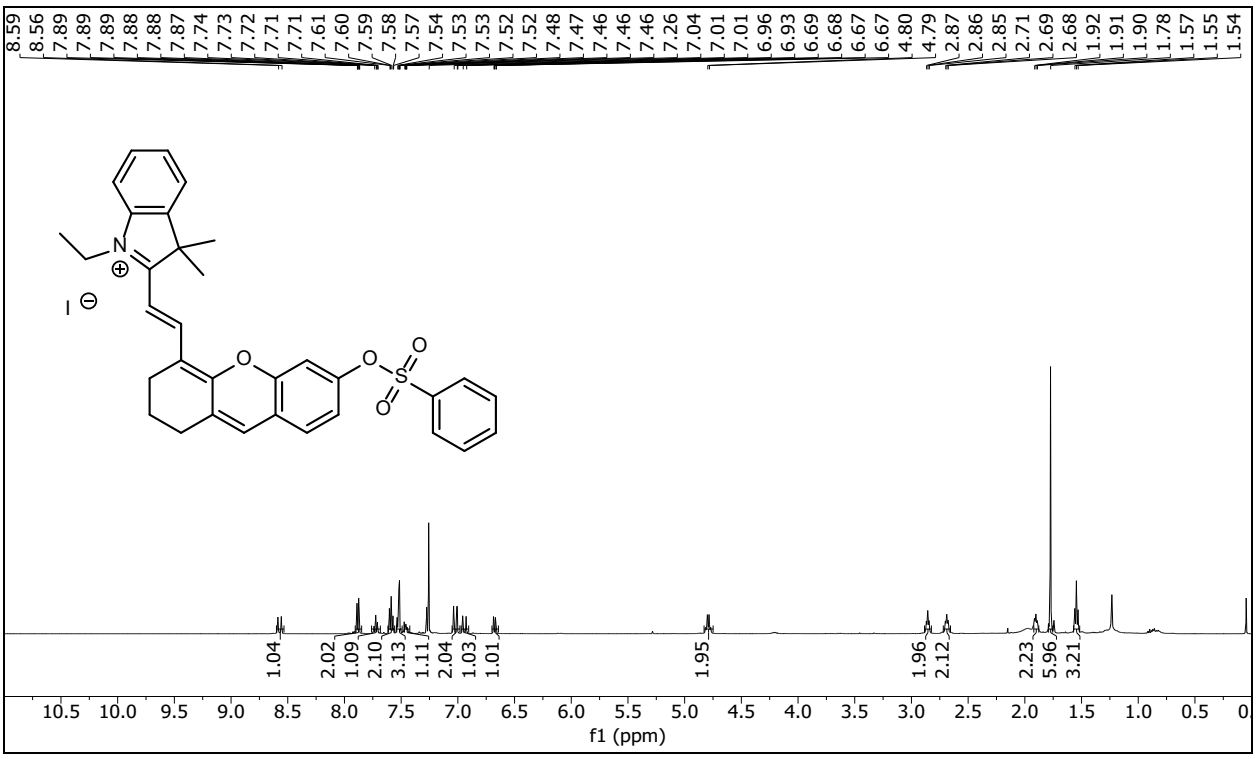

Compound 17: ^{13}C NMR (125 MHz, $CDCl_3$)

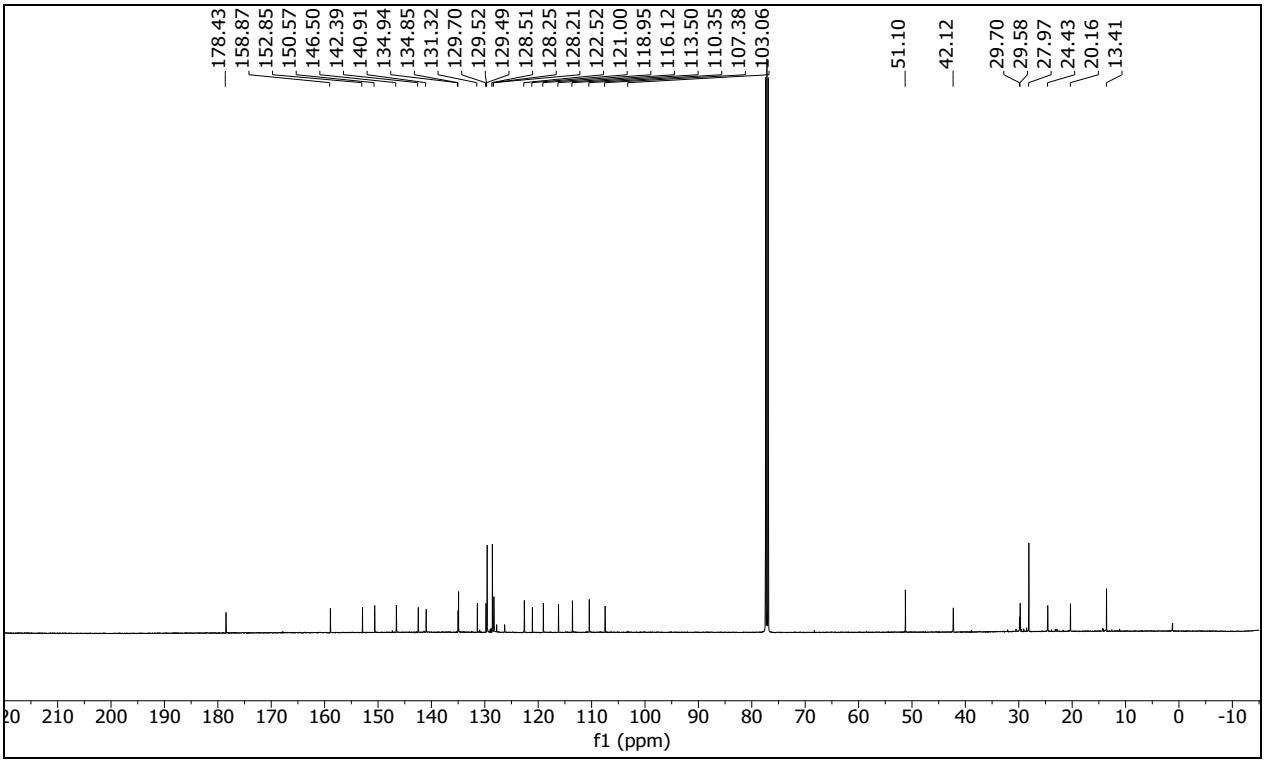

Compound 18: ^{1}H NMR (500 MHz, $CDCl_3$)

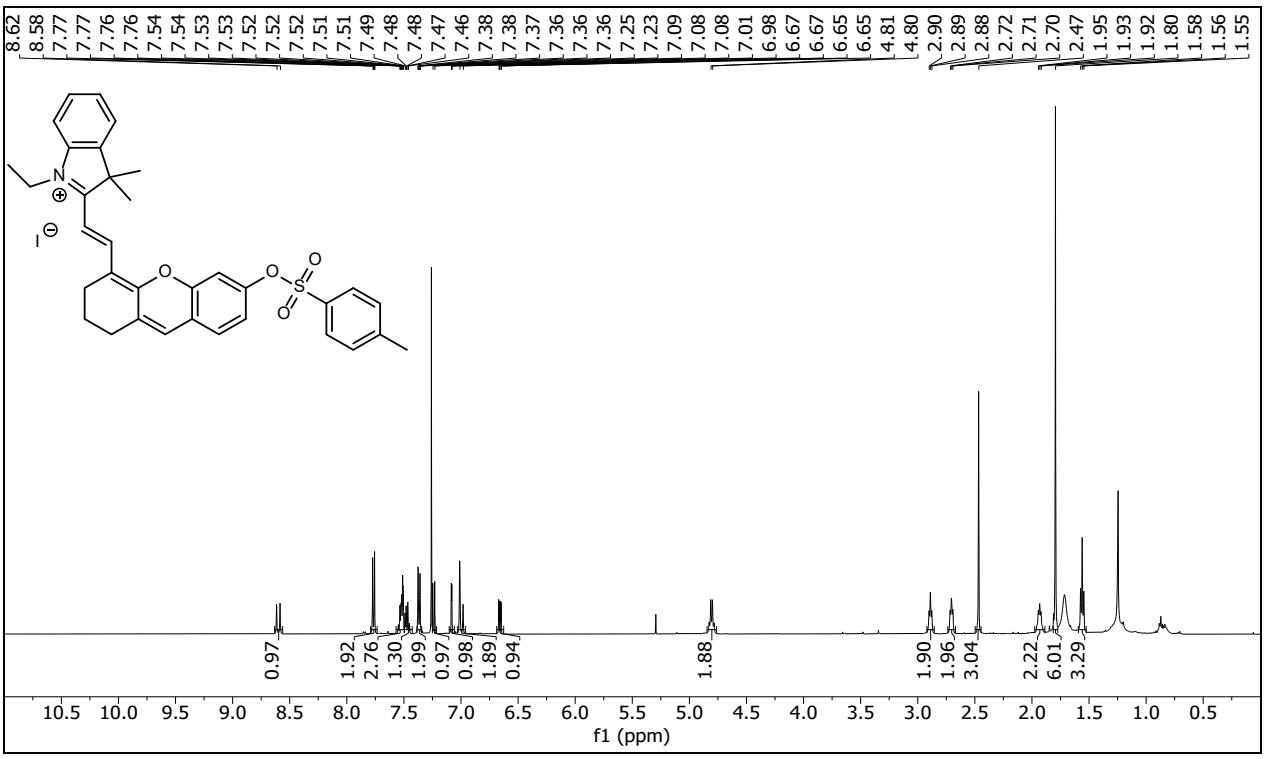

Compound 18: ^{13}C NMR (125 MHz, $CDCl_3$)

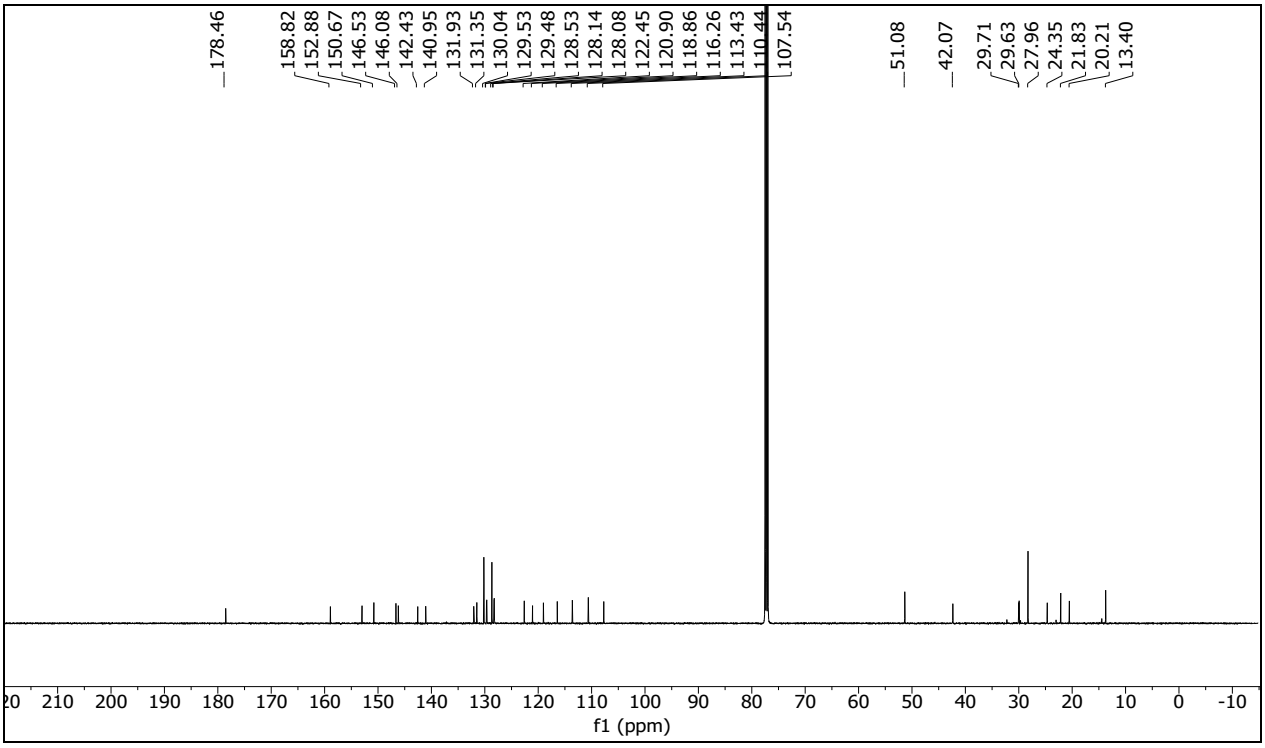

Compound 19: ^{1}H NMR (500 MHz, $CDCl_3$)

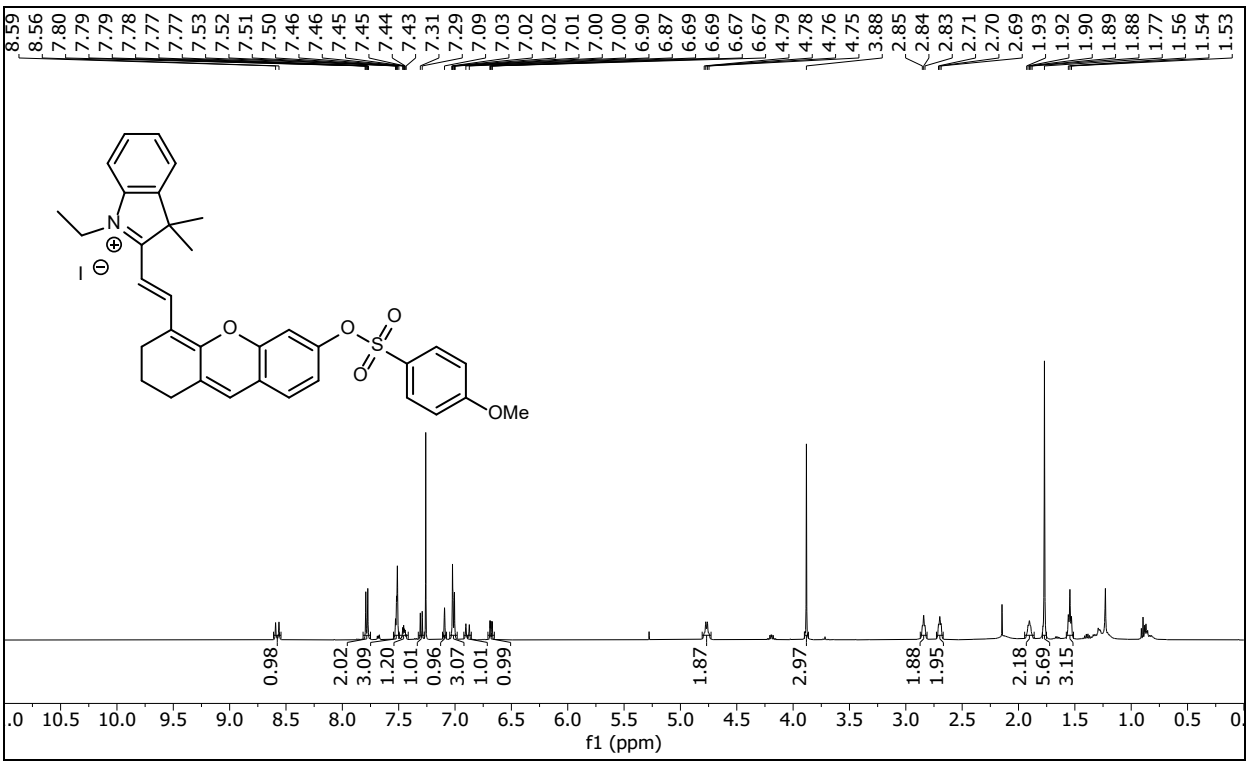

Compound 19: ^{13}C NMR (125 MHz, $CDCl_3$)

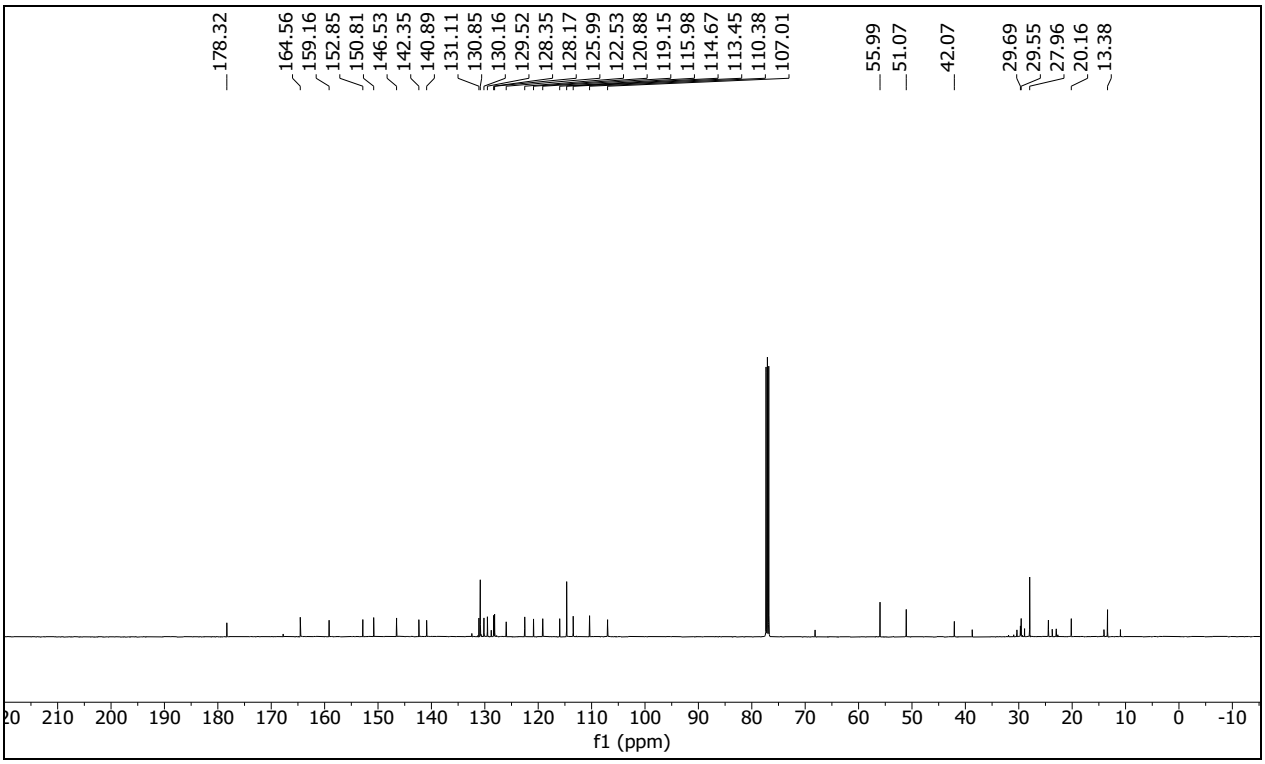

Compound 20: ^{1}H NMR (500 MHz, $CDCl_3$)

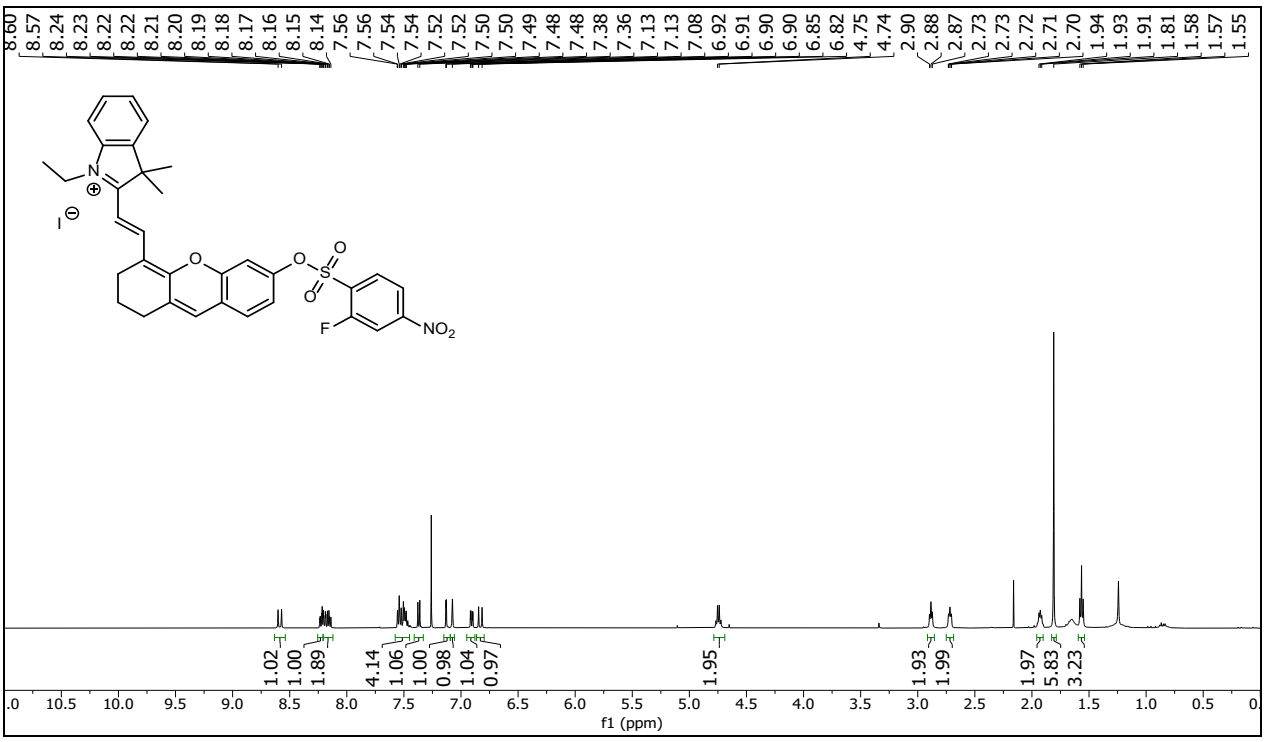

Compound 20: ^{13}C NMR (125 MHz, $CDCl_3$)

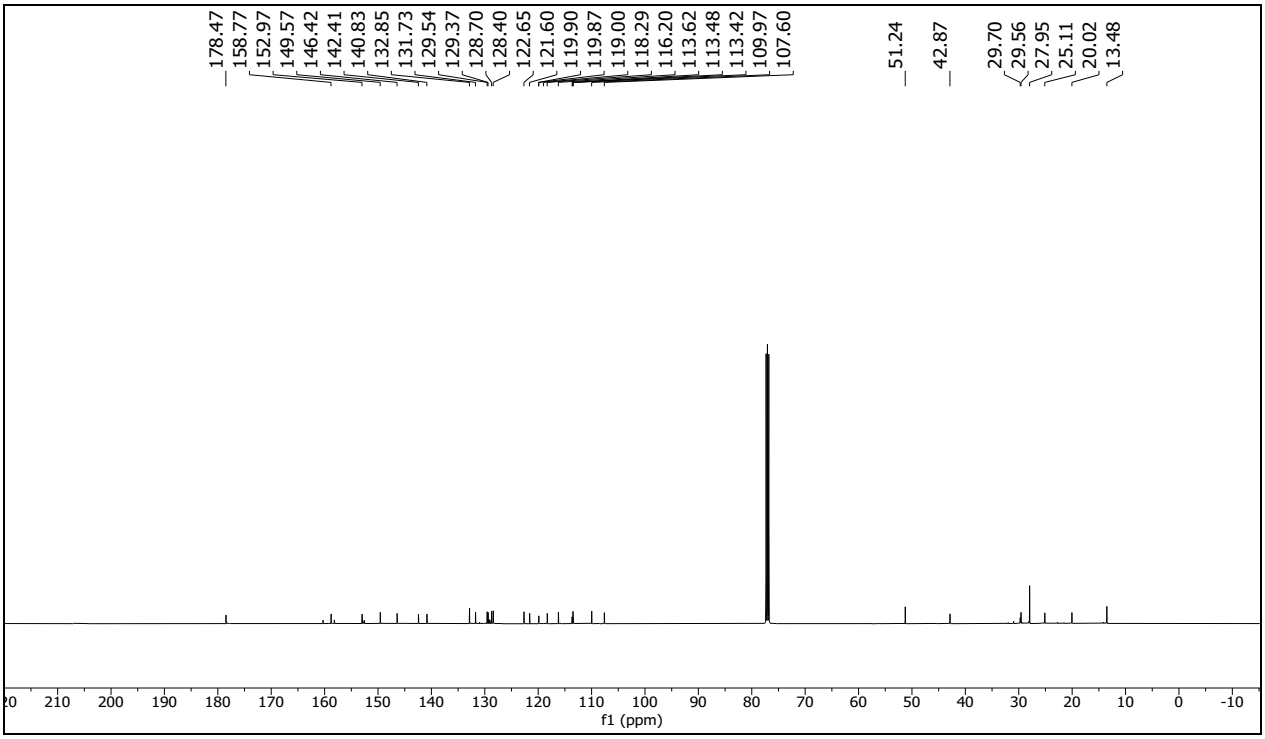

Compound 21: ^{1}H NMR (500 MHz, $CDCl_3$)

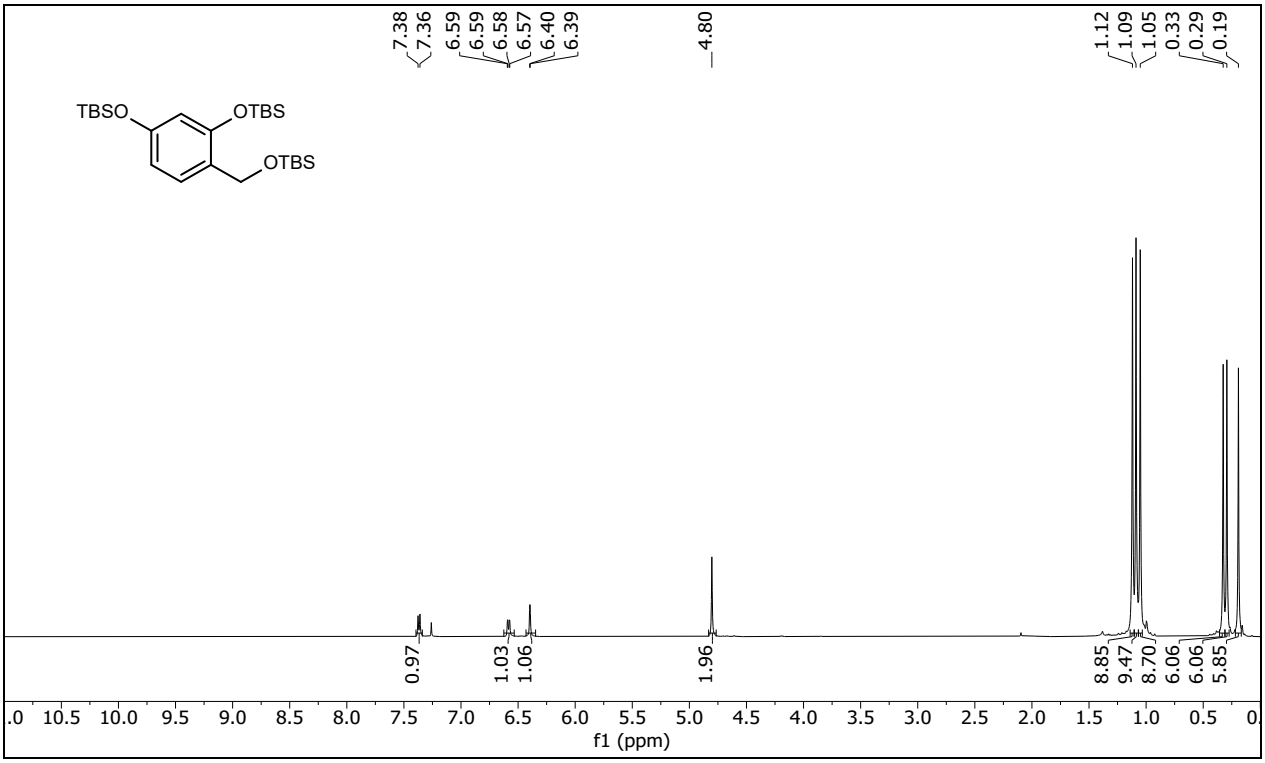

Compound 21: ^{13}C NMR (125 MHz, $CDCl_3$)

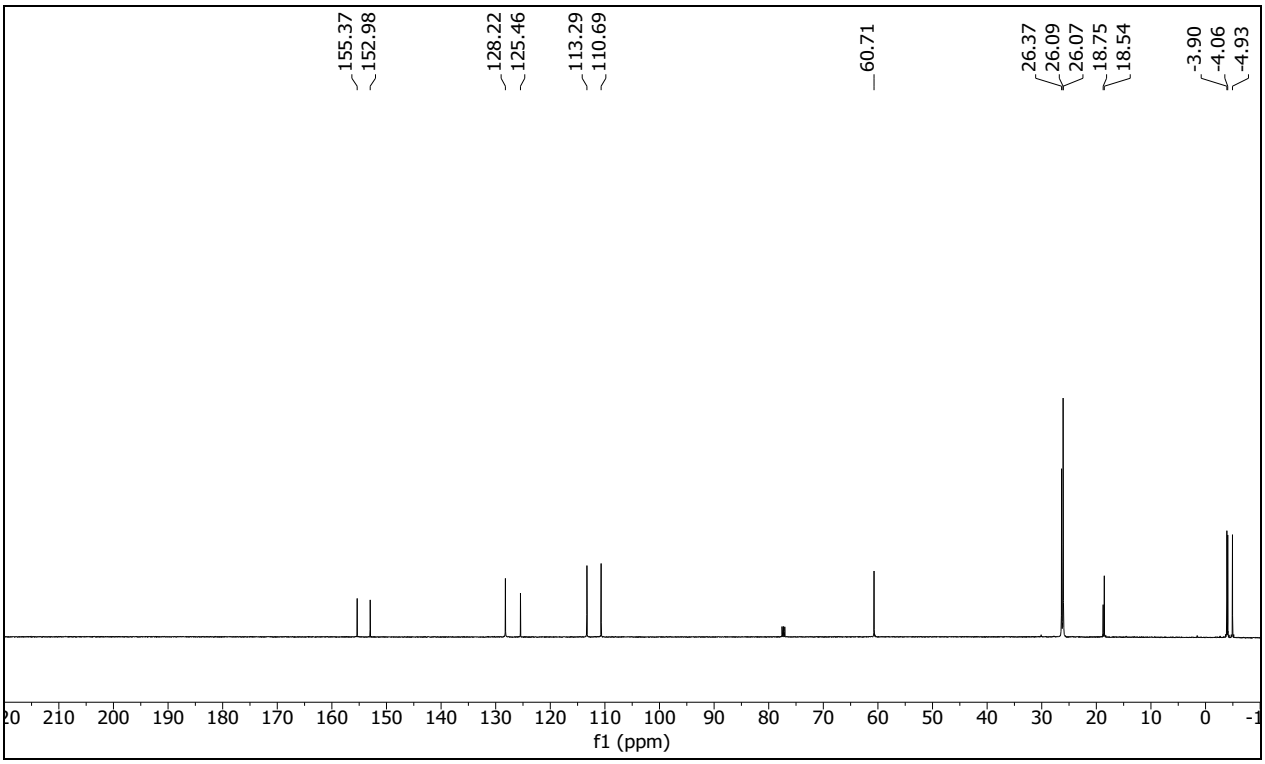

Compound 22: ^{1}H NMR (500 MHz, DMSO-d_6)

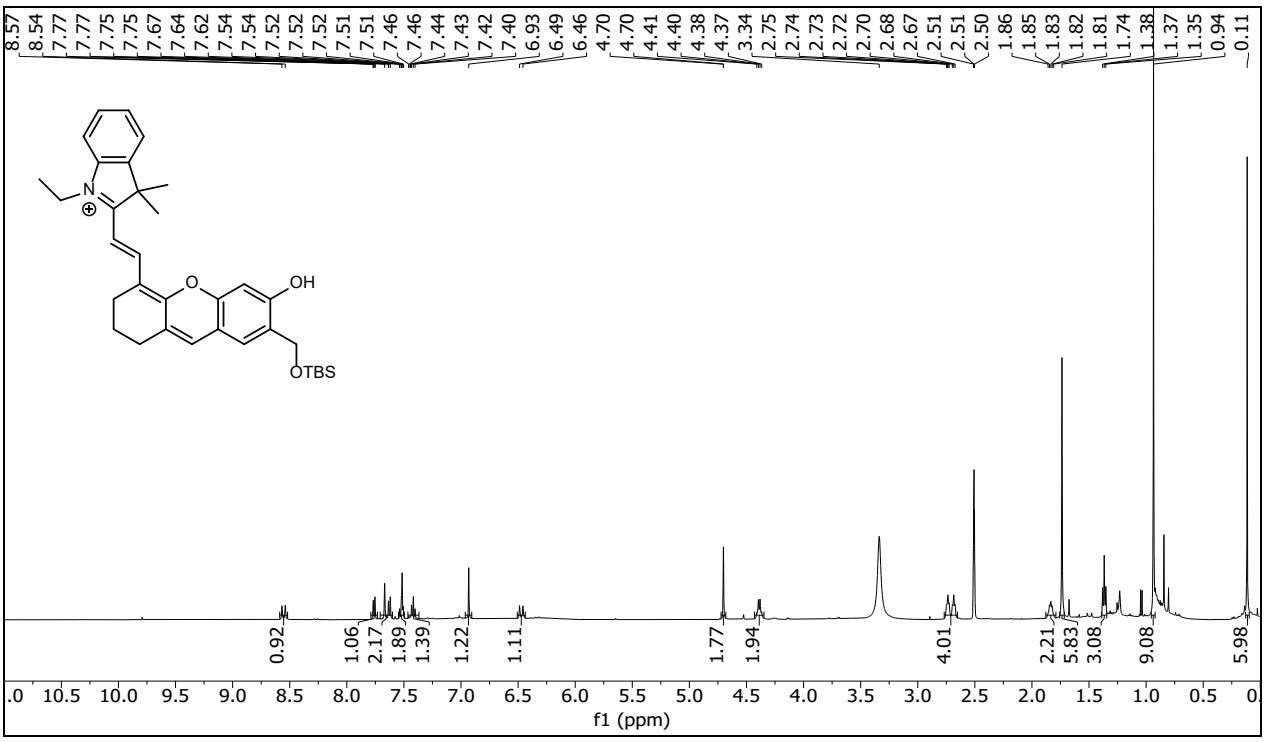

Compound 22: ^{13}C NMR (125 MHz, DMSO-d_6)

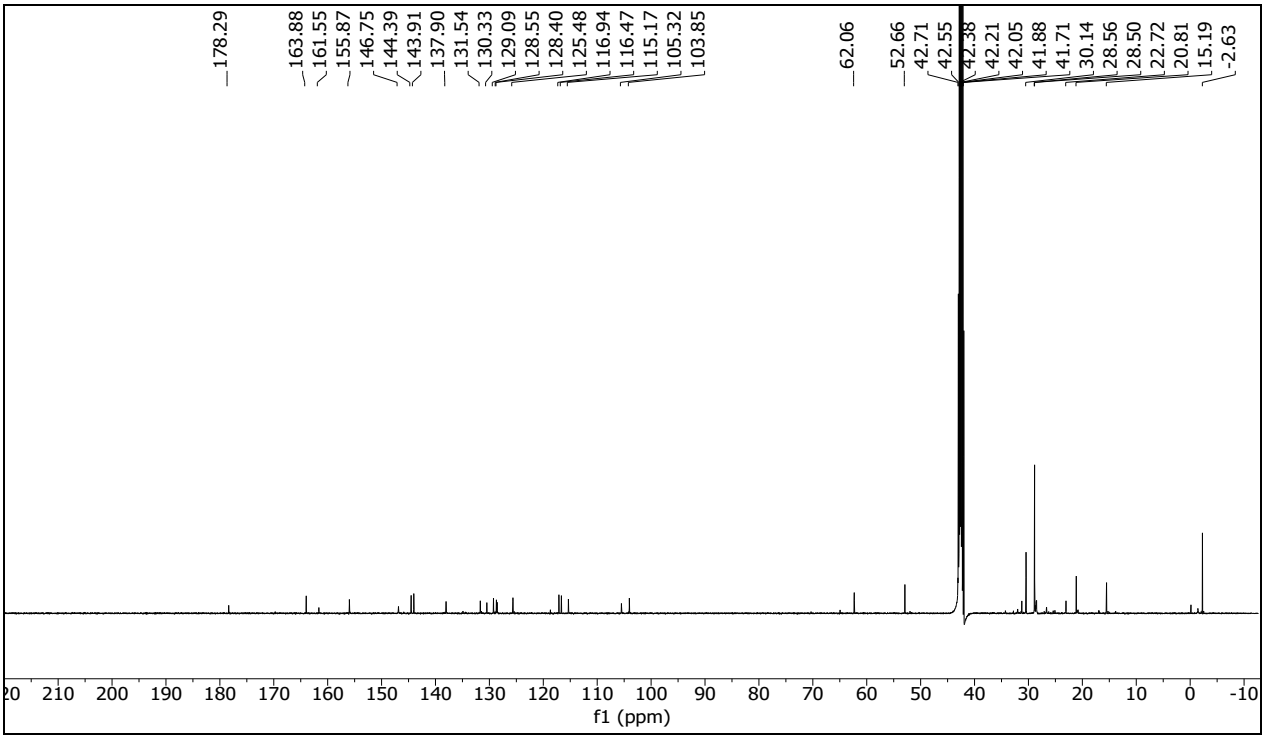

Compound 22-1: ^{1}H NMR (500 MHz, 1:10 CD_3OD:$CDCl_3$)

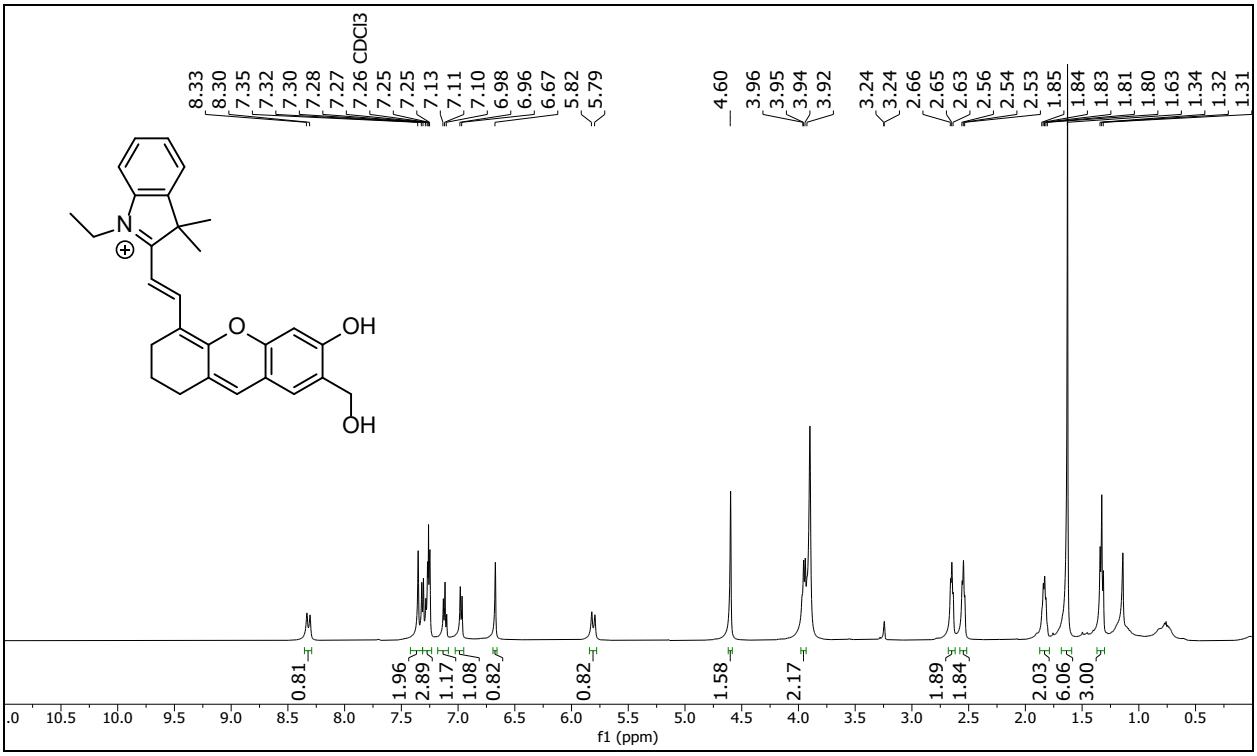

Compound 22-1: ^{13}C NMR (125 MHz, 1:10 CD_3OD:$CDCl_3$)

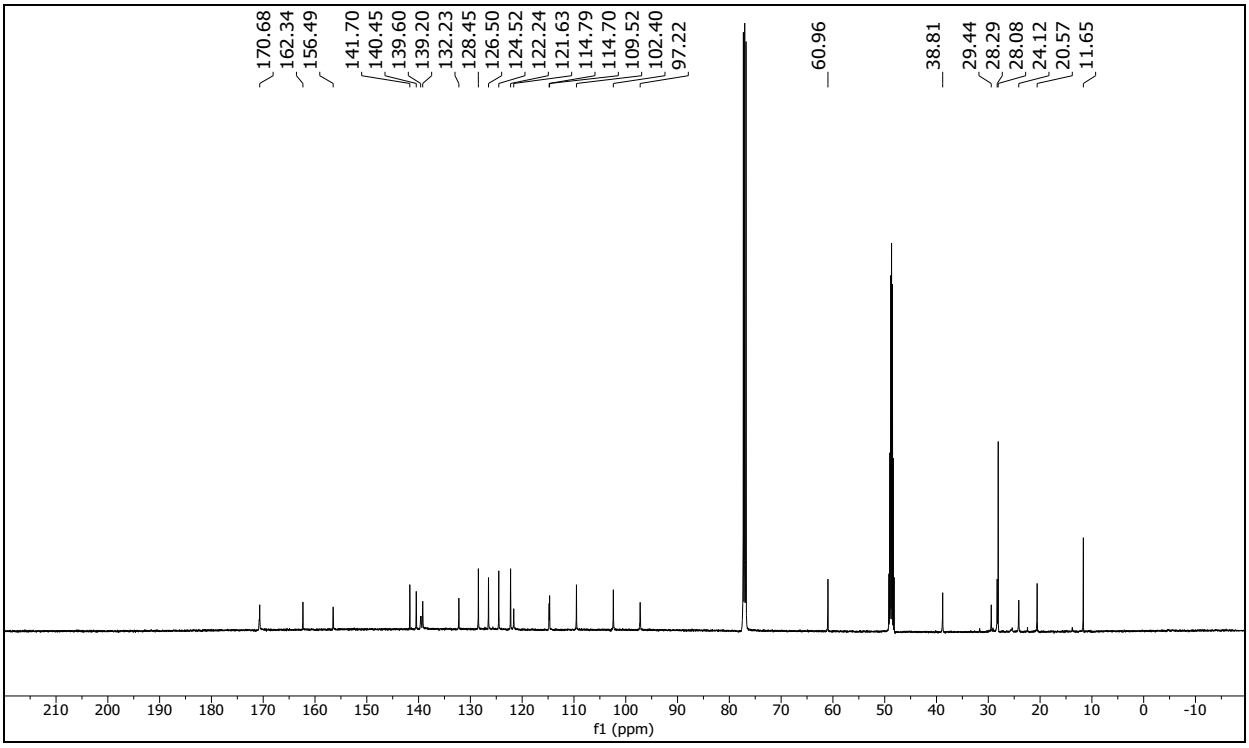

Compound 23: ^{1}H NMR (500 MHz, $CDCl_3$)

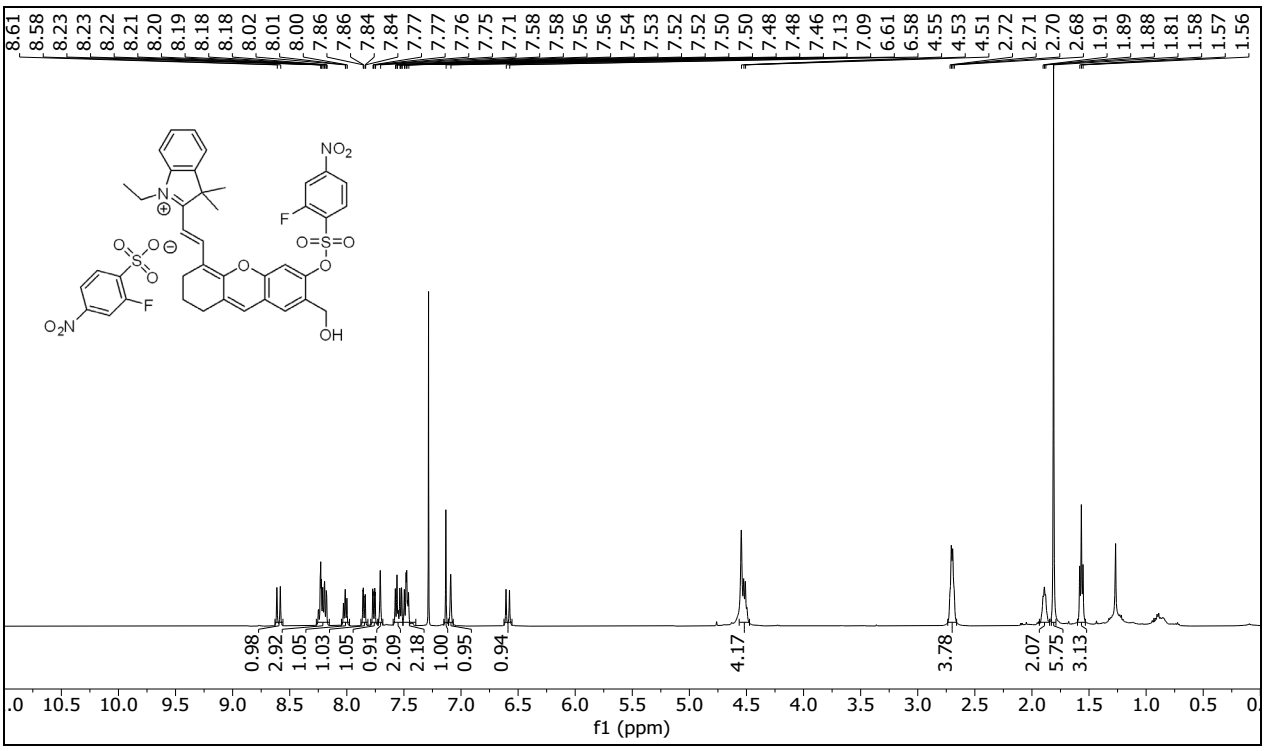

Compound 23: ^{13}C NMR (125 MHz, $CDCl_3$)

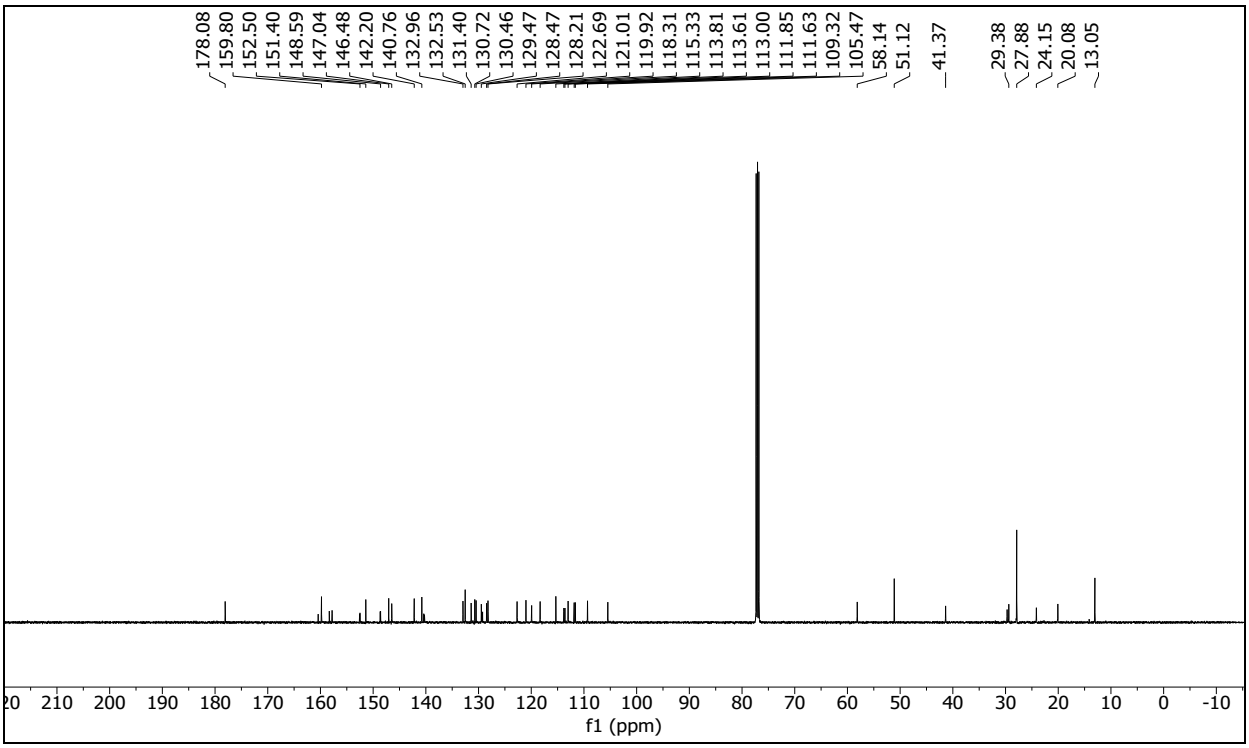

Compound 24: ^{1}H NMR (500 MHz, CD_3OD)

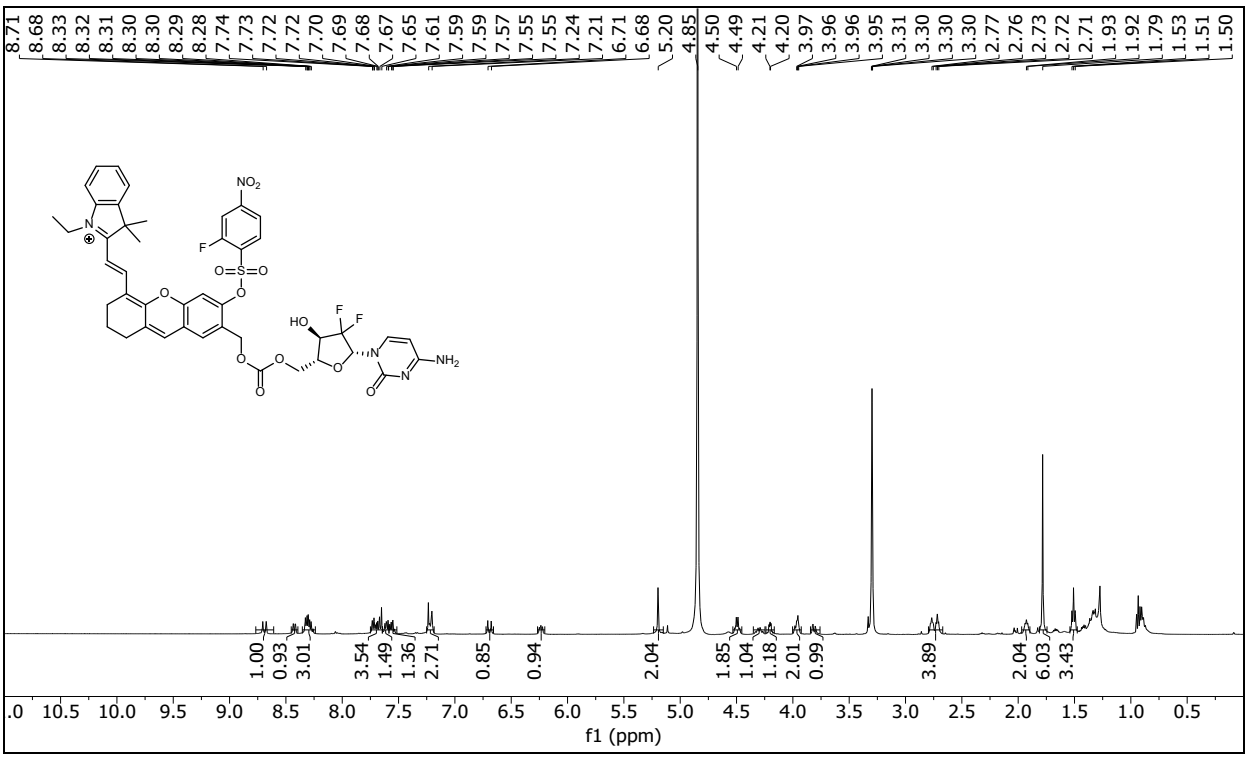

Compound 24: ^{13}C NMR (125 MHz, CD_3OD)

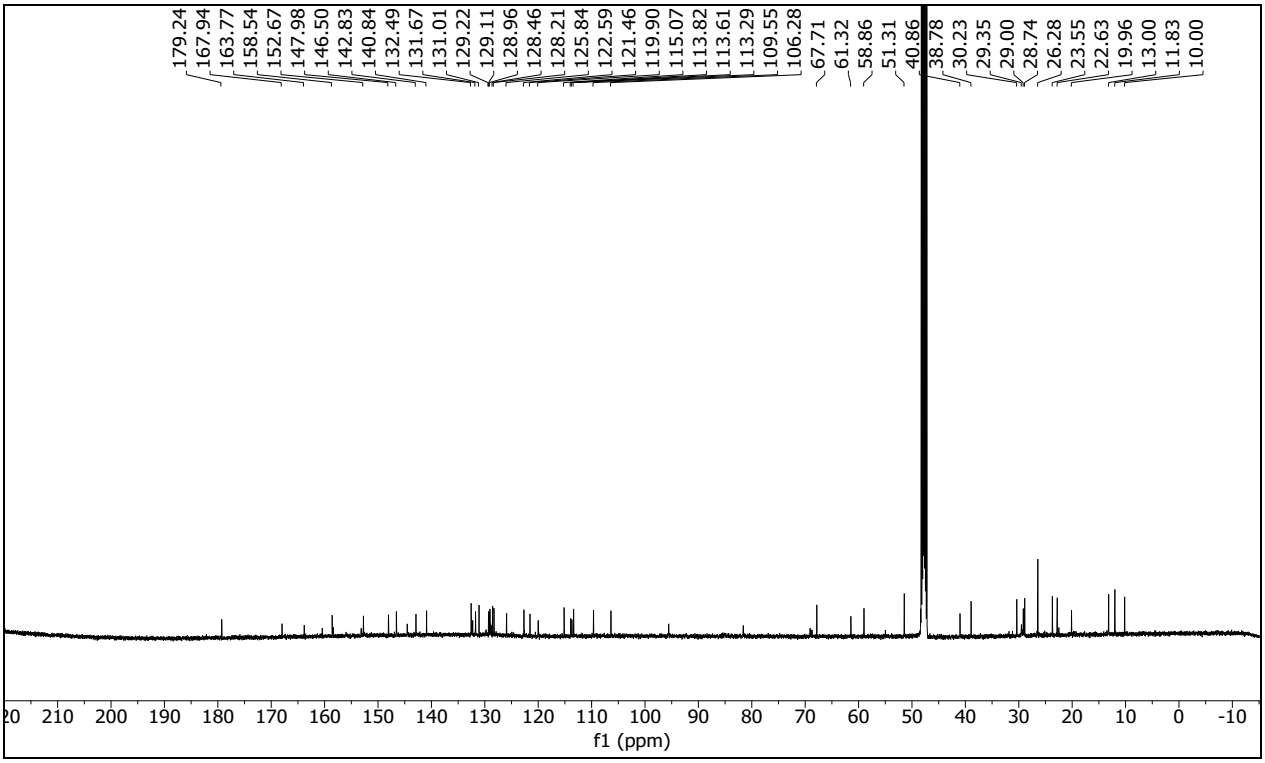

Compound 25: ^{1}H NMR (500 MHz, $CDCl_3$)

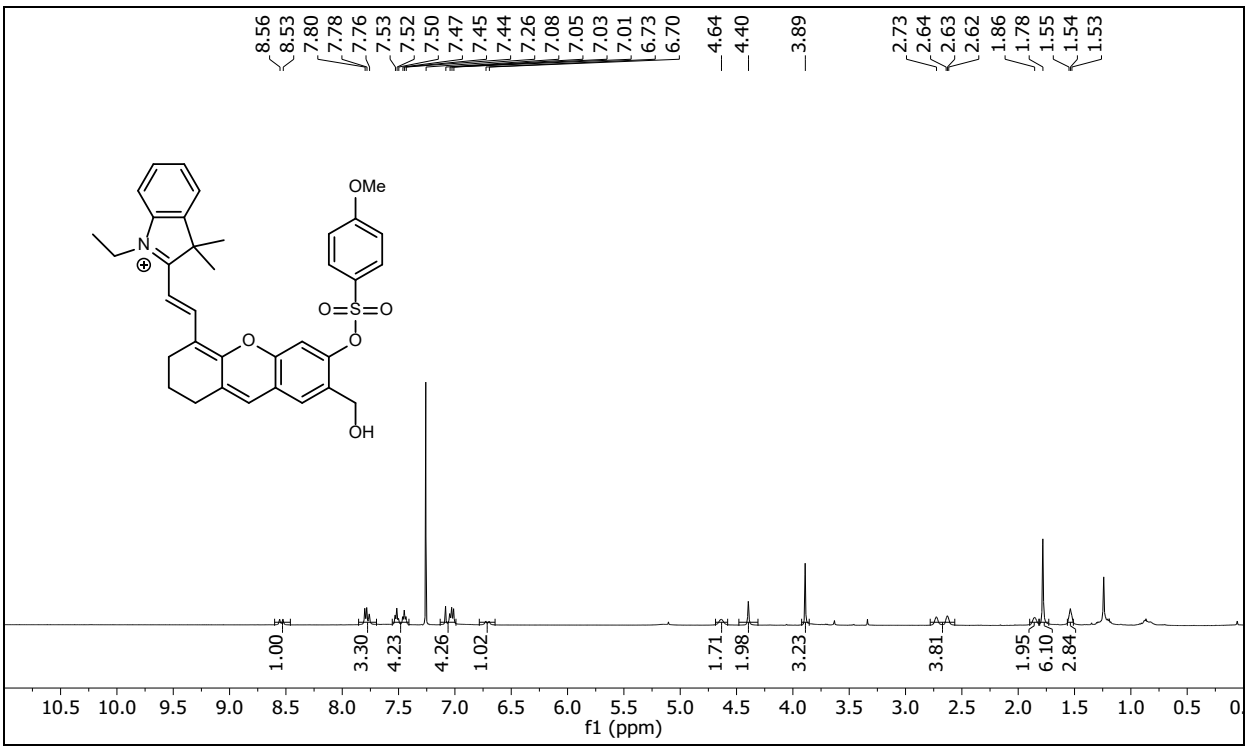

Compound 25: ^{13}C NMR (125 MHz, $CDCl_3$)

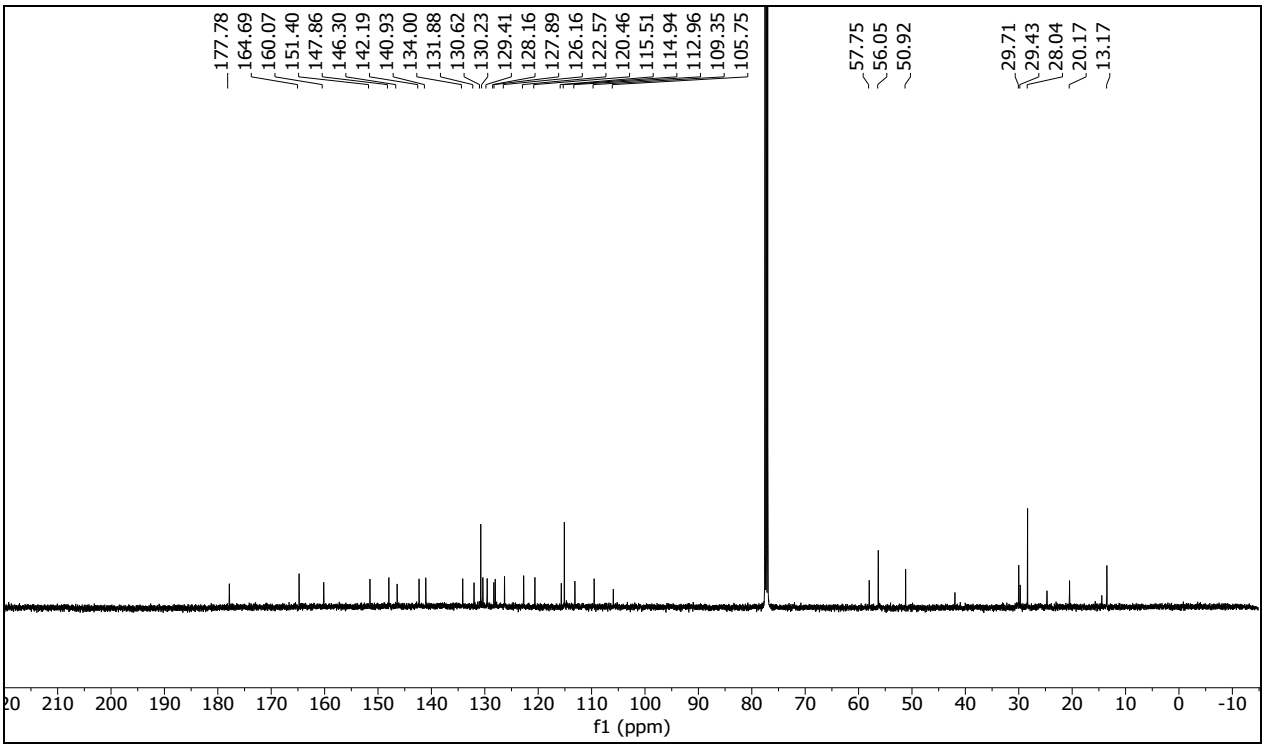

Compound 26: ^{1}H NMR (500 MHz, CD_3OD)

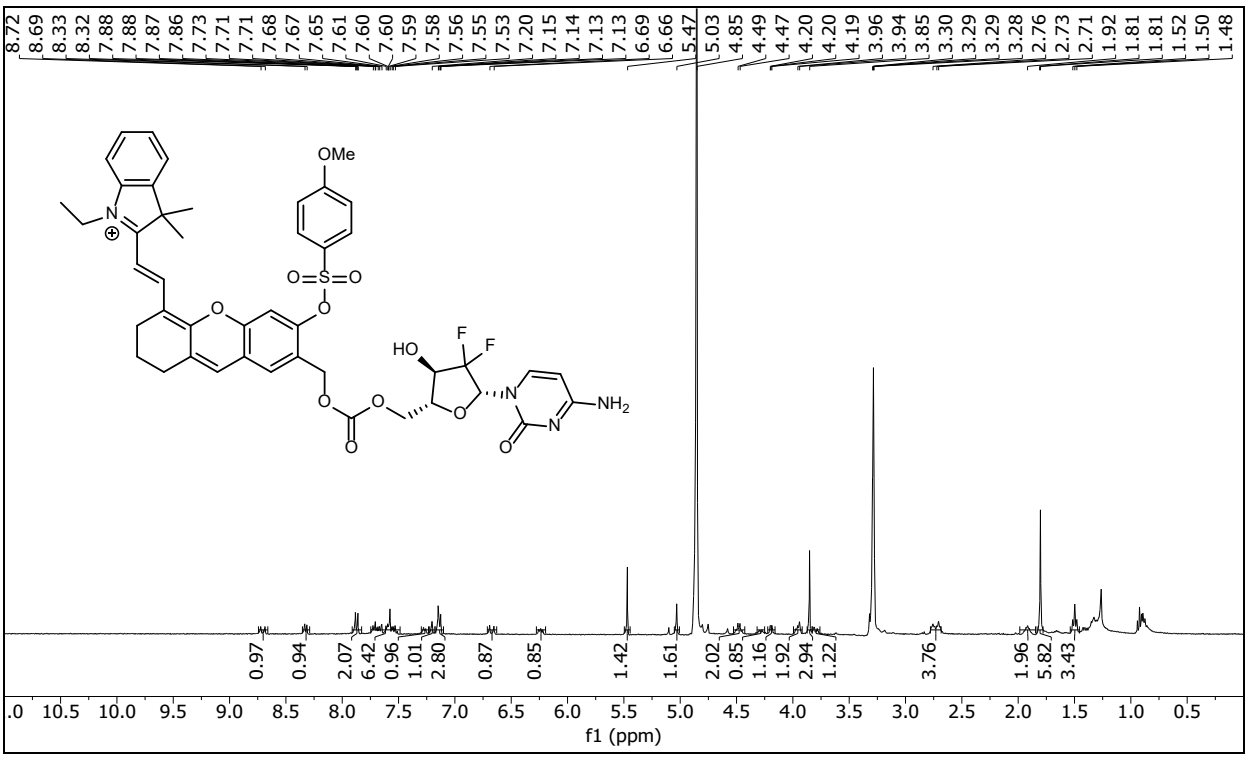

Compound 26: ^{13}C NMR (125 MHz, CD_3OD)

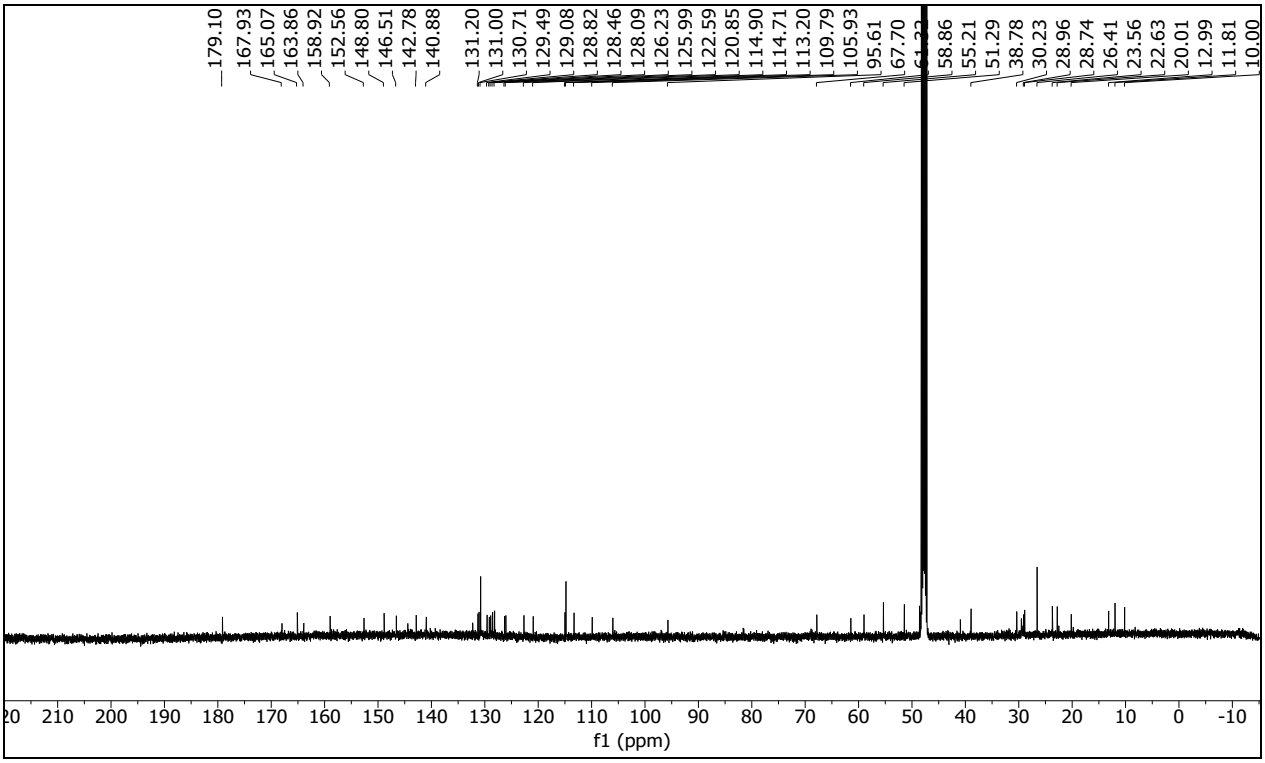

Compound Cl-Ph-S-BenzoCy7: ^{1}H NMR (500 MHz, CD_2Cl_2)

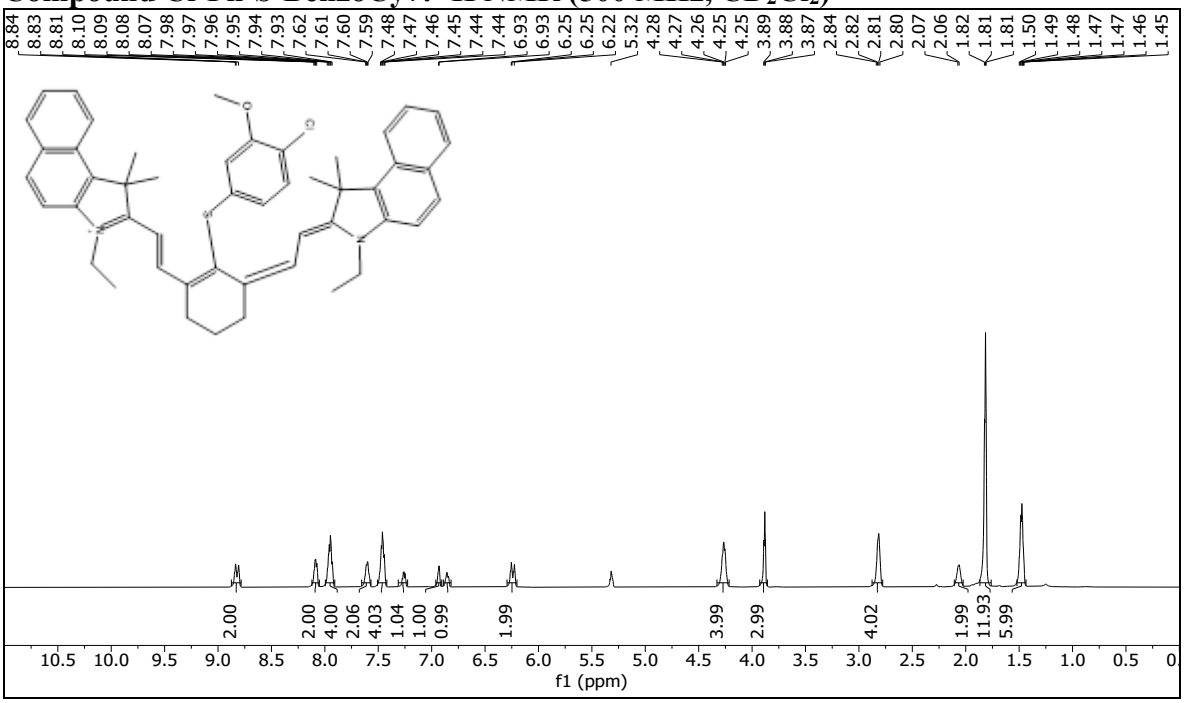

Compound Cl-Ph-S-BenzoCy7: ^{13}C NMR (125 MHz, CD_2Cl_2)

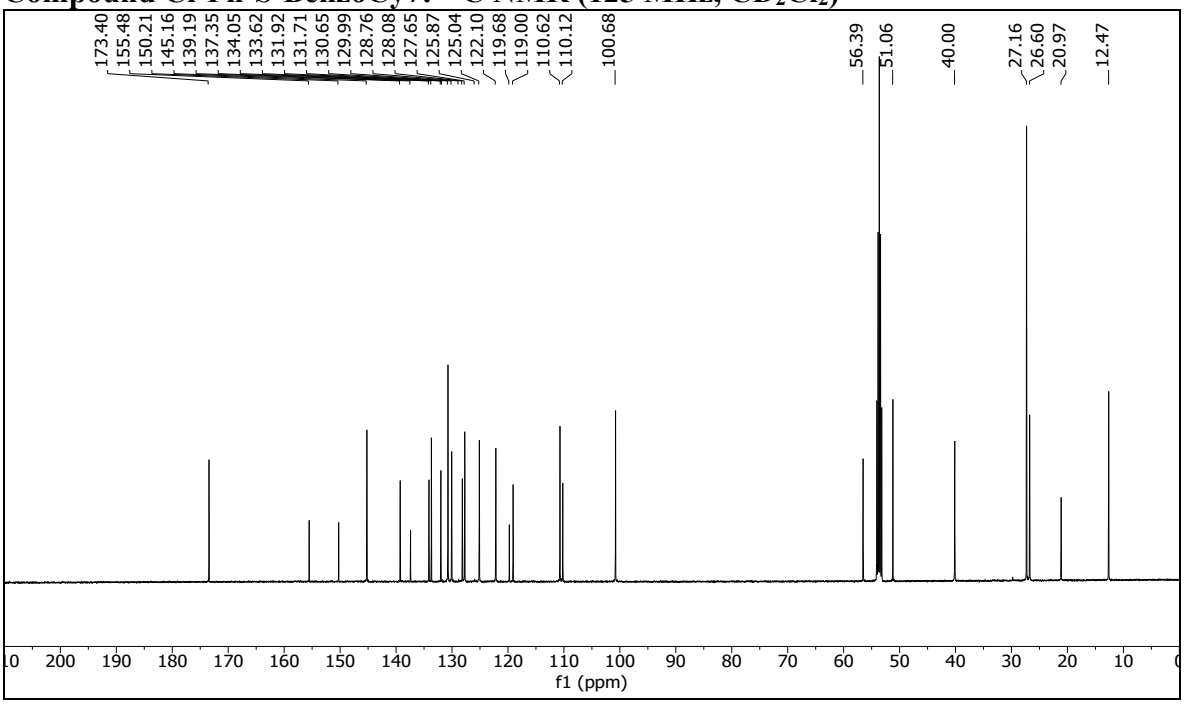

Compound Benzo-PA-HD-Cl: ^{1}H NMR (500 MHz, CD_2Cl_2)

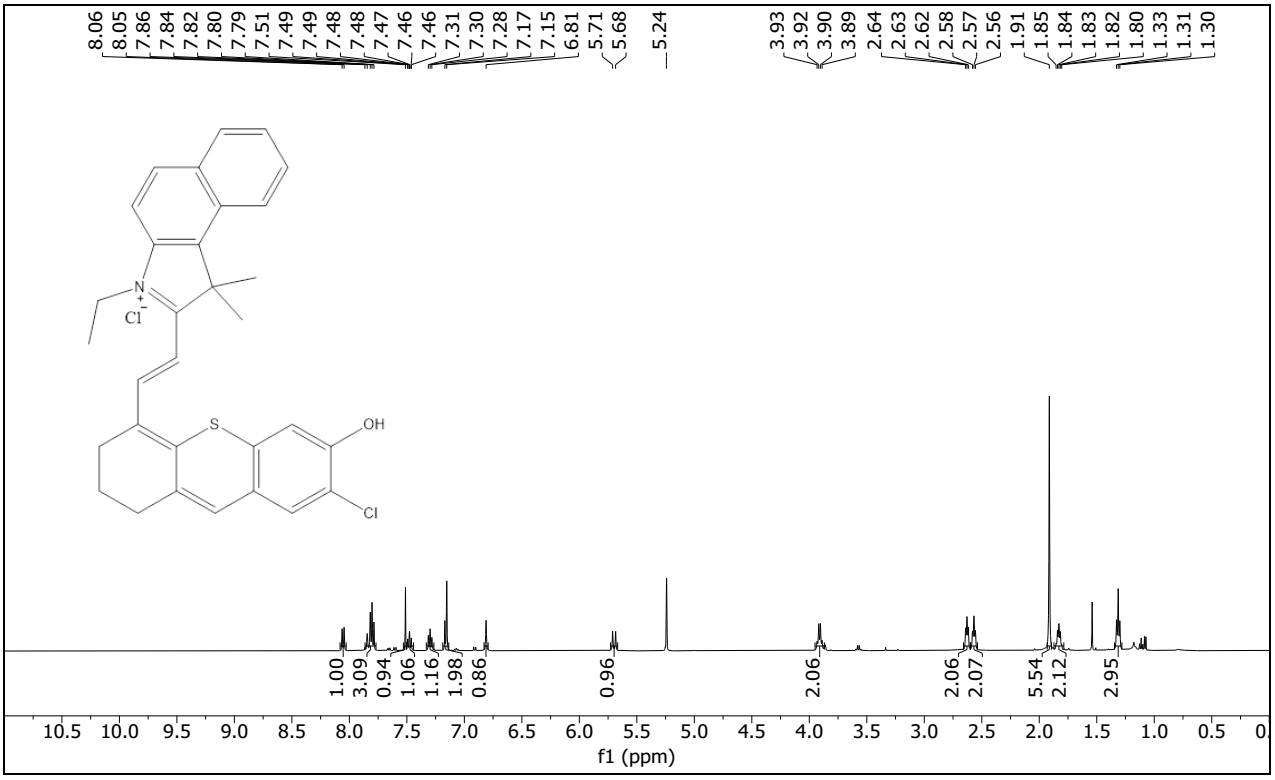

Compound Benzo-PA-HD-Cl: ^{13}C NMR (125 MHz, CD_2Cl_2)

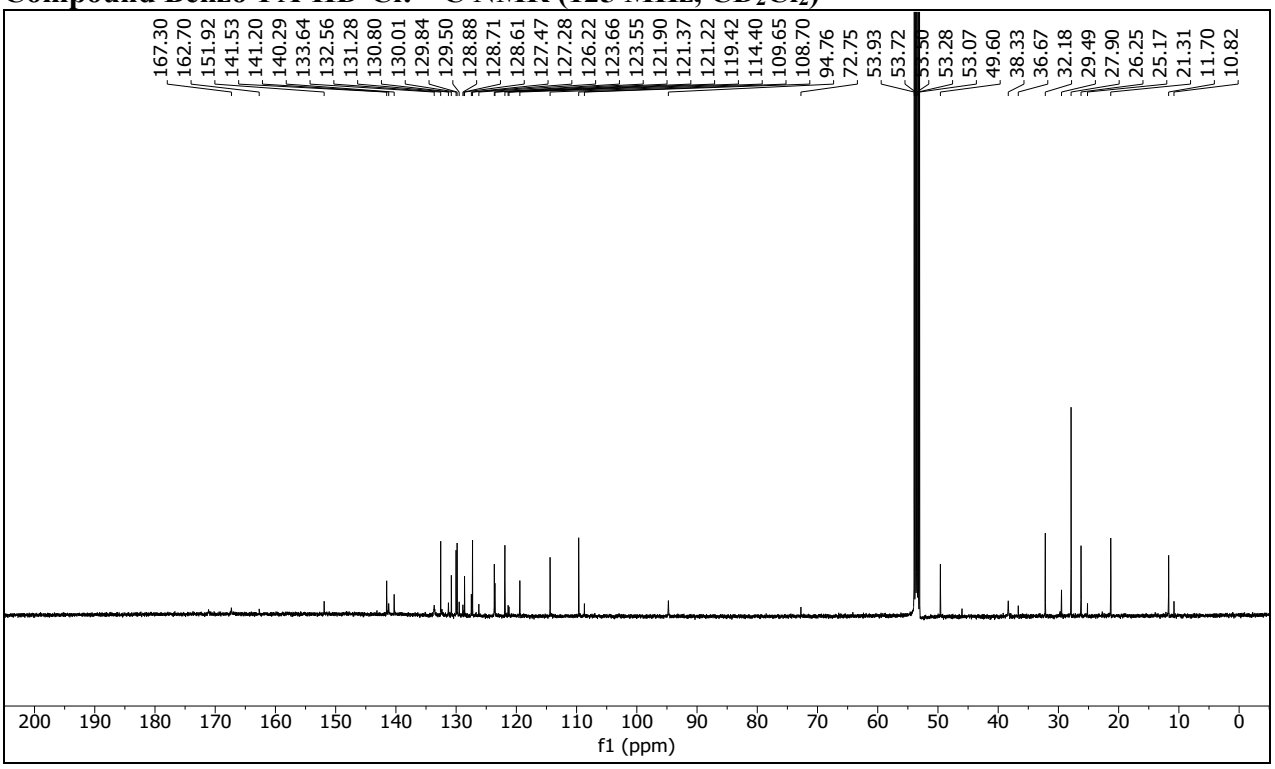

Compound PA-HD-GSH: ^{1}H NMR (500 MHz, DMSO-d_6)

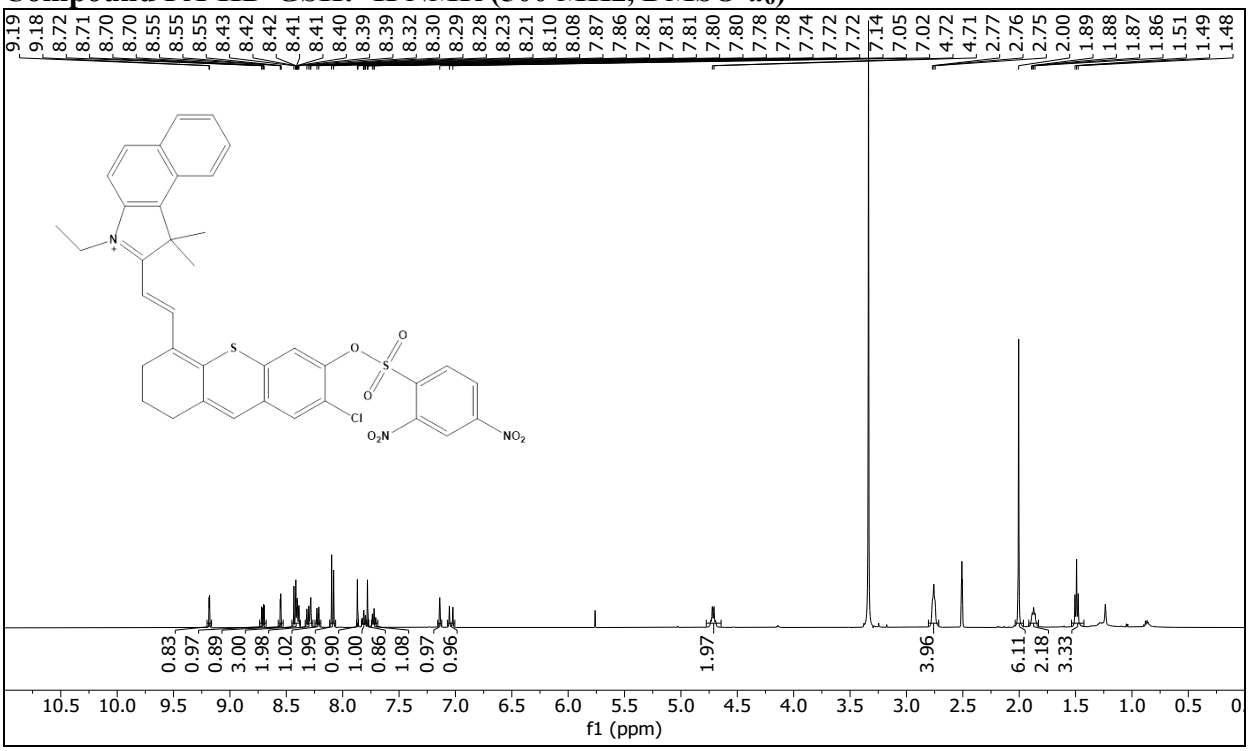

Compound PA-HD-GSH: ^{13}C NMR (125 MHz, CD_2Cl_2)

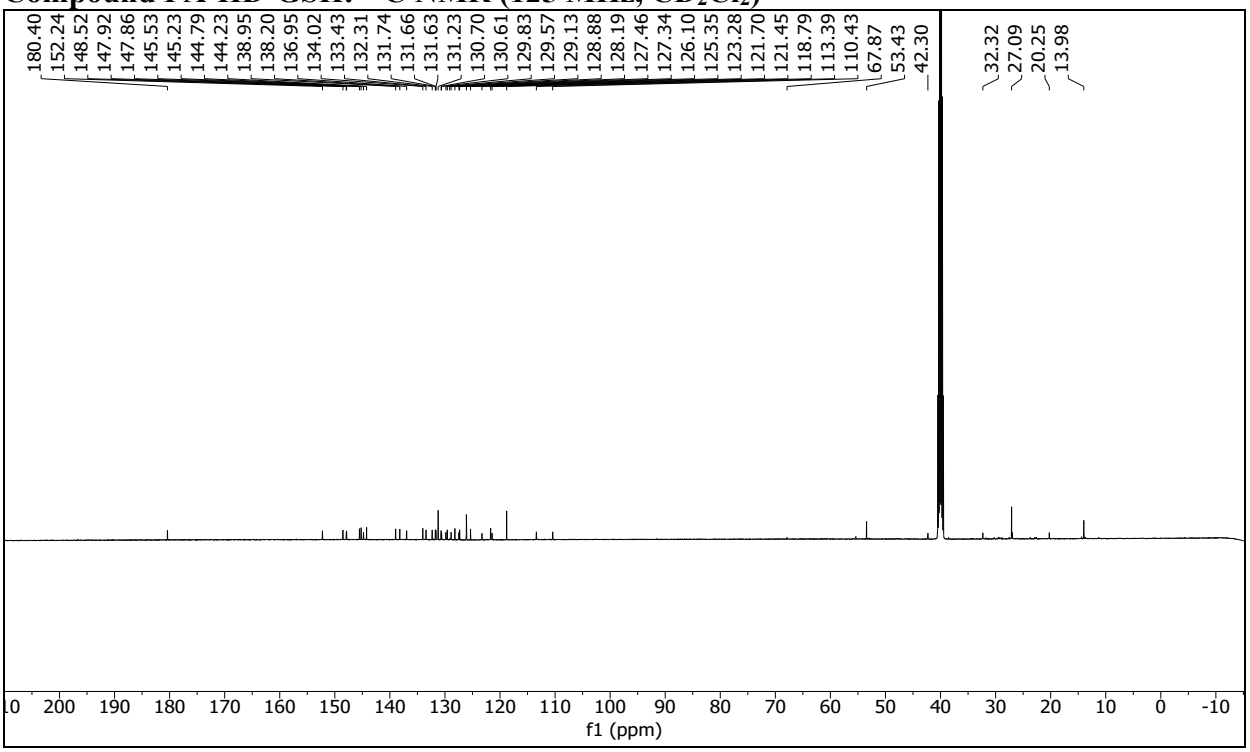

3.13 Acknowledgement of contributions

M.Y.L. performed all experiments in this study that include chemical synthesis, *in vitro* characterization, cellular studies, tumor model studies, *in vivo* imaging, and sample preparation for *ex vivo* analysis. J.C. assisted with the blinded animal study.

CHAPTER 4: A NIR-II PHOTOACOUSTIC PROBE FOR NITRIC OXIDE IN MURINE CANCER MODELS[4]

4.1 Background and significance

Most small-molecule PA ABS probes have been designed on NIR-I dye platforms which have absorbance maxima between 650 and 900 nm. As mentioned, this absorbance region leads to undesirable high background signal due to biological chromophores. Notable NIR-I examples include our first-generation probe (APNO-5) and the second-generation congener (SR-APNO-3) that facilitated the detection of nitric oxide (NO) in live mice but were limited to subcutaneous models of inflammation and breast cancer, respectively.[27,30] To overcome these limitations and obtain improved signal-to-noise ratios, enhanced sensitivity, and deeper tissue penetration, our plan was to red-shift our probes into the NIR-II region (>1000 nm).98–100 To this end, we proposed to develop a NIR-II PA probe for NO by tuning the two main components: the NO-responsive moiety and the dye platform. In phase 1 tuning, we performed Hammett and Brønsted analyses to identify a highly reactive and selective aniline-based trigger that reacts with NO via N-nitrosation chemistry. In phase 2, we synthesized a panel of NIR-II probes to identify the probe that had the lowest propensity to aggregate since this can diminish the PA signal. Next, we evaluated the optimal NIR-II probe in a head-to-head comparison with its NIR-I analogue. To evaluate the deep-tissue imaging capabilities of the probe *in vivo*, we performed PA imaging in an orthotopic breast cancer model and a heterotopic lung cancer model.

[4] Portions of this chapter are reprinted or adapted with permission from the following publication: Lucero, M. Y. *et al.* Development of NIR-II Photoacoustic Probes Tailored for Deep-Tissue Sensing of Nitric Oxide. *Journal of the American Chemical Society* **143**, 7196–7202 (2021).

4.2 Design and development of APNO-1080

We decided to move our previous *N*-nitrosation-based detection strategy to the cyanine dye platform as that is the most structurally similar dye to well-established NIR-II dyes. We accomplished using a physical organic approach where we first installed a panel of anilines bearing different substitutions at the *para* position (−Br, −H, −CH_2OH, −Et, −Me, −OEt, and −OMe) at the meso-chloro of Cy7-Cl (a readily accessible NIR-I cyanine) to afford probes 27–33. The *para* position was selected over our previous *ortho* substitution pattern to limit steric effects. The corresponding Hammett plot revealed a ρ value of −0.94 which is consistent with a modest positive charge character accumulating at the transition state that is promoted by increased electron density. This was further confirmed in our Brønsted plot which demonstrated a strong correlation between the pK_a of the conjugate acid of the aniline and the initial rate of the reaction (R^2 = 0.87). Importantly, the *p*-anisidine trigger exhibited near-complete turnover with NO (100 equiv. at 25 °C) in less than 30 s and was selected for phase 2 tuning.

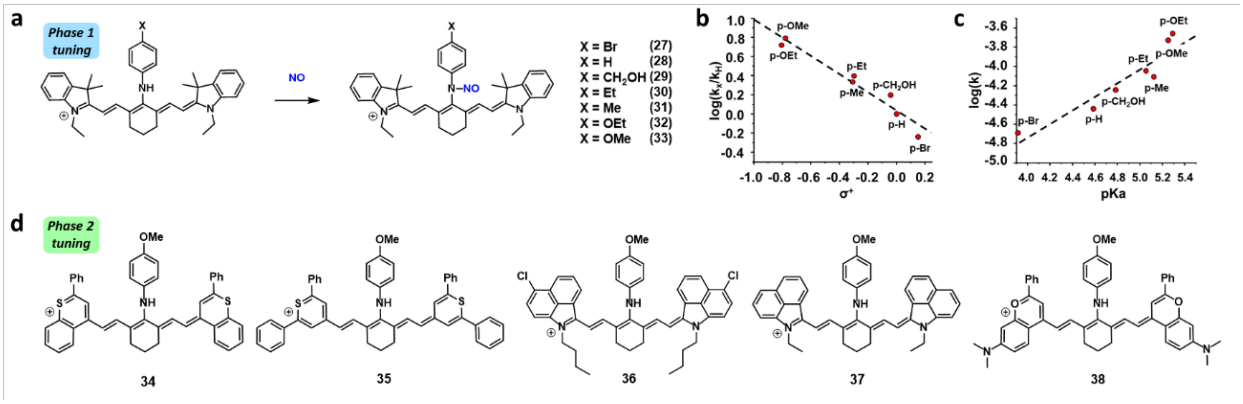

Figure 17. a. Schematic showing the reaction between the various NIR-I APNOs (probes 27−33) and NO to form an *N*-nitroso product. b. Hammett plot for the *N*-nitrosation reaction between para-substituted APNOs and NO (introduced as MAHMA-NONOate) at 25 °C. Dotted line represents the best linear fit. $R^2 = 0.94$. c. Brønsted plots indicating the linear relationship between log(*k*) and the pK_a value of the conjugate acid form of each aniline. Dotted line represents the best linear fit. $R^2 = 0.87$. d. Chemical structures of NIR-II APNOs (probes 34–38) derived from IR-26, IR-1061, IR-1048, Et-1080, and Flav7.

In phase 2, we installed *p*-anisidine onto three commercial NIR-II cyanines (IR-26, IR-1061, and IR-1048), as well as Et-1080 and Flav7 to afford probes 34–38, respectively (Figure 17).101,102 It is important to mention that the cyanine holds intrinsic lipophilic and cationic character that can be leveraged to target cancer cells.103 In phase 2, we aimed to identify probes that satisfy the following criteria for optimal deep tissue imaging. First, the ε must be large ($>10^4$ M^{-1} cm^{-1}) to generate a strong PA signal. Second, the probe must have a low tendency to form insoluble aggregates in aqueous solution, since aggregation commonly results in broad absorbance bands and lower PA signal intensity. In addition, probes can become unreactive in their aggregated form. Third, the probe must respond rapidly to NO due to the short half-life of NO. Fourth, a large spectral shift between the wavelength of maximum absorbance (λ_{abs}) of the probe and the NO-reacted product is ideal for spectral unmixing. Fifth, the probe must be photostable for continuous monitoring over several minutes.

4.3 Evaluating APNO-1080 for *in vitro* performance and biocompatibility

Each probe in the phase 2 panel had a large extinction coefficient ($\sim 10^5$ $M^{-1}cm^{-1}$) with an absorbance maximum in the NIR II window (Supplementary Table 1). However, probes 34, 35, and 38 were poorly soluble in all the aqueous buffer systems used. This resulted in broad absorbance spectra and a weaker PA signal. Probes 36 and 37 exhibited improved solubility in aqueous buffer and provided well-defined spectral properties. In addition, both probes exhibited significantly stronger PA signal upon irradiation. These were the only probes that reacted completely when they were incubated with an excess of NO. Probes 34 and 38 were unreactive possibly due to aggregation. Probe 35, on the other hand, exhibited partial NO-response after an extended incubation period of 1 h. The data are consistent with our previous work that indicated that solubility impacts the rate of *N*-nitrosation *in vitro*. Probe 36 (herein referred to as APNO-

1080) underwent rapid conversion to the *N*-nitrosated product with a 206 nm shift in the absorbance maximum from 874 to 1080 nm. It is important to note that APNO-1080 was selected over probe 37 because the λ_{abs} of the *N*-nitrosated product is more red-shifted by nearly 40 nm. Importantly, we did not observe any photo-oxidation or photodenitrosylation upon continuous irradiation of APNO-1080 and its *N*-nitrosated product, respectively. In fact, we found that APNO-1080 was more stable than the NIR-I congener. Specifically, 97% of activated APNO-1080 remained after 5 minutes and only 41% was present of the NIR-I congener (Supplementary Figure 46).

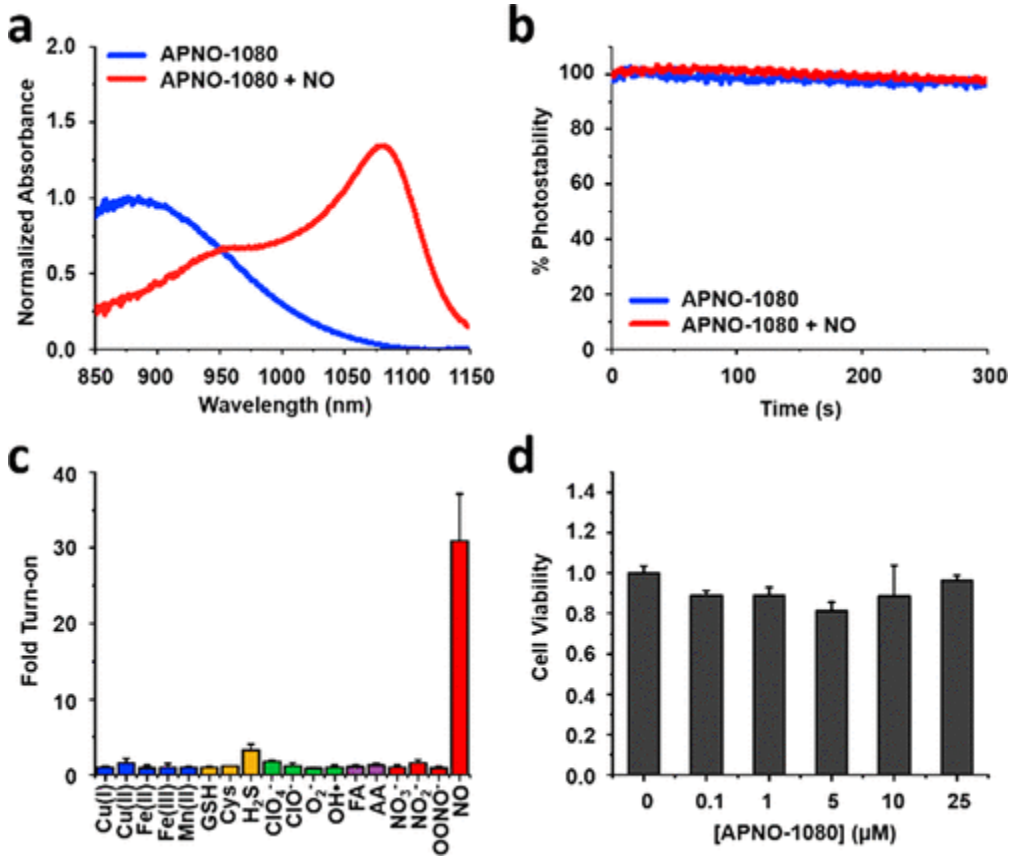

Figure 18. a. Normalized absorbance spectra of APNO-1080 with (red) and without (blue) NO treatment. b. Photostability assay in which APNO-1080 or the *N*-nitrosated product (50 μM) is continuously irradiated with a pulsed laser at their respective λ_{abs} for 300 s. c. Reaction of APNO-1080 (5 μM) with biologically relevant metal ions (1 mM), GSH (1 mM), Cys (500 μM), H_2S (100 μM), reactive oxygen species (1 mM), reactive carbonyl species (1 mM), reactive nitrogen species (1 mM), $ONOO^-$ (50 μM), and NO (100 μM) after 1 h incubation. d. MTT viability assay in A549 cells after 24 h incubation at 37 °C.

Furthermore, APNO-1080 exhibited high selectivity towards NO. To demonstrate this, we treated APNO-1080 with a panel of biologically relevant analytes for 1 h and measuring the absorbance at 1080 nm. We tested GSH since it has the potential to displace the trigger and generate a red-shifted GSH-cyanine adduct.104 Reactive carbonyl species were tested, such as formaldehyde, due to the potential to form red-shifted iminium products and subsequent false positives. Next, we performed an MTT viability assay in A549 cells in which no cytotoxicity was observed at concentrations up to 25 μM for 24 h to determine the potential for cellular and *in vivo* applications (Figure 18). Lastly, we assessed whether APNO-1080 would be metabolically stable by incubating it with RLM rich in CYP450 enzymes at 37 °C for 1 h. This revealed no increase in absorbance at 1080 nm, suggesting APNO-1080 was stable in the presence of RLMs. We performed this experiment again to confirm stability by using ESI-MS analysis. Indeed, APNO-1080 was stable for 24 h under these conditions (Supplementary Figure 47).

4.4 Comparing NIR-I and NIR-II photoacoustic imaging in tissue phantoms

Next, we wanted to directly compare the deep-tissue capabilities of APNO-1080 and its NIR-I analogue, probe 33 (herein referred to as APNO-780) in a head-to-head experiment. First, we activated each probe by treating with an NO-donor (MAHMA-NONOate). The resulting products were then embedded in a 3 cm thick tissue-mimicking phantom (six times the size of a standard phantom used with our MSOT InVision 128 system) and imaged at their absorbance maxima. APNO-1080 can be clearly observed, while APNO-780 was not visible from the background at these imaging depths. This corresponds to a 17.7-fold increase in sensitivity when corrected for wavelength-dependent differences in fluence (Figure 19). We also performed the same experiment with the unreacted probes, and it is important to note that the signal intensity of

both were similar. This suggests that the increased penetration of the excitation light is driving the difference in sensitivity.

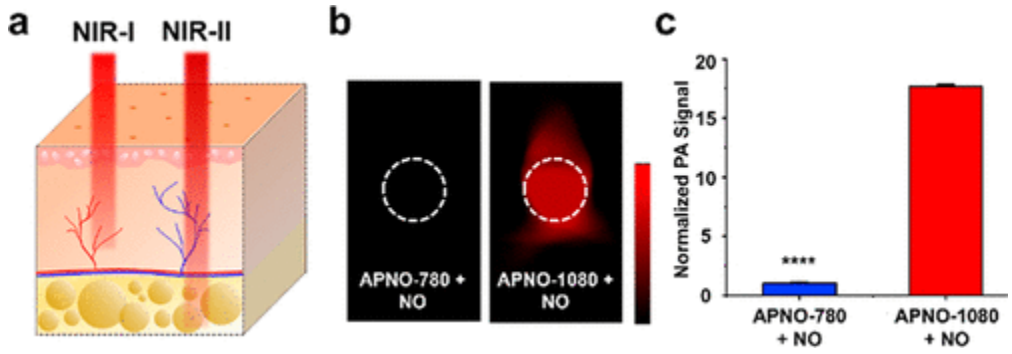

Figure 19. a. Schematic illustrating that NIR-II light can penetrate deeper into tissue compared to NIR-I light. b. Representative PA images of APNO-780 and APNO-1080 (10 μM) treated with NO and overlaid with a 3 cm thick tissue imaging phantom. c. Quantified data from b. Error bars = SD ($n = 3$) Statistical analysis was performed using a two-tailed Student's t test ($\alpha = 0.05$). ****: $P < 0.0001$.

4.5 Photoacoustic imaging of nitric oxide in breast and lung cancer models

NO is believed to have a role in modulating the tumor microenvironment, therefore it is critical to be able to detect endogenous NO. Tumor-associated macrophages produce low steady-state concentrations of NO (<200 nM) and it is believed that this may cause a chronic inflammatory state that drives tumor progression, leading to poorer clinical prognosis.105 To demonstrate the utility of APNO-1080 for imaging NO in cancer, we first applied it in an orthotopic 4T1-Luc breast cancer model. It is important to note the different between an orthotopic model and a subcutaneous model of breast cancer is that tumors are allowed to grow deeper within the body. This is ideal for evaluating the deep-tissue imaging capability of APNO-1080. Importantly, using a luciferase-expressing cell line allows us to employ bioluminescence imaging to monitor tumor burden. Once the tumors had grown to a volume of ~400 mm^3, APNO-1080 was administered systemically and PA imaging was performed with spectral unmixing. We observed a 1.3 ± 0.1-fold turn-on response (defined as $PA_{Final}/PA_{Initial}$) in the tumor-bearing mice as compared to 1.0 ± 0.2-fold in the tumor-free control. It is important to note here, that the PA fold turn-on was significantly higher than previously reported by our group using NIR-I NO PA probes. To further showcase the ability of APNO-1080 to image in deeper tissue, we surgically implanted A549-Luc2 lung cancer cells into the liver of Nu/J mice. Tumors were detectable several weeks post-implantation using bioluminescence imaging. APNO-1080 was administered systemically and imaged 30 minutes post-injection. Overall, we observed a 1.65 ± 0.07-fold turn-on response in tumor-bearing mice relative to 1.00 ± 0.07-fold in mice that received a sham surgery (Figure 20). Again, APNO-1080 provided significantly higher PA turn-on compared to our other NIR-I probes for NO.

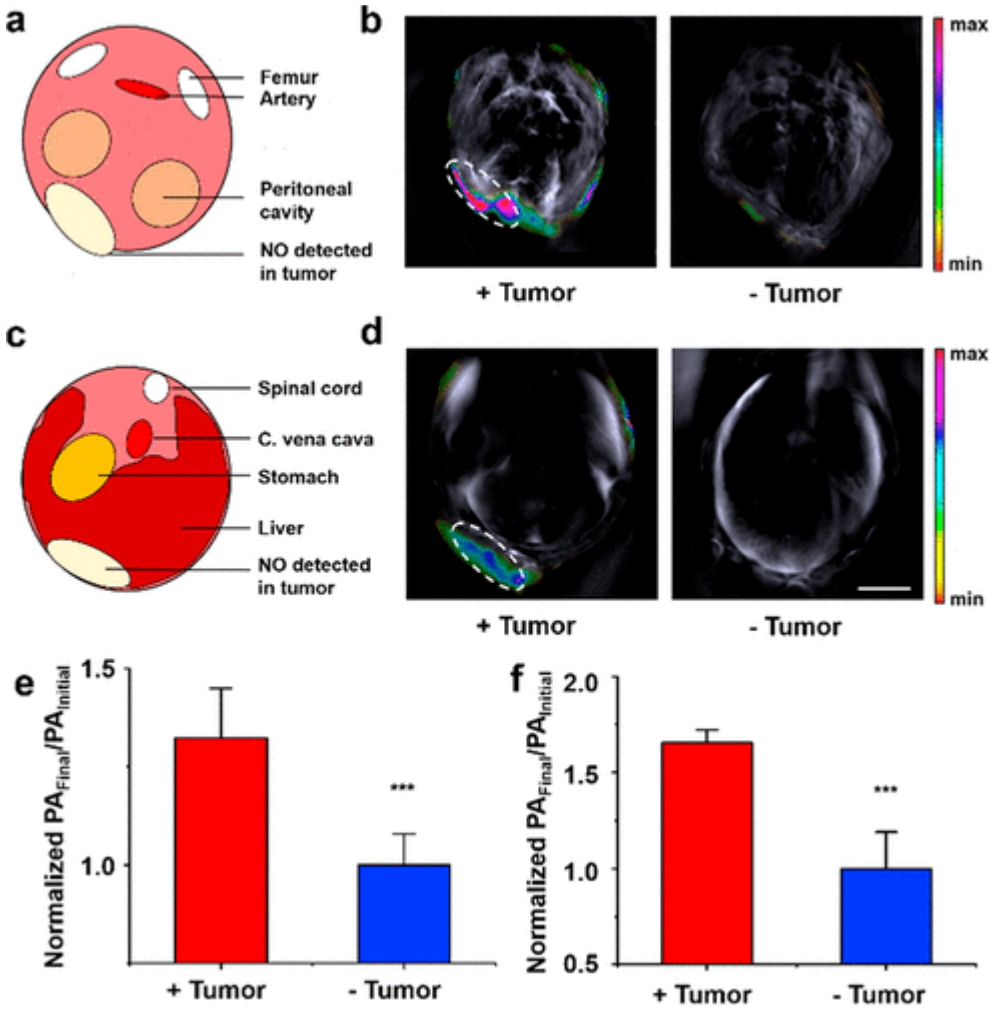

Figure 20. a. Cartoon schematic depicting the cross-sectional anatomy of the images in b. b. Representative PA images of a 4T1-Luc tumor, as well as the tumor-less control after treatment with APNO-1080 (50 μM). Scale bar = 5 mm. c. Cartoon schematic depicting the cross-sectional anatomy of images in d. d. Representative PA images of a heterotopic A549-Luc2 tumor, as well as the tumor-less control after treatment with APNO-1080. Scale bar = 5 mm. e. Normalized PA fold turn-on in 4T1-Luc tumors after treatment with APNO-1080. Error bars = SD (n = 6). (f) Normalized PA fold turn-on in A549 tumors (n = 6) and the tumor-less control (n = 3) after treatment with APNO-1080. Error bars = SD. Statistical analysis was performed using a two-tailed Student's t test ($\alpha = 0.05$). ***: $P < 0.001$.

4.6 Summary and outlook

In conclusion, we successfully employed a two-phase tuning approach to develop the first NIR-II PA ABS probe for the detection of endogenous, cancer-derived NO within deep-tissue. With this approach we developed APNO-1080 which features an optimized *p*-anisidine trigger on a NIR-II cyanine platform (IR-1048). Upon reaction with NO, the *N*-nitrosated product exhibits a larger extinction coefficient relative to the probe (Supplementary Figure 48) and absorbs maximally at 1080 nm with no spectral overlap with the probe. While there are many NO probes, most examples are only fluorescent or compatible with NIR-I excitation which is typically limited to cellular studies. It is evident that there are very few probes that are applicable for *in vivo* applications, however even fewer than that are sensitive enough to detect NO in cancer where the steady-state concentrations are in the low nM range. Prior to the development of APNO-1080, SR-APNO (our most responsive probe) could only detect NO in subcutaneous models using NIR-I PA imaging. Here we have highlighted the benefit of shifting the λ_{abs} of PA imaging agents into the NIR-II window to achieve greater imaging depths and enhanced sensitivity. Without optimizing the reactivity of our trigger and the PA properties of our PA-compatible NIR-II dye, it would not have been possible to detect endogenous NO in the two deep-tissue murine models of cancer that we employed in this study. We envision that this work will further be utilized for the development of other NIR-II PA ABS probes for analytes such as metal ions, thiols, reactive nitrogen and oxygen species.

4.7 Experimental methods

Materials. Materials were purchased from commercial vendors and used without further purification. All deuterated solvents were purchased from Cambridge Isotope Laboratories. Acetone, dichloromethane, DMSO, glacial acetic acid, PBS (Corning), Matrigel (Corning),

Cremophor EL (Fluka), potassium phosphate dibasic, potassium phosphate monobasic, sodium bicarbonate, sodium carbonate, sodium chloride, and sodium hydroxide were purchased from Thermo Fisher Scientific. Sodium hypochlorite (14.5 % available chlorine in water) was purchased from Alfa Aesar. Agarose LE (Molecular Biology Grade) was purchased from Gold Biotechnology. Acetonitrile, anhydrous methanol, concentrated hydrochloric acid, hydrogen peroxide (30% v/v) and sodium hydroxide were purchased from Macron Fine Chemicals. IR-1061, IR-1048, acetic anhydride, anhydrous dichloromethane, anhydrous dimethylformamide, *p*-amino-benzyl alcohol, aniline, *p*-bromo-aniline, *p*-ethyl-aniline, *p*-methyl-aniline, *p*-ethoxy-aniline, iron(II) sulfate heptahydrate, iron(III) chloride (anhydrous), copper chloride, potassium superoxide, sodium nitrite, sodium nitrate, manganese(II) chloride, NADPH, formaldehyde (37 % w/w in water), glutathione (reduced), Mohr's salt, hexanes, l-ascorbic acid, l-N^G-nitroarginine, RLM (pooled, male), and MTT reagent were purchased from Millipore-Sigma Aldrich. IR-26 was purchased from Exciton. Potassium iodide, HEPES, *p*-anisidine, and sodium sulfate (anhydrous) were purchased from Oakwood Chemicals. Sodium α-oxyhyponitrite (Angeli's salt), DEA-NONOate and MAHMA-NONOate were purchased from Cayman Chemical. D-Luciferin were purchased from AK Scientific. A549, A549-Luc2, 4T1, and 4T1-Luc2 cells were purchased from ATCC. Cells were incubated at 37 °C under 5% CO_2.

Instruments and Software. ^{1}H and ^{13}C NMR spectra were acquired on the Carver B500 spectrometer. The following abbreviations were used to describe coupling constants: singlet (s), doublet (d), triplet (t), or multiplet (m). Spectra were visualized and analyzed using MestReNova (version 10.0) and referenced to trace non-deuterated solvent. High-resolution mass spectra were acquired on a Waters Q-TOF Ultima ESI mass spectrometer or a Waters Synapt G2-Si ESI/LC-MS spectrometer. Ultraviolet-visible spectroscopy was performed on a Cary 60 or Cary 5000.

Ultraviolet-visible spectroscopy and fluorimetry was performed with a micro fluorescence quartz cuvette (Science Outlet). Cells were visualized on an EVOS FL epifluorescence microscope. SpectraMax M2 plate reader was used for cell viability assays. Cell images were analyzed using ImageJ.[96] Data was analyzed using Microsoft Excel. *In vivo* bioluminescence imaging was performed using an IVIS Spectrum CT live-animal imaging system (Perkin-Elmer, USA). Photoacoustic imaging was performed using the MSOT InVision 128 (iTheraMedical). Reported values correspond to mean PA signals in regions of interest (ROIs) of equal area.

Statistical Analysis. Statistical analysis was performed using Microsoft Excel. For *in vivo* and phantom imaging, statistical analysis was performed using the Student's *t*-test. The *n* value is indicated in the corresponding figure captions.

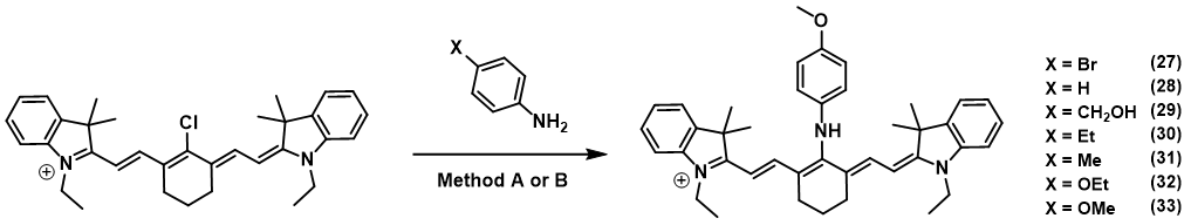

Supplementary Scheme 3.

Synthetic Procedures. TLC was performed on glass-backed TLC plates precoated with silica gel containing an UV254 fluorescent indicator (Macherey-Nagel). TLC's were visualized with a 254/365 nm UV hand-held lamp (UVP). Flash silica gel chromatography was performed using 0.04–0.063 mm 60 M silica (Macherey-Nagel). All glassware used under anhydrous reaction conditions were flame-dried under vacuum and cooled immediately before use.

Method A: Cy7-Cl (1 equiv) and the corresponding *p*-aniline (5 equiv) were dissolved in anhydrous DMSO and then treated with triethylamine (5 equiv). The reaction was heated at 55 °C for 8 h before cooling to room temperature. The DMSO was blown off using N_2, resuspended in CH_2Cl_2, and washed with 1 M HCl. The organic solution was washed 3× with an aqueous potassi-

um iodide solution (saturated, 3× 25 mL), dried (Na_2SO_4) and the solvent was removed under reduced pressure. The product was purified twice via silica gel chromatography (5% MeOH/CH_2Cl_2 and then 10%/45%/45% MeOH/toluene/CH_2Cl_2).

Method B: Cy7-Cl (1 equiv) and the corresponding *p*-aniline (3 equiv) were dissolved in anhydrous DMF and then treated with triethylamine (3 equiv). The reaction was heated at 55 °C for 8 h before cooling to room temperature. The reaction was diluted in brine and extracted with CH_2Cl_2 (3×). The organic solution was washed 3× with an aqueous potassi-um iodide solution (saturated, 3× 25 mL), dried (Na_2SO_4) and the solvent was removed under reduced pressure. The product was purified via silica gel chromatography (5% MeOH/CH_2Cl_2).

Synthesis of Compound 27. Method A was used and afforded a purple solid (8.2 mg, 0.011 mmol, 1.4% yield). Cy7-Cl (500 mg, 0.80 mmol, 1 equiv), *p*-bromoaniline (673 mg, 4.0 mmol, 5 equiv), DMSO (13 mL), and triethylamine (545 μL, 4.0 mmol, 5 equiv) were used. ^{1}H NMR (500 MHz, CD_3OD) δ 8.11 (d, *J* = 13.9 Hz, 2H), 7.36 (dt, *J* = 12.2, 5.7 Hz, 6H), 7.20 (d, *J* = 8.3 Hz, 2H), 7.16 (dd, *J* = 12.8, 7.1 Hz, 2H), 6.88 (d, *J* = 8.5 Hz, 2H), 6.10 (d, *J* = 13.9 Hz, 2H), 4.10 (q, *J* = 7.2 Hz, 4H), 2.67 (t, *J* = 6.3 Hz, 4H), 1.98 (t, *J* = 6.2 Hz, 2H), 1.40 (s, 12H), 1.35 (t, *J* = 7.2 Hz, 6H). ^{13}C NMR (125 MHz, CD_3OD): δ 170.91, 162.17, 143.00, 141.94, 132.30, 128.53, 128.25, 127.82, 124.87, 124.18, 121.93, 117.43, 111.29, 109.77, 98.08, 48.54, 38.34, 36.17, 29.38, 26.88, 24.16, 20.07, 10.77. MS (ES+): *m*/*z* calcd for $C_{40}H_{45}BrN_3$ 646.2791 and 648.2771, found 646.2766 and 648.2747.

Synthesis of Compound 28. Method A was used and afforded a blue solid (54.3 mg, 0.078 mmol, 10.0% yield). Cy7-Cl (500 mg, 0.80 mmol, 1 equiv), aniline (684 mg, 4.0 mmol, 5 equiv), DMSO (13 mL), and triethylamine (4.0 mmol, 5 equiv) were used. ^{1}H NMR (500 MHz, CD_3OD): δ 8.17 (d, *J* = 13.8 Hz, 2H), 7.36 (ddt, *J* = 6.1, 4.7, 1.9 Hz, 4H), 7.27 (dd, *J* = 8.5, 7.3 Hz, 2H), 7.21–7.12

(m, 5H), 7.05–6.99 (m, 2H), 6.82 (t, J = 7.4 Hz, 1H), 6.07 (d, J = 13.7 Hz, 2H), 4.10 (q, J = 7.2 Hz, 4H), 2.69 (t, J = 6.3 Hz, 4H), 2.00 (p, J = 6.4 Hz, 2H), 1.39 (s, 12H), 1.36 (t, J = 7.2 Hz, 6H). ^{13}C NMR (125 MHz, CD_3OD): δ 170.56, 159.23, 146.93, 143.07, 142.01, 140.85, 129.56, 128.53, 128.19, 127.82, 124.35, 123.93, 121.85, 120.21, 116.47, 109.56, 97.51, 78.08, 38.22, 26.99, 24.19, 21.57, 10.71. MS (ES+): m/z calcd for $C_{40}H_{46}N_3$ 568.3686, found 568.3681.

Synthesis of Compound 29. Method B was used and afforded a blue solid (67.3 mg, 0.112 mmol, 11.5% yield). Cy7-Cl (500 mg, 0.80 mmol, 1 equiv), *p*-amino-benzyl alcohol (360.7 mg, 2.3 mmol, 3 equiv), DMF (8 mL), and triethylamine (327 μL, 2.3 mmol, 3 equiv) were used. ^{1}H NMR (500 MHz, CD_3OD): δ 8.13 (d, J = 13.8 Hz, 2H), 7.34 (dt, J = 7.7, 3.9 Hz, 5H), 7.25 (d, J = 8.2 Hz, 2H), 7.21–7.11 (m, 4H), 7.00 (d, J = 8.4 Hz, 2H), 6.05 (d, J = 13.8 Hz, 2H), 4.46 (s, 2H), 4.07 (q, J = 7.2 Hz, 4H), 2.66 (t, J = 6.3 Hz, 4H), 1.98 (t, J = 6.3 Hz, 2H), 1.37 (s, 12H), 1.34 (t, J = 7.2 Hz, 6H). ^{13}C NMR (125 MHz, CD_3OD): δ 170.50, 159.35, 152.70, 149.85, 142.98, 142.02, 140.83, 138.62, 138.00, 137.69, 133.50, 128.61, 128.18, 124.17, 123.90, 121.85, 116.58, 109.53, 97.42, 63.45, 38.19, 27.00, 24.18, 23.40, 21.58, 19.33, 12.53, 10.70. MS (ES+): m/z calcd for $C_{41}H_{48}N_3O$ 598.3792, found 598.3784.

Synthesis of Compound 30. Method B was used and afforded a blue solid (110.2 mg, 0.152 mmol, 19.4% yield). Cy7-Cl (500 mg, 0.80 mmol, 1 equiv), *p*-ethyl aniline (284.4 mg, 2.3 mmol, 3 equiv), DMF (8 mL) and triethylamine (327 μL, 2.3 mmol, 3 equiv) were used. ^{1}H NMR (500 MHz, $CDCl_3$): δ 8.02 (d, J = 13.7 Hz, 2H), 7.27–7.16 (m, 4H), 7.13–6.97 (m, 6H), 6.95–6.85 (m, 2H), 5.90 (d, J = 13.7 Hz, 2H), 3.95 (q, J = 7.2 Hz, 4H), 2.54 (t, J = 6.3 Hz, 5H), 2.42 (q, J = 7.6 Hz, 2H), 1.86 (q, J = 6.33, 2H), 1.26 (s, 12H), 1.23 (t, J = 7.2 Hz, 6H). ^{13}C NMR (125 MHz, $CDCl_3$): δ 170.13, 156.30, 148.58, 148.20, 147.78, 142.81, 142.07, 140.74, 129.00, 128.16, 123.73, 123.47,

121.81, 117.56, 109.38, 96.94, 48.10, 38.07, 27.75, 27.06, 24.18, 21.66, 14.98, 10.63. MS (ES+): *m*/*z* calcd for $C_{42}H_{50}N_3$ 596.3999, found 596.3979.

Synthesis of Compound 31. Method B was used and afforded a blue solid (66.4 mg, 0.094 mmol, 12.0% yield). Cy7-Cl (500 mg, 0.80 mmol, 1 equiv), *p*-toluidine (360.7 mg, 2.3 mmol, 3 equiv), DMF (8 mL), and triethylamine (408 µL, 2.3 mmol, 3 equiv) were used. ^{1}H NMR (500 MHz, CD_3OD): δ 8.11 (d, *J* = 13.7 Hz, 2H), 7.33 (t, *J* = 7.1 Hz, 4H), 7.18–7.06 (m, 6H), 6.97 (d, *J* = 8.2 Hz, 2H), 6.01 (d, *J* = 13.7 Hz, 2H), 4.06 (q, *J* = 7.2 Hz, 4H), 2.64 (t, *J* = 6.3 Hz, 4H), 2.21 (s, 3H), 1.96 (t, *J* = 6.3 Hz, 2H), 1.37 (s, 12H), 1.33 (t, *J* = 7.2 Hz, 6H). ^{13}C NMR (125 MHz, CD_3OD): δ 170.13, 160.21, 144.08, 142.81, 142.08, 140.74, 131.32, 130.37, 130.07, 128.16, 123.73, 123.63, 121.83, 117.44, 109.41, 97.03, 38.13, 27.00, 24.23, 21.66, 19.24, 10.69. MS (ES+): *m*/*z* calcd for $C_{41}H_{48}N_3$ 582.3843, found 582.3832.

Synthesis of Compound 32. Method B was used and afforded a blue solid (182.5 mg, 0.247 mmol, 31.5% yield). Cy7-Cl (500 mg, 0.80 mmol, 1 equiv), *p*-ethoxyaniline (322.0 mg, 2.3 mmol, 3 equiv), DMF (8 mL), and triethylamine (327 µL, 2.3 mmol, 3 equiv) were used. ^{1}H NMR (500 MHz, CD_3OD): δ 8.12 (d, *J* = 13.6 Hz, 2H), 7.34 (td, *J* = 7.3, 1.3 Hz, 4H), 7.19–7.12 (m, 5H), 7.11–7.05 (m, 2H), 6.90 (d, *J* = 8.9 Hz, 2H), 5.99 (d, *J* = 13.6 Hz, 2H), 4.06 (q, *J* = 7.2 Hz, 4H), 3.98 (q, *J* = 7.0 Hz, 2H), 2.64 (t, *J* = 6.3 Hz, 4H), 2.03–1.93 (m, 2H), 1.40 (s, 12H), 1.34 (td, *J* = 7.1, 3.2 Hz, 9H). ^{13}C NMR (125 MHz, CD_3OD): δ 169.74, 142.46, 142.13, 140.61, 139.59, 129.36, 128.13, 123.57, 122.92, 121.79, 119.51, 115.88, 109.23, 96.51, 63.58, 27.05, 24.22, 21.71, 13.79, 13.79, 10.58. MS (ES+): *m*/*z* calcd for $C_{42}H_{50}N_3O$ 612.3948, found 612.3936.

Synthesis of Compound 33. Method B was used and afforded a blue solid (101.9 mg, 0.140 mmol, 18.0% yield). Cy7-Cl (500 mg, 0.80 mmol, 1 equiv), *p*-anisidine (289.1 mg, 2.3 mmol, 3 equiv), DMF (8 mL), and triethylamine (408 µL, 2.3 mmol, 3 equiv) were used. ^{1}H NMR (500 MHz,

$CDCl_3$): δ 8.06 (d, *J* = 13.6 Hz, 2H), 7.27 (ddd, *J* = 10.9, 5.4, 3.1 Hz, 5H), 7.24–7.18 (m, 2H), 7.08 (t, *J* = 7.4 Hz, 2H), 7.04 (d, *J* = 8.1 Hz, 2H), 6.94 (d, *J* = 7.9 Hz, 2H), 5.79 (d, *J* = 13.6 Hz, 2H), 3.97 (q, *J* = 7.2 Hz, 4H), 2.56 (t, *J* = 6.4 Hz, 4H), 1.98–1.86 (m, 2H), 1.37 (s, 12H), 1.37–1.33 (m, 6H). ^{13}C NMR (125 MHz, $CDCl_3$): δ 169.43, 160.69, 143.50, 142.90, 142.24, 140.74, 131.88, 130.84, 130.18, 129.03, 128.77, 128.29, 128.23, 125.29, 123.64, 123.59, 122.07, 118.91, 109.07, 96.87, 48.40, 28.34, 24.77, 21.70, 20.62, 11.88. MS (ES+): *m*/*z* calcd for $C_{41}H_{48}N_3O$ 598.3792, found 598.3779.

Synthesis of Compound 34. *p*-Anisidine (14 mg, 0.11 mmol) was added to a solution of IR-26 (40 mg, 0.056 mmol) in DMF (1 mL), and the reaction mixture was stirred for 0.5 h at room temperature. The solvent was removed under reduced pressure, and the resulting solid was dissolved in CH_2Cl_2 (25 mL). The organic solution was washed 3× with an aqueous potassium iodide solution (saturated, 3 × 25 mL), dried (Na_2SO_4), and concentrated under reduced pressure. The crude mixture was purified via trituration (cold acetone) to afford the title compound as a shiny red solid (15 mg, 0.021 mmol, 38%). ^{1}H NMR (400 MHz, DMSO-d_6): δ 11.66 (s, 1H), 8.31 (s, 2H), 7.95 (m, 2H), 7.66 (m, 6H), 7.61–7.49 (m, 10H), 7.39 (m, 4H), 7.13 (d, *J* = 12.4 Hz, 2H), 6.87 (d, *J* = 8.4 Hz, 2H), 3.42 (s, 3H), 2.81 (br. s, 4H), 1.88 (s, 2H). The product was too insoluble to obtain a ^{13}C NMR spectrum. MS (ES+): *m*/*z* calcd for $C_{47}H_{38}OS_2$ 696.2395, found 696.2385.

Synthesis of Compound 35. *p*-Anisidine (13 mg, 0.11 mmol) was added to a solution of IR-1061 (40 mg, 0.053 mmol) in DMF (1 mL), and the reaction mixture was stirred for 1 h at room temperature. The solvent was removed under reduced pressure, and the resulting solid was dissolved in CH_2Cl_2 (25 mL). The organic solution was washed 3× with an aqueous potassium iodide solution (saturated, 3× 25 mL) and dried (Na_2SO_4), and the solvent was removed under reduced pressure. The crude mixture was purified via silica column chromatography (5%

MeOH/CH_2Cl_2) followed by trituration (Et_2O) to afford the title compound as a shiny red solid (22 mg, 0.029 mmol, 55%). ^{1}H NMR (500 MHz, $CDCl_3$): δ 8.06 (d, *J* = 13.2 Hz, 2H), 7.69–7.64 (m, 4H), 7.52 (m, 4H), 7.40–7.29 (m, 17H), 7.05 (s, 2H), 6.60 (d, *J* = 8.5 Hz, 2H), 6.21 (d, *J* = 13.2 Hz, 2H), 3.39 (s, 3H), 2.52 (t, *J* = 6.3 Hz, 4H), 1.78 (q, *J* = 6.4 Hz, 2H). ^{13}C NMR (125 MHz, $CDCl_3$): δ 162.35, 156.26, 145.98, 145.78, 144.59, 140.06, 137.31, 136.50, 136.45, 130.32, 130.21, 129.19, 127.16, 126.31, 123.86, 121.00, 119.84, 114.64, 55.25, 28.84, 25.49, 21.78. MS (ES+): *m*/*z* calcd for $C_{51}H_{42}NOS_2$ 748.2708, found 748.2703.

Synthesis of Compound 36 (APNO-1080). *p*-Anisidine (27 mg, 0.10 mmol) was added to a solution of IR-1048 (80 mg, 0.11 mmol) in DMF (1 mL), and the reaction mixture was stirred for 4 h at room temperature. The reaction mixture was partitioned with CH_2Cl_2 (50 mL) and brine (50 mL). The organic layer was further washed with brine (6× 25 mL), dried (Na_2SO_4), and concentrated under reduced pressure. The crude mixture was purified via silica column chromatography (5% MeOH/CH_2Cl_2) followed by trituration (Et_2O) to afford the title compound as a dark solid (21 mg, 0.029 mmol, 25%). ^{1}H NMR (500 MHz, $CD_3OD/CDCl_3$): δ 8.35 (d, *J* = 12.8 Hz, 2H), 8.11 (d, *J* = 8.2 Hz, 2H), 7.64 (t, *J* = 7.9 Hz, 2H), 7.51 (d, *J* = 7.8 Hz, 2H), 7.34 (br. s, 2H), 7.27 (d, *J* = 8.4 Hz, 2H), 6.95 (m, 4H), 6.36 (d, *J* = 13.4 Hz, 2H), 4.08 (m, 4H), 3.76 (s, 3H), 2.77 (m, 4H), 2.11–2.00 (m, 2H), 1.83 (m, 4H), 1.48 (m, 4H), 1.01 (m, 6H). ^{13}C NMR (125 MHz, $CDCl_3$): δ 161.24, 157.18, 151.36, 140.85, 140.12, 136.77, 129.84, 128.37, 128.31, 126.52, 126.32, 125.02, 122.17, 114.97, 106.04, 102.96, 30.36, 25.07, 21.52, 20.26, 13.65. MS (ES+): *m*/*z* calcd for $C_{47}H_{38}OS_2$ 738.3018, found 738.3021.

Synthesis of Compound 37. *p*-Anisidine (100 mg, 0.81 mmol) was added to a solution of Et-1080 (2) (50 mg, 0.08 mmol) in DMF (2 mL), and the reaction mixture was heated to 40 °C for 24 h. The solvent was removed under reduced pressure, and the resulting solid was dissolved in CH_2Cl_2

(25 mL). The organic solution was washed 3× with an aqueous potassium iodide solution (saturated, 3× 25 mL) and dried (Na_2SO_4), and the solvent was removed under reduced pressure. The crude mixture was purified via silica column chromatography (5% MeOH/CH_2Cl_2) followed by trituration (Et_2O followed by MeOH) to afford the title compound as a dark solid (18 mg, 0.027 mmol, 34%). ^{1}H NMR (500 MHz, DMSO-d_6): δ 10.10 (s, 1H), 8.27 (d, J = 13.2 Hz, 2H), 8.07 (d, J = 8.1 Hz, 2H), 7.66 (t, J = 7.7 Hz, 2H), 7.58 (m, 4H), 7.37 (m, 2H), 7.31 (m, 4H), 7.02 (d, J = 8.4 Hz, 2H), 6.54 (d, J = 13.3 Hz, 2H), 4.27 (m, 4H), 3.70 (s, 3H), 2.80 (m, 4H), 1.97–1.91 (m, 2H), 1.31 (m, 6H). ^{13}C NMR (125 MHz, DMSO-d_6): δ 161.11, 156.96, 150.90, 141.54, 140.12, 137.62, 130.29, 130.15, 129.98, 129.65, 126.78, 126.08, 125.51, 122.58, 120.75, 115.41, 107.29, 103.57, 55.91, 38.29, 25.24, 21.68, 13.81. MS (ES+): m/z calcd for $C_{43}H_{40}N_3O$ 614.3171, found 614.3181.

Synthesis of Compound 38. *p*-Anisidine (76 mg, 0.62 mmol) was added to a solution of Flav7 (3) (50 mg, 0.075 mmol) in DMF (2 mL), and the reaction mixture was heated to 40 °C for 24 h. The reaction mixture was partitioned with CH_2Cl_2 (50 mL) and brine (50 mL). The organic layer was further washed with brine (6 × 25 mL), dried (Na_2SO_4), and concentrated under reduced pressure. The crude mixture was purified via silica column chromatography (5% MeOH/CH_2Cl_2) followed by trituration (Et_2O) to afford the title compound as a dark red solid (10 mg, 0.013 mmol, 18%). ^{1}H NMR (500 MHz, $CDCl_3$): δ 8.26 (m, 1H), 7.98 (m, 3H), 7.68 (m, 2H), 7.47–7.42 (m, 6H), 7.39 (d, J = 8.5 Hz, 2H), 7.23 (s, 2H), 6.71 (d, J = 9.0 Hz, 2H), 6.65 (d, J = 8.5 Hz, 2H), 6.51 (d, J = 13.0 Hz, 2H), 6.40–6.36 (m, 2H), 3.44 (s, 3H), 3.03 (s, 12H), 2.64 (s, 4H), 1.90 (s, 2H). The product was too insoluble to obtain a ^{13}C NMR spectrum. MS (ES+): m/z calcd for $C_{51}H_{48}N_3O_3$ 750.3696, found 750.3674.

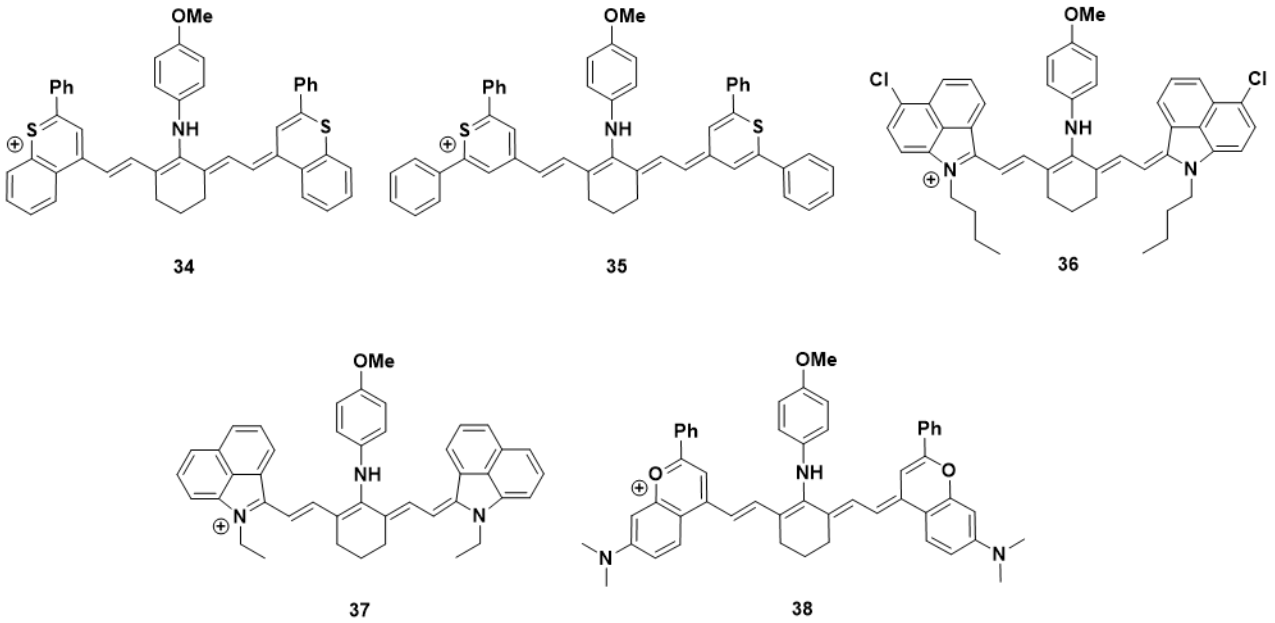

Structures of NIR-II NO Probes.

Photophysical Characterization. Extinction coefficients were acquired in experimental triplicate. Extinction coefficients were acquired via a known concentration of the probe within the linear range (absorbance = 0.05 to 1.5). 50% EtOH/potassium phosphate buffer (pH = 7.4). *N*-nitrosated products were generated by reacting probes 1-7 (2 μM) with MAHMA-NONOate (100 equiv.) at 25 °C in both 50 mM HEPES buffer in 0.01% CrEL (pH = 7.2) and 50% EtOH potassium phosphate buffer (pH = 7.4) for 30 minutes and 5 seconds, respectively, where complete conversion was monitored via UV-Vis spectroscopy.

Kinetics Measurements. Kinetic measurements were obtained in experimental triplicate. APNOs 1-7 (2 μM) were suspended in 50 mM HEPES buffer in 0.01% CrEL (pH = 7.2). MAHMA-NONOate (100 equiv.) was titrated into the solution at 25 °C. UV-Vis measurements (250-900 nm) were taken every 30 seconds for 10 minutes, and the change in absorbance of the *N*-nitrosated

product was monitored. Hammet[84] and pK_a values were obtained and related to the experimental relative rates.

***In Vitro* Buffer Preparation.** 20 mM potassium phosphate solution was prepared by adding 242 mg of K_2HPO_4 and 83 mg of KH_2PO_4 to 100 mL of DI water. An equal volume of ethanol was added to prepare ethanolic potassium phosphate buffer. Adjustments to pH were made via addition of 1 M HCl or 1 M NaOH. pH values were determined using a Mettler-Toledo SevenCompact pH meter calibrated using pH 4.0, 7.0 and 10.0 standard buffers at 25 °C.

Epifluorescence imaging of nitric oxide under AneroPack® Hypoxic Conditions. 24 well plates were seeded with 25,000 4T1 murine mammary carcinoma cells (0.5 mL of 50,000 cell/mL) in RPMI 1640 media containing 10% FBS and allowed to incubate at 37 °C with 5% CO_2 for 24 h. The media was removed, and the cells were stained with APNO-780 (5 μM) in serum-free RPMI 1640 media for 90 minutes under the same conditions. After staining was complete, the solution was removed, and the cells were washed with PBS (0.5 – 1.0 mL) and incubated in serum-free RPMI media for 6 h at 37 ºC in a sealed container either with or without an AneroPack® (Mitsubishi Gas Company). When performing inhibition studies, the solution was prepared with l-NG-nitroarginine (L-NNA, 10 μM, non-selective NOS inhibitor). Each well was imaged (n = 3) using the Cy7 filter cube (EVOS fluorescence microscope) and analyzed using ImageJ. The average fluorescence was measured as the mean of five randomly selected cells and the error is reported between biological replicates (n = 3).

Selectivity Studies. The initial absorbance (800 - 1200 nm or 500 - 950 nm) was measured before the addition of reactive metals (1 mM), thiols (GSH (1mM); Cys (500 μM); H_2S (100 μM)), oxygen (1 mM), carbonyl (1 mM), and nitrogen species (1 mM; $ONOO^-$ (50 μM); NO (100 μM)).

After addition, the reaction was sealed and incubated for 1 h. Final measurements were recorded, and relative turn-on was determined by change in absorption at λ_{abs} of the probe and turnover product. All metal solutions were prepared in water from their chloride salt, except for $FeSO_4 \cdot (H_2O)_7$. Aqueous perchlorate, nitrite, and nitrate solutions were prepared for their corresponding sodium salts. Superoxide anion was added as a solution of potassium superoxide in DMSO. Nitroxyl was generated *in situ* from a solution of Angeli's salt in degassed 10 mM potassium hydroxide solution. NO was generated *in situ* from a solution of MAHMA-NONOate in degassed 10 mM potassium hydroxide. Hydroxyl radical was generated via Fenton chemistry between Mohr's salt (solution in degassed 1 M aqueous hydrochloric acid) and hydrogen peroxide. Peroxynitrite was synthesized according to a literature report.[98] All other analytes were prepared by dilution from commercially available sources.

Microsome Assay. The initial absorbance of 10 μM APNO-1080 with 10 μL RLM in 0.1 M potassium phosphate buffer (pH 7.4) was measured. After addition of 50 μM NADPH, the reaction was incubated at 37 °C for 1h. The final absorbance was measured after quenching with acetonitrile.

Cytotoxicity Assay. A549 cells were plated ($5x10^4$ cells/well) in a 24-well plate in Ham's F12-K (10% FBS) media for 24 h. A549 cells were then incubated with 0.0, 0.1, 5.0, 10.0, and 25 μM APNO-1080 at 37 °C in serum-free DMEM media. After 24 h, media was replaced with 5 mg/mL MTT reagent (1:20 in PBS) and incubated for 1 h at 37 °C. Cells were then lysed using 500 μL DMSO, transferred to a 96-well plate and absorbances were measured using a plate reader at 555 nm. Viability was measured relative to absorbance of control wells.

Tissue Phantom Preparation. Tissue phantoms were prepared by suspending agarose LE (750 mg) in deionized water (50 mL). The suspension was heated for 1 minute in a microwave until a viscous, translucent gel was produced. Immediately, 1 mL of 2% milk was added. The hot gel was poured into a mold (0.5, 1, and 3 cm in depth) containing two plastic straws (3 mm diameter) and cooled at room temperature for at least 20 minutes. After cooling, the straws were removed and the gel was removed from the mold, yielding a tissue phantom with two parallel channels for the placement of FEP tubes containing sample solutions.

Tissue Phantom PA Imaging. A solution of APNO-1080 (50 μM, ethanolic potassium phosphate, pH 7.4) with or without 100 μM MAHMA-NONOate was injected into a tube which was then inserted into the cylindrical tissue phantom for imaging. The phantom was placed into the holder and excited from 700 – 1150 nm with 5 nm intervals. The spectrum that was obtained was later used for spectral unmixing.

In the head-to-head phantom study to evaluate PA signal in varying tissue phantom depths with APNO-1080 and APNO-780, 10 μM in ethanolic potassium phosphate buffer (pH 7.4) with or without 100 μM MAHMA-NONOate was used.

Photostability Assay. A solution of APNO-1080 (50 μM, ethanolic potassium phosphate, pH 7.4) was injected into a tube which was then inserted into the cylindrical tissue phantom for imaging. The phantom was placed into the holder and irradiated at 905 nm continuously for 300 s. A solution of APNO-1080 or APNO-780 (50 μM, ethanolic potassium phosphate, pH 7.4) containing 100 μM MAHMA-NONOate was injected into a tube which was then inserted into the cylindrical tissue phantom for imaging. The phantom was placed into the holder and irradiated at 1045 or 705 nm continuously for 300 s, respectively.

Live-subject Statement. All animal experiments were performed with the approval of the IACUC of the University of Illinois at Urbana–Champaign, following the principles outlined by the American Physiological Society on research animal use.

Orthotopic Bioluminescent Breast Cancer Model. 6 to 8-week-old female BALB/c mice were inoculated with 4T1-Luc cells (100 µL of 1 × 106 cells/mL in 1:1 serum-free RPMI 1640 media and Matrigel) via subcutaneous injection into the mammary fat pad. Tumor volumes were measured using the caliper method and the body weight of the mice was monitored over the course of the experiment. After 30 days, the tumors had grown to a final volume of 300-400 mm^3.

Heterotopic Bioluminescent Lung Cancer Animal Model. 4 to 5-week-old female Nu/J mice were used to surgically inject cancer cells into the liver. The mice were anesthetized, and aseptic technique was followed throughout the procedure. A laparotomy was performed, then $5x10^6$ A549-Luc2 cells (50 µL, 1:1 PBS:Matrigel) were slowly injected into the liver. 5-0 Vicryl sutures and wound clips were used to close the abdominal wall and skin, respectively. Tumor growth was monitored for up to 10 weeks via bioluminescence imaging. We acknowledge Drs. Herndon and Xu for performing these procedures.

***In Vivo* Bioluminescence Imaging.** A fresh solution of D-Luciferin in DPBS (15 mg/mL) was prepared before imaging. Each mouse was administered 150 mg D-Luciferin/kg of body weight via IP injection. Each mouse was imaged using the IVIS Spectrum CT to monitor tumor burden in A549-Luc2 xenografts at 15 minutes post-injection.

***In Vivo* PA Imaging.** A549-Luc2 and 4T1-Luc tumor bearing mice were administered APNO-1080 (50 µM, 100 µL in saline containing 10% DMSO) via retro-orbital injection. The mice were continuously anesthetized using isoflurane and placed in the prone position in the animal holder for imaging immediately before injection and 30 minutes post injection. The temperature of the

imaging chamber was set to 36 °C and the animal was allowed to equilibrate to the temperature for 10 minutes before imaging. Cross-sectional images were acquired either at the abdomen or lower mammary region of the mouse for either liver or mammary fat pad imaging with a step size of 0.3 mm. The imaging position was guided by the built-in anatomy atlas in the MSOT InVision 128 and was kept consistent for all scans. The major wavelengths used were selected based on the absorbance of *N*-nitrosated APNO-1080 and endogenous absorbers (700 nm, 730 nm, 760 nm, 800 nm, 850 nm, 874 nm, 900 nm, 905 nm, 930 nm, 1000 nm, 1065 nm, 1079 nm, 1150 nm). 10 frames were recorded at every imaging wavelength. Subsequently, spectral unmixing was used to separate signals coming from HB and HbO_2.

Field of View Selection. The field of view for all experiments performed on the MSOT InVision 128 imaging system (iTheraMedical) was selected by using the built-in, cross-sectional anatomy guide to correctly position the animals to image the mammary fat pad or liver.

4.8 Supplemental figures, tables, and spectra

Compound	λ_{abs} (nm)	λ_{abs} of *N*-nitrosated product (nm)	ε (10^4 M^{-1} cm^{-1})
1	**763**	**800**	**ND**
2	**758**	**808**	**ND**
3	**744**	**804**	**ND**
4	**746**	**808**	**ND**
5	**744**	**806**	**ND**
6	**727**	**802**	**ND**
7 (APNO-780)	**727**	**807**	**3.5**
8	**Insoluble**	**Insoluble**	**ND**
9	**816**	**1078**	**ND**
10 (APNO-1080)	**874**	**1080**	**9.2**
11	**878**	**1043**	**ND**
12	**790**	**No turnover**	**ND**

Supplementary Table 3. Photophysical properties in ethanolic potassium phosphate buffer. ND = Not determined.

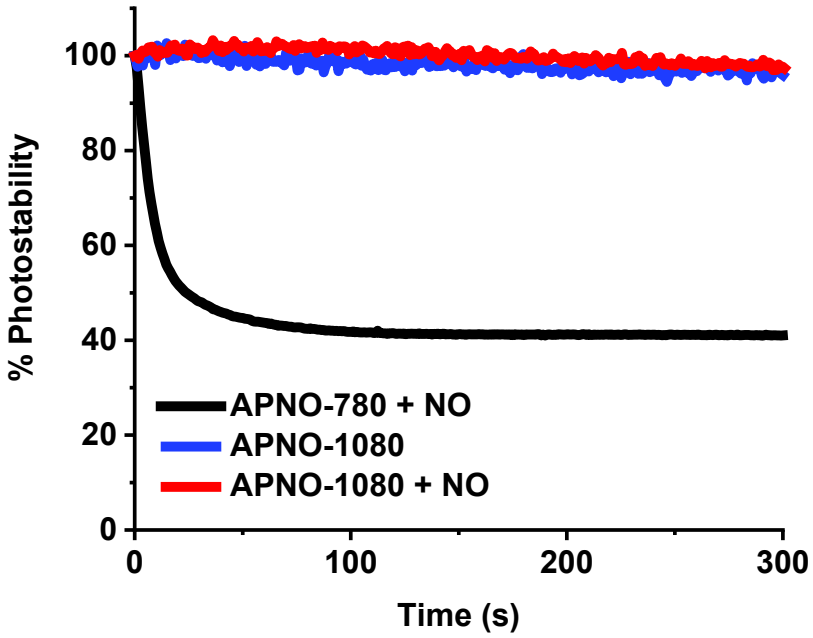

Supplementary Figure 46. Photostability assay where APNO-1080 with (red) and without (blue) NO treatment is continuously irradiated with a pulsed laser at their respective λ_{abs} for 300 s. Photostability assay where APNO-780 with (black) NO treatment is continuously irradiated with a pulsed laser at its respective λ_{abs} for 300 s.

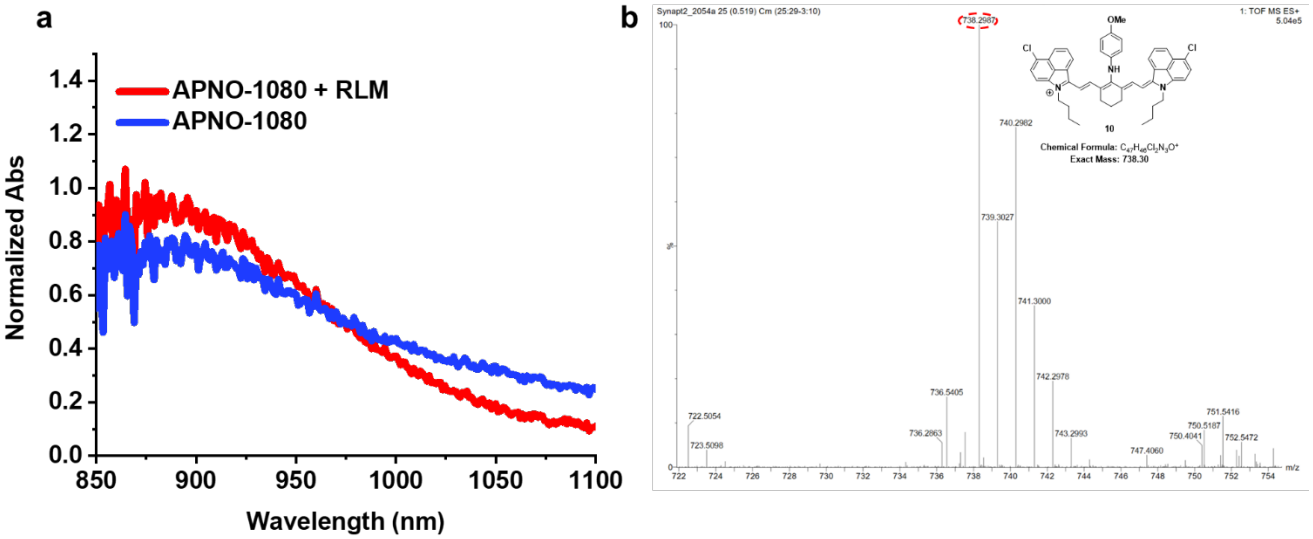

Supplementary Figure 47. a. Normalized absorbance spectra of APNO-1080 after 1 h incubation with RLM (red) and 1 h without RLM (blue). b. ESI-MS of RLM assay shown in Supplementary Figure 49a.

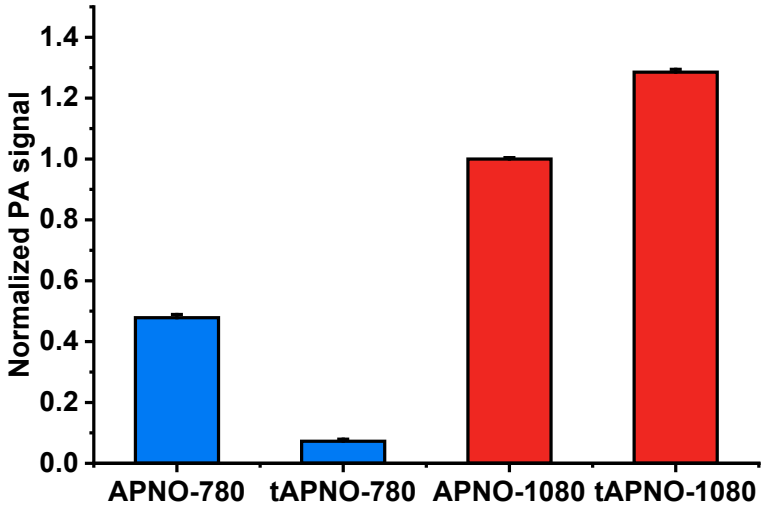

Supplementary Figure 48. Quantified PA imaging data of APNO-780 and APNO-1080 treated with and without NO. Solutions were overlayed with a 3 cm thick tissue imaging phantom. Error bars = SD (n = 3).

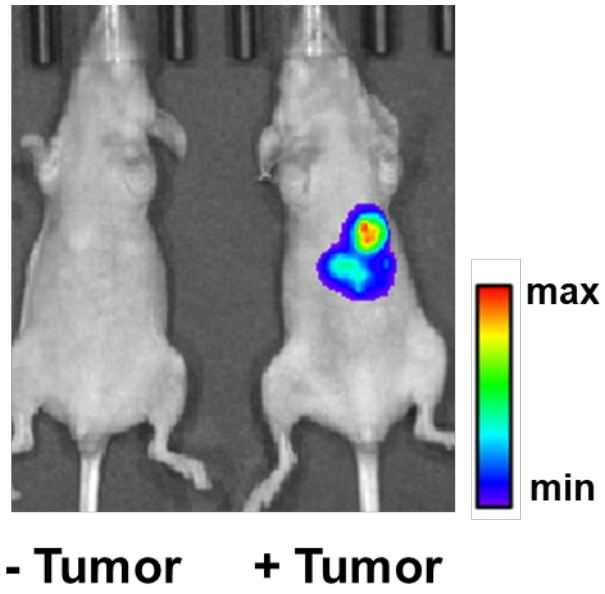

Supplementary Figure 49. Representative bioluminescent images of heterotopic A549-Luc2 xenograft model of liver metastasis.

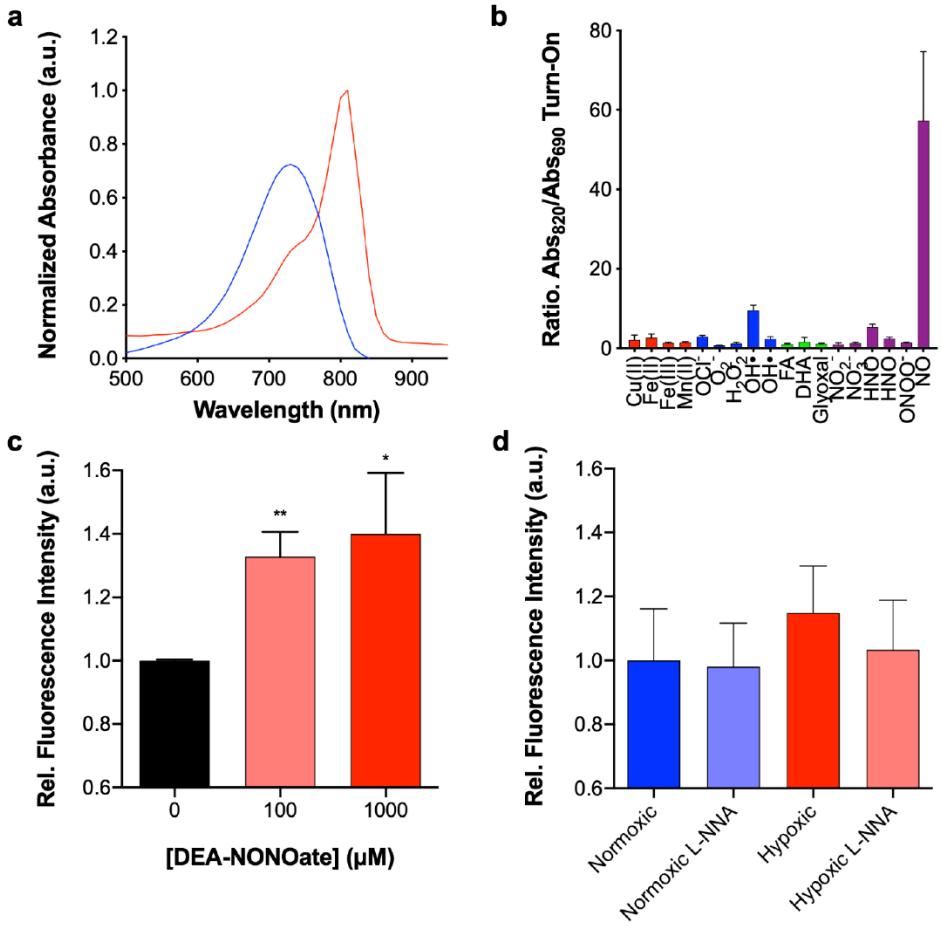

Supplementary Figure 50. a. Normalized absorbance spectra of APNO-780 with (red) and without (blue) NO treatment. b. APNO-780 (5 μM) absorption enhancement following 1 h treatment with excess (100 equiv.) reactive metal (red), carbonyl (green), oxygen (blue), or nitrogen (purple) species except for hydroxyl radical and peroxynitrite (10 equiv). c. Relative fluorescence observed following exogenous NO administration or d. endogenous hypoxic NO stimulation in 4T1 breast cancer cells. All spectra and assays were performed in 50 mM HEPES buffer (pH = 7.4) containing 0.1% CrEL (v/v). Relative fluorescence intensity was compared using an unpaired *t*-test (α = 0.05). *, $P < 0.05$; **, $P < 0.01$. Data presented as mean ± SD ($n = 3$) for b-c.

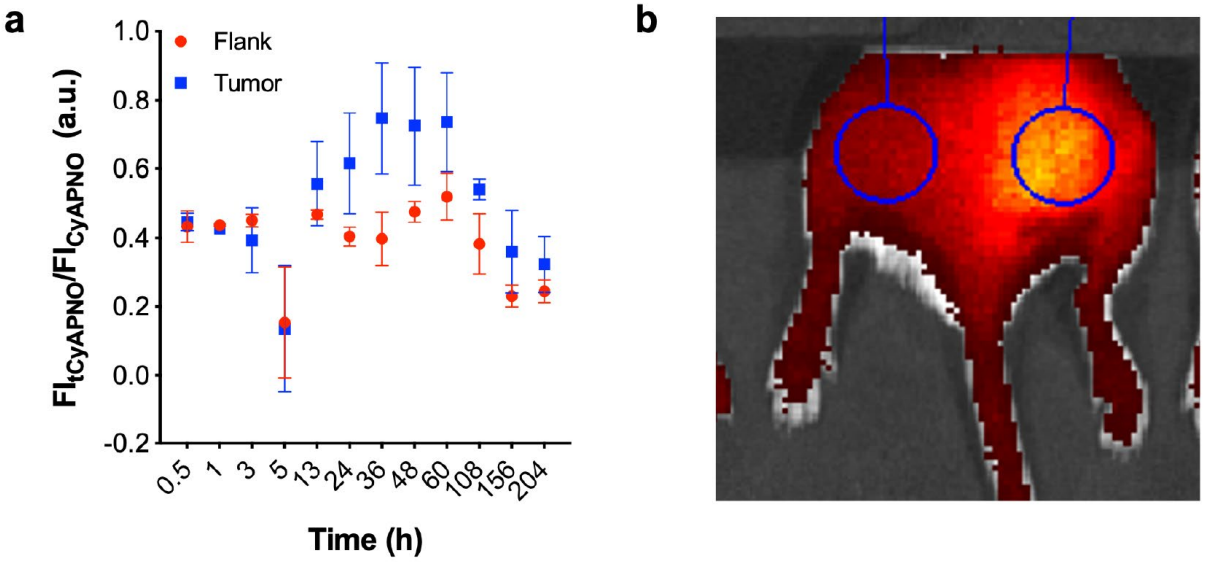

Supplementary Figure 51. a. Ratiometric fluorescence imaging of NO in a heterotopic 4T1 breast cancer model following systemic administration of APNO-780 (100 µL, 100 µM, retro-orbital). b. Representative image of fluorescence corresponding to the turnover product of APNO-780 in the flank (left) and tumor (right). Fluorescence intensity corresponding to APNO-780 is similar in the flank at tumor. Data presented as mean ± SD (n = 3). These results indicate APNO-780 is not suitable for *in vivo* imaging of cancer.

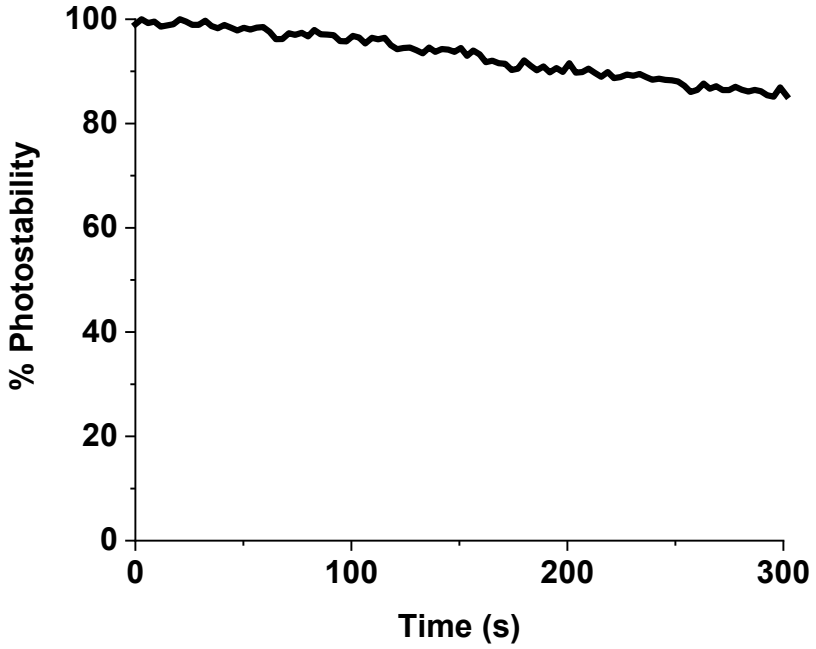

Supplementary Figure 52. Photostability assay where ICG (50 μM) is continuously irradiated with a pulsed laser at 810 nm 300 s.

Compound 27: ^{1}H NMR (500 MHz, CD_3OD)

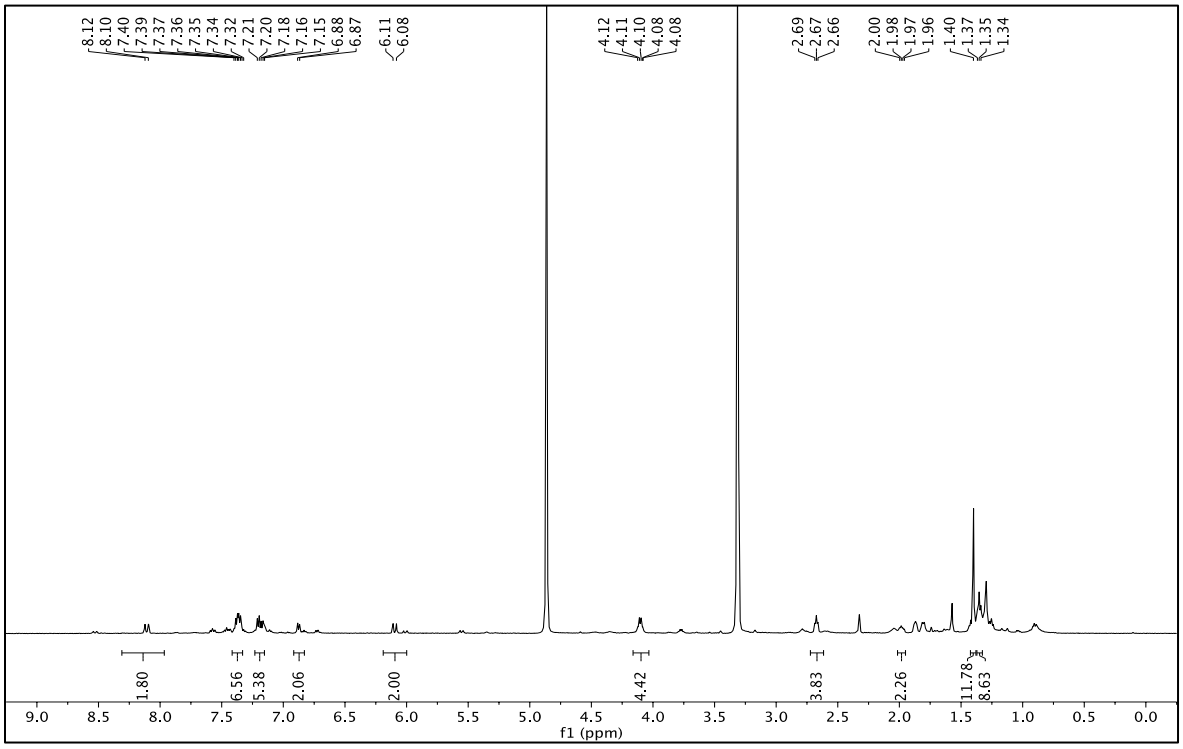

Compound 27: ^{13}C NMR (125 MHz, CD_3OD)

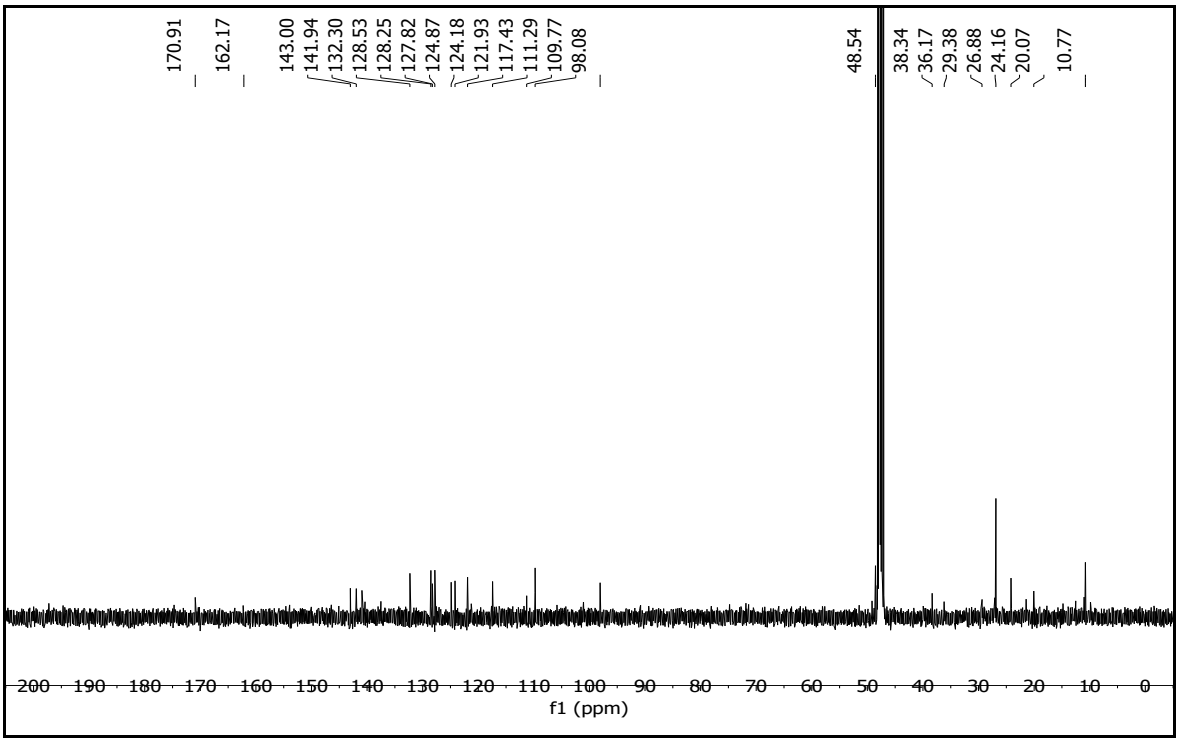

Compound 28: ^{1}H NMR (500 MHz, CD_3OD)

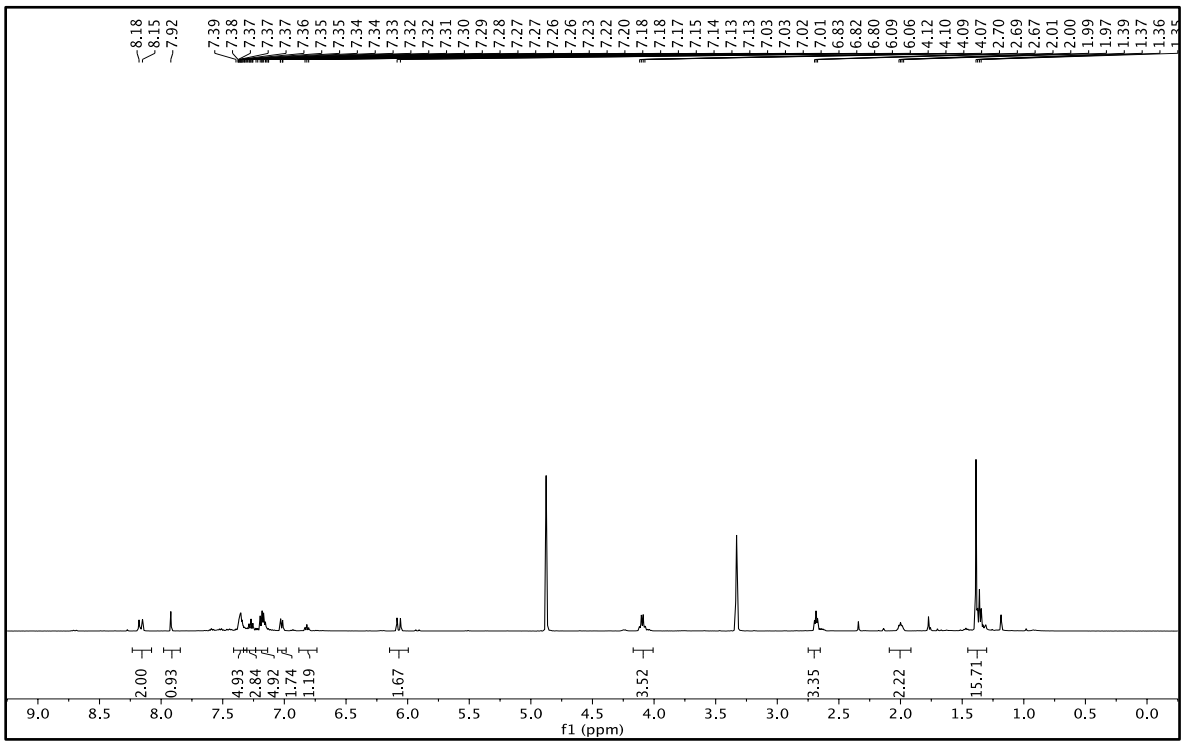

Compound 28: ^{13}C NMR (125 MHz, CD_3OD)

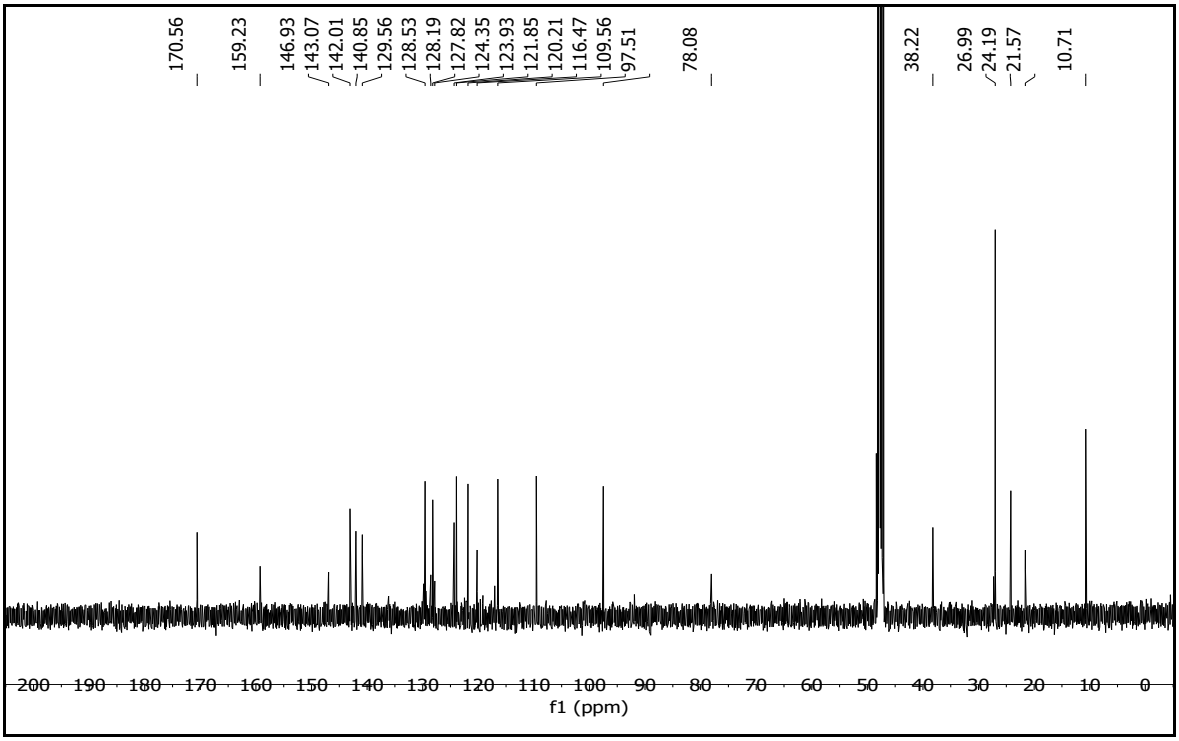

Compound 29: ^{1}H NMR (500 MHz, CD_3OD)

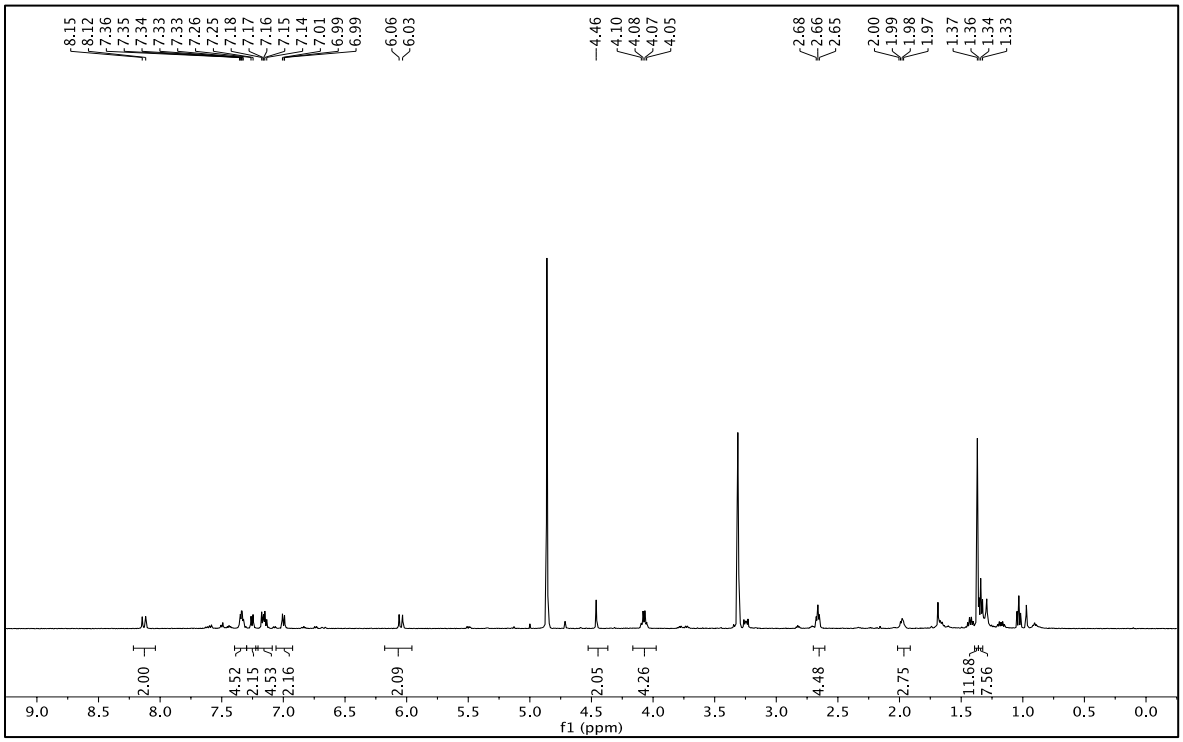

Compound 29: ^{13}C NMR (125 MHz, CD_3OD)

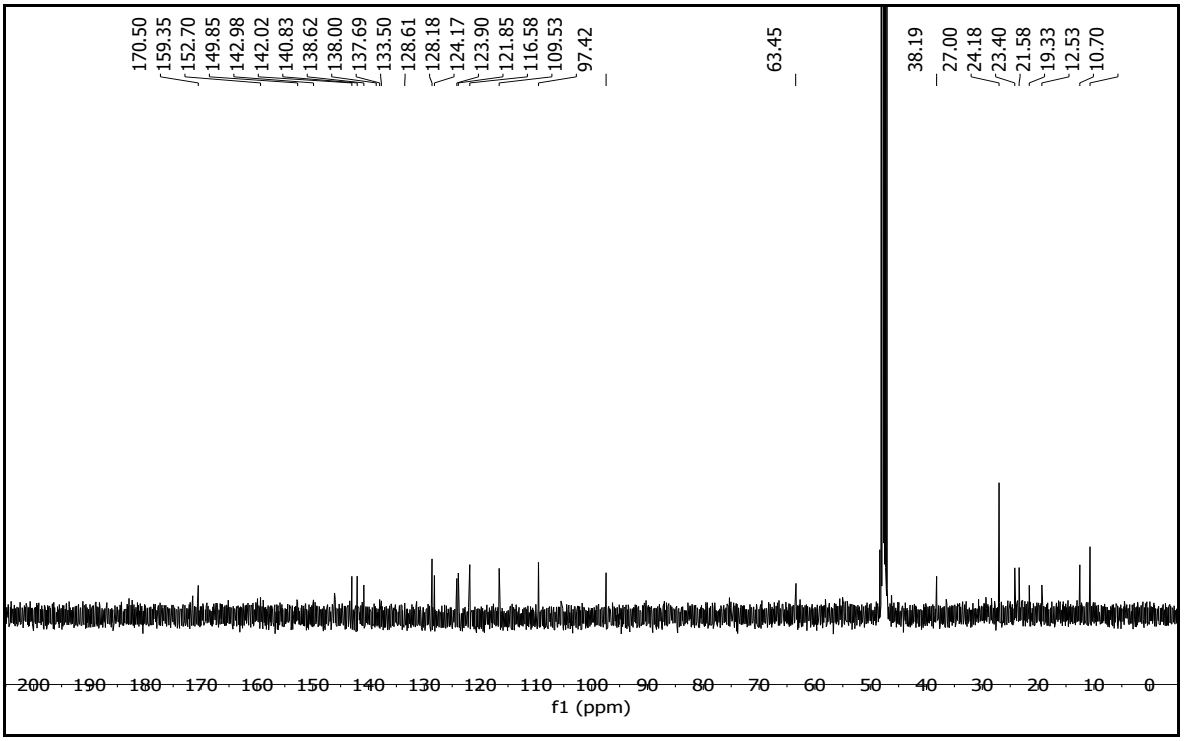

Compound 30: ^{1}H NMR (500 MHz, $CDCl_3$)

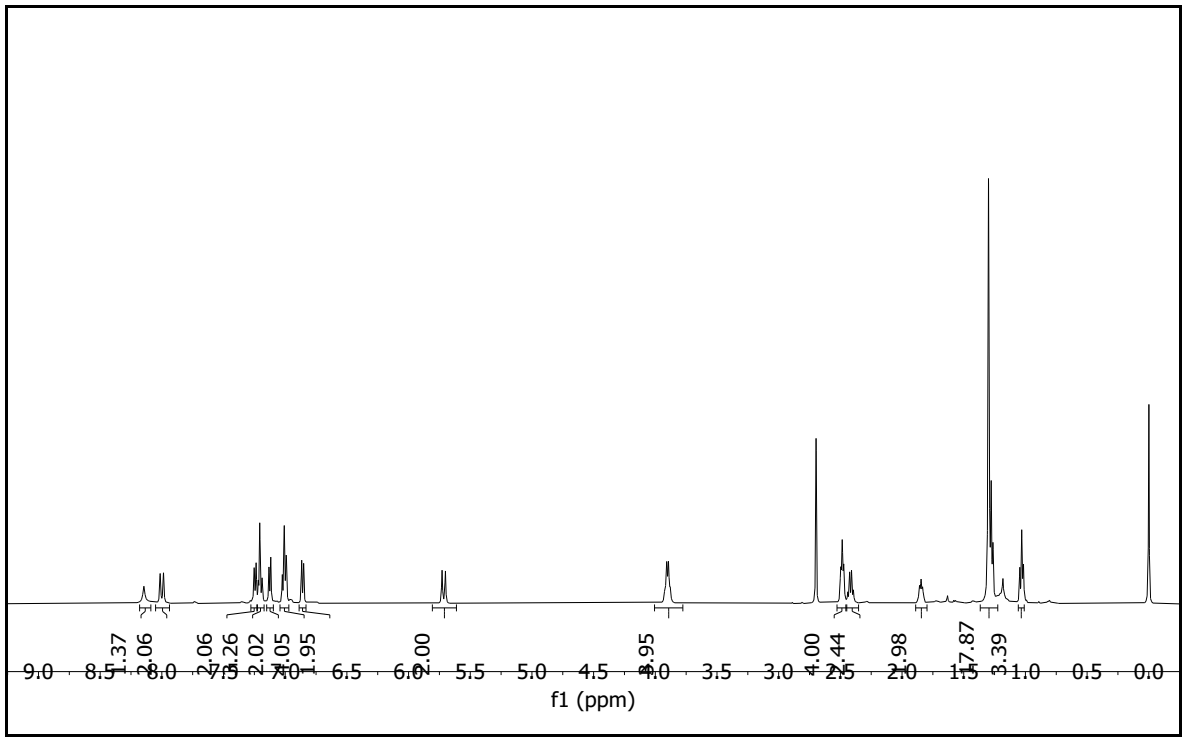

Compound 30: ^{13}C NMR (125 MHz, $CDCl_3$)

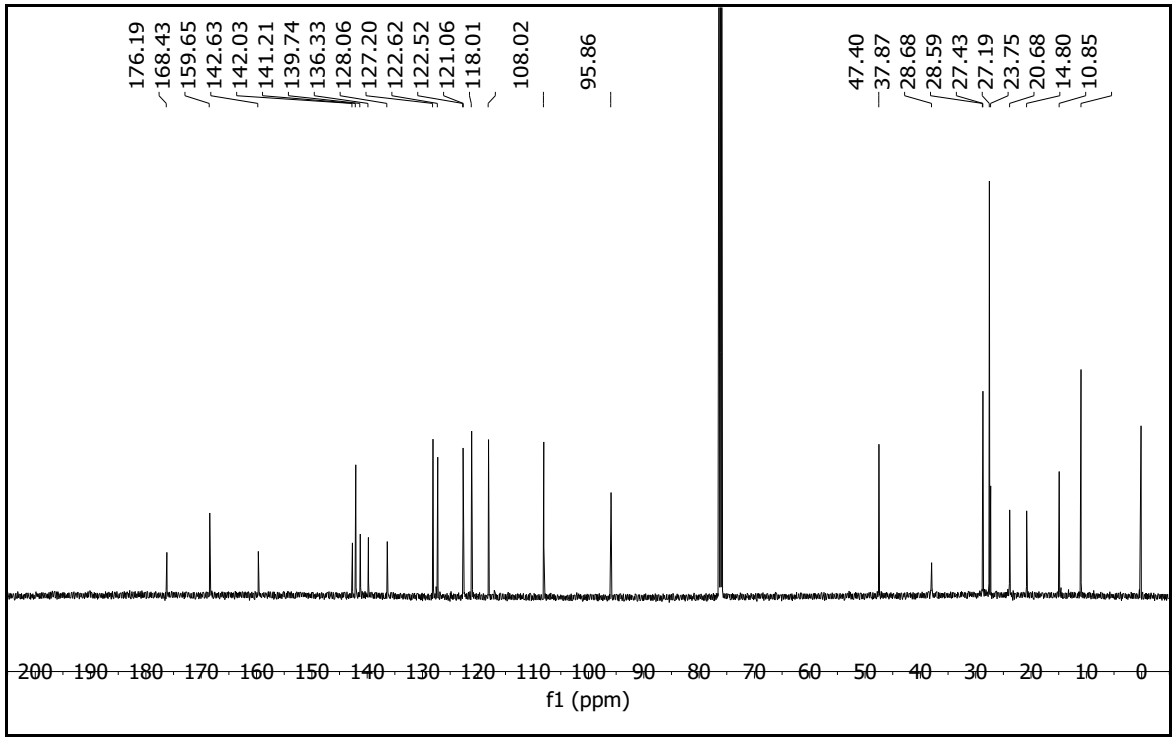

Compound 31: ^{1}H NMR (500 MHz, CD_3OD)

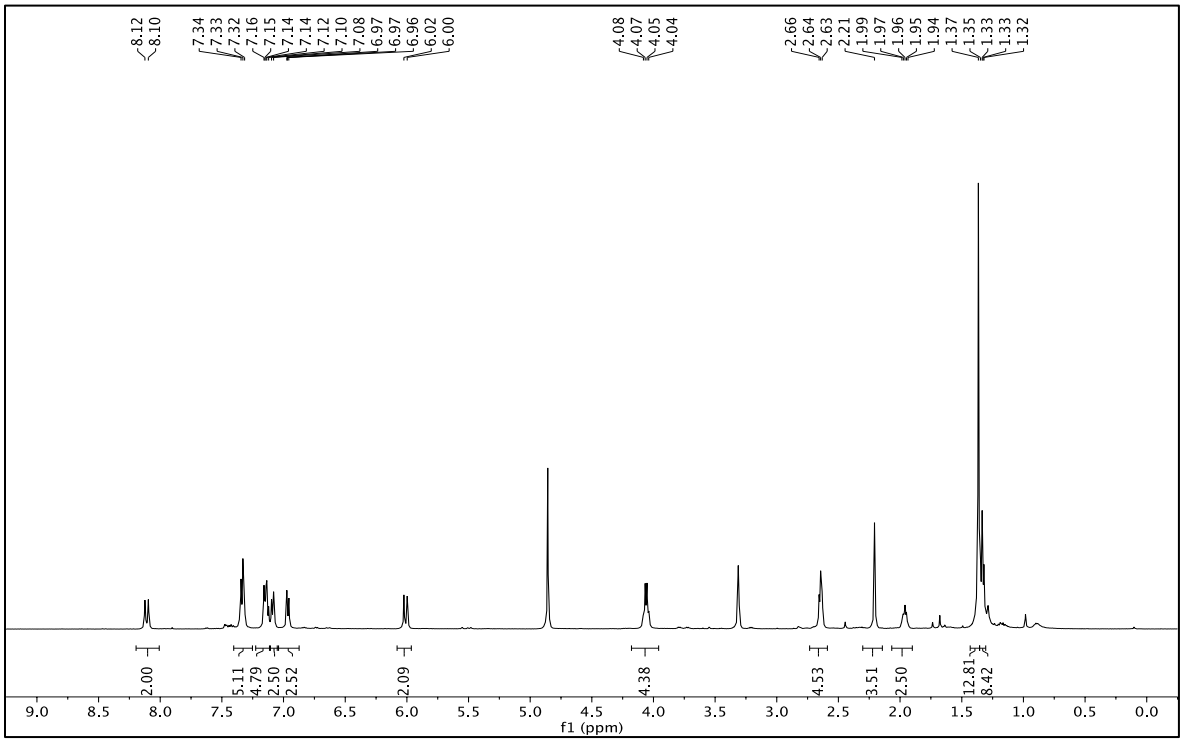

Compound 31: ^{13}C NMR (125 MHz, CD_3OD)

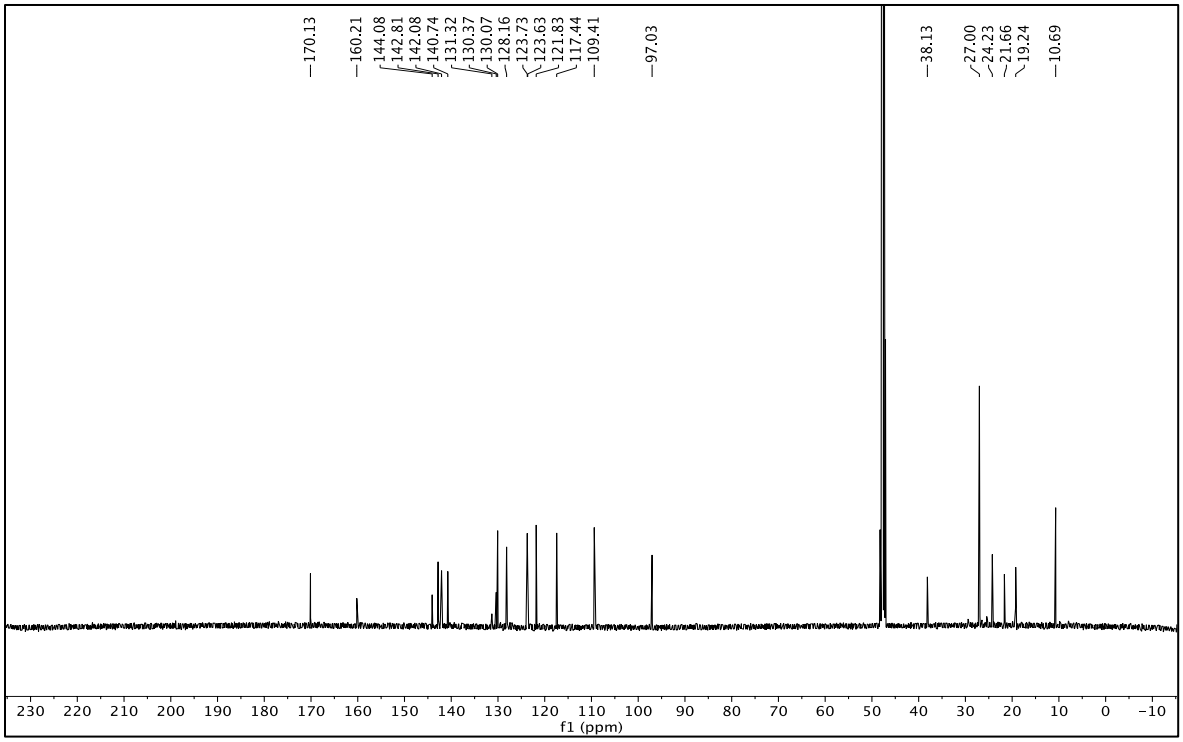

Compound 32: ^{1}H NMR (500 MHz, CD_3OD)

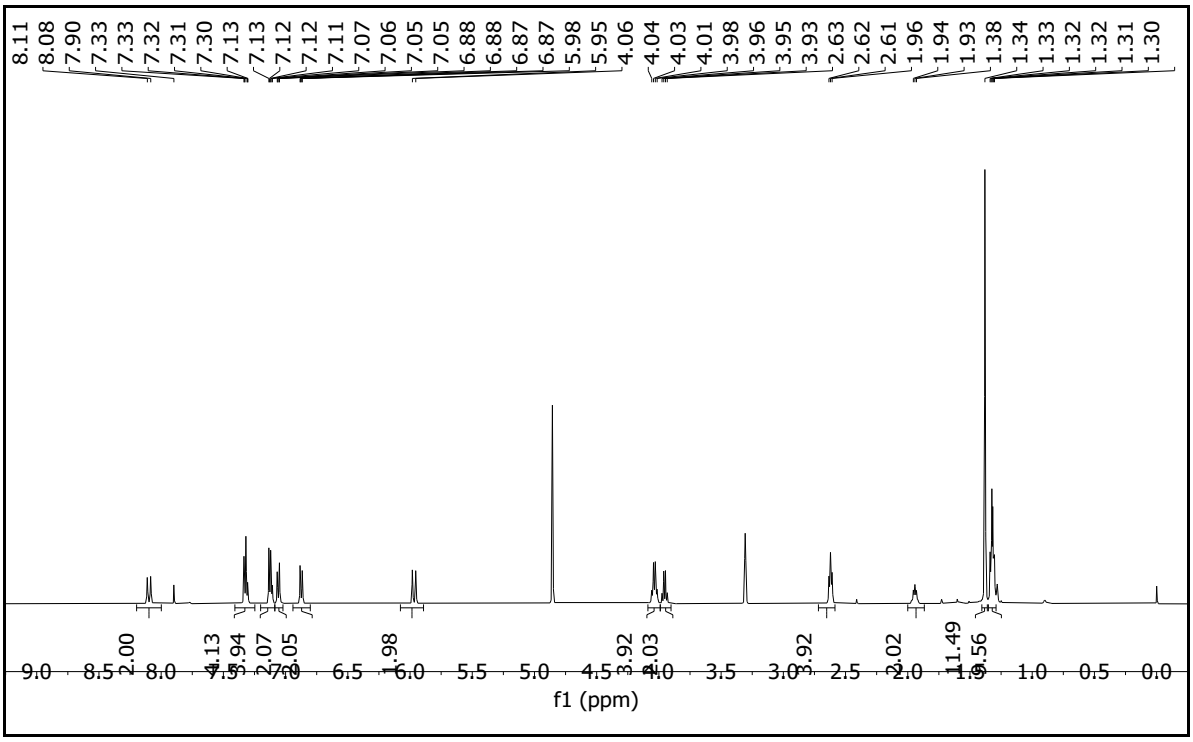

Compound 32: ^{13}C NMR (125 MHz, CD_3OD)

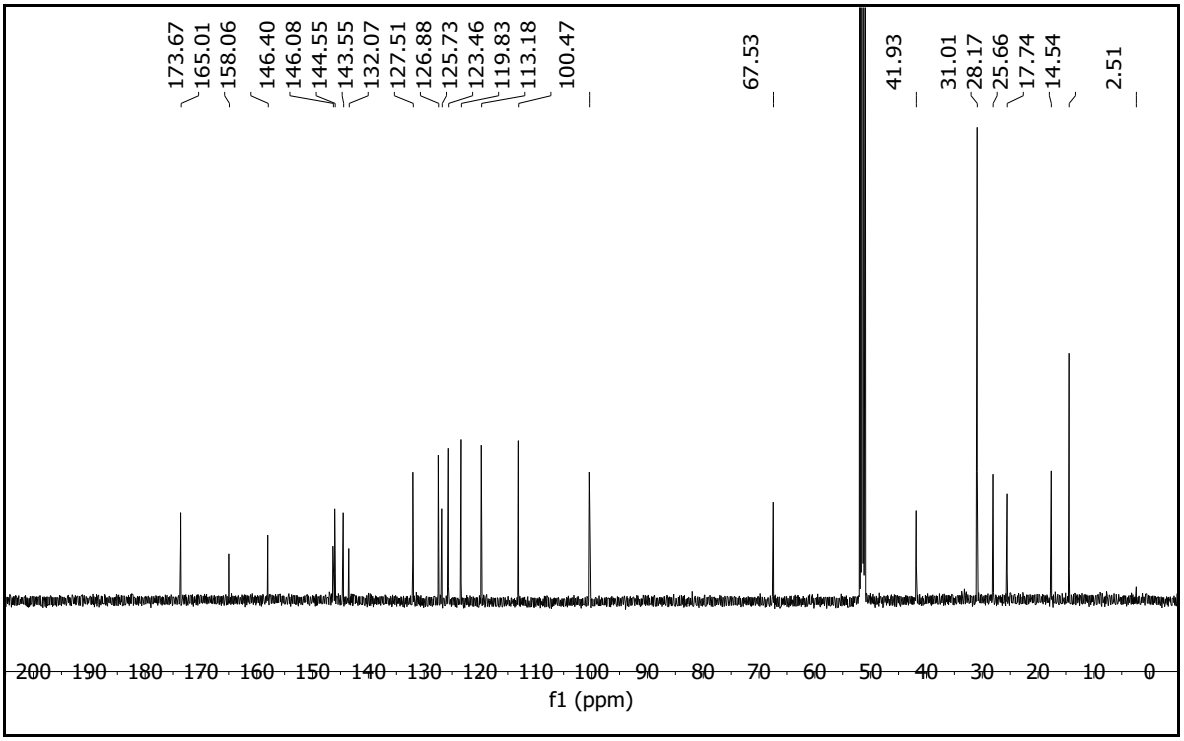

Compound 33: ^{1}H NMR (500 MHz, CD_3OD)

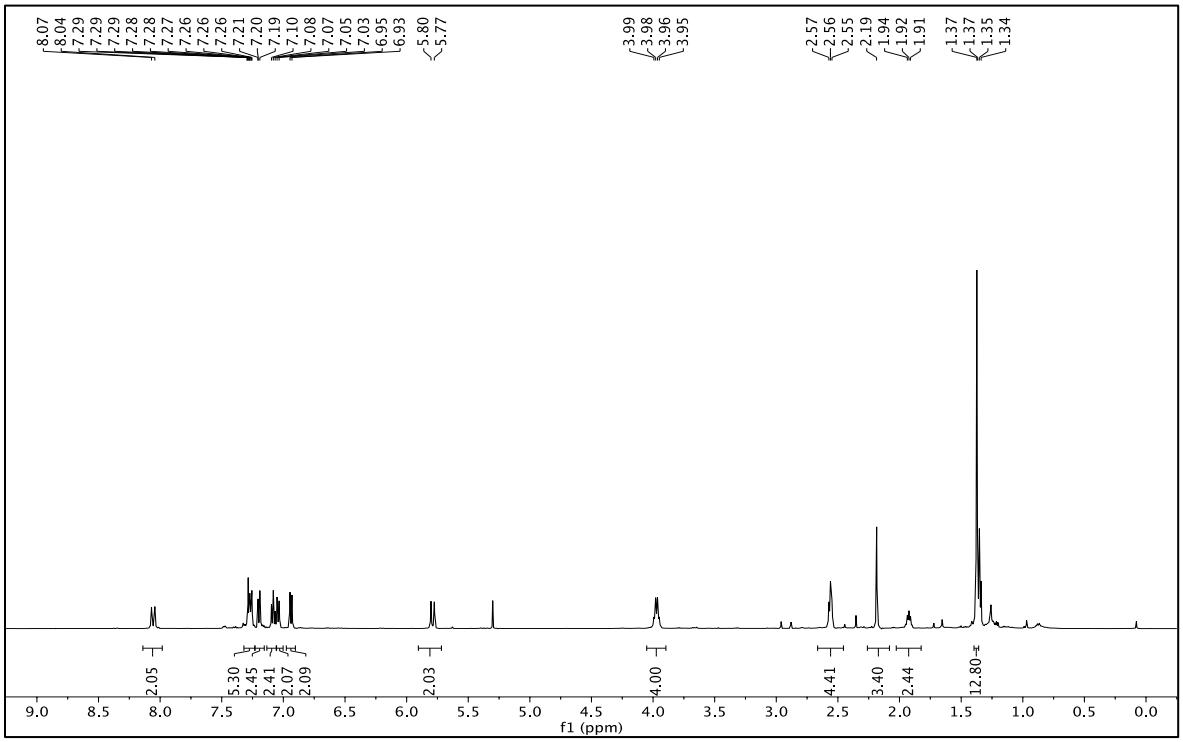

Compound 33: ^{13}C NMR (125 MHz, CD_3OD)

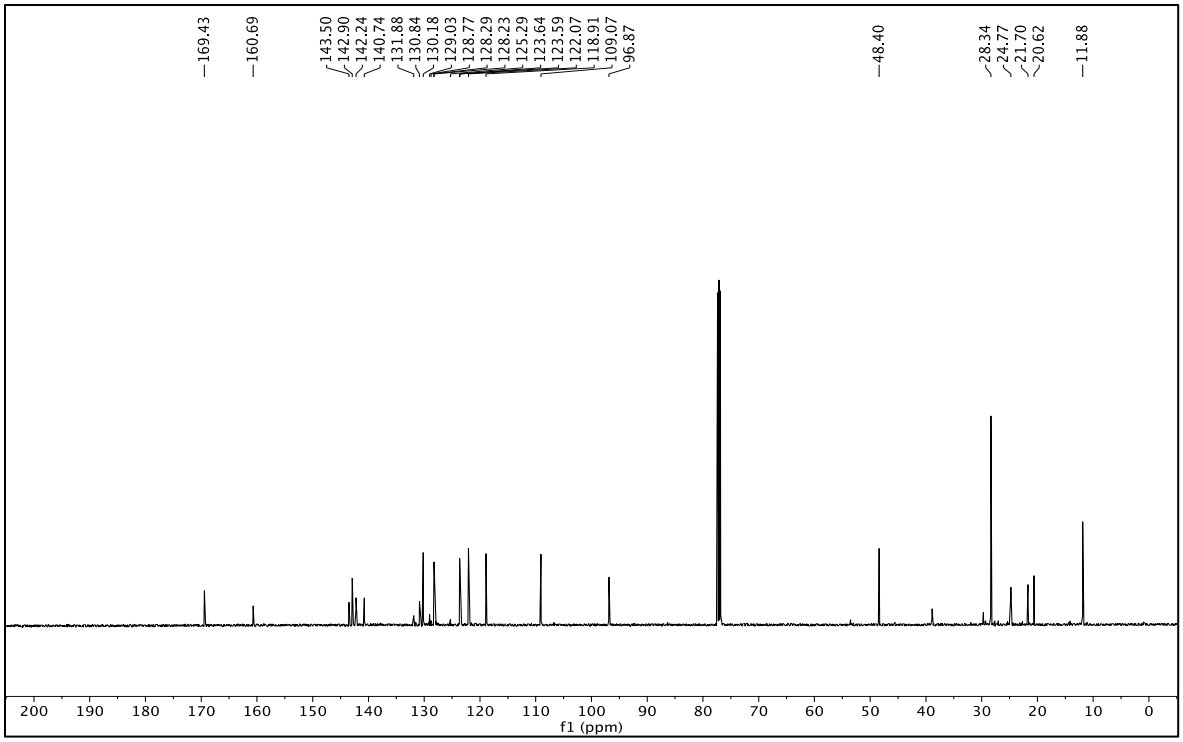

Compound 34: ^{1}H NMR (400 MHz, DMSO-d_6)

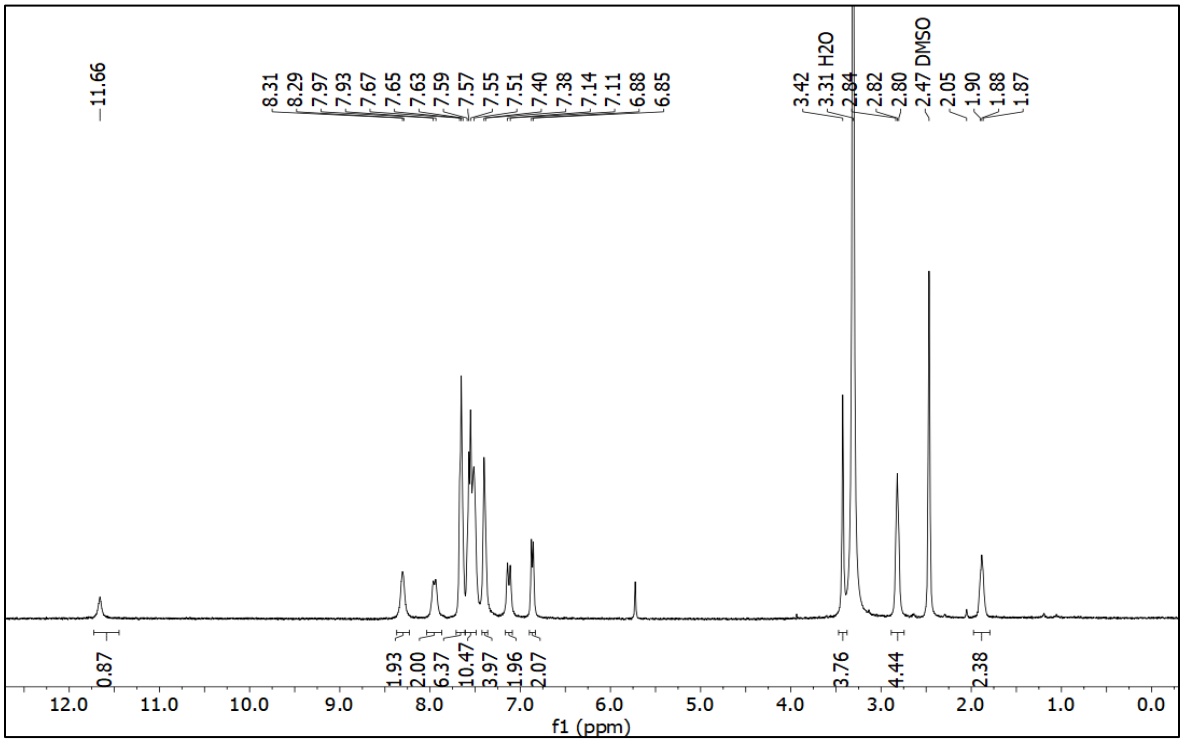

Compound 35: ^{1}H NMR (500 MHz, $CDCl_3$)

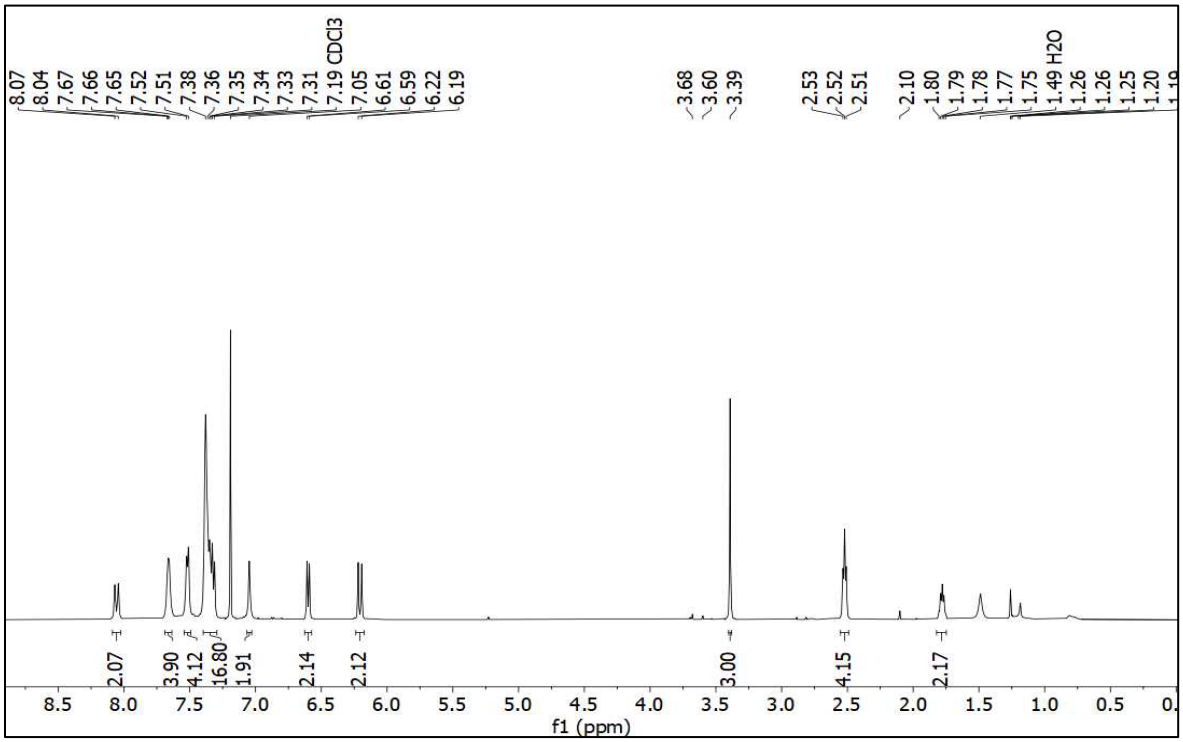

Compound 35: ^{13}C NMR (125 MHz, $CDCl_3$)

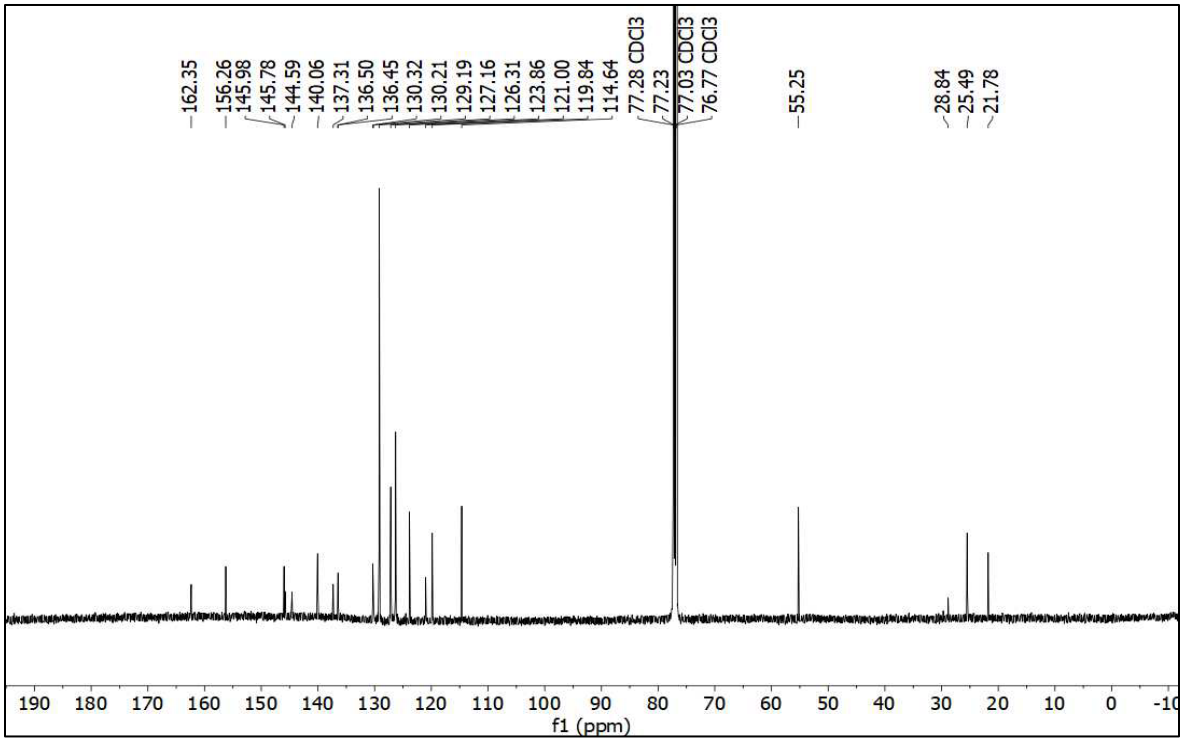

Compound 36: ^{1}H NMR (500 MHz, $CD_3OD/CDCl_3$)

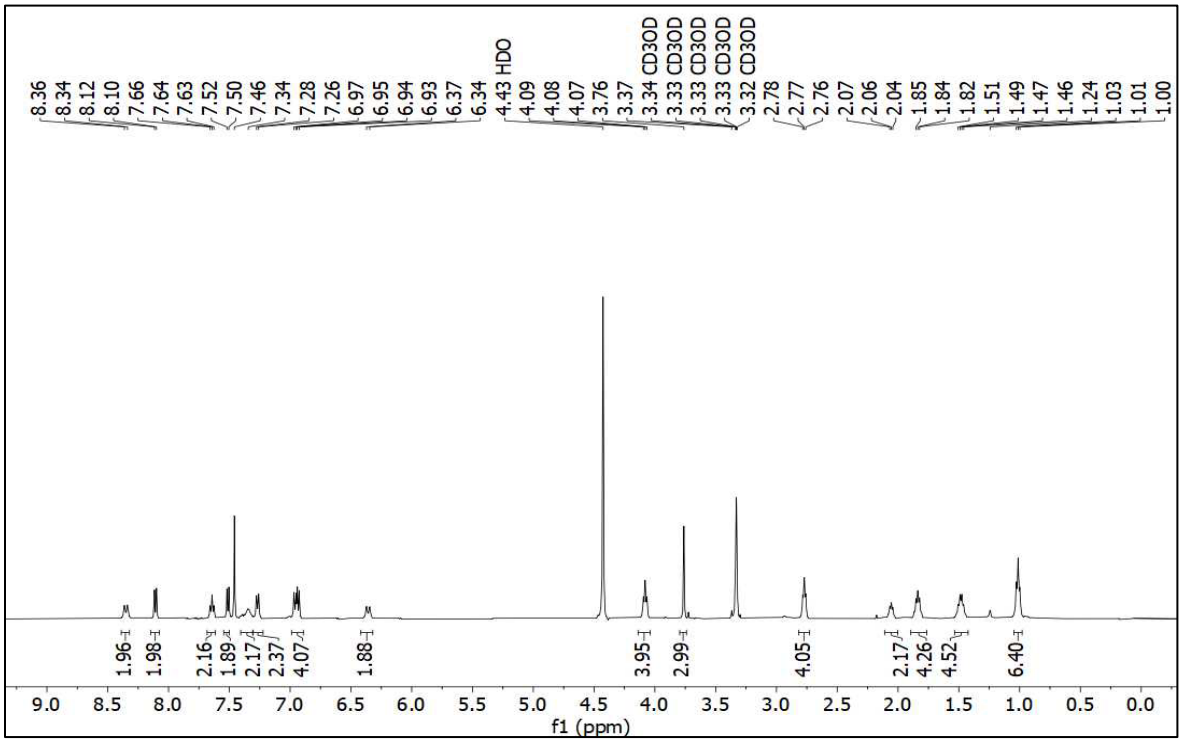

Compound 36: ^{13}C NMR (125 MHz, $CD_3OD/CDCl_3$)

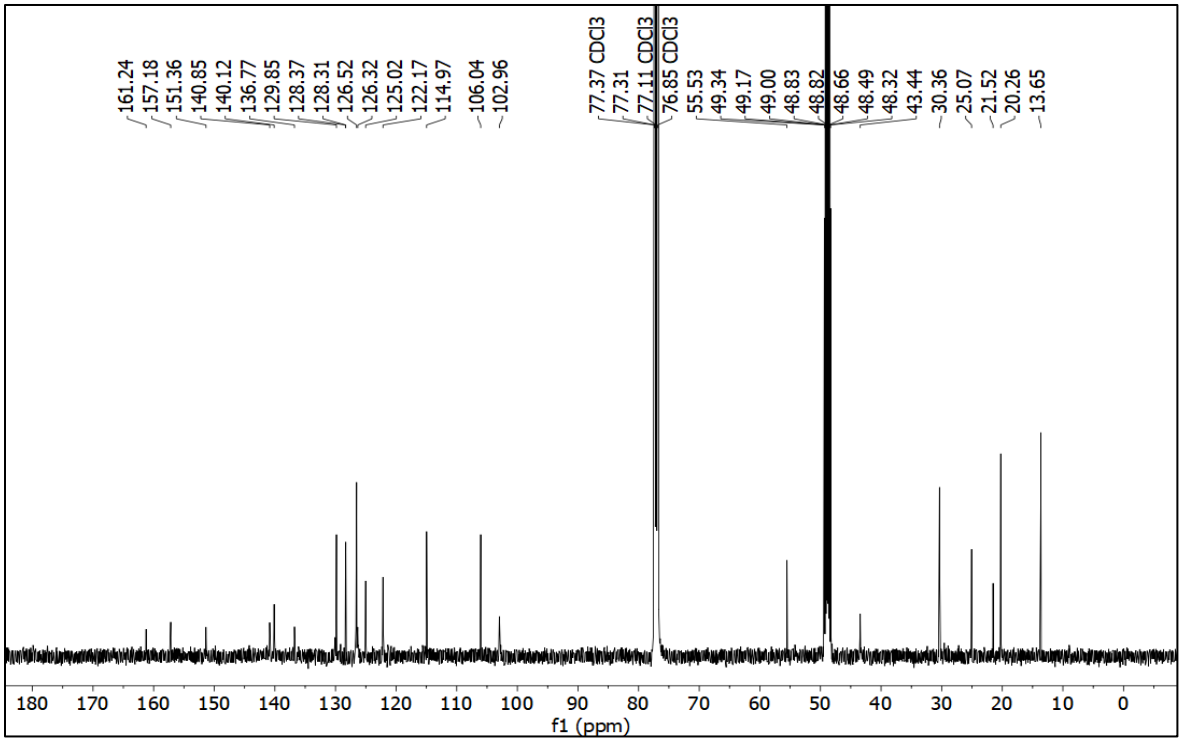

Compound 37: ^{1}H NMR (500 MHz, DMSO-d_6)

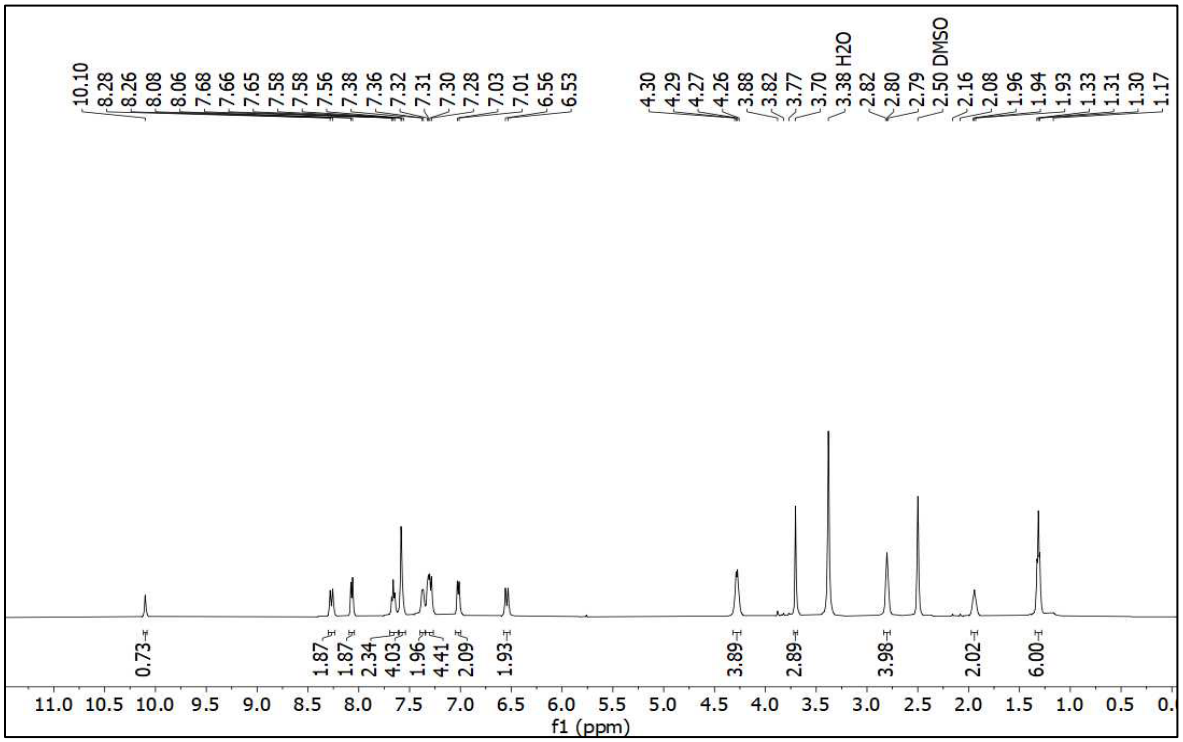

Compound 37: ^{13}C NMR (125 MHz, DMSO-d_6)

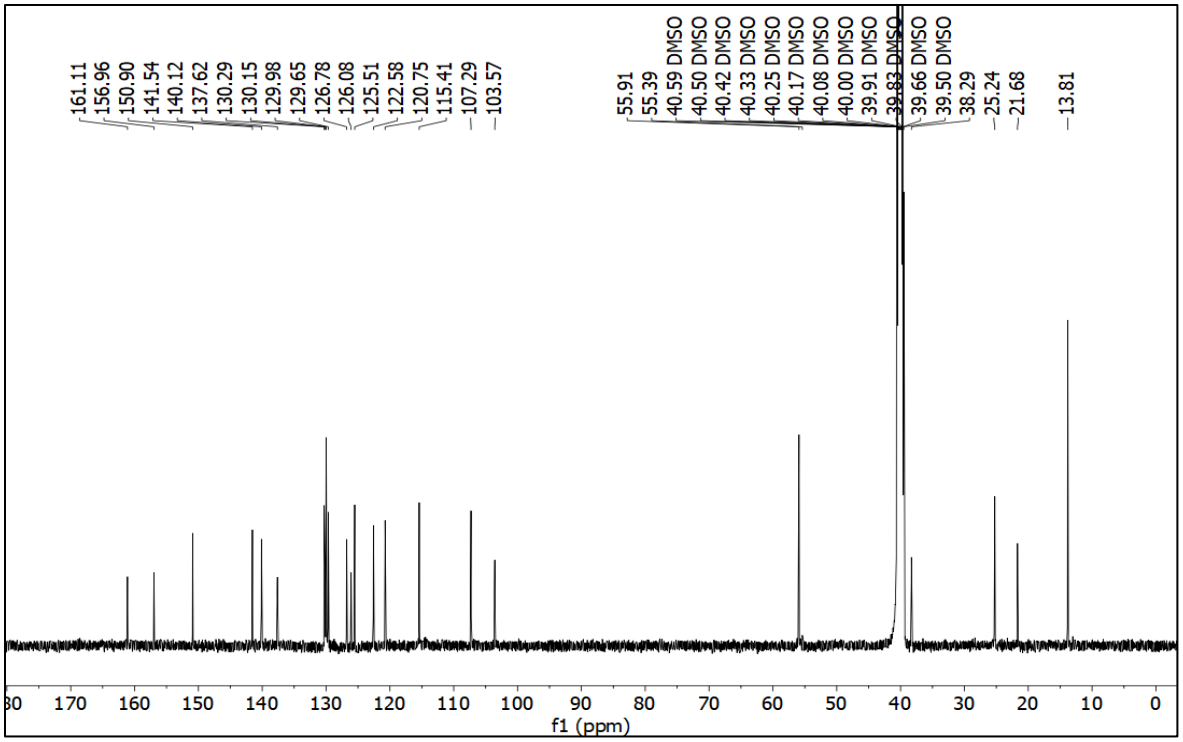

Compound 38: ^{1}H NMR (500 MHz, $CDCl_3$)

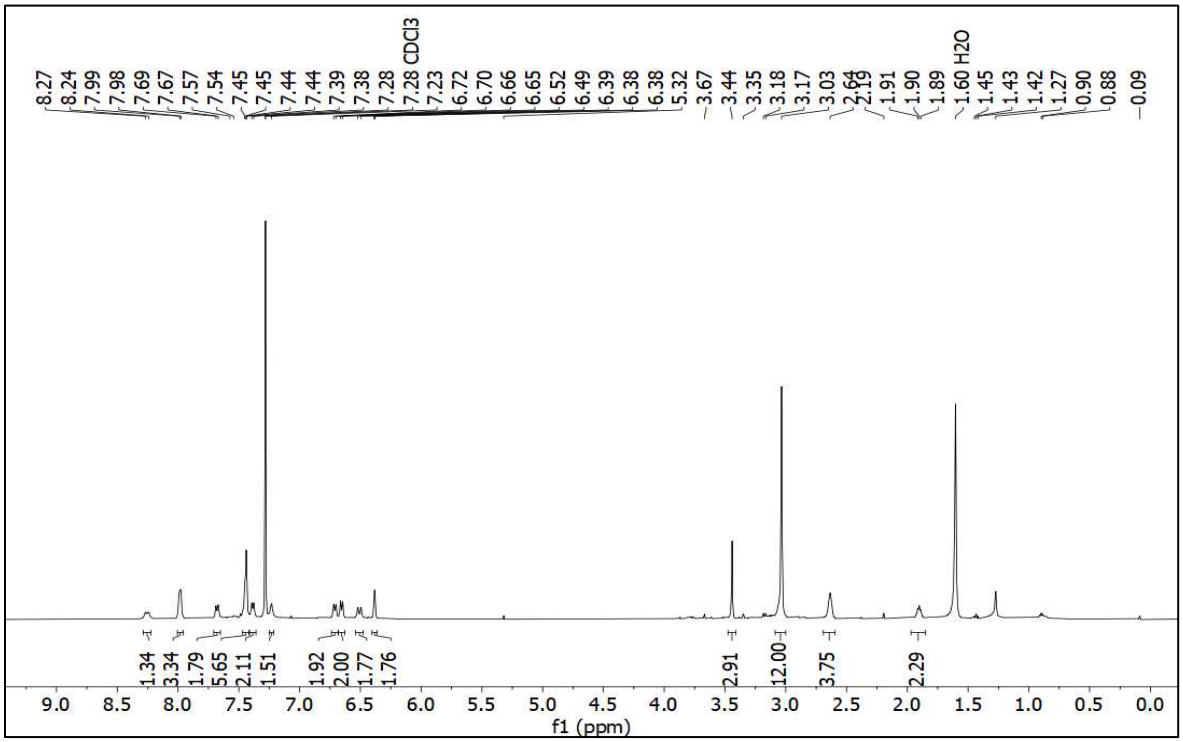

4.9 Acknowledgement of contributions

M.Y.L., A.K.E., and A.C.S. synthesized PA ABS probes. A.K.E. performed linear free-energy relationship measurements. M.Y.L. performed *in vitro* characterization and PA imaging of probes in tissue mimicking phantom. M.C.L. generated the breast cancer model. M.Y.L. generated the liver metastasis model and performed all *in vivo* imaging with S.S. C.J.R. performed preliminary studies. All authors analyzed and interpreted the data.

CHAPTER 5: VISUALISING FATTY ACID AMIDE HYDROLASE AND MONOACYLGLYCEROL LIPASE ACTIVITY IN HIGH-FAT DIETS

5.1 Background and significance

Fatty acid amide hydrolase (FAAH) and monoacylglycerol lipase (MGL) are important enzymes involved in lipid metabolism. They are found in the brain and throughout the body. Recently, they have arisen as targets for inflammatory and nervous system disorders as they have shown to regulate inflammation in the brain. FAAH is a membrane-bound serine hydrolase which primary function is to metabolize signalling fatty acids such as arachidonoylethanolamide, oleoylethanolamide and palmitoylethanolamide. These signalling molecules activate cannabinoid receptors in the brain that protect cells from inflammation. Therefore, FAAH can regulate pain, inflammation, and feeding behaviour.[106–109] Similarly, MGL is a serine hydrolase that degrades 2-arachidonoyglycerol into glycerol and arachidonic acid which also bind to cannabinoid receptors. As a result, these are both important targets for understanding diseases involving inflammation. Apart from being potential therapeutic targets, their biological roles are not completely known. Specifically, the enteric nervous system has been underexplored where FAAH and MGL can play major roles. Currently, FAAH and MGL are detected using *in vitro* assays and high throughput screens. There are few examples of activatable probes for *in vivo* imaging, however all these use wavelengths that are too short or are only capable of fluorescence imaging which limits biological applications to cellular and thin tissue specimen assays.[110–119] Although there has been considerable improvement on probes for cell imaging, there are currently no probes for *in vivo* animal imaging. Although FAAH has been explored with PET, these chemical tools involve using toxic ionizing radiation and radiotracers which

limits its use for long term biological studies.[120–129] This is necessary to study the enzymatic activity of FAAH and MGL and how it relates to inflammation. Importantly, being able to study this in a relevant animal model allows us to potentially translate this information to human health.

Obesity is a major health issue which has been associated with a variety of diseases. Interestingly, obesity has been shown to worsen prognosis of certain diseases such as cancer. This may be explained by the inflammation caused by high fat diets. It is not known whether FAAH and MGL play a role in high fat diet induced inflammation in humans. However, there are *ex vivo* studies that show FAAH knockout animal models affect weight gain and eating behaviour when placed on a high fat diet.[130–135] These studies reveal the complexity of FAAH and MGL in the body, and potentially demonstrates how a high fat diet model may not be suitable for drawing conclusions about other factors as they relate to FAAH. To overcome such limitations, it is necessary to study FAAH and MGL in their native environment. Here, we have addressed this by using PA imaging. Using an ABS approach allows us to leverage the chemical reactivity of the target to selectively image with high sensitivity without perturbing the native environment.

In our previous work, we have studied NO activity in high fat and low-fat diet murine models.[9] NO is a fleeting species that plays a key role in signalling inflammation. Indeed, we observed an overproduction of NO in animals placed on high-fat diets. This work will provide further insights on the mechanism of inflammation in high-fat diets using the first PA probes for *in vivo* imaging of FAAH and MGL.

5.2 Design and development of PA-HD-FAAH and PA-HD-MGL

Our group first reported the use of PA-HD *in vivo* for the detection of hydrogen peroxide, nitroreductase, and beta-galactosidase.[94] We demonstrated optimized PA properties which was due to the exchange of the traditional oxygen atom in the hemicyanine dye to a sulfur atom. The newly introduced sulphur atom enhanced planarity of the conjugated system which improved overall PA brightness. More specifically, PA-HD exhibited a lower pK_a, higher ε, lower Φ_{Fl}, and a bathochromic shift in absorbance. There are a number of criteria to highlight when developing an PA ABS probe. First, the probe must be PA and biologically compatible. This entails having an extinction coefficient greater than 10^4 M^{-1} cm^{-1}, a near-infrared excitation wavelength, a low Φ_{Fl}, aqueous solubility, minimal toxicity, and a spectroscopic change upon reacting with the analyte. The probe must also be able to react relatively fast for practical *in vivo* imaging. Additionally, it needs to be selective to avoid off-target effects. With these criteria in mind, we chose to attach a sulfonate group to PA-HD which would help with solubility. In the case of the FAAH probe (PA-HD-FAAH), we chose arachidonic acid as the trigger which upon binding should lead to hydrolysis of the amide to generate NH_2-PA-HD. Arachidonic acid (AA) is the most biologically similar to the normal substrate of FAAH, which we expect to provide good selectivity over other enzymes that metabolize amides. For MGL, we needed to have an ester as the attachment group in order to have MGL recognize it as a substrate. Importantly, we included a chloro group ortho to the trigger to decrease the pK_a and enhance the turn-on. PA-HD-FAAH and PA-HD-MGL were both synthetically accessible and followed procedures from our previously published work. It involved a retro-Knoevenagel reaction with the corresponding thiols and cyanine to generate the PA-HDs in good yield.

Next, the acid chloride of AA was used to synthesize the amide and ester for FAAH-PA-HD and MGL-PA-HD, respectively (Figure 21). The probes were characterized by NMR and ESI-MS.

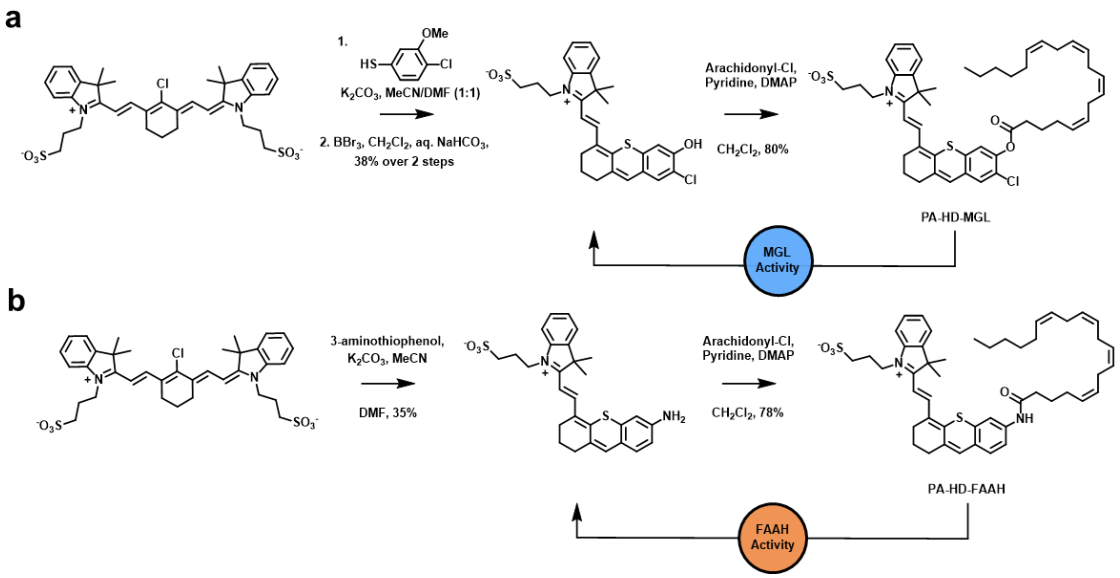

Figure 21. a. Synthesis of PA-HD-MGL and schematic of MGL-catalyzed activation. B. Synthesis of PA-HD-FAAH and schematic of FAAH-catalyzed activation.

5.3 Evaluating PA-HD-FAAH and PA-HD-MGL *in vitro*

After successful synthesis of the probes, we determined the theoretical turn-on for FAAH-PA-HD to be 4.1-fold PA enhancement. Similarly, MGL-PA-HD exhibited a theoretical turn-on of 7.0-fold PA enhancement. Next, we measured the quantum yields for each probe and their respective turnover products. Specifically, PA-HD-MGL exhibited a fluorescence quantum yield equal to 1.6%, while PA-HD gave 14.4%, PA-HD-FAAH gave 4.6% and NH_2-PA-HD provided a quantum yield of 8.4%. Although the fluorescence quantum yields are low, these probes can still provide useful fluorescence data. The extinction coefficients were determined to be 6.5×10^4, 1.5×10^5, 7.8×10^4, and 9.8×10^4 M^{-1} cm^{-1} for PA-HD-MGL, PA-HD, PA-HD-FAAH, and NH_2-PA-HD, respectively. It is important to note that these ε are all significantly higher than the traditional O-HD. As mentioned previously, our design carefully tuned the pK_a of MGL-PA-HD to improve the turn-on at physiological pH. It is important to note that during inflammation the local environment undergoes acidosis which produces a pH of about 5.5. This means that MGL-PA-HD must feature a low pK_a to display the optimal turn-on *in vivo*. Finally, we determined that the maximum absorbance wavelengths were 600, 740, 658, and 730 nm for PA-HD-MGL, PA-HD, PA-HD-FAAH, and NH_2-PA-HD, respectively. Importantly, the absorbance data obtained here is pertinent to the performance of the probes as absorbance acts as a proxy for PA imaging.

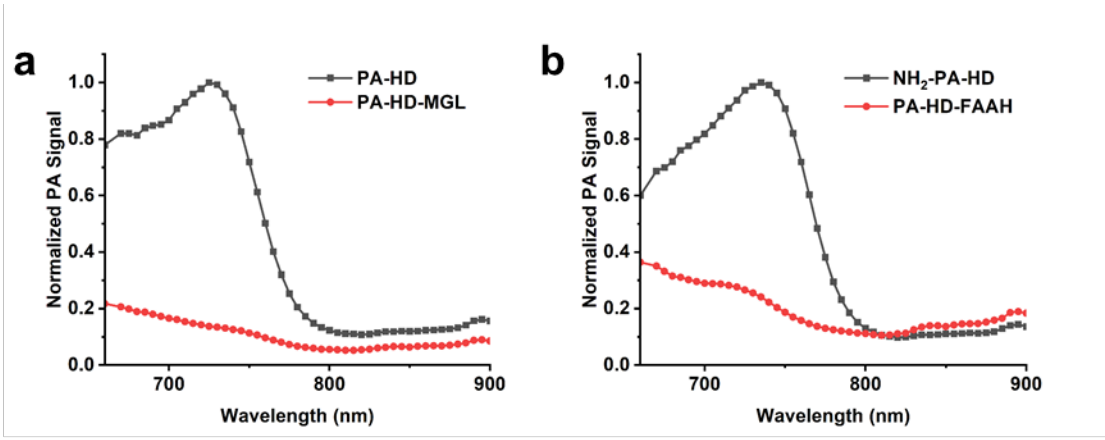

c

Compound	λ_{abs} (nm)	λ_{PA} (nm)	ε ($M^{-1}cm^{-1}$)	Φ_F	PABF ($M^{-1}cm^{-1}$)	pK_a
PA-HD-MGL	600	< 660	6.5×10^4	0.016	6.4×10^4	-
PA-HD	740	725	1.5×10^5	0.144	1.3×10^5	6.59
PA-HD-FAAH	658	< 660	7.8×10^4	0.046	7.4×10^4	-
NH_2-PA-HD	730	735	9.8×10^4	0.084	9.0×10^4	n/a

Figure 22. a. Normalized PA spectra of PA-HD and PA-HD-MGL in 70% PBS/MeCN, pH 7.4. b. Normalized PA spectra of NH_2-PA-HD and PA-HD-FAAH in 70% PBS/MeCN, pH 7.4. c. Table of photophysical properties of PA-HD-MGL, PA-HD, PA-HD-FAAH, and NH_2-PA-HD.

5.4 Assessing the performance of PA-HD-FAAH and PA-HD-MGL via photoacoustic imaging

To determine whether the probes and their turnover products were suitable for *in vivo* PA imaging, we performed tissue-mimicking phantom imaging. The PA spectra corresponded well with the previous absorbance data. Indeed, NH_2-PA-HD exhibited maximum PA signal with an excitation at 735 nm while PA-HD had maximum signal at 725 nm. Both probes absorbed maximally below 660 nm which can similarly be demonstrated via PA imaging. In addition, these experiments allowed us to obtain resolved spectra that will be used for future spectrally unmixed PA imaging (Figure 22).

Since PA-HD-FAAH and PA-HD-MGL will be employed for *in vivo* imaging, it was necessary to demonstrate that it is biocompatible and will not have off-target reactivity with other enzymes such CYP450, esterase, catalase, COX-1 and COX-2. In addition, we saw no reactivity with other analytes such as metal ions, reactive nitrogen and oxygen species.

5.5 PA-HD-FAAH and PA-HD-MGL in cells

We determined whether the probes could turnover with their respective enzymes. This was primarily performed using cell lysates. Specifically, LNCaP cells (prostate cancer) were used as they have been shown to highly express FAAH and MGL. After treating the cells with the probes, we observed an approximate 16-fold and 8-fold fluorescence enhancement for FAAH-PA-HD and MGL-PA-HD, respectively. After showing the probes could act as substrates for FAAH and MGL, we investigated whether the probes were solely being turned over by FAAH or MGL. First, we performed an inhibitor assay using PF 3845 and JZL 184 which are known potent inhibitors of FAAH

and MGL, respectively. We observed a decrease of fluorescence fold turn-on in both cases (Figure 23).

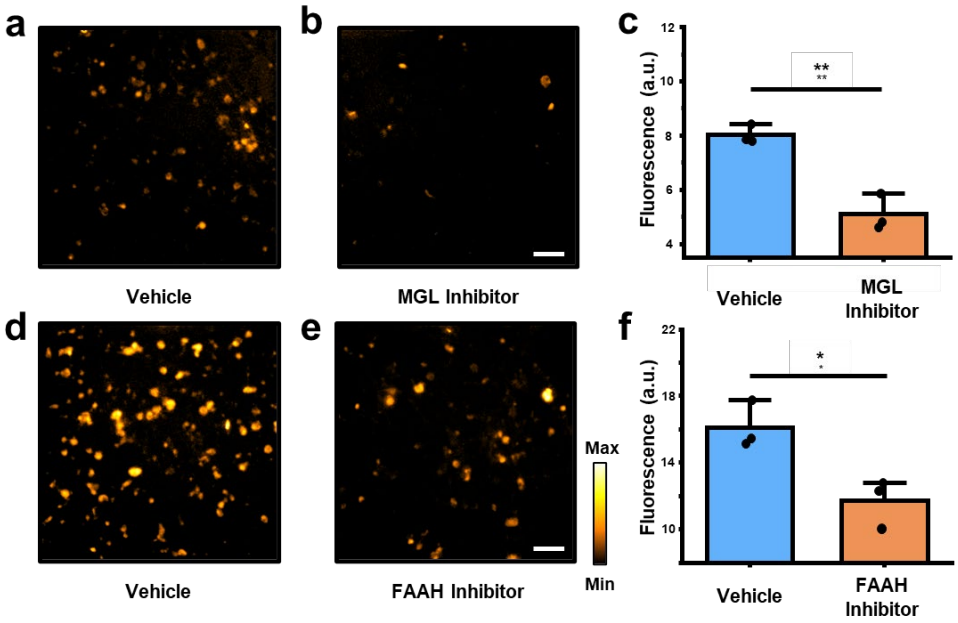

Figure 23. Fluorescent imaging of MGL activity in LNCaP cells treated with a. vehicle control or b. FAAH inhibitor (40 µM PF-3845) using PA-HD-MGL. Scale bar represents 50 µm. c, Quantification of data in a and b. Fluorescent imaging of FAAH activity in LNCaP cells treated with d. vehicle control or e. FAAH inhibitor (40 µM JZL 184) PA-HD-FAAH. Scale bar represents 50 µm. f. Quantification of data in d and e. Statistical analysis was performed using a two-tailed Student's *t*-test ($\alpha = 0.05$), $^{**}P < 0.01$, $^{*}P < 0.05$.

5.6 *In vivo* imaging of FAAH in a high-fat diet murine model

Nest, we wanted to image FAAH in a live system. Using a standard high fat diet to model obesity, we expected increased inflammation throughout the body. Specifically, FAAH has been underexplored in the enteric nervous system, however it is known that FAAH plays important roles in inflammation in the brain. We hypothesized that FAAH would be overexpressed in the gut of obese animals. To test this, we treated mice that were fed a high-fat diet with PA-HD-FAAH via IP injection. Interestingly, we observed an increase in signal in the intestines of all mice. Additionally, we noted that PA-HD-FAAH rapidly accumulated and generated signal in the intestines and cleared from the gut within 1 h. To determine if this increase in signal was due to overexpressed FAAH induced by a high-fat diet, we imaged mice that were fed low-fat diets. The mice fed a low-fat diet consistently generated lower PA signal after treatment with PA-HD-FAAH (Figure 24). These results were further confirmed via *ex vivo* imaging of the intestines.

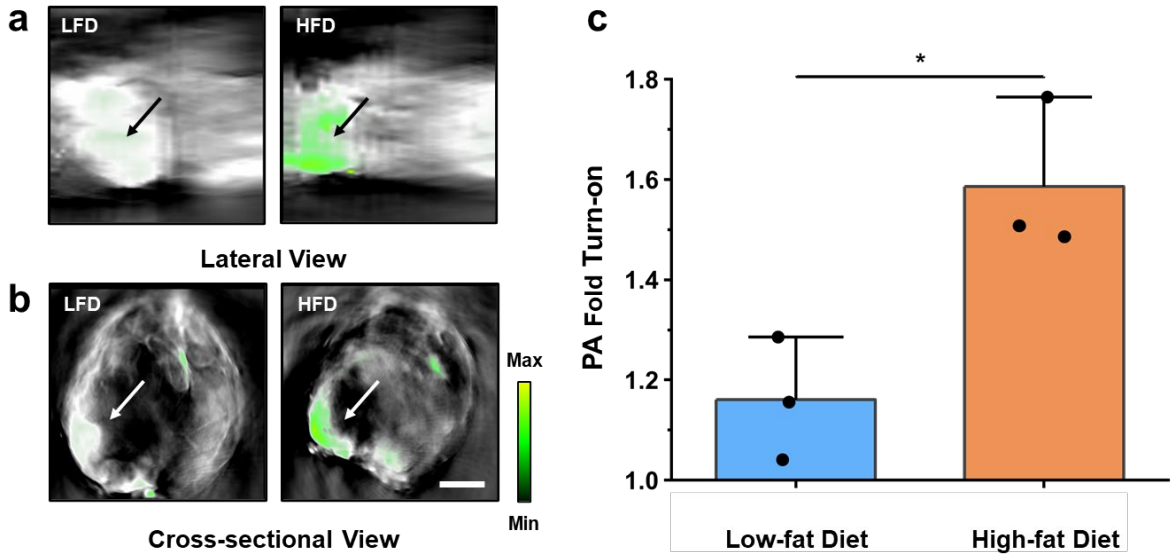

Figure 24. Representative MSOT images showing the a. lateral and b. cross-sectional views of mice fed low-fat and high-fat diets treated with PA-HD-FAAH (200 µM, 200 µL DMSO in saline). Images were acquired 0.5 h post-injection of the probe. Images shown are spectrally unmixed to show probe activation (in green) and arrow indicates intestines. Scale bar represents 5 mm. c. Average PA fold turn-on from MSOT imaging ($n = 3$ independent animals). Statistical analysis was performed using a two-tailed *t*-test ($\alpha = 0.05$, * $P < 0.05$).

5.7 *In vivo* imaging of MGL in a high-fat diet murine model

Since MGL is closely related to FAAH, we also treated the same animals with PA-HD-MGL. Similarly, MGL has not been studied extensively in the enteric nervous system. However, we hypothesize that it would be overexpressed during inflammation caused by obesity. HFD and LFD mice were treated with PA-HD-MGL, then Interestingly we found that the HFD mice exhibited higher PA signal in the intestines compared to LFD mice (Figure 25). We also observed that there was no enhanced PA signal from the liver. Although MGL is expressed in the liver, we suspect that MGL-PA-HD does not readily target or accumulate in the liver. With a HFD, we suspect a systemic increase in MGL expression. Again, the results of the in vivo imaging studies were confirmed after excising the intestines and other organs.

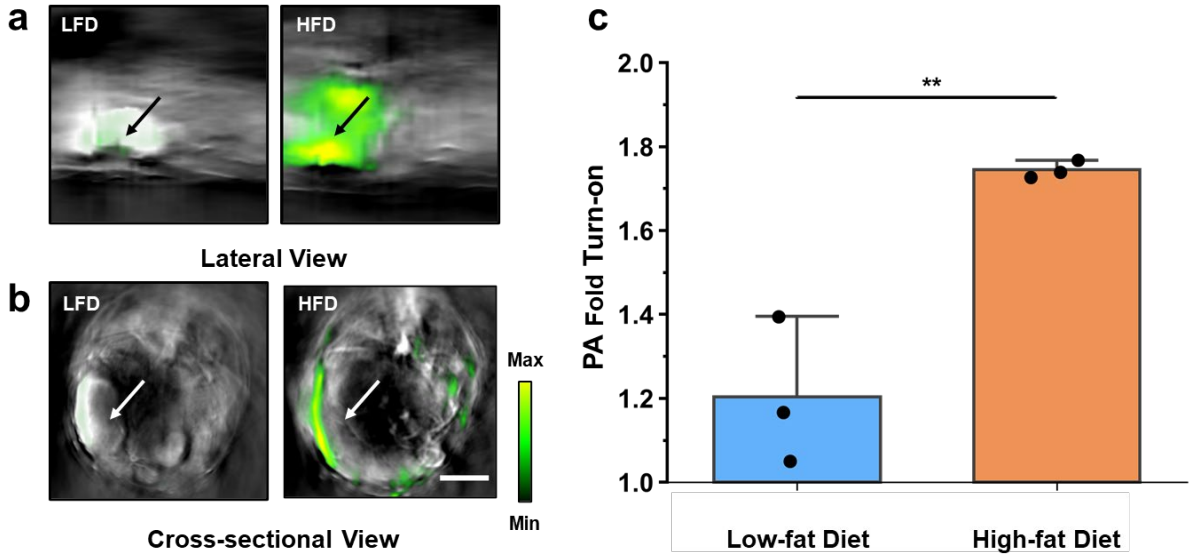

Figure 25. Representative MSOT images showing the a. lateral and b. cross-sectional views of mice fed low-fat and high-fat diets treated with PA-HD-MGL (200 µM, 200 µL DMSO in saline). Images were acquired 0.5 h post-injection of the probe. Images shown are spectrally unmixed to show probe activation (in green) and arrow indicates intestines. Scale bar represents 5 mm. c. Average PA fold turn-on from MSOT imaging ($n = 3$ independent animals). Statistical analysis was performed using a two-tailed *t*-test ($\alpha = 0.05$, ** $P < 0.01$).

5.8 Summary and outlook

There is an unmet need for noninvasively measuring levels of FAAH and MGL *in vivo*. In addition, the relatively obvious enteric nervous system as it relates to FAAH and MGL has not been explored using PA imaging. Indeed, a number of PET-based inhibitors have been used to study the brain and to aid in drug development, however PET has its own limitations. To address this, we have developed the first safe, non-toxic activity-based PA probes for FAAH and MGL. Due to the use of NIR light, PA-HD-FAAH/MGL may be used multiple times in one subject to study FAAH/MGL over time. Here, we have shown that both FAAH and MGL are elevated in HFD. In combination with past results in our lab, we demonstrate that NO, FAAH, and MGL are all important inflammatory biomarkers that are elevated with a HFD. This is important to note since all of these biomarkers may interfere with different therapies during treatment of diseases, such as cancer. It is important to mention the various studies investigating the relationship of FAAH and MGL with obesity. Typically, these studies use a FAAH knockout model, which has been concluded to promote obesity due to increased behaviour of high fat intake. This is contrary to what we have observed in the gut of HFD animals (higher FAAH activity). However, these studies primarily looked at the liver which is typically not the first-pass organ of fat. Similarly, we did not observe significant signal in the liver which is in agreement with other studies that saw no increase or decrease expression of FAAH. These interesting results help to further elucidate the role of FAAH and MGL in different organs. We envision that PA-HD-MGL may be used further for monitoring inflammation over the course of treatment of various disease states. Moreover, there is additional work to be done towards the development of targeted probes for FAAH and MGL in other organs. This will lead to further advancements in targeted therapies and drug development.

5.9 Experimental methods

Materials. JZL 184, PF-3845, human FAAH, and human MGL were purchased from Cayman Chemical. LNCaP cells were obtained from ATCC. Trypsin (0.25%, 2.21 mM EDTA, 1x sodium bicarbonate) and PBS was purchased from Corning. 96-well plates were purchased from Fisher. MTT reagent was purchased from Sigma Aldrich. All media was provided from Dr. Sandra McMasters in the Cell Media Facility in the School of Chemical Sciences at the University of Illinois Urbana-Champaign.

Instruments. Cells were counted on a Countess II FL Cell Counter (Invitrogen, Thermo Fisher Scientific). Cells were imaged on a an EVOS cell imaging system with the Cy7 filter (Thermo Fisher Scientific). MTT absorbance was read on a Spectra Max M2 plate reader (Molecular Devices). Fluorescence spectra were acquired on a QuantaMaster400 scanning spectrofluorometer (Photon International Technology).

Software. Cell imaging data was processed in Fiji Image J and Microsoft Excel. Figures and graphs were created using Origin and Microsoft PowerPoint.

Statistical Analysis. Unpaired student's *t*-tests and outlier tests were completed using GraphPad.

Cell Culture. LNCaP cells were cultured in RPMI 1640 + 10% FBS + 1% pen-strep.

PA-HD-MGL Lysate Assay. LNCaP cells were trypsinized and counted on a Countess II FL Cell Counter (Invitrogen, Thermo Fisher Scientific). Cells were pelleted (1000 rpm, 5 min., RT) and washed with 5 mL PBS. Cells were resuspended to 3×10^6 cells/mL in PBS with 10% protease inhibitor solution (1 protease inhibitor mini tablet/ 10mL PBS, Pierce, Thermo Fisher Scientific). Cells were lysed via sonication for 2 minutes (pulse, 01, 01, 40%) with a sonicator (Fisher Scientific). Lysate further diluted in PBS to create other concentration conditions. Probe (4 μM)

was then added to lysates in quartz cuvettes and turn-on at 763 nm was measured on a QuantaMaster400 scanning spectrofluorometer (Photon International Technology).

PA-HD-FAAH Lysate Assay. LNCaP cells were trypsinized and counted on a Countess II FL Cell Counter (Invitrogen, Thermo Fisher Scientific). Cells were pelleted (1000 rpm, 5 min., RT) and washed with 5 mL PBS. Cells were resuspended to 1×10^7 cells/mL in PBS with 10% protease inhibitor solution (1 protease inhibitor mini tablet/ 10mL PBS, Pierce, Thermo Fisher Scientific). Cells were lysed via sonication for 2 minutes (pulse, 01, 01, 40%) with a sonicator (Fisher Scientific). Lysate further diluted in PBS to create other concentration conditions. Probe (4 μM) was then added to lysates in quartz cuvettes and turn-on at 750 nm was measured on a QuantaMaster400 scanning spectrofluorometer (Photon International Technology).

MTT Assay for Cell Viability. LNCaP cells were counted on a Countess II FL Cell Counter (Invitrogen, Thermo Fisher Scientific). $6x10^5$ cells were then plated into each well on a clear Nuncon Delta Surface 96-well plate (Thermo Fisher Scientific). The cells were then incubated overnight (37 ºC, 5% CO_2) to allow adhesion to the plate. Wells were aspirated and refilled with varying amounts of PA-HD-FAAH was applied to each well and incubated for either 1, 2, or 4 h. Following each wells set incubation time, the wells were aspirated and refilled with 0.5 mg/mL MTT reagent in PBS, and wells were allowed to incubate for 2 h. 200 μL of DMSO was then directly added to each well containing the MTT reagent and transferred to a cuvette. The empty wells were resuspended in 300 μL of DMSO to solubilize any leftover formazan crystals. This solution was transferred to a cuvette and the absorbance of each was measured at 570 nm using a Spectra Max M2 plate reader (Molecular Devices). The absorbance of FAAH treated cells were normalized to a DMSO volume control to determine the percentage of viable cells.

PA-HD-MGL Cell Imaging. LNCaP cells were trypsinized, counted, and plated at $3.0x10^5$ cells/well in poly-l-lysine (Cultrex, R&D Systems) coated 8-well chamber slides (Lab Tek, Thermo Fisher Scientific). Cells were added to each well using a 25G syringe to a final density of $3.0x10^5$ cells/well. Cells were allowed to attach to the well overnight in the cell incubator (37 °C, 5% CO_2). Wells were then aspirated and refilled with RPMI 1640 media containing 10% FBS and either 40 μM JZL 184 or vehicle. Wells were left to incubate in the cell incubator (37 °C, 5% CO_2) for 3 h. Probe was added to each well (4 μM final concentration), and wells were incubated for 1 h. Wells were then aspirated and refilled with RPMI 1640 media containing 10% FBS and either 40 μM JZL 184 or vehicle. Wells were imaged on an EVOS cell imaging system (Thermo Fisher Scientific) with a Cy7 filter (80%).

PA-HD-FAAH Cell Imaging. LNCaP cells were trypsinized, counted, and plated at $3.0x10^5$ cells/well in poly-l-lysine (Cultrex, R&D Systems) coated 8-well chamber slides (Lab Tek, Thermo Fisher Scientific). Cells were added to each well using a 25G syringe to a final density of $2.5x10^5$ cells/well. Cells were allowed to attach to the well overnight in the cell incubator (37 °C, 5% CO_2). Wells were then aspirated and refilled with RPMI 1640 media containing 10% FBS and either 40 μM PF-3845 or vehicle. Wells were left to incubate in the cell incubator (37 °C, 5% CO_2) for 3 h. Probe was added to each well (2 μM final concentration), and wells were incubated for 1 h. Wells were then aspirated and refilled with RPMI 1640 media containing 10% FBS and either PF-3845 or vehicle. Wells were imaged on an EVOS cell imaging system (Thermo Fisher Scientific) with a Cy7 filter (90%).

Image Fluorescence Quantification. Three background measurements were taken using the oval selection tool in areas of the image not containing cells. Cell patches with an area between $2\text{-}3x10^5$ were chosen with the freehand selection tool. The corrected fluorescence of each patch was

determined by subtracting the product of the area of the cell patch and the background fluorescence from the cell patch's integrated density. Three cell patches were measured to get an image average. Three image averages were averaged to get a well average. Well averages were used for statistics and comparison between conditions.

Live-subject Statement. All animal experiments were performed with the approval of the IACUC of the University of Illinois at Urbana–Champaign, following the principles outlined by the American Physiological Society on research animal use.

Generation of Obesity Murine Models. For 12 weeks, BALB/c mice (six to eight weeks old) were placed on a control diet (Research Diets No. D12450B,) or a high-fat diet (Research Diets No. D12452) where 10% or 60% of calories are from fat, respectively.

***In Vivo* MSOT Imaging.** Mice were given an IP injection of PA-HD-FAAH or PA-HD-MGL (200 μM, 200 μL in saline containing 10% DMSO). The mice were continuously anesthetized using isoflurane and placed in the prone position in the animal holder for imaging immediately before injection and 0.5 h post injection. The temperature of the imaging chamber was set to 36 °C and the animal was allowed to equilibrate to the temperature for 15 minutes before imaging. Cross-sectional images were acquired at the abdomen of the mouse for imaging with a step size of 0.3 mm. The imaging position was guided by the built-in anatomy atlas in the MSOT InVision 128 and was kept consistent for all scans. The major wavelengths used were selected based on the absorbance of compound 2 or compound 3 and endogenous absorbers (660 nm, 700 nm, 735 nm, 760 nm, 800 nm, and 850 nm). 10 frames were recorded at every imaging wavelength. Subsequently, spectral unmixing was used to separate signals coming from HB and HbO_2.

Field of View Selection. The field of view for all experiments performed on the MSOT inVision 128 imaging system (iTheraMedical) was selected by using the built-in, cross-sectional anatomy guide to correctly position the animals to image the gut.

Image Processing of Background Signal. An initial scan prior to the administration of PA-HD-FAAH or PA-HD-MGL was performed for all PA imaging experiments. This is used to account for any background signal that originates from endogenous pigments such as hemoglobin found in blood. After the final scan is taken, a ratio ($PA_{Final}/PA_{Initial}$) is calculated to determine the change in PA intensity. Furthermore, we used the built-in spectral unmixing feature to distinguish between signal coming from PA-HD-FAAH or PA-HD-MGL and blood based on the absorbance spectra of HbO_2 and Hb.

***Ex Vivo* PA Imaging.** BALB/c mice were anesthetized using isoflurane (1.5 – 2.0%) and IP injected with either a solution of PA-HD-FAAH or PA-HD-MGL (200 μM, 10% DMSO in sterilized saline, 200 μL). After 0.5 h, the mice were euthanized, the intestines, stomach, kidneys, heart, and liver were excised. Photoacoustic imaging was performed using wavelengths 660 nm, 700 nm, 735 nm, 760 nm, 800 nm, and 850 nm.

Analyte Selectivity Studies. The absorbance (400 - 900 nm) was measured 10 minutes after the addition of reactive metals (1 mM), thiols (GSH (1mM); Cys (500 μM); Hcy (500 μM)), oxygen (1 mM), carbonyl (1 mM), and nitrogen species (1 mM; $ONOO^-$ (50 μM); NO (100 μM)). The relative turn-on was determined by change in absorption at λ_{abs} of the probe and turnover product compared to the vehicle control. All metal solutions were prepared in water from their chloride salt, except for $FeSO_4 \cdot (H_2O)_7$. Aqueous nitrite and nitrate solutions were prepared from their corresponding sodium salts. Superoxide anion was added as a solution of potassium superoxide in DMSO. NO was generated *in situ* from a solution of MAHMA-NONOate in degassed 10 mM

potassium hydroxide. Hydroxyl radical was generated via Fenton chemistry between Mohr's salt (solution in degassed 1 M aqueous hydrochloric acid) and hydrogen peroxide. Peroxynitrite was synthesized according to a literature report. All other analytes were prepared by dilution from commercially available sources.

Tissue Phantom Preparation. Tissue phantoms were prepared by suspending agarose LE (750 mg) in deionized water (50 mL). The suspension was heated for 1 minute in a microwave until a viscous, translucent gel was produced. Immediately, 1 mL of 2% milk was added. The hot gel was poured into a mold containing two plastic straws (3 mm diameter) and cooled at room temperature for at least 20 minutes. After cooling, the straws were removed and the gel was removed from the mold, yielding a tissue phantom with two parallel channels for the placement of FEP tubes containing sample solutions.

Tissue Phantom PA Imaging. A solution of PA-HD-FAAH, PA-HD-MGL, compound 2, or compound 3 (10 μM, 70% PBS/MeCN, pH 7.4) was injected into a tube which was then inserted into the cylindrical tissue phantom for imaging. The phantom was placed into the holder and excited from 680 – 900 nm with 5 nm intervals. The spectrum that was obtained was later used for spectral unmixing.

Supplementary Scheme 4. Synthesis of Compound 39

Compound 39. Sodium acetate (0.53 g, 6.46 mmol, 1.2 equiv.) was added to a suspension of indolene sulfonate[1] (1.50 g, 5.33 mmol, 1.0 equiv.) and imine[2] (0.96 g, 2.97 mmol, 0.6 equiv.) in absolute ethanol (54 mL). The reaction mixture was refluxed for 3.5 h under a N_2 atmosphere, cooled to room temperature and concentrated under vacuum. The residue was dissolved in a minimum volume of methanol and the product was precipitated using diethyl ether to give greenish solid which was filtered and washed with diethyl ether (1.30 g, 1.86 mmol, 35% yield). ^{1}H NMR (500 MHz, DMSO-d_6) δ 8.25 (d, J = 14.0 Hz, 2H), 7.59 (d, J = 7.3 Hz, 2H), 7.49 (d, J = 7.9 Hz, 2H), 7.41 (t, J = 7.6 Hz, 2H), 7.27 (t, J = 7.5 Hz, 2H), 6.47 (d, J = 14.2 Hz, 2H), 4.34 (t, J = 7.8 Hz, 4H), 2.72 (t, J = 6.3 Hz, 4H), 2.60 (t, J = 6.9 Hz, 4H), 2.03 (p, J = 6.9 Hz, 4H), 1.82 (h, J = 6.0 Hz, 2H), 1.66 (s, 12H). ^{13}C NMR (125 MHz, DMSO-d_6) δ 172.49, 148.31, 143.50, 142.27, 141.35, 128.92, 126.85, 125.37, 122.70, 111.74, 102.10, 49.19, 48.02, 43.05, 27.75, 26.19, 23.55, 20.76. HRMS $[M]^-$ calculated mass for $C_{36}H_{42}N_2O_6S_2Cl$ = 697.2173, found = 697.2158.

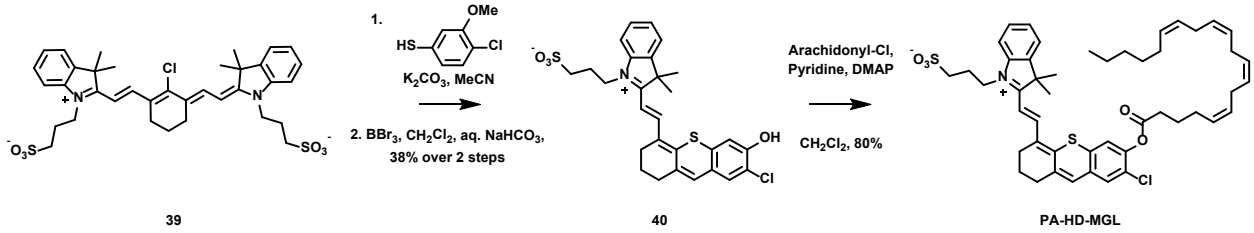

Supplementary Scheme 5. Synthesis of PA-HD-MGL

Compound 40. A solution of 4-chloro-3-methoxybenzenethiol[3] (0.20 g, 1.14 mmol, 2.0 equiv.) in anhydrous acetonitrile (5 mL) was treated with K_2CO_3 (0.16 g, 1.14 mmol, 2.0 equiv.) and stirred at room temperature for 10 minutes under a N_2 atmosphere. After the addition of **1** (0.40 g, 0.57 mmol, 1.0 equiv.) in DMF (5 mL), the reaction was stirred at 50 °C for ~2 h and monitored by TLC. The reaction was cooled to room temperature, evaporated, and the crude material was used directly in the next reaction. The residue was dissolved in anhydrous CH_2Cl_2 (5 mL) under a N_2 atmosphere and cooled to 0 °C in an ice-bath. A 1.0 M solution of BBr_3 in CH_2Cl_2 (2.86 mL, 2.86 mmol, 5 equiv.) was added dropwise. After stirring for 3 h, the reaction was quenched with sat. $NaHCO_3$ and stirred for an additional 3 h at room temperature. The reaction mixture was concentrated and purified by silica gel column chromatography (2:23 v/v MeOH:CH_2Cl_2) to give **40** as a blue solid in 30% yield (90 mg, 0.17 mmol). ^{1}H NMR (500 MHz, 1:1 v/v CD_3OD:$CDCl_3$) δ 8.38 (d, *J* = 14.3 Hz, 1H), 7.61 (dd, *J* = 14.3, 7.8 Hz, 2H), 7.56 (s, 1H), 7.53 (t, *J* = 7.1 Hz, 1H), 7.45 (t, *J* = 7.4 Hz, 1H), 7.13 (d, *J* = 13.0 Hz, 2H), 6.85 (d, *J* = 14.5 Hz, 1H), 4.62 – 4.54 (m, 2H), 3.00 (t, *J* = 6.5 Hz, 2H), 2.77 (q, *J* = 5.6 Hz, 4H), 2.32 (p, *J* = 7.6 Hz, 2H), 1.94 (p, *J* = 6.5 Hz, 2H), 1.80 (s, 6H). ^{13}C NMR (125 MHz, 1:1 v/v CD_3OD:$CDCl_3$) δ 178.75, 156.04, 154.88, 146.75, 143.05, 142.23, 135.73, 134.50, 133.82, 132.55, 130.28, 128.77, 128.54, 123.81, 123.40, 123.05, 113.86, 112.24, 106.94, 51.74, 44.99, 33.20, 30.39, 28.54, 27.61, 24.37, 21.25. HRMS $[M+H]^+$ calculated mass for $C_{28}H_{29}NO_4S_2Cl$ = 542.1227, found = 542.1224.

PA-HD-MGL. A solution of **40** (20 mg, 0.04 mmol, 1.0 equiv.) in pyridine (3 mL) was cooled to 0 °C and was treated with a solution of arachidonyl-Cl[4,5] (13.1 mg, 0.04 mmol, 1.1 equiv.) in anhydrous CH_2Cl_2 dropwise under a N_2 atmosphere. DMAP (1 mg, 0.01 mmol, 0.2 equiv.) was added and stirring was continued at room temperature. The volatiles were evaporated under vacuum and the crude residue was purified by silica gel column chromatography (1:19 v/v

MeOH:CH_2Cl_2) to give **PA-HD-MGL** as a blue solid in 54% yield (18 mg, 0.02 mmol). ^{1}H NMR (500 MHz, 1:1 v/v CD_3OD:$CDCl_3$) δ 8.36 (d, *J* = 14.6 Hz, 1H), 7.64 (d, *J* = 7.9 Hz, 1H), 7.58 – 7.53 (m, 3H), 7.51 (s, 1H), 7.34 (s, 1H), 7.04 (d, *J* = 14.6 Hz, 1H), 7.00 (s, 1H), 5.48 – 5.39 (m, 2H), 5.39 – 5.28 (m, 6H), 4.65 (t, *J* = 8.0 Hz, 2H), 2.97 (t, *J* = 6.2 Hz, 2H), 2.87 – 2.81 (m, 4H), 2.78 (q, *J* = 6.0 Hz, 6H), 2.66 (t, *J* = 7.4 Hz, 2H), 2.35 – 2.26 (m, 2H), 2.23 (q, *J* = 7.1 Hz, 2H), 2.02 (q, *J* = 7.0 Hz, 2H), 1.94 (d, *J* = 6.4 Hz, 2H), 1.86 (p, *J* = 7.5 Hz, 2H), 1.79 (s, 6H), 1.32 (t, *J* = 7.5 Hz, 2H), 1.29 – 1.24 (m, 4H), 0.87 – 0.83 (m, 3H). ^{13}C NMR (125 MHz, 1:1 v/v CD_3OD:$CDCl_3$) δ 179.60, 171.62, 151.31, 147.81, 147.41, 143.01, 141.42, 136.52, 132.53, 132.30, 131.58, 130.85, 130.19, 130.17, 129.83, 129.15, 129.06, 128.92, 128.72, 128.48, 128.26, 127.99, 127.07, 123.13, 120.37, 114.17, 109.13, 51.82, 47.62, 45.07, 33.70, 33.07, 31.97, 29.77, 28.41, 27.64, 26.88, 26.07, 25.06, 24.39, 22.99, 20.67, 14.28. HRMS $[M+H]^+$ calculated mass for $C_{48}H_{59}NO_5S_2Cl$ = 828.3523, found = 828.3496.

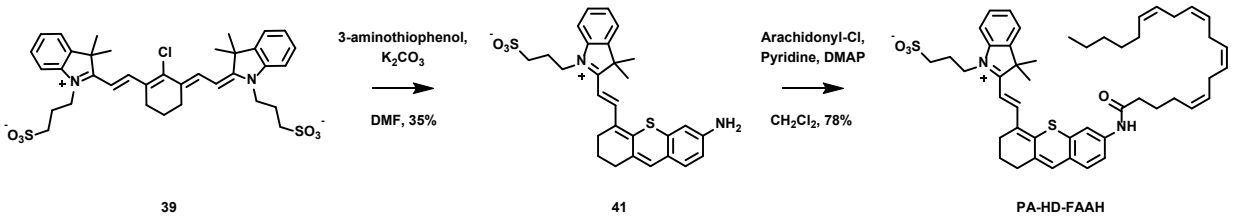

Supplementary Scheme 6. Synthesis of PA-HD-FAAH

Compound 41. A solution of 3-aminothiophenol (0.14 g, 1.14 mmol, 2.0 equiv.) in anhydrous acetonitrile (5 mL) was treated with K_2CO_3 (0.16 g, 1.14 mmol, 2.0 equiv.) and stirred at room temperature for 15 minutes under a N_2 atmosphere. After the addition of a solution of **39** (0.40 g, 0.57 mmol, 1 equiv.) in DMF (10 mL), the reaction was stirred at 50 °C for ~2 h and monitored by TLC. The reaction was cooled to room temperature, evaporated, and purified by silica gel

column chromatography (1:9 v/v MeOH:CH_2Cl_2) to give **41** as a blue solid in 28% yield (84 mg, 0.16 mmol). ^{1}H NMR (500 MHz, DMSO-d_6) δ 8.15 (d, J = 14.0 Hz, 1H), 7.69 (d, J = 7.5 Hz, 1H), 7.63 (d, J = 8.1 Hz, 1H), 7.51 – 7.42 (m, 3H), 7.36 (t, J = 7.4 Hz, 1H), 6.88 (d, J = 2.3 Hz, 1H), 6.79 (dd, J = 8.6, 2.2 Hz, 1H), 6.70 – 6.62 (m, 3H), 4.46 (t, J = 7.7 Hz, 2H), 2.70 (p, J = 6.0 Hz, 4H), 2.57 (t, J = 6.6 Hz, 2H), 2.05 (p, J = 6.6 Hz, 2H), 1.81 (p, J = 6.3 Hz, 2H), 1.72 (s, 6H). ^{13}C NMR (125 MHz, DMSO-d_6) δ 174.40, 154.34, 152.02, 142.39, 141.79, 141.57, 139.13, 137.23, 133.32, 129.19, 128.75, 125.84, 125.19, 122.56, 118.87, 116.25, 112.26, 106.79, 103.12, 49.49, 47.64, 43.24, 31.61, 27.98, 26.10, 23.64, 20.34. HRMS $[M+H]^+$ calculated mass for $C_{28}H_{31}N_2O_3S_2$ = 507.1776, found = 507.1775.

PA-HD-FAAH. A solution of **41** (18.1 mg, 0.04 mmol, 1.0 equiv.) in pyridine (3 mL) was cooled to 0 °C and was treated with a solution of arachidonyl-Cl (12.7 mg, 0.04 mmol, 1.1 equiv.) in anhydrous CH_2Cl_2 dropwise under N_2 atmosphere. Then DMAP (1 mg, 0.01 mmol, 0.2 equiv.) was added and stirring was continued at room temperature. After the reaction was complete the volatiles were evaporated under vacuum and the crude residue was purified by silica gel column chromatography (7:93 v/v MeOH:CH_2Cl_2) to give **PA-HD-FAAH** as a blue solid in 55% yield (16 mg, 0.02 mmol). ^{1}H NMR (500 MHz, 1:1 v/v CD_3OD:$CDCl_3$) δ 8.39 (d, J = 14.2 Hz, 2H), 7.56 – 7.54 (m, 2H), 7.52 (t, J = 7.7 Hz, 1H), 7.45 (dd, J = 8.4, 3.1 Hz, 2H), 7.29 (dd, J = 8.5, 2.1 Hz, 1H), 7.17 (s, 1H), 6.84 (d, J = 14.3 Hz, 1H), 5.40 (t, J = 4.8 Hz, 2H), 5.36 – 5.23 (m, 6H), 2.98 (t, J = 6.3 Hz, 2H), 2.78 (dq, J = 18.3, 5.8 Hz, 9H), 2.43 (t, J = 7.4 Hz, 2H), 2.31 (s, 2H), 2.21 – 2.14 (m, 2H), 2.01 (q, J = 6.3 Hz, 2H), 1.94 (s, 2H), 1.80 (s, 6H), 1.35 – 1.27 (m, 5H), 0.87 – 0.83 (m, 3H). ^{13}C NMR (125 MHz, 1:1 v/v CD_3OD:$CDCl_3$) δ 178.23, 174.06, 155.76, 146.67, 142.70, 141.84, 141.14, 136.32, 135.56, 134.41, 131.84, 130.87, 130.03, 129.51, 129.46, 129.01, 128.70, 128.65, 128.62, 128.33, 128.28, 128.09, 125.82, 123.16, 120.09, 115.16, 113.49, 106.55, 51.41,

47.95, 44.67, 36.95, 33.10, 32.05, 29.86, 28.75, 27.70, 27.33, 27.11, 26.15, 26.11, 25.84, 24.15, 23.07, 20.95, 14.30. HRMS $[M+H]^+$ calculated mass for $C_{48}H_{60}N_2O_4S_2$ = 793.4073, found = 793.4058.

5.10 Supplemental figures, tables, and spectra

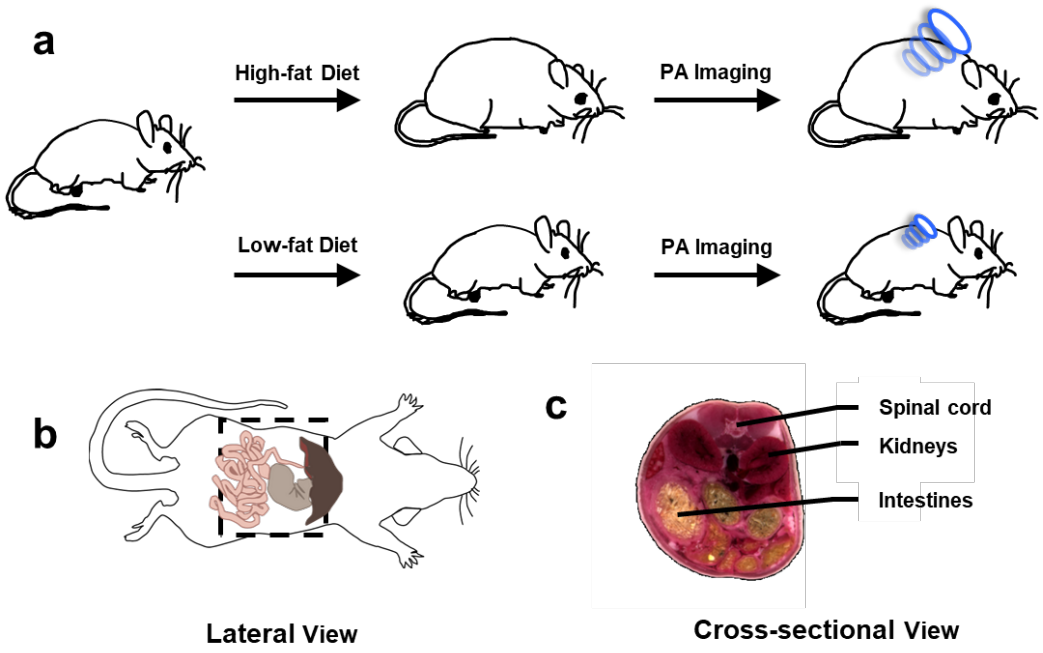

Supplementary Figure 53. a. Schematic representing workflow for the generation of murine models to study the effect of diet on MGL and FAAH activity using in vivo photoacoustic imaging. b. Lateral schematic of a mouse where the field of view is indicated by the dotted box. c. Cross-sectional schematic of a mouse to reference the positioning of the spinal cord, kidneys, and intestines.

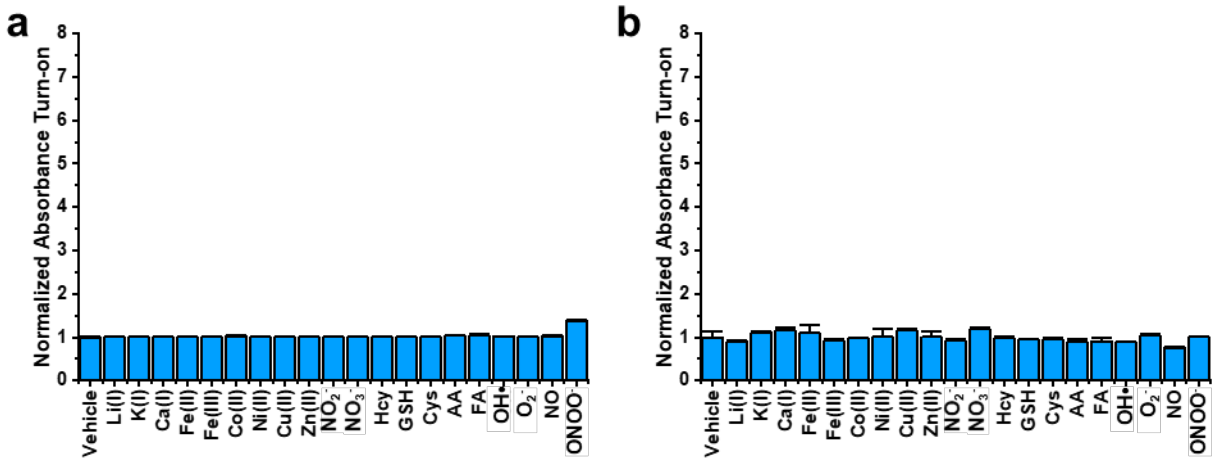

Supplementary Figure 54. Normalized absorbance turn-on of a. PA-HD-FAAH and b. PA-HD-MGL in the presence of a panel of metal ions, reactive oxygen species, and reactive nitrogen species.

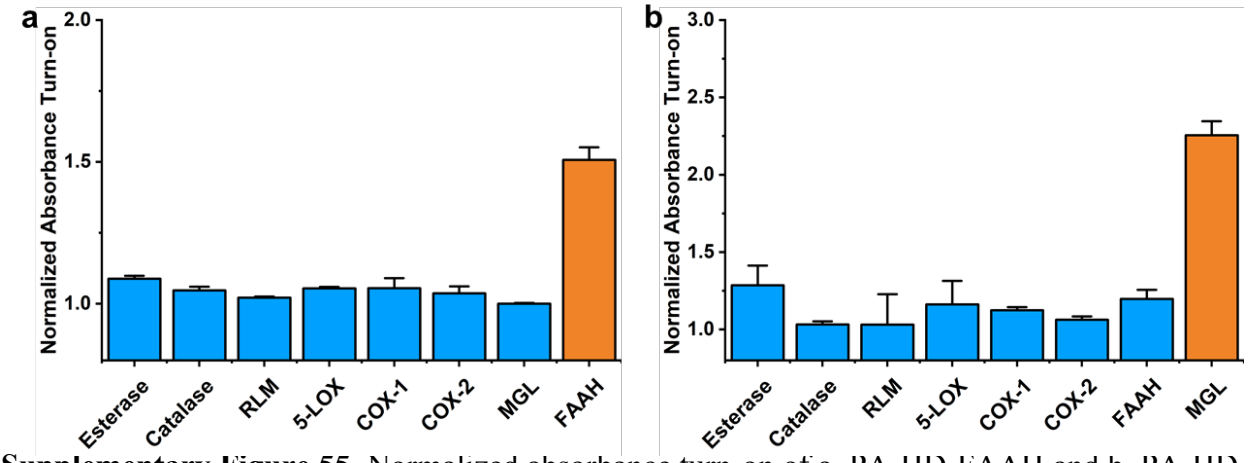

Supplementary Figure 55. Normalized absorbance turn-on of a. PA-HD-FAAH and b. PA-HD-MGL in the presence of a panel of relevant enzymes.

Compound 39: ^{1}H NMR (500 MHz, DMSO-d_6)

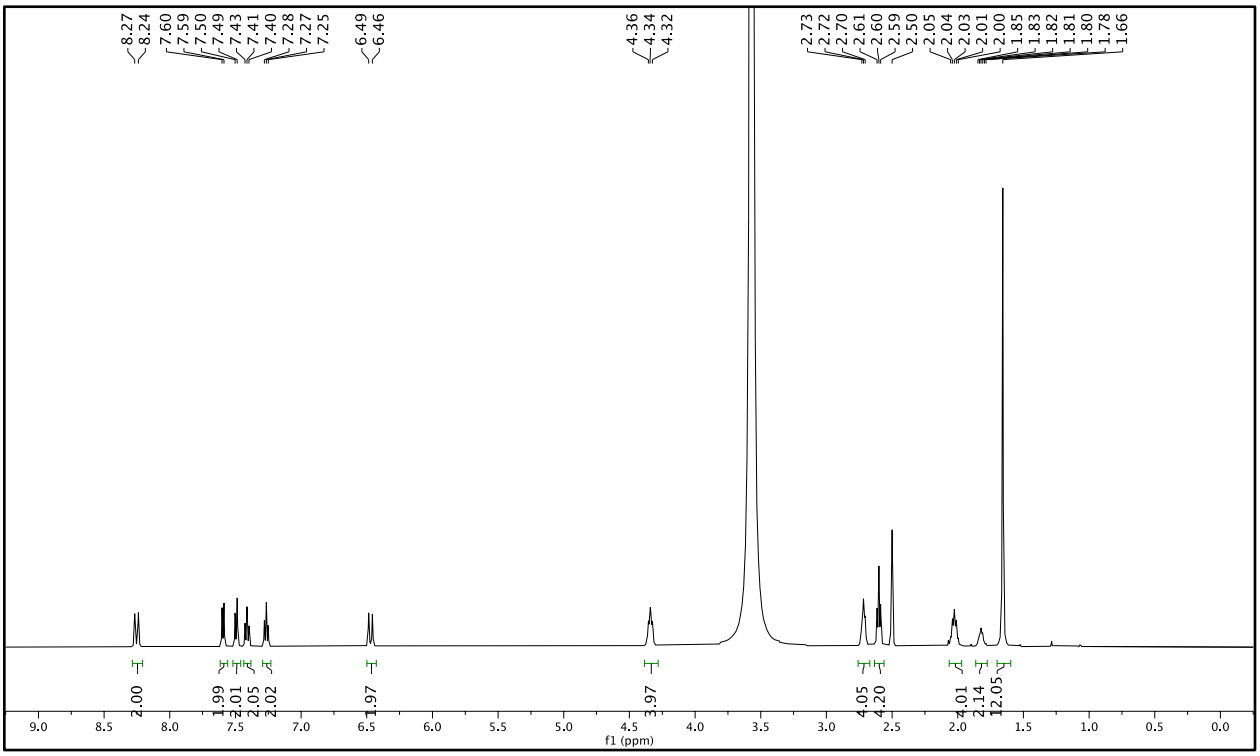

Compound 39: ^{13}C NMR (125 MHz, DMSO-d_6)

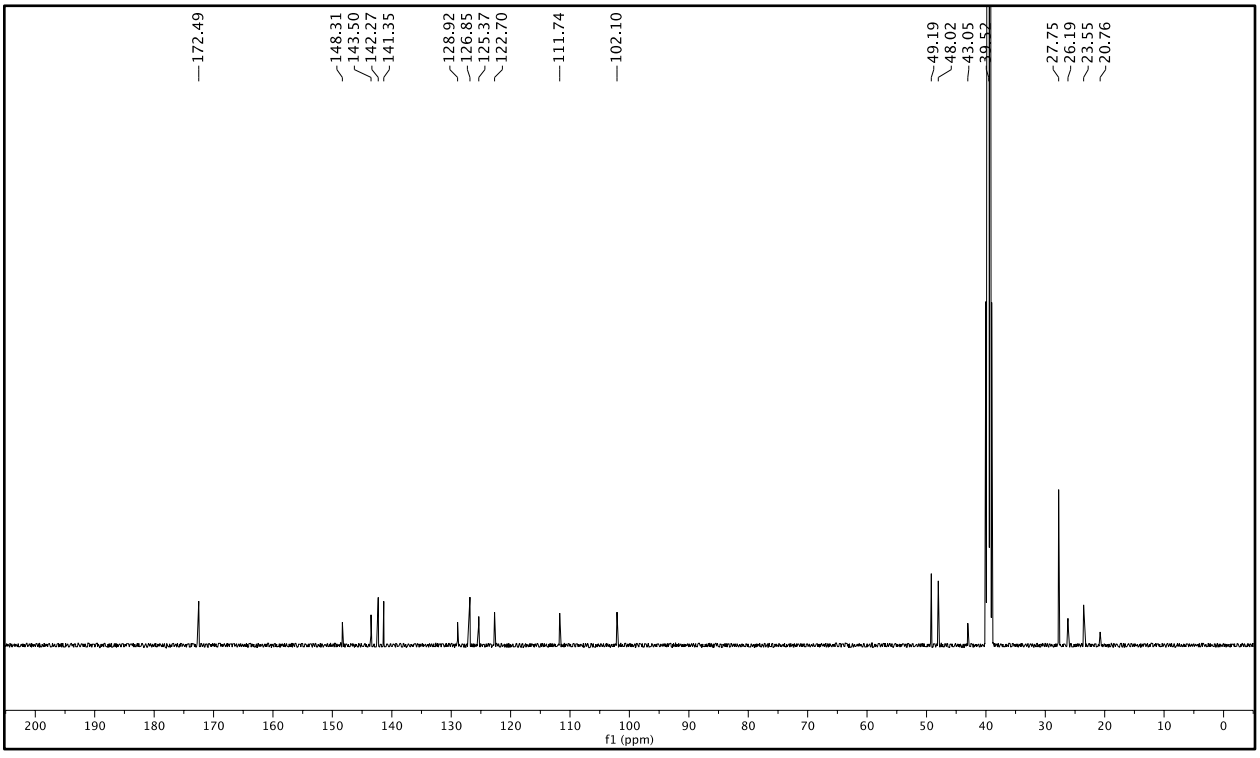

Compound 40: ^{1}H NMR (500 MHz, 1:1 v/v CD_3OD:$CDCl_3$)

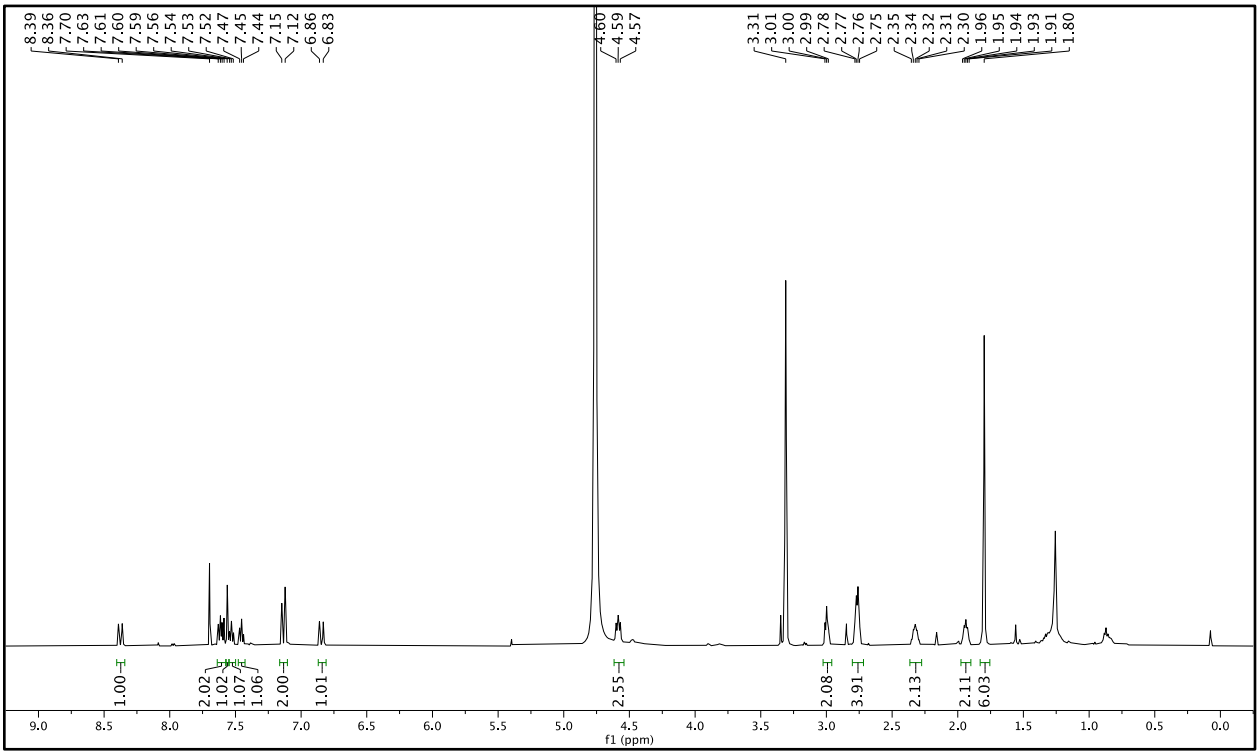

Compound 40: ^{13}C NMR (125 MHz, 1:1 v/v CD_3OD:$CDCl_3$)

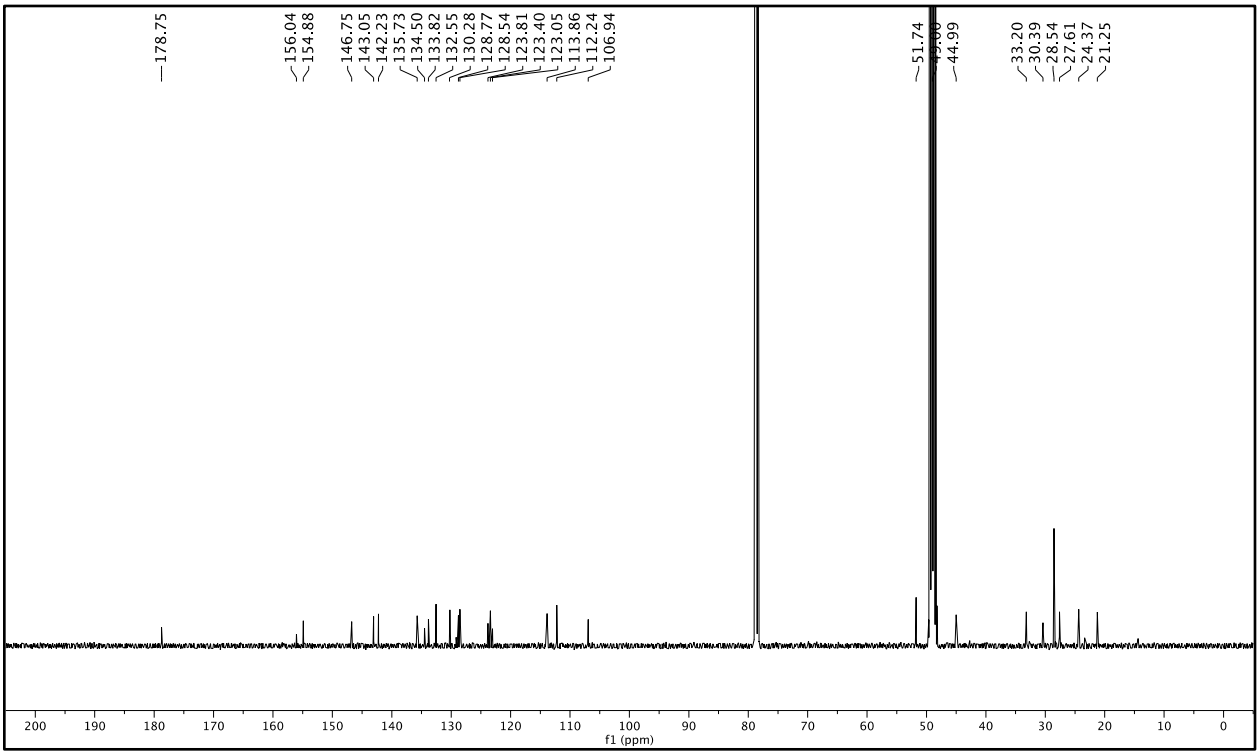

Compound PA-HD-MGL: ^{1}H NMR (500 MHz, 1:1 v/v CD_3OD:$CDCl_3$)

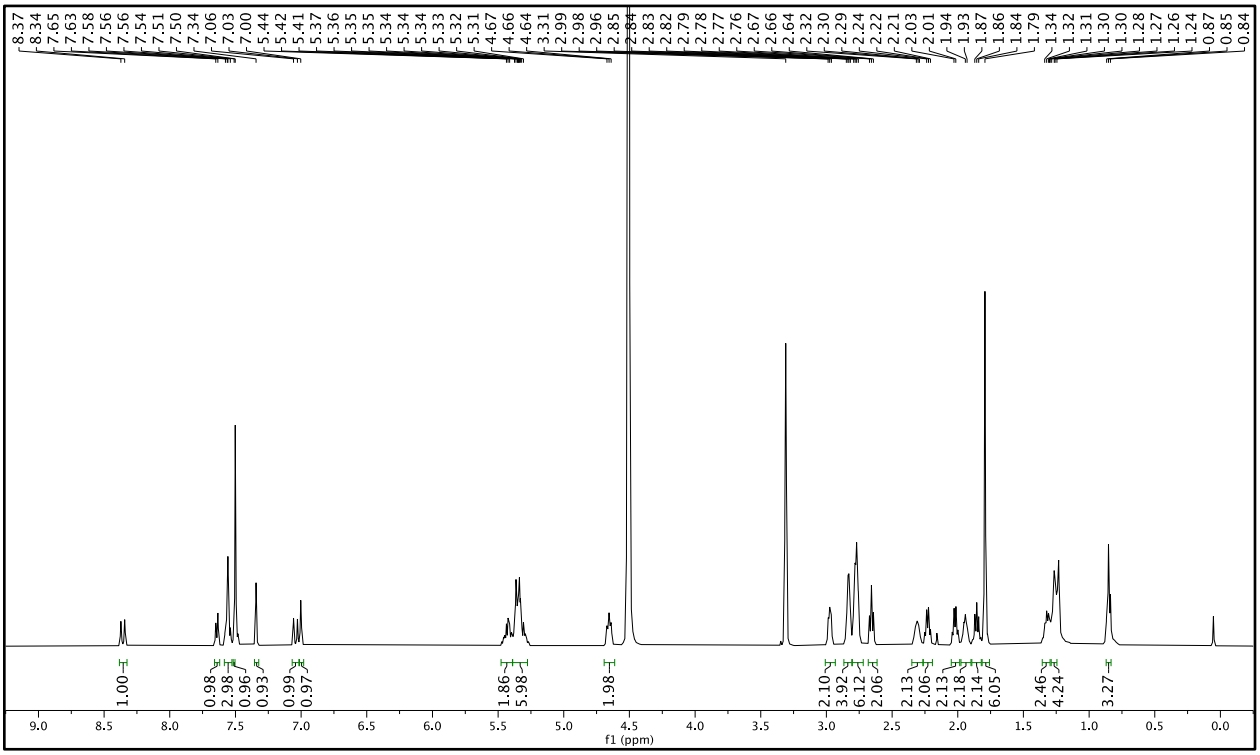

Compound PA-HD-MGL: ^{13}C NMR (125 MHz, 1:1 v/v CD_3OD:$CDCl_3$)

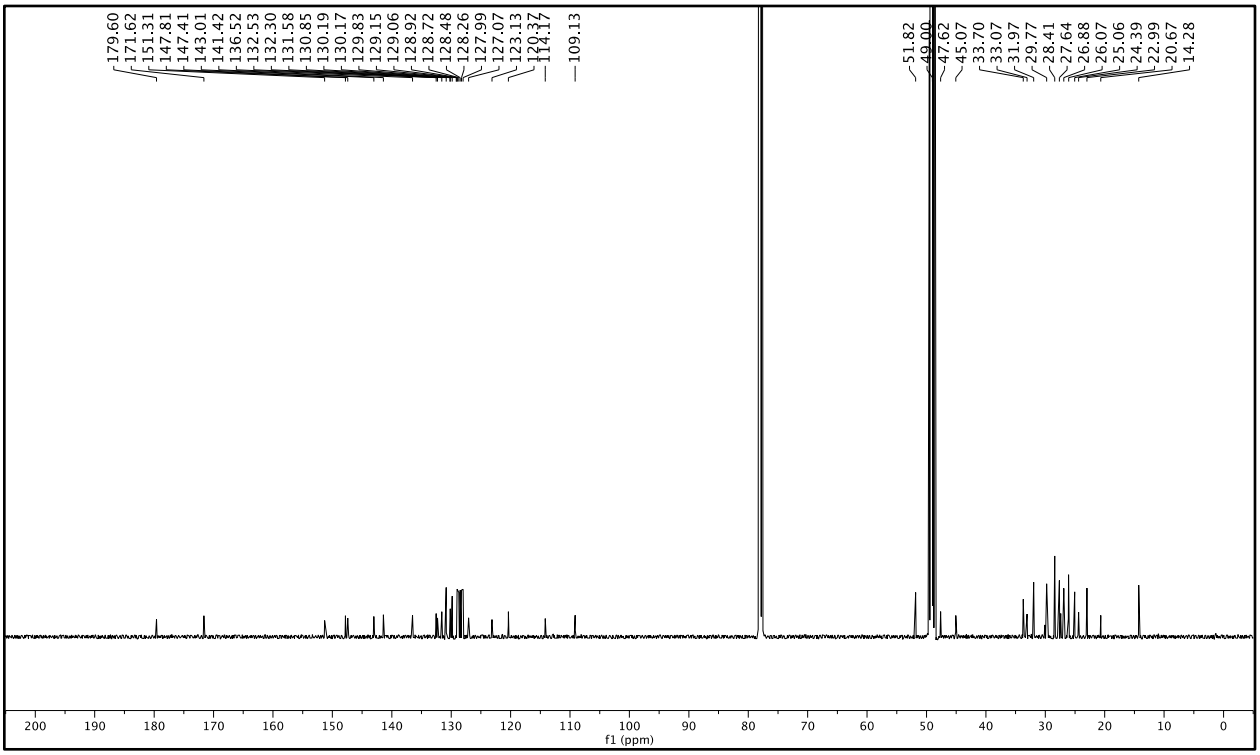

Compound 41: ^{1}H NMR (500 MHz, DMSO-d_6)

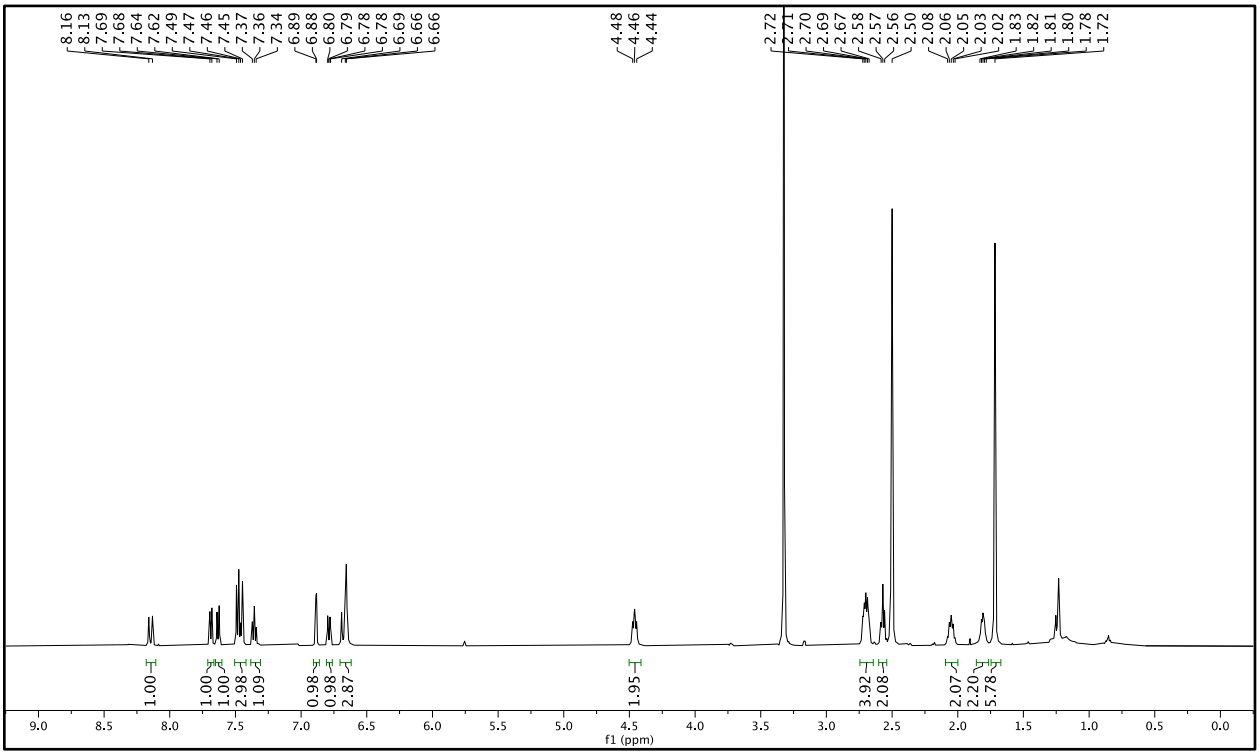

Compound 41: ^{13}C NMR (125 MHz, DMSO-d_6)

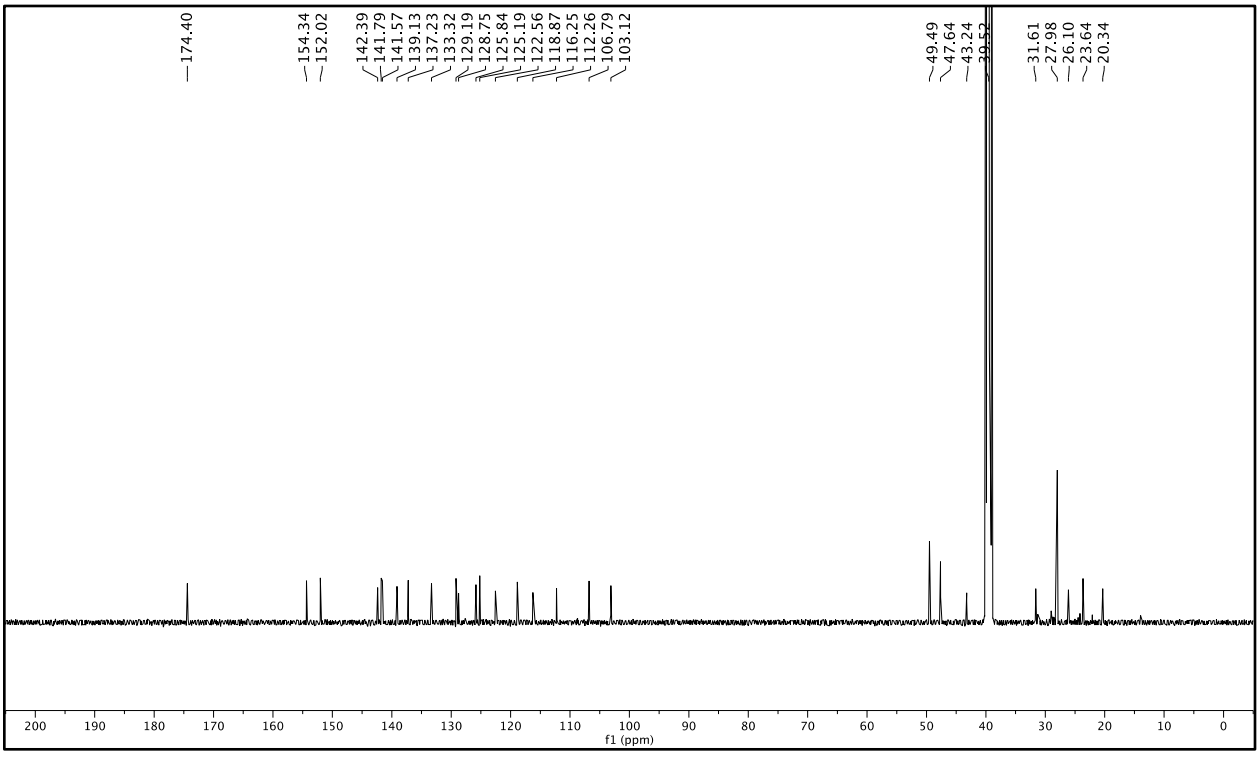

Compound PA-HD-FAAH: ^{1}H NMR (500 MHz, 1:1 v/v CD_3OD:$CDCl_3$)

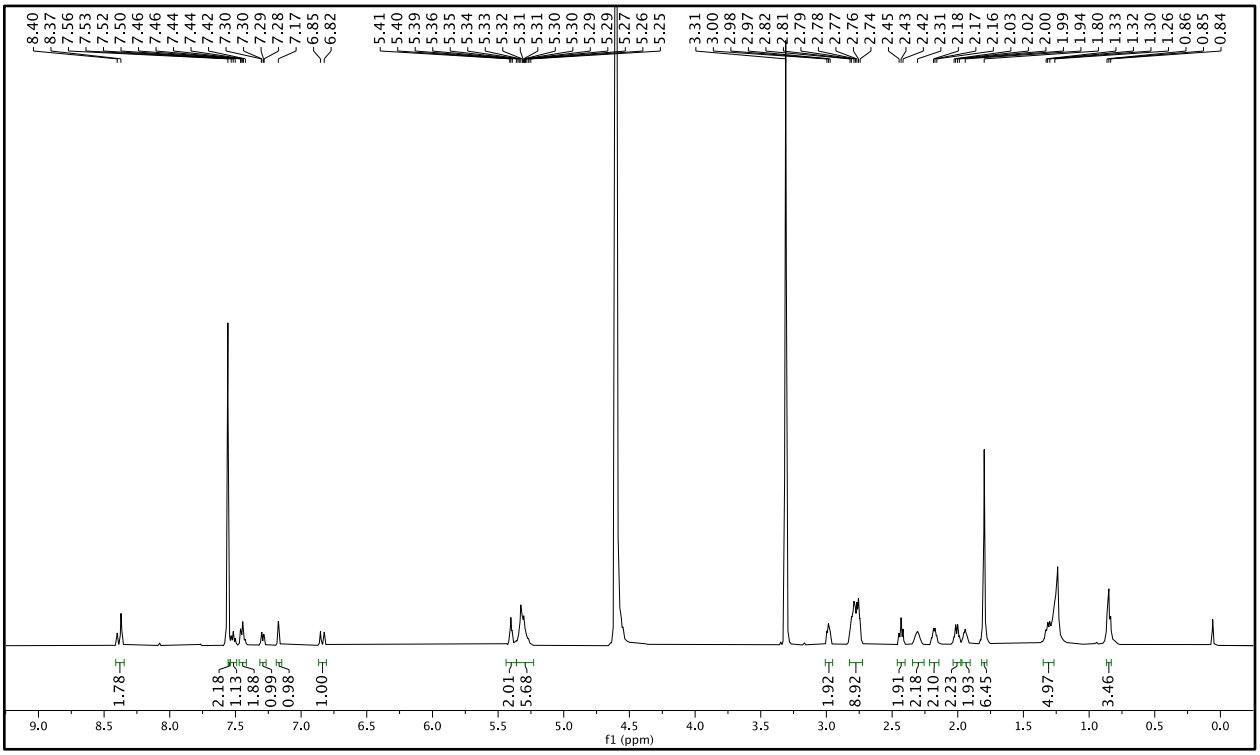

Compound PA-HD-FAAH: ^{13}C NMR (125 MHz, 1:1 v/v CD_3OD:$CDCl_3$)

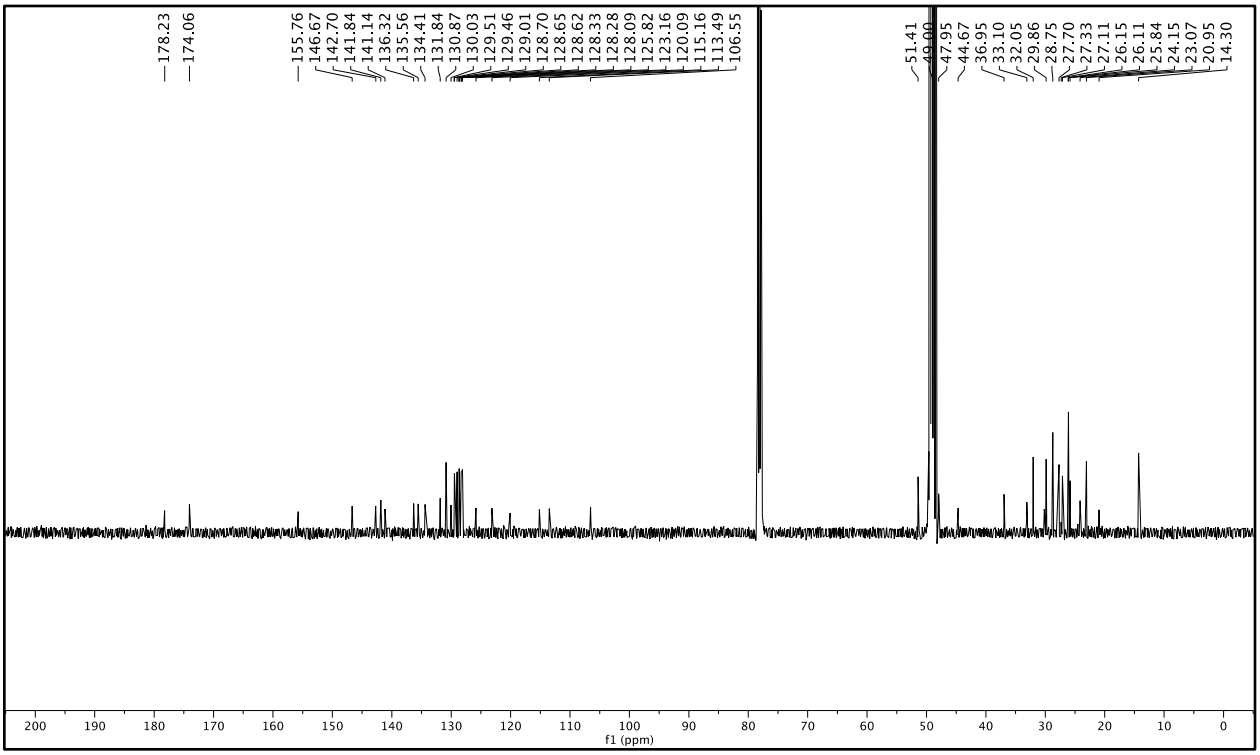

5.11 Acknowledgement of contributions

M.Y.L. and S.H.G. performed *in vitro*, *in cellulo*, and animal imaging with assistance from Z.Z. and A.B.. A.K.Y synthesized PA ABS probes. All authors analyzed and interpreted the data.

REFERENCES

1. Albers, A. E., Rawls, K. A. & Chang, C. J. Activity-based fluorescent reporters for monoamine oxidases in living cells. *Chemical Communications* 4647–4649 (2007) doi:10.1039/B713190A.
2. Bruemmer, K. J., Crossley, S. W. M. & Chang, C. J. Activity-Based Sensing: A Synthetic Methods Approach for Selective Molecular Imaging and Beyond. *Angewandte Chemie International Edition* **59**, 13734–13762 (2020).
3. Ibrahim, M. A., Hazhirkarzar, B. & Dublin, A. B. Gadolinium Magnetic Resonance Imaging. *StatPearls* (2021).
4. Carroll, V. *et al.* A boronate-caged [18F]FLT probe for hydrogen peroxide detection using positron emission tomography. *Journal of the American Chemical Society* **136**, 14742–14745 (2014).
5. Longkumer, I. Y. & Kumar, R. Bioluminescence in Insect. *Int.J.Curr.Microbiol.App.Sci* **7**, 187–193 (2018).
6. Cohen, I. B. A History of Luminescence From the Earliest Times Until 1900. By E. Newton Harvey. [Memoirs of the American Philosophical Society, Volume 44]. (Philadelphia: the Society. 1957. Pp. xxiv, 692. $6.00.). *The American Historical Review* **63**, 937–939 (1958).
7. Green, A. A. & McElroy, W. D. Crystalline firefly luciferase. *Biochimica et Biophysica Acta* **20**, 170–176 (1956).
8. Williams, S. J. & Prescher, J. A. Building Biological Flashlights: Orthogonal Luciferases and Luciferins for in Vivo Imaging. *Accounts of Chemical Research* 3039–3050 (2019) doi:10.1021/ACS.ACCOUNTS.9B00391/ASSET/IMAGES/ACS.ACCOUNTS.9B00391.SOCIAL.JPEG_V03.
9. Yadav, A. K. *et al.* Activity-Based NIR Bioluminescence Probe Enables Discovery of Diet-Induced Modulation of the Tumor Microenvironment via Nitric Oxide. *ACS Central Science* acscentsci.1c00317 (2022) doi:10.1021/ACSCENTSCI.1C00317.
10. Yevtodiyenko, A. *et al.* Portable bioluminescent platform for in vivo monitoring of biological processes in non-transgenic animals. *Nature Communications 2021 12:1* **12**, 1–12 (2021).
11. Bruemmer, K. J. *et al.* Chemiluminescent Probes for Activity-Based Sensing of Formaldehyde Released from Folate Degradation in Living Mice. *Angewandte Chemie International Edition* **57**, 7508–7512 (2018).
12. Yang, Y. *et al.* NIR-II Chemiluminescence Molecular Sensor for In Vivo High-Contrast Inflammation Imaging. *Angewandte Chemie* **132**, 18538–18543 (2020).
13. Fan, J., Yang, M., Zhang, J., Shabat, D. & Peng, X. Near-infrared chemiluminescent probe for real-time monitoring singlet oxygen in cells and mice model. *ACS Sensors* **5**, 3158–3164 (2020).
14. Wang, Y. *et al.* Toward in vivo biopsy of melanoma based on photoacoustic and ultrasound dual imaging with an integrated detector. *Biomedical Optics Express, Vol. 7, Issue 2, pp. 279-286* **7**, 279–286 (2016).
15. Zhang, J., Duan, F., Liu, Y. & Nie, L. High-resolution photoacoustic tomography for early-stage cancer detection and its clinical translation. *Radiology: Imaging Cancer* **2**, (2020).

16. Zhang, P. *et al.* High-resolution deep functional imaging of the whole mouse brain by photoacoustic computed tomography in vivo. *Journal of Biophotonics* **11**, e201700024 (2018).
17. Shemetov, A. A. *et al.* A near-infrared genetically encoded calcium indicator for in vivo imaging. *Nature Biotechnology 2020 39:3* **39**, 368–377 (2020).
18. Li, M., Tang, Y. & Yao, J. Photoacoustic tomography of blood oxygenation: A mini review. *Photoacoustics* **10**, 65–73 (2018).
19. Mantri, Y. *et al.* Photoacoustic monitoring of angiogenesis predicts response to therapy in healing wounds. *Wound Repair and Regeneration* **30**, 258–267 (2022).
20. Hochuli, R., An, L., Beard, P. C. & Cox, B. T. Estimating blood oxygenation from photoacoustic images: can a simple linear spectroscopic inversion ever work? *https://doi.org/10.1117/1.JBO.24.12.121914* **24**, 121914 (2019).
21. James, M. L. & Gambhir, S. S. A molecular imaging primer: Modalities, imaging agents, and applications. *Physiological Reviews* **92**, 897–965 (2012).
22. East, A. K., Lucero, M. Y. & Chan, J. New directions of activity-based sensing for in vivo NIR imaging. *Chemical Science* **12**, 3393–3405 (2021).
23. Gardner, S. H., Reinhardt, C. J. & Chan, J. Advances in Activity-Based Sensing Probes for Isoform-Selective Imaging of Enzymatic Activity. *Angewandte Chemie International Edition* **60**, 5000–5009 (2021).
24. Levi, J. *et al.* Design, synthesis, and imaging of an activatable photoacoustic probe. *Journal of the American Chemical Society* **132**, 11264–11269 (2010).
25. Levi, J. *et al.* Molecular photoacoustic imaging of follicular thyroid carcinoma. *Clinical Cancer Research* **19**, 1494–1502 (2013).
26. Li, H., Zhang, P., Smaga, L. P., Hoffman, R. A. & Chan, J. Photoacoustic Probes for Ratiometric Imaging of Copper(II). *Journal of the American Chemical Society* **137**, 15628–15631 (2015).
27. Reinhardt, C. J., Zhou, E. Y., Jorgensen, M. D., Partipilo, G. & Chan, J. A Ratiometric Acoustogenic Probe for in Vivo Imaging of Endogenous Nitric Oxide. *Journal of the American Chemical Society* **140**, 1011–1018 (2018).
28. Knox, H. J., Kim, T. W., Zhu, Z. & Chan, J. Photophysical Tuning of N-Oxide-Based Probes Enables Ratiometric Photoacoustic Imaging of Tumor Hypoxia. *ACS Chemical Biology* **13**, 1838–1843 (2018).
29. Zhou, E. Y., Knox, H. J., Liu, C., Zhao, W. & Chan, J. A Conformationally Restricted Aza-BODIPY Platform for Stimulus-Responsive Probes with Enhanced Photoacoustic Properties. *Journal of the American Chemical Society* **141**, 17601–17609 (2019).
30. Reinhardt, C. J., Xu, R. & Chan, J. Nitric oxide imaging in cancer enabled by steric relaxation of a photoacoustic probe platform. *Chemical Science* **11**, 1587–1592 (2020).
31. Knox, H. J. *et al.* A bioreducible N-oxide-based probe for photoacoustic imaging of hypoxia. *Nature Communications 2017 8:1* **8**, 1–9 (2017).
32. Moore, C. *et al.* Activatable Carbocyanine Dimers for Photoacoustic and Fluorescent Detection of Protease Activity. *ACS Sensors* **6**, 2356–2365 (2021).
33. Zhou, E. Y. *et al.* Near-Infrared Photoactivatable Nitric Oxide Donors with Integrated Photoacoustic Monitoring. *Journal of the American Chemical Society* **140**, 11686–11697 (2018).
34. Reinhardt, C. J. & Chan, J. Development of Photoacoustic Probes for in Vivo Molecular Imaging. *Biochemistry* **57**, 194–199 (2018).

35. Knox, H. J. & Chan, J. Acoustogenic Probes: A New Frontier in Photoacoustic Imaging. *Accounts of Chemical Research* **51**, 2897–2905 (2018).
36. Yu, X. *et al.* Deciphering of cerebrovasculatures via ICG-assisted NIR-II fluorescence microscopy. *Journal of Materials Chemistry B* **7**, 6623–6629 (2019).
37. Polom, W., Markuszewski, M., Rho, Y. S. & Matuszewski, M. Usage of invisible near infrared light (NIR) fluorescence with indocyanine green (ICG) and methylene blue (MB) in urological oncology. Part 1. *Central European Journal of Urology* **67**, 142 (2014).
38. Hong, G. *et al.* Multifunctional in vivo vascular imaging using near-infrared II fluorescence. Nature Medicine. *Nature Publishing Group* **18**, 1841–1846 (2012).
39. Bhavane, R., Starosolski, Z., Stupin, I., Ghaghada, K. B. & Annapragada, A. NIR-II fluorescence imaging using indocyanine green nanoparticles. *Scientific Reports 2018 8:1* **8**, 1–10 (2018).
40. Dong, Y. *et al.* Anti-tumor evaluation of a novel methoxyphenyl substituted chlorin photosensitizer for photodynamic therapy. *Journal of Photochemistry and Photobiology B: Biology* **211**, 112015 (2020).
41. Hopkins, T., Ukani, R. & Kopelman, R. Intracellular Photodynamic Activity of Chlorin e6 Containing Nanoparticles. *International journal of nanomedicine and nanosurgery* **2**, (2016).
42. Randall, L. M., Wenham, R. M., Low, P. S., Dowdy, S. C. & Tanyi, J. L. A phase II, multicenter, open-label trial of OTL38 injection for the intra-operative imaging of folate receptor-alpha positive ovarian cancer. *Gynecologic Oncology* **155**, 63–68 (2019).
43. Zhang, J., Duan, F., Liu, Y. & Nie, L. High-resolution photoacoustic tomography for early-stage cancer detection and its clinical translation. *Radiology: Imaging Cancer* **2**, (2020).
44. Kim, J. *et al.* Towards clinical photoacoustic and ultrasound imaging: Probe improvement and real-time graphical user interface. *Experimental Biology and Medicine* **245**, 321–329 (2020).
45. Valluru, K. S. & Willmann, J. K. Clinical photoacoustic imaging of cancer. *Ultrasonography* **35**, 267 (2016).
46. Wang, S., Lin, J., Wang, T., Chen, X. & Huang, P. Recent advances in photoacoustic imaging for deep-tissue biomedical applications. *Theranostics* **6**, 2394–2413 (2016).
47. Mantri, Y. *et al.* Point-of-Care Ultrasound as a Tool to Assess Wound Size and Tissue Regeneration after Skin Grafting. *Ultrasound in Medicine & Biology* **47**, 2550–2559 (2021).
48. Mantri, Y. *et al.* Photoacoustic monitoring of angiogenesis predicts response to therapy in healing wounds. *medRxiv* 2021.10.13.21264867 (2021) doi:10.1101/2021.10.13.21264867.
49. Lin, C. Y. *et al.* Photoacoustic Imaging for Noninvasive Periodontal Probing Depth Measurements. *Journal of Dental Research* **97**, 23–30 (2018).
50. Moore, C. & Jokerst, J. v. Photoacoustic Ultrasound for Enhanced Contrast in Dental and Periodontal Imaging. *Dental Ultrasound in Periodontology and Implantology* 215–230 (2021) doi:10.1007/978-3-030-51288-0_11.
51. Moore, C. *et al.* Photoacoustic imaging for monitoring periodontal health: A first human study. *Photoacoustics* **12**, 67 (2018).
52. Yang, S., Tan, X., Tang, L. & Yang, Q. Near-Infrared-II Bioimaging for in Vivo Quantitative Analysis. *Frontiers in Chemistry* **9**, 926 (2021).

53. Chen, T. *et al.* Dual activated NIR-II fluorescence and photoacoustic imaging-guided cancer chemo-radiotherapy using hybrid plasmonic-fluorescent assemblies. *Nano Research 2020 13:12* **13**, 3268–3277 (2020).
54. Lyu, Y., Li, J. & Pu, K. Second Near-Infrared Absorbing Agents for Photoacoustic Imaging and Photothermal Therapy. *Small Methods* **3**, 1900553 (2019).
55. Yin, C. *et al.* Organic Semiconducting Polymer Nanoparticles for Photoacoustic Labeling and Tracking of Stem Cells in the Second Near-Infrared Window. *ACS Nano* **12**, 12201–12211 (2018).
56. Wang, H. *et al.* Three-dimensional interventional photoacoustic imaging for biopsy needle guidance with a linear array transducer. *Journal of Biophotonics* **12**, e201900212 (2019).
57. Steinberg, I. *et al.* Photoacoustic clinical imaging. *Photoacoustics* **14**, 77 (2019).
58. Reinhardt, C. J., Zhou, E. Y., Jorgensen, M. D., Partipilo, G. & Chan, J. A Ratiometric Acoustogenic Probe for in Vivo Imaging of Endogenous Nitric Oxide. *Journal of the American Chemical Society* **140**, 1011–1018 (2018).
59. Shanbhag, V. C. *et al.* Copper metabolism as a unique vulnerability in cancer. *Biochimica et Biophysica Acta (BBA) - Molecular Cell Research* **1868**, 118893 (2021).
60. Yücel, I. *et al.* Serum copper and zinc levels and copper/zinc ratio in patients with breast cancer. *Biological Trace Element Research 1994 40:1* **40**, 31–38 (1994).
61. Adachi, S., Takemoto, K., Ohshima, S., Shimizu, Y. & Takahama, M. Metal concentrations in lung tissue of subjects suffering from lung cancer. *International Archives of Occupational and Environmental Health 1991 63:3* **63**, 193–197 (1991).
62. Zhang, X. & Yang, Q. Association between serum copper levels and lung cancer risk: A meta-analysis. *Journal of International Medical Research* **46**, 4863–4873 (2018).
63. Cotruvo, J. A., Aron, A. T., Ramos-Torres, K. M. & Chang, C. J. Synthetic fluorescent probes for studying copper in biological systems. *Chemical Society reviews* **44**, 4400 (2015).
64. Zhou, E. Y., Knox, H. J., Liu, C., Zhao, W. & Chan, J. A Conformationally Restricted Aza-BODIPY Platform for Stimulus-Responsive Probes with Enhanced Photoacoustic Properties. *Journal of the American Chemical Society* **141**, 17601–17609 (2019).
65. Wang, S. *et al.* Activatable Small-Molecule Photoacoustic Probes that Cross the Blood–Brain Barrier for Visualization of Copper(II) in Mice with Alzheimer's Disease. *Angewandte Chemie International Edition* **58**, 12415–12419 (2019).
66. Taki, M., Iyoshi, S., Ojida, A., Hamachi, I. & Yamamoto, Y. Development of highly sensitive fluorescent probes for detection of intracellular copper(I) in living systems. *Journal of the American Chemical Society* **132**, 5938–5939 (2010).
67. Traverso, N. *et al.* Role of glutathione in cancer progression and chemoresistance. *Oxidative Medicine and Cellular Longevity* (2013) doi:10.1155/2013/972913.
68. Lu, S. C. Dysregulation of glutathione synthesis in liver disease. *Liver Research* **4**, 64–73 (2020).
69. Butler, I. B., Schoonen, M. A. A. & Rickard, D. T. Removal of dissolved oxygen from water: A comparison of four common techniques. *Talanta* **41**, 211–215 (1994).
70. Shanbhag, V. C. *et al.* Copper metabolism as a unique vulnerability in cancer. *Biochimica et Biophysica Acta (BBA) - Molecular Cell Research* **1868**, 118893 (2021).
71. Baldari, S., Rocco, G. di & Toietta, G. Current Biomedical Use of Copper Chelation Therapy. *International Journal of Molecular Sciences 2020, Vol. 21, Page 1069* **21**, 1069 (2020).

72. Khan, G. & Merajver, S. Copper chelation in cancer therapy using tetrathiomolybdate: an evolving paradigm. *http://dx.doi.org/10.1517/13543780902845622* **18**, 541–548 (2009).
73. Dracopoli, N. C. & Boguski, M. S. The Evolution of Oncology Companion Diagnostics from Signal Transduction to Immuno-Oncology. *Trends in Pharmacological Sciences* **38**, 41–54 (2017).
74. Agarwal, A., Ressler, D. & Snyder, G. Pharmacogenomics and Personalized Medicine Dovepress The current and future state of companion diagnostics. *Pharmacogenomics and Personalized Medicine* **8**, 99–110 (2015).
75. Forman, H. J., Zhang, H. & Rinna, A. Glutathione: Overview of its protective roles, measurement, and biosynthesis. *Molecular Aspects of Medicine* **30**, 1–12 (2009).
76. Balendiran, G. K., Dabur, R. & Fraser, D. The role of glutathione in cancer. *Cell biochemistry and function* **22**, 343–352 (2004).
77. Gamcsik, M. P., Kasibhatla, M. S., Teeter, S. D. & Colvin, O. M. Glutathione Levels in Human Tumors. *Biomarkers : biochemical indicators of exposure, response, and susceptibility to chemicals* **17**, 671 (2012).
78. Giustarini, D. *et al.* Glutathione, glutathione disulfide, and S-glutathionylated proteins in cell cultures. *Free Radical Biology and Medicine* **89**, 972–981 (2015).
79. Selective Modulation of Glutathione Levels in Human Normal versus Tumor Cells and Subsequent Differential Response to Chemotherapy Drugs1 | Cancer Research | American Association for Cancer Research. https://aacrjournals.org/cancerres/article/46/6/2845/490895/Selective-Modulation-of-Glutathione-Levels-in.
80. Zhang, J. *et al.* Synthesis and characterization of a series of highly fluorogenic substrates for glutathione transferases, a general strategy. *Journal of the American Chemical Society* **133**, 14109–14119 (2011).
81. Shibata, A. *et al.* Fluorogenic probes using 4-substituted-2-nitrobenzenesulfonyl derivatives as caging groups for the analysis of human glutathione transferase catalyzed reactions. *The Analyst* **138**, 7326–7330 (2013).
82. Lee, M. H. *et al.* Disulfide-cleavage-triggered chemosensors and their biological applications. *Chemical reviews* **113**, 5071–5109 (2013).
83. Maeda, H. *et al.* 2,4-Dinitrobenzenesulfonyl fluoresceins as fluorescent alternatives to Ellman's reagent in thiol-quantification enzyme assays. *Angewandte Chemie (International ed. in English)* **44**, 2922–2925 (2005).
84. Hansch, C., Leo, A. & Taft, R. W. A survey of Hammett substituent constants and resonance and field parameters. *Chemical Reviews* **91**, 165–195 (2002).
85. van Iersel, M. L. P. S. *et al.* Inhibition of glutathione S-transferase activity in human melanoma cells by alpha,beta-unsaturated carbonyl derivatives. Effects of acrolein, cinnamaldehyde, citral, crotonaldehyde, curcumin, ethacrynic acid, and trans-2-hexenal. *Chemico-biological interactions* **102**, 117–132 (1996).
86. Rahman, I., Kode, A. & Biswas, S. K. Assay for quantitative determination of glutathione and glutathione disulfide levels using enzymatic recycling method. *Nature protocols* **1**, 3159–3165 (2006).
87. Manegold, C. Gemcitabine (Gemzar) in non-small cell lung cancer. *Expert review of anticancer therapy* **4**, 345–360 (2004).

88. Hayashi, H., Kurata, T. & Nakagawa, K. Gemcitabine: efficacy in the treatment of advanced stage nonsquamous non-small cell lung cancer. *Clinical Medicine Insights. Oncology* **5**, 177–184 (2011).
89. Toschi, L., Finocchiaro, G., Bartolini, S., Gioia, V. & Cappuzzo, F. Role of gemcitabine in cancer therapy. *Future oncology (London, England)* **1**, 7–17 (2005).
90. Miao, H., Chen, X. & Luan, Y. Small Molecular Gemcitabine Prodrugs for Cancer Therapy. *Current medicinal chemistry* **27**, 5562–5582 (2020).
91. Ullman-Culleré, M. H. & Foltz, C. J. Body Condition Scoring: A Rapid and Accurate Method for Assessing Health Status in Mice. (1999).
92. Milovanovic, I., Stjepanovic, M. & Mitrovic, D. Distribution patterns of the metastases of the lung carcinoma in relation to histological type of the primary tumor: An autopsy study. *Annals of thoracic medicine* **12**, 191–198 (2017).
93. Huang, J., Jiang, Y., Li, J., Huang, J. & Pu, K. Molecular Chemiluminescent Probes with a Very Long Near-Infrared Emission Wavelength for in Vivo Imaging. *Angewandte Chemie International Edition* **60**, 3999–4003 (2021).
94. Gardner, S. H. *et al.* A General Approach to Convert Hemicyanine Dyes into Highly Optimized Photoacoustic Scaffolds for Analyte Sensing**. *Angewandte Chemie - International Edition* **60**, 18860–18866 (2021).
95. Glutathione Probes. https://ursabioscience.com/technology/gsh-probes.
96. Schindelin, J. *et al.* Fiji: an open-source platform for biological-image analysis. *Nature Methods 2012 9:7* **9**, 676–682 (2012).
97. Yuan, L. *et al.* A unique approach to development of near-infrared fluorescent sensors for in vivo imaging. *Journal of the American Chemical Society* **134**, 13510–13523 (2012).
98. Uppu, R. M. Synthesis of peroxynitrite using isoamyl nitrite and hydrogen peroxide in a homogeneous solvent system. *Analytical Biochemistry* **354**, 165–168 (2005).
99. Faustino-Rocha, A. *et al.* Estimation of rat mammary tumor volume using caliper and ultrasonography measurements. *Lab animal* **42**, 217–224 (2013).
100. Zhang, J., Ning, L., Zeng, Z. & Pu, K. Development of Second Near-Infrared Photoacoustic Imaging Agents. *Trends in Chemistry* **3**, 305–317 (2021).
101. Sun, A. *et al.* Evaluation of visible NIR-I and NIR-II light penetration for photoacoustic imaging in rat organs. *Optics express* **28**, 9002 (2020).
102. Upputuri, P. K. & Pramanik, M. Photoacoustic imaging in the second near-infrared window: a review. *Journal of biomedical optics* **24**, 1 (2019).
103. Feng, W. *et al.* Lighting Up NIR-II Fluorescence in Vivo: An Activable Probe forNoninvasive Hydroxyl Radical Imaging. *Anal. Chem* **91**, 1 (2019).
104. Cosco, E. D. *et al.* Flavylium Polymethine Fluorophores for Near- and Shortwave Infrared Imaging. *Angewandte Chemie* **129**, 13306–13309 (2017).
105. Usama, S. M., Lin, C. M. & Burgess, K. On the Mechanisms of Uptake of Tumor-Seeking Cyanine Dyes. *Bioconjugate Chemistry* **29**, 3886–3895 (2018).
106. Wang, X. *et al.* Screening and investigation of a cyanine fluorescent probe for simultaneous sensing of glutathione and cysteine under single excitation. *Chemical communications (Cambridge, England)* **50**, 15439–15442 (2014).
107. Lin, Y., Xu, J. & Lan, H. Tumor-associated macrophages in tumor metastasis: biological roles and clinical therapeutic applications. *Journal of hematology & oncology* **12**, (2019).
108. Hermes, D. J. *et al.* GPR18 drives FAAH inhibition-induced neuroprotection against HIV-1 Tat-induced neurodegeneration. *Experimental Neurology* **341**, (2021).

109. Chiurchiù, V. *et al.* Detailed characterization of the endocannabinoid system in human macrophages and foam cells, and anti-inflammatory role of type-2 cannabinoid receptor. *Atherosclerosis* **233**, 55–63 (2014).
110. Gasperi, V. *et al.* Regulation of inflammation and proliferation of human bladder carcinoma cells by type-1 and type-2 cannabinoid receptors. *Life Sciences* **138**, 41–51 (2015).
111. Yapa, U. *et al.* High-performance liquid chromatography-tandem mass spectrometry assay of fatty acid amide hydrolase (FAAH) in blood: FAAH inhibition as clinical biomarker. *Analytical Biochemistry* **421**, 556–565 (2012).
112. Yuan, Y. *et al.* Intracellular Self-Assembly of Cyclic d -Luciferin Nanoparticles for Persistent Bioluminescence Imaging of Fatty Acid Amide Hydrolase. *ACS Nano* **10**, 7147–7153 (2016).
113. Tian, M. *et al.* A NIR fluorescent probe for fatty acid amide hydrolase bioimaging and its application in development of inhibitors. *Journal of Materials Chemistry B* **9**, 6460–6465 (2021).
114. Dato, F. M., Maaßen, A., Goldfuß, B. & Pietsch, M. Characterization of fatty acid amide hydrolase activity by a fluorescence-based assay. *Analytical Biochemistry* **546**, 50–57 (2018).
115. Mofford, D. M., Adams, S. T., Reddy, G. S. K. K., Reddy, G. R. & Miller, S. C. Luciferin Amides Enable in Vivo Bioluminescence Detection of Endogenous Fatty Acid Amide Hydrolase Activity. *Journal of the American Chemical Society* **137**, 8684–8687 (2015).
116. Boldrup, L., Wilson, S. J., Barbier, A. J. & Fowler, C. J. A simple stopped assay for fatty acid amide hydrolase avoiding the use of a chloroform extraction phase. *Journal of Biochemical and Biophysical Methods* **60**, 171–177 (2004).
117. Wang, Y. *et al.* A novel scintillation proximity assay for fatty acid amide hydrolase compatible with inhibitor screening. *Analytical Biochemistry* **354**, 35–42 (2006).
118. Wang, Y. *et al.* High-throughput screening for the discovery of inhibitors of fatty acid amide hydrolase using a microsome-based fluorescent assay. *Journal of Biomolecular Screening* **11**, 519–527 (2006).
119. Mofford, D. M. & Miller, S. C. Luciferins Behave Like Drugs. *ACS Chemical Neuroscience* **6**, 1273–1275 (2015).
120. Wang, Y. *et al.* A novel scintillation proximity assay for fatty acid amide hydrolase compatible with inhibitor screening. *Analytical Biochemistry* **354**, 35–42 (2006).
121. Cumming, P. & Vasdev, N. Molecular Imaging Studies of Second Messenger Pathways: Looking Deeper than the Membrane. in 137–148 (2012). doi:10.1007/7657_2012_52.
122. Rempel, B. P., Price, E. W. & Phenix, C. P. Molecular Imaging of Hydrolytic Enzymes Using PET and SPECT. *Molecular Imaging* vol. 16 (2017).
123. Boileau, I. *et al.* The fatty acid amide hydrolase C385A variant affects brain binding of the positron emission tomography tracer [11C] CURB. *Journal of Cerebral Blood Flow and Metabolism* **35**, 1237–1240 (2015).
124. Green, D. G. J. *et al.* Fatty acid amide hydrolase binding is inversely correlated with amygdalar functional connectivity: A combined positron emission tomography and magnetic resonance imaging study in healthy individuals. *Journal of Psychiatry and Neuroscience* **46**, E238–E246 (2021).

125. Skaddan, M. B. *et al.* The synthesis and in vivo evaluation of [18F]PF-9811: A novel PET ligand for imaging brain fatty acid amide hydrolase (FAAH). *Nuclear Medicine and Biology* **39**, 1058–1067 (2012).
126. Sadovski, O. *et al.* Development and characterization of a promising fluorine-18 labelled radiopharmaceutical for in vivo imaging of fatty acid amide hydrolase. *Bioorganic and Medicinal Chemistry* **21**, 4351–4357 (2013).
127. Wyffels, L. *et al.* Synthesis, in vitro and in vivo evaluation, and radiolabeling of aryl anandamide analogues as candidate radioligands for in vivo imaging of fatty acid amide hydrolase in the brain. *Journal of Medicinal Chemistry* **52**, 4613–4622 (2009).
128. Pandey, M. K. *et al.* Synthesis and preliminary evaluation of N-(16-18F-fluorohexadecanoyl) ethanolamine (18F-FHEA) as a PET probe of N-acylethanolamine metabolism in mouse brain. *ACS Chemical Neuroscience* **5**, 793–802 (2014).
129. Veronesi, M. *et al.* Fluorine nuclear magnetic resonance-based assay in living mammalian cells. *Analytical Biochemistry* **495**, 52–59 (2016).
130. Rotstein, B. H. *et al.* PET imaging of fatty acid amide hydrolase with [18F]DOPP in nonhuman primates. *Molecular Pharmaceutics* **11**, 3832–3838 (2014).
131. Wang, L. *et al.* Synthesis and preclinical evaluation of sulfonamidobased [11C-Carbonyl]-carbamates and ureas for imaging monoacylglycerol lipase. *Theranostics* **6**, 1145–1159 (2016).
132. Melford, S. E., Taylor, A. H. & Konje, J. C. Nitric oxide positively affects endometrial receptivity via FAAH and NAPE-PLD in vitro. *Reproduction and Fertility* **2**, 107–116 (2021).
133. Peciña, M. *et al.* FAAH selectively influences placebo effects. *Molecular Psychiatry* **19**, 385–391 (2014).
134. Tourïo, C., Oveisi, F., Lockney, J., Piomelli, D. & Maldonado, R. FAAH deficiency promotes energy storage and enhances the motivation for food. *International Journal of Obesity* **34**, 557–568 (2010).
135. Bachkangi, P., Taylor, A. H., Bari, M., Maccarrone, M. & Konje, J. C. Prediction of preterm labour from a single blood test: The role of the endocannabinoid system in predicting preterm birth in high-risk women. *European Journal of Obstetrics and Gynecology and Reproductive Biology* **243**, 1–6 (2019).
136. Coria, S. M. *et al.* Strain differences in the expression of endocannabinoid genes and in cannabinoid receptor binding in the brain of Lewis and Fischer 344 rats. *Progress in Neuro-Psychopharmacology and Biological Psychiatry* **53**, 15–22 (2014).
137. Cable, J. C., Tan, G. D., Alexander, S. P. & O'Sullivan, S. E. The activity of the endocannabinoid metabolising enzyme fatty acid amide hydrolase in subcutaneous adipocytes correlates with BMI in metabolically healthy humans. *Lipids in Health and Disease* **10**, (2011).